

SMR  
(1+3)

# NASA CR-175288

**DESIGN AND FABRICATION OF A LONG-LIFE STIRLING CYCLE  
COOLER FOR SPACE APPLICATION**

**Phases I and II - Engineering Model**

**F. Stolfi, M. Goldowsky, C. Keung, L. Knox, E. Lindale,  
R. Maresca, J. Ricciardelli, P. Shapiro**

**PHILIPS LABORATORIES**

**A Division of North American Philips Corporation  
Briarcliff Manor, New York 10510**

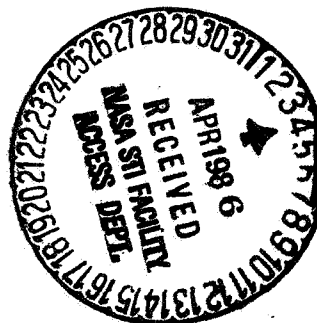
(NASA-CR-175288) DESIGN AND FABRICATION OF  
A LONG-LIFE STIRLING CYCLE COOLER FOR SPACE  
APPLICATION. PHASES 1 AND 2: ENGINEERING  
MODEL Final Report, 29 Sep. 1978 - 31 Dec.  
1982 (Philips Labs.) 221 p

N86-21714  
THRU  
N86-21717  
Unclas  
00564

CSCL 131 00/31

**March 1983**

**Final Report for Period September 1978 - December 1982**



**Prepared for**

**NASA  
GODDARD SPACE FLIGHT CENTER  
Greenbelt, Maryland 20771**

DESIGN AND FABRICATION OF A LONG-LIFE STIRLING CYCLE  
COOLER FOR SPACE APPLICATION

Phases I and II - Engineering Model

F. Stolfi, M. Goldowsky, C. Keung, L. Knox, E. Lindale,  
R. Maresca, J. Ricciardelli, P. Shapiro

PHILIPS LABORATORIES  
A Division of North American Philips Corporation  
Briarcliff Manor, New York 10510

March 1983  
Final Report for Period September 1978 - December 1982

Prepared for  
NASA  
GODDARD SPACE FLIGHT CENTER  
Greenbelt, Maryland 20771



## PREFACE

The attainment of long life cryogenic refrigeration for spaceborne missions has been an elusive goal. Designs which use traditional mechanical elements, namely bearings, seals, linkages, and lubrication, are only marginally suitable due to traditional mechanical reasons, namely wear, fatigue, and friction. It was clear that a new approach was needed. The refrigerator system described herein is undeniably mechanical and yet, also undeniably, has eliminated the aforementioned mechanical problems by electronic means. The close interactions between the mechanics and electronics can be seen in this work; the disciplines of Thermodynamics, Dynamics and Material Science interact with the disciplines of Electromagnetics, Circuits, and Control Theory.

This report presents the problems associated with the life limiting aspects of conventional Stirling machines, and the novel means by which these problems are solved in the present model. Key topics are:

- The influence of mechanical and control system dynamics on the system design which would normally be constrained only by thermodynamic considerations.
- The analysis, design, fabrication, and testing of linear magnetic bearings, first proposed and reduced to practice by Philips Laboratories. A radial position sensor was developed and tested that is capable of measuring small displacements without temperature drifts.
- The development of linear dc motors and axial control electronics for a rectilinear drive. A dedicated fixture was designed and built to test the piston linear motor and controls.
- The use of only metal and ceramic materials for the internal parts to avoid organic contamination. This required the development of special fabrication techniques and the use of clearance seals.
- The design of a simple, passive counterbalance to minimize the vibration imposed on the cooler by the longitudinal motion of the piston and displacer.

For high efficiency, this laboratory prototype refrigerator, called the Engineering Model, uses the Stirling cycle, a thermodynamically reversible



derivation of an engine proposed by a Scottish minister, Robert Stirling, in 1816. Readers unfamiliar with the cycle are referred to the appendices which review the theory of the Stirling refrigerator and describe the analysis of the linear resonant approach, the novel features of which are applied to this design.

By successfully achieving the design goal of 5 Watts of refrigeration at 65°K, this laboratory prototype, has proved the concept feasibility of the approach, using magnetic bearings, clearance seals, and a rectilinear drive. By fabricating the unit of only metal and ceramic components and by eliminating any mechanical contact and wear, long unattended operation, although not proven, is obviously realizable. All of the design goals were met.

To apply this technology to a spaceborne mission, three further developments are needed:

- Reduction of input power and weight, and examination of the overall packaging of the refrigerator and electronics.
- Analysis, design, and test of the ability of the configuration to survive launch.
- Fabrication of a set of redundant electronics designed for high reliability.

The first two of these developments had been proposed for the next phase of this program, a flight prototype model, and the work is currently underway.

## ACKNOWLEDGMENTS

The authors wish to express their appreciation to Dr. A. Sherman and M. Gasser of NASA Goddard Space Flight Center for their continued support, beginning with the project's conception and infancy in 1978, but more especially during its puberty in 1980. They had the managerial strength and wisdom to offer technical advice when asked, but to listen, understand and defer technical decision in the difficult times.

The authors also wish to acknowledge the cryogenic staff of Philips Laboratories under the leadership of A. Daniels, our mentor for all low temperature research. Those individuals include thermodynamicist: Dr. A. Sereny; materials engineers: Dr. R. Sweet, R. Bronnes, R. Eggleston and H. Meehan; electrical engineers: R. Geyer and G. Matuskovic; mechanical engineers: D. Lehrfeld and L. Skala; designers: J. Hedjuk, R. Wilhelm, and W. Slade; and technicians: H. Kolbinger, W. Hafner and J. O'Grady. In a real sense, it is only through their vision that success was achieved.

The authors wish to thank L. Miller for his administration of the contract and J. Lebid for his perseverance and creativity in editing this report and all other technical documentation for the program.

Finally, the authors realize that it is only through the diligence and skill of E. Harkins, R. Adams, R. Donnelly, M. Gaa, D. Kelly, J. Meehan, T. Nalesnik, A. Valinoti, H. Zwiefel and other members of the Philips instrument shop that this idea was transformed from paper concept to metal reality.



## TABLE OF CONTENTS

<u>Section</u>	<u>Page</u>
PREFACE.....	iii
ACKNOWLEDGMENTS.....	v
LIST OF ILLUSTRATIONS.....	xi
LIST OF TABLES.....	xv
1. INTRODUCTION.....	1-1
2. DESCRIPTION OF SYSTEM.....	2-1
2.1 Background.....	2-1
2.2 Major Features of System.....	2-4
2.2.1 Rectilinear Drive.....	2-4
2.2.2 Linear Electric Motors.....	2-5
2.2.3 Magnetic Bearings.....	2-7
2.2.4 Clearance Seals.....	2-8
2.2.5 All-Metal/Ceramic Surfaces.....	2-11
2.2.6 Electronic Axial-Control System.....	2-12
2.3 Engineering Model Cooler.....	2-14
2.3.1 General.....	2-14
2.3.2 Expander Subassembly.....	2-17
2.3.3 Compressor Subassembly.....	2-18
2.3.4 Counterbalance Subassembly.....	2-19
3. THERMODYNAMIC AND DYNAMIC DESIGN.....	3-1
3.1 Introduction.....	3-1
3.2 Coupling of Thermodynamics and Dynamics of a Free- Displacer, Free-Piston, Stirling Cycle Refrigerator.....	3-5
3.2.1 Description of Linear Drive Mechanisms.....	3-5
3.2.2 Pressure Variation in a Stirling Refrigerator....	3-5
3.2.3 Cold Production and Input Power.....	3-7
3.2.4 Modeling of Electromechanics of Displacer and Piston.....	3-8
3.2.5 Control System Modeling.....	3-11
3.2.6 Summary.....	3-12
3.3 Clearance Seal Leakage.....	3-13
4. MAGNETIC BEARINGS.....	4-1
4.1 Introduction.....	4-1
4.2 Description of Bearing System.....	4-1
4.3 Linearized Analysis of Electromagnetic Actuators and Shaft Dynamics.....	4-4
4.3.1 General.....	4-4
4.3.2 Analysis.....	4-5

## TABLE OF CONTENTS (Cont'd.)

<u>Section</u>	<u>Page</u>
4.4 Determination of Magnetic Bearing Loads.....	4-20
4.4.1 Introduction.....	4-20
4.4.2 General Analysis.....	4-21
4.4.3 Calculation of Piston and Displacer Bearing Loads.....	4-34
4.5 Vibration Analysis.....	4-40
4.6 Radial Position Sensors.....	4-45
4.6.1 General.....	4-45
4.6.2 Measurement and Calibration.....	4-49
4.6.3 Sensor Electronics.....	4-54
4.6.4 Results.....	4-55
4.7 Bearing Current Driver.....	4-56
4.7.1 General.....	4-56
4.7.2 Circuit Analysis.....	4-57
4.8 Control System Modelling.....	4-59
4.8.1 General.....	4-59
4.8.2 Model.....	4-60
4.8.3 Predictions.....	4-62
4.9 Bearing Test Fixtures.....	4-72
4.9.1 General.....	4-72
4.9.2 Measurement Techniques.....	4-74
4.9.3 Results.....	4-76
4.10 Summary.....	4-78
5. LINEAR MOTORS AND AXIAL CONTROL ELECTRONICS.....	5-1
5.1 Introduction.....	5-1
5.2 Linear Motors.....	5-1
5.2.1 Description.....	5-1
5.2.2 General Analysis.....	5-4
5.2.3 Design Parameters.....	5-10
5.2.4 Piston Motor Test Fixture.....	5-12
5.2.5 Test Results.....	5-16
5.2.6 Summary.....	5-18
5.3 Axial Control Electronics.....	5-19
5.3.1 Description.....	5-19
5.3.2 Frequency Control Electronics.....	5-21
5.3.3 Phase Control Electronics.....	5-23
5.3.4 Motor Driver.....	5-25
5.3.5 Axial Position Transducers.....	5-28
5.3.6 Position Control Compensation.....	5-29
5.3.7 Summary.....	5-32
5.4 Conclusions.....	5-32
6. ELECTRONICS.....	6-1
6.1 Interlock System.....	6-1
6.2 Heater (Load) Control.....	6-5
6.3 Battery Backup.....	6-7
6.4 Pressure Transducer Amplifier.....	6-7

## TABLE OF CONTENTS (Cont'd.)

<u>Section</u>	<u>Page</u>
6.5 Instrument Rack Assembly.....	6-8
6.5.1 Description.....	6-8
6.5.2 Control Panel.....	6-11
7. COUNTERBALANCING SYSTEM.....	7-1
7.1 Design.....	7-1
7.1.1 General Description.....	7-1
7.1.2 Leaf Spring Suspension.....	7-1
7.1.3 Coil Spring.....	7-3
7.1.4 Resonant Behavior.....	7-4
7.1.5 Summary.....	7-5
7.2 Performance Estimates.....	7-5
7.3 Performance Data.....	7-8
7.4 Summary.....	7-10
8. MECHANICAL FABRICATION, CLEANING, AND ASSEMBLY.....	8-1
8.1 Fabrication.....	8-1
8.2 Cleaning and Assembly.....	8-3
9. TEST RESULTS.....	9-1
9.1 Measurements.....	9-1
9.2 Cooldown Curve.....	9-2
9.3 Performance Verification.....	9-3
10. CONCLUSIONS.....	10-1
 APPENDIX	
A A Small Free-Piston Stirling Refrigerator.....	A1
B Basic Theory of Stirling Cycle Refrigerator.....	B1



## LIST OF ILLUSTRATIONS

<u>Figure</u>		<u>Page</u>
2-1.	Schematic representation of a conventional Stirling refrigerator.....	2-1
2-2.	Contaminated displacer/regenerator.....	2-2
2-3.	Cross-sectional view of contaminated displacer/regenerator.	2-2
2-4.	Illustration of wear associated with dry seals.....	2-3
2-5.	Cross-sectional view of displacer and piston motors.....	2-5
2-6.	Cross-sectional view of piston motor.....	2-6
2-7.	Cross-sectional view of displacer motor.....	2-7
2-8.	Method of magnetically suspending shaft.....	2-7
2-9.	Typical cross section of magnetic bearing.....	2-8
2-10.	Schematic of conventional piston seal configuration.....	2-9
2-11.	Schematic of clearance seal configuration.....	2-10
2-12.	Block diagram of axial-control system.....	2-13
2-13.	Photograph of Engineering Model Cooler.....	2-15
2-14.	Cross-sectional view of Engineering Model Cooler.....	2-16
2-15.	Cross section of expander subassembly.....	2-17
2-16.	Cross section of compressor subassembly.....	2-18
2-17.	Cross section of counterbalance subassembly.....	2-19
3-1.	Cross section of Engineering Model showing helium passages.	3-4
3-2.	Water jacket of ambient heat exchanger.....	3-4
3-3.	Schematic of force balance.....	3-9
3-4.	Equivalent circuit of linear motor.....	3-9
3-5.	Block diagram of electromechanical dynamics.....	3-11
3-6.	Transfer function block for displacer impedance.....	3-12
4-1.	Geometry of magnetic bearing.....	4-2
4-2.	Radial force generation in magnetic bearing plane.....	4-2
4-3.	Eddy current sensor.....	4-3
4-4.	Block diagram of bearing control system.....	4-3
4-5.	Block diagram showing linearized effects of a common bias..	4-9
4-6.	Root locus showing effects of a common bias current.....	4-9
4-7.	Bearing representation showing center of gravity.....	4-10
4-8.	Geometry of motion about center of gravity.....	4-11
4-9.	Circumferential fluid flow and resulting pressure gradient.	4-12
4-10.	Cross section of magnetic bearing pole piece.....	4-15



# LIST OF ILLUSTRATIONS (Cont'd.)

<u>Figure</u>		<u>Page</u>
4-11.	Cross section which approximates pole piece.....	4-16
4-12.	Vector diagram of current, voltage, and flux in core.....	4-17
4-13.	Cross sections of piston motor.....	4-21
4-14.	Cross sections of displacer motor.....	4-23
4-15.	Permanent magnet segment showing parallel magnetic field which exists and ideal radial field.....	4-24
4-16.	Piston-motor magnet ring showing magnet segments and field misalignments.....	4-24
4-17.	Radial instability of nonconcentric cylinders.....	4-26
4-18.	Demagnetization curve of samarium cobalt.....	4-28
4-19.	2-D model of piston motor for determining fringing forces with MAGGY program.....	4-29
4-20.	2-D model of displacer motor for MAGGY analysis.....	4-29
4-21.	Model showing torsional instability of a magnet ring.....	4-30
4-22.	Linear motor stator-coil geometry.....	4-31
4-23.	Current flow cancellation in an even numbered layer winding.....	4-32
4-24.	Static bearing loads.....	4-32
4-25.	Displacer vibration model.....	4-40
4-26.	Piston vibration model.....	4-41
4-27.	Displacer calculated mode shapes.....	4-43
4-28.	Piston calculated mode shapes.....	4-43
4-29.	Configuration of eddy-current probes.....	4-46
4-30.	Phasor diagram of induced e.m.f. in coil.....	4-48
4-31.	Circuit model for eddy current probe.....	4-49
4-32.	Effective parallel resistance vs. position.....	4-52
4-33.	Test fixture for measuring resistance vs. position.....	4-51
4-34.	Effective parallel resistance vs. probe temperature.....	4-52
4-35.	Test Fixture for measuring resistance vs. temperature.....	4-52
4-36.	Sensor differential bridge.....	4-53
4-37.	Block diagram of sensor electronics.....	4-54
4-38.	Block diagram showing transfer functions of blocks.....	4-56
4-39.	Impedance of actuator pole pieces.....	4-58
4-40.	Measured closed-loop frequency response.....	4-59

# LIST OF ILLUSTRATIONS (Cont'd.)

<u>Figure</u>	<u>Page</u>
4-41. Block diagram of bearing control system.....	4-60
4-42. Magnetic circuit computer analysis output.....	4-64
4-43. Average calculated flux density in pole piece and armature.	4-65
4-44. Model of displacer mass and moment of inertia.....	4-66
4-45. Open loop transfer function of front displacer bearing.....	4-70
4-46. Step response of front displacer bearing.....	4-70
4-47. Frequency response of piston and displacer bearings.....	4-71
4-48. Bearing test fixture - 1st generation.....	4-73
4-49. Bearing test fixture - 2nd generation.....	4-73
4-50. Fixture in test stand.....	4-74
4-51. Technique for measuring open loop frequency response.....	4-75
4-52. AC "stiffness" of magnetic bearing system.....	4-76
4-53. Static load characteristic of magnetic bearing.....	4-77
4-54. Open-loop frequency response - test fixture.....	4-77
5-1. Schematic of linear motor for piston.....	5-2
5-2. Flux plot of linear motor for piston.....	5-2
5-3. Schematic of linear motor for displacer.....	5-4
5-4. Model for calculating efficiency of linear motor.....	5-6
5-5. Armature of piston motor with permanent magnets attached (on mandrel).....	5-11
5-6. Piston motor showing armature mounted to shaft and stator assembly ready for insertion into motor housing.....	5-11
5-7. Completed displacer.....	5-12
5-8. Piston-motor test fixture.....	5-14
5-9. Electronic axial control system.....	5-19
5-10. Block diagram of frequency controller.....	5-21
5-11. Harmonic distortion of cosine output of frequency controller.....	5-23
5-12. Block diagram of phase controller.....	5-24
5-13. Block diagram of motor current amplifier.....	5-25
5-14. Transformer equivalent model of linear motor.....	5-26
5-15. Effective impedance of piston system.....	5-27
5-16. Effective impedance of displacer system .....	5-28
5-17. Schematic of LVDT.....	5-29

# LIST OF ILLUSTRATIONS (Cont'd.)

<u>Figure</u>		<u>Page</u>
5-18.	General block diagram of piston and displacer axial control loop.....	5-30
5-19.	Frequency response of piston dynamics.....	5-31
5-20.	Frequency response of displacer dynamics.....	5-31
6-1.	System interlock control panel.....	6-4
6-2.	Block diagram of heater controller.....	6-6
6-3.	Photograph of Instrument Rack.....	6-9
6-4.	Control panel of Instrument Rack.....	6-12
7-1.	Schematic of vibration absorber.....	7-2
7-2.	Transverse stiffness and bending stress for flexure springs.....	7-3
7-3.	Vibration model of cooler/counterbalance system.....	7-5
7-4.	Transfer function of force transmitted to base.....	7-7
7-5.	Transfer function of residual force on cooler.....	7-8
7-6.	Vibration spectrum of cooler.....	7-9
8-1.	Cold finger/Dewar showing instrumentation.....	8-6
8-2.	Schematic of compressor subassembly during assembly procedure.....	8-8
8-3.	Completed compressor subassembly.....	8-9
8-4.	Completed expander subassembly on test stand.....	8-10
9-1.	Cooldown curve (temperature vs. time).....	9-2

# LIST OF TABLES

<u>Table</u>	<u>Page</u>
3-1. Thermodynamic Design Values.....	3-3
4-1. Distance from Bearing to Center of Motor.....	4-35
4-2. Data Used in Calculations of Gravity Loads.....	4-36
4-3. Linear Motor Forces.....	4-37
4-4. Summary of Piston Loads.....	4-38
4-5. RSS Load Summary for Piston Bearings.....	4-38
4-6. Summary of Displacer Loads.....	4-39
4-7. RSS Load Summary of Displacer Bearings.....	4-39
4-8. Displacer Model Parameters.....	4-41
4-9. Piston Model Parameters.....	4-42
4-10. Vibration Test Results.....	4-44
4-11. Characteristics of Radial Position Sensor.....	4-55
4-12. Transfer Function Parameters.....	4-57
4-13. Pole Piece Parameters.....	4-63
4-14. Parameters of Coil Dynamics Block.....	4-65
4-15. Parameters of Distributed Mass System.....	4-66
4-16. Parameters for Lumped Mass System.....	4-67
4-17. Parameters for Front Displacer Clearance Seal.....	4-67
4-18. Parameters for Shaft Dynamics Block.....	4-68
4-19. Compensator Parameters.....	4-69
4-20. Magnetic Bearings Performance.....	4-69
5-1. Motor Parameters.....	5-10
5-2. Piston Motor Efficiency.....	5-17
5-3. Controller Frequency - Measured vs. Displayed.....	5-22
5-4. Parametric Values of Piston and Displacer Compensators.....	5-32
6-1. Interlock System Channel Assignment.....	6-2
6-2. Measurement of Accuracy of Heater Controller.....	6-6
6-3. Board Locations of Card Cage #1.....	6-10
6-4. Board Locations of Card Cage #2.....	6-10
6-5. Radial Position Displayed Versus Channel Selection.....	6-16
6-6. Temperature Displayed Versus Position of Sensor Selector Switch.....	6-16
7-1. Performance of Counterbalance.....	7-10
9-1. Design Versus Measured Performance.....	9-1
9-2. Parameters for 50 Hour Performance Verification.....	9-3

71

1. INTRODUCTION

The efforts to explore outer space would be significantly enhanced by the availability of very low temperatures aboard orbiting or planetary spacecraft. Applications requiring such temperatures in space include: earth observation; atmospheric measurements; infrared, X-ray, and gamma-ray astronomy; magnetic field measurements; and data processing. Although several methods to store or to generate the desired low temperatures have been used in various satellite-borne experiments, none of those methods have proven capable of meeting the extended life and very high reliability associated with future spaceborne missions.

Philips Laboratories, in June 1978, in response to a NASA solicitation, proposed a novel concept for a cryogenic refrigerator deemed capable of long-life, reliable operation in space. Under the sponsorship of the NASA Goddard Space Flight Center, the proposed concept was translated into a preliminary design which was presented to the Sponsor at a review meeting in May 1979. The completion of the preliminary design was followed by a final design phase in which the critical components were tested in dedicated fixtures and by the fabrication and test of a laboratory prototype (the Engineering Model) with which to demonstrate the feasibility of the proposed concept. The work on this Engineering Model was successfully completed in July 1982.

Cryogenic refrigerators designed for use in outer space have to be efficient, be capable of long maintenance-free life, possess high reliability, and have physical characteristics (i.e., weight and size) compatible with spacecraft limitations. The Engineering Model program, with its major aim of proving concept feasibility, addressed the problems of efficiency, long life, and reliability. To meet the efficiency requirement, the cooler uses the Stirling cycle, a thermodynamically reversible process, as its refrigeration method. To attain the desired life and reliability, its design incorporates features which eliminate wear and reduce working-gas contamination.

This report covers the efforts associated with the design, manufacture, and test of the Engineering Model.

## 2. DESCRIPTION OF REFRIGERATION SYSTEM

This section describes the major characteristics of the refrigeration system, with emphasis on the rationale that led to the concept and the principal elements of the system.

### 2.1 Background

The most significant life-limiting mechanisms in a typical cryogenic refrigerator are degradation of its operating temperature by contamination of the working fluid and wear of its bearing and seal surfaces.

The contamination and wear mechanisms are interrelated. The nature of that relationship is illustrated with the aid of Figure 2-1, a schematic representation of a conventional Stirling machine.

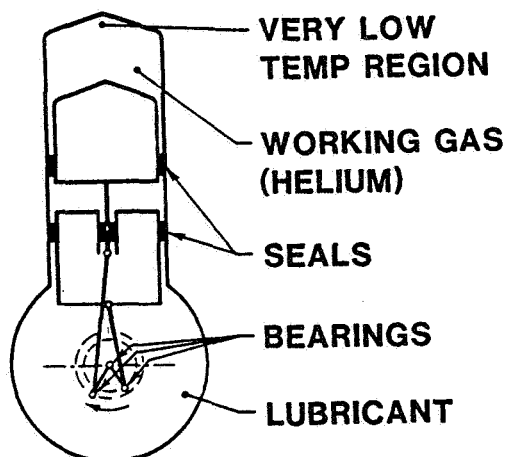


Figure 2-1. Schematic representation of a conventional Stirling refrigerator.

For long, reliable operation, bearings and seals are normally oil-lubricated. In Stirling machines, however, the seal separating the "thermodynamic" working spaces from the crankcase which contains the drive mechanism, and consequently the bearings, is not perfect, or truly hermetic. Consequently, the lubricant, which is "gettered" (or attracted) by the low-temperature region, migrates past the seal and contaminates the working space.

It should be noted that substances other than oil (or hydrocarbons) are also subject to gettering; and consequently, if present in the refrigerator, contribute to contamination of the working space. The most common contaminants are air, small traces of which are difficult to remove from the

refrigerator during purging; hydrogen, adsorbed during brazing of refrigerator components; CO and CO<sub>2</sub>, which are outgassing products of many organic materials; and water, which is adsorbed on all refrigerator surfaces during assembly.

Figure 2-2 shows tangible evidence of the contamination process just described. The crankcase of a small cryogenic refrigerator was intentionally contaminated with very small quantities of water, air, and CO<sub>2</sub>, and operated for several hours. At the end of that period, the cold head of the refrigerator was removed in a dry helium chamber, and the displacer was thus exposed for viewing and photographing. The contaminants, which leaked past the piston and displacer seals (see Fig. 2-3), then froze out on the "warm" end of the displacer/regenerator subassembly. The resulting "ice" layer increased the thermal losses which normally occur in the annular gap between the cold finger and displacer; the increased losses, of course, degraded refrigerator performance by increasing its operating temperature.

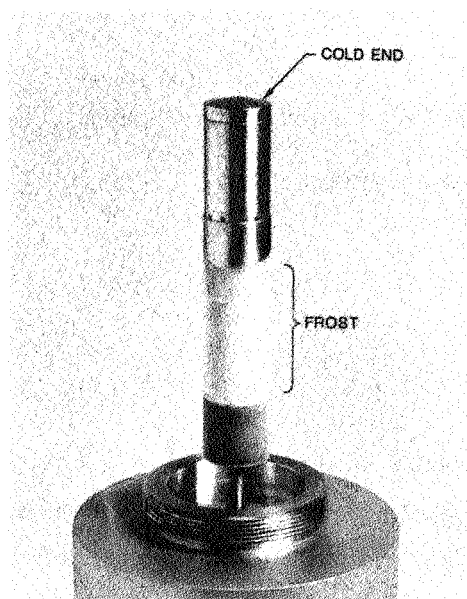


Figure 2-2. Contaminated displacer/regenerator.

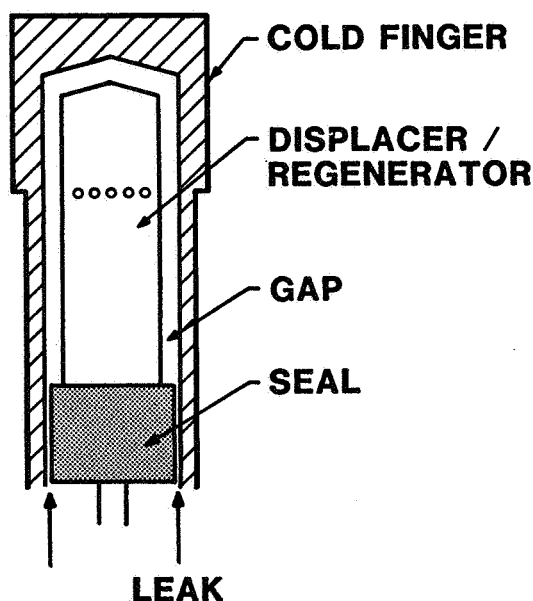


Figure 2-3. Cross-sectional view of contaminated displacer/regenerator.

An obvious solution to the degradation problem is to eliminate the sources of contamination. This suggests either dry or boundary lubricated seals and bearings. Indeed, many cryogenic refrigerator designs rely on reinforced Teflon seals reciprocating against hardened metal surfaces, and on essen-

tially dry bearings. The problem this approach creates, however, is illustrated in Figure 2-4, a photograph of a reinforced Teflon seal and the adjoining surfaces after several hundred hours of refrigerator operation. As the photograph indicates, seal wear has taken place. This wear mechanism not only increases the leakage past the seal, but also generates solid particles which clog critical passages in the refrigerator, a condition which also contributes to performance deterioration. Indeed, during the few hundred hours of operation, the temperature of the refrigerator degraded by several degrees.

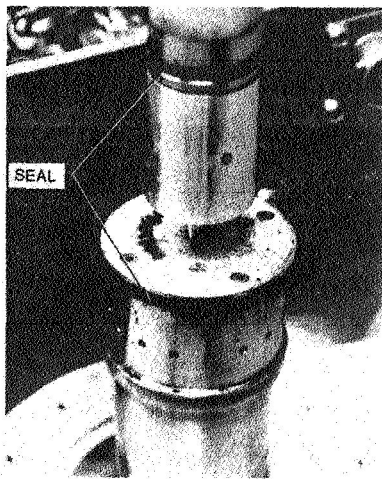


Figure 2-4. Illustration of wear associated with dry seals.

The problems discussed and illustrated above suggest that if "years" of life are to be attained, methods have to be found to either eliminate or minimize seal and bearing wear, and to prevent contaminants from reaching the working spaces of the refrigerator.

To eliminate the life-related problems just outlined, the refrigerator developed at Philips Laboratories contains six major features: a purely rectilinear drive, linear electric motors, magnetic bearings, clearance seals, "all-metal/ceramic" working-space surfaces, and an electronic axial-control system. Each of these features is discussed in the following paragraphs.



## 2.2 Major Features of System

### 2.2.1 Rectilinear Drive

The Stirling cycle requires the interphased reciprocating motion of its two major elements, the piston and the displacer. Traditionally, this motion was generated by either conventional crank-type mechanisms or by the Philips rhombic drive. In both instances, the rotary motion supplied by an electric motor had to be translated into the required rectilinear motion.

In the early 1970's, the Philips Research Laboratory in Eindhoven, The Netherlands, designed a linear-resonant Stirling cryogenic refrigeration system in which a linear electric motor drove the piston which, in turn, by pneumatic force coupling, drove a free displacer. The mass of the moving piston armature was designed to resonate on a gas spring resulting from the compression and expansion in the Stirling cycle. The displacer was mounted on a mechanical spring, and the resonance of this spring-mass system was chosen to maintain the proper phase relationship between the piston and displacer. This novel approach, embodied in the MC80 refrigerator, eliminated the problems involved with bearings, lubricants, and mechanism-induced side loads, while permitting the use of lightly loaded clearance seals of Rulon (a fiberglass impregnated Teflon). Since the drive embodiment first described offers constructional simplicity and high reliability, it was chosen as the means of actuating the displacer and piston of the Engineering Model, with one significant change: the displacer was to be motor-driven, i.e., no spring was to be used.

A cross section of the drive for the Engineering Model is shown schematically in Figure 2-5. The displacer, motor-driven, contains the regenerator and the armature (moving magnets) of the motor. In a similar fashion, the piston is directly coupled to the armature, or moving-magnet assembly, of its motor.

The design and understanding of the rectilinear drive requires a knowledge of the operating loads on the linear motors. This means that the pressure variations induced by the drive in the refrigerator and the motion of the displacer and piston must be mathematically formulated. A summary of these formulations for the MC80 linear drive is given in Appendix A.

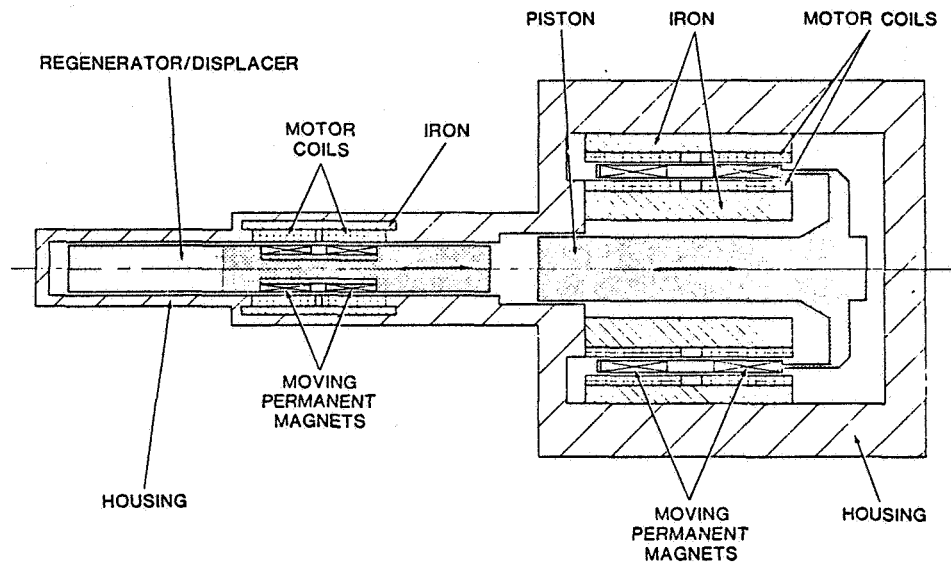


Figure 2-5. Cross-sectional view of displacer and piston motors.

### 2.2.2 Linear Electric Motors

The rectilinear drive configuration just described makes use of linear electric motors to produce the reciprocating motions of the displacer and piston. These motors are direct-current devices which operate in response to a voltage applied to their coil windings. When a current flows in the motor coils, a proportional force is imparted to the load. When the polarity of the current is reversed, the direction of force is reversed; hence, the reciprocating motion.

To obtain the desired force, the linear motor uses a dc flux field to interact with the ac flux field generated by the applied current. Such a dc flux field can be obtained either from an additional dc winding or from permanent magnets. The motor designs in the Engineering Model use the latter approach, for two major reasons. A dc coil would require power to sustain the field, while permanent magnets supply the field with no power requirement. Furthermore, the availability of samarium-cobalt permanent magnetic materials having comparatively high energy products results in compact, highly-efficient, motor designs.

The linear motors in the Engineering Model use stationary coils and moving magnets. This design approach offers a significant advantage in an application where long life and high reliability are critical: there are no flexing power-carrying leads (i.e., wires). One drawback is that magnetic attraction forces due to small asymmetries of construction and inhomogeneities in the properties of the permanent magnets result in radial magnetic loads which must be supported by the bearings.

The major features of the moving-magnet motor that drives the piston are illustrated in the cross-sectional view of Figure 2-6. Samarium cobalt

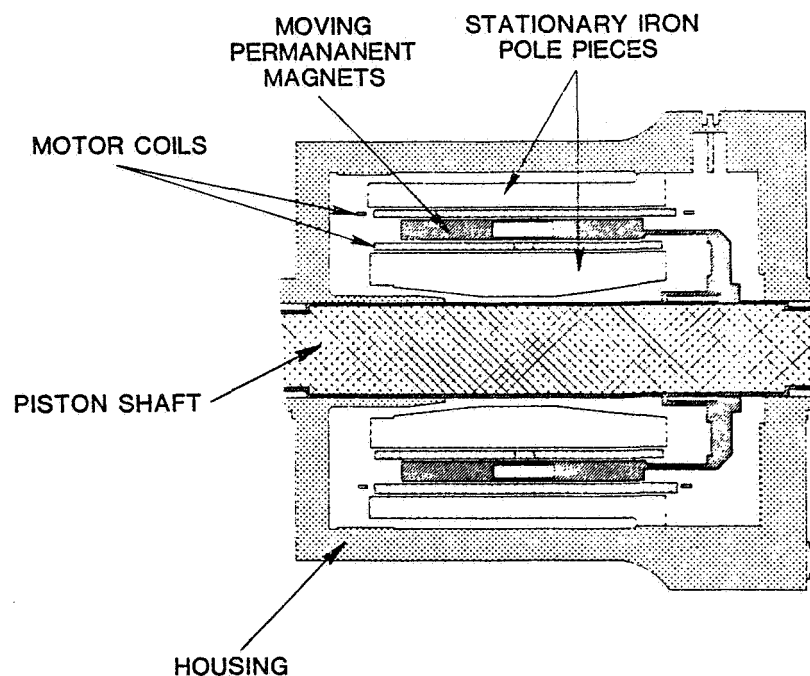


Figure 2-6. Cross-sectional view of piston motor.

permanent magnets are affixed to a hollow arbor (armature) which, in turn, is fastened to the reciprocating member - in this case, the piston rod. The motor coil is circumferentially wrapped around the permanent-magnet structure. The coil is enveloped by ferromagnetic pole pieces designed to provide the required magnetic flux paths.

The displacer is driven by a motor basically similar to that used for the piston, but with a somewhat different geometry, as illustrated in Figure 2-7. As shown, the inner-iron return path is an integral part of the displacer armature, resulting in a more compact structure.

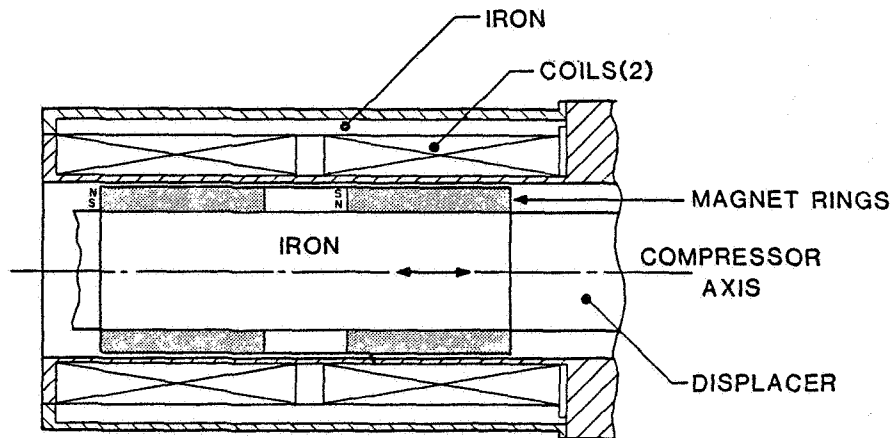


Figure 2-7. Cross-sectional view of displacer motor.

### 2.2.3 Magnetic Bearings

To eliminate the possibility of wear, the displacer and piston are supported and guided by magnetic bearings. Although contactless relative motion between machine elements has been attained in the recent past through the use of rotary magnetic bearings, the current application is the first use, to our knowledge, of linear magnetic bearings. Therefore, the design, construction, and control of these bearings constitute "new technology", and are one of the most important aspects of the work presented in this report.

The method used to achieve the magnetically suspended linear motion is illustrated in Figure 2-8. Electromagnetic coils positioned on orthogonal planes provide the attractive forces designed to float the reciprocating ferromagnetic shaft. Radial displacements of the shaft induced by either design or stray loads are detected with the aid of eddy-current position

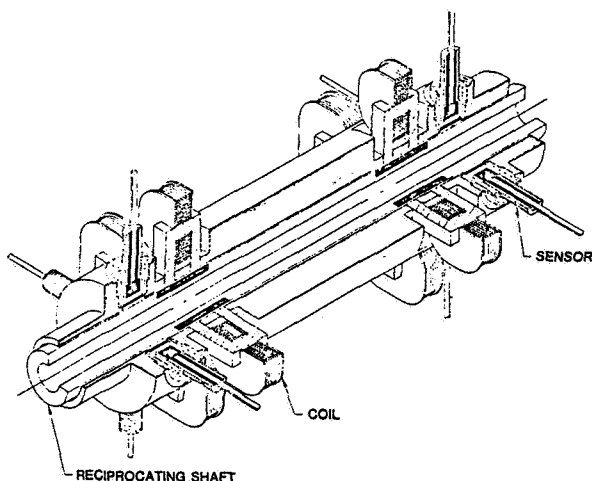


Figure 2-8. Method of magnetically suspending shaft.

sensors which provide a signal proportional to shaft position. An electronic control system compares this signal with the center-position reference and creates a correction signal which produces a change in the current to the electromagnets and a corresponding restorative force which reduces the error in the radial position of the shaft.

A more detailed view of the suspension method, without the associated sensor, is shown in Figure 2-9. The gap which is established between the reciprocating shaft and the adjoining housing is shown (out of proportion for clarity) on both sides of the view. It should be noted that the gap, which acts as the clearance seal between the working volumes of the Stirling cycle, is made possible by the magnetic suspension and the accuracy with which the position of the suspended shaft can be controlled.

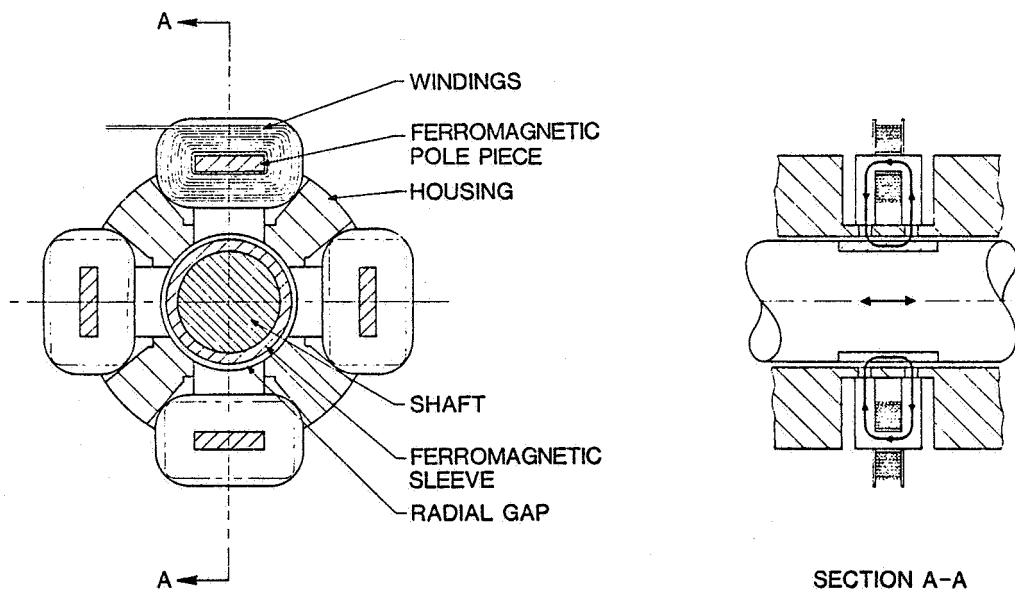


Figure 2-9. Typical cross section of magnetic bearing.

#### 2.2.4 Clearance Seals

The problem of hermetically containing gases subjected to periodic pressure variations is still unsolved. Although methods exist to minimize gas leakage past pistons which reciprocate in cylindrical housings (a configuration typical of Stirling cryogenic refrigerators), there are, at the present time, no methods to prevent it. The sealing method most widely used in Stirling refrigerators has reinforced Teflon piston rings and wear rings

riding in intimate contact against hardened metal cylindrical surfaces, as illustrated schematically in Figure 2-10.

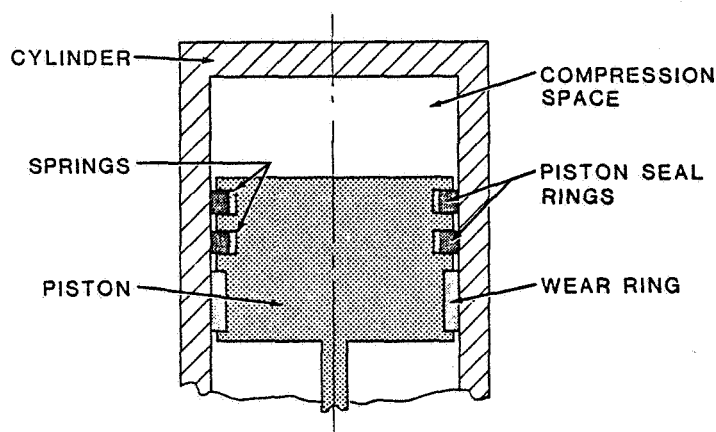


Figure 2-10. Schematic of conventional piston seal configuration.

The sealing approach is a very important consideration in Stirling refrigerator designs; the seal has to be "close to" hermetic, have acceptable endurance life, and be free of contaminants. The sealing configuration shown in Figure 2-10 meets these criteria to some degree. The leakage associated with it appears to be acceptable in most applications; its useful life is reported to range from a "few hundred" to a "few thousand" hours; and although it is not contamination-free, the amount of impurities it generates is less than that produced by alternate sealing approaches.

However, for applications which require "years" of reliable refrigerator operation, the sealing method of Figure 2-10 is inadequate. Although its lack of hermeticity is acceptable, the life-limiting wear associated with a tight, and therefore relatively leak-free, ring-to-mating surface contact, are not. It is interesting to note that wear not only increases leakage, but also generates contaminants: the friction between the reinforced Teflon and the mating surface is associated with localized high-temperature spots which generate combustion products detrimental to the thermal stability of the refrigerator. To avoid the problems just discussed, Philips Laboratories incorporated clearance seals in the design of the Engineering Model refrigerator.

In general terms, a clearance seal is a long, narrow, annular gap established between the outside surface of a reciprocating cylindrical element

and the internal surface of a mating cylinder. Sealing is attained by the flow restriction provided by the long narrow gap. Further, since the pressure gradient imposed on the seal is oscillatory from the reciprocating motion of the moving member, the net volume of gas which traverses the seal is extremely small. The manner in which clearance seals were incorporated into the overall refrigerator design is illustrated in Figure 2-11.

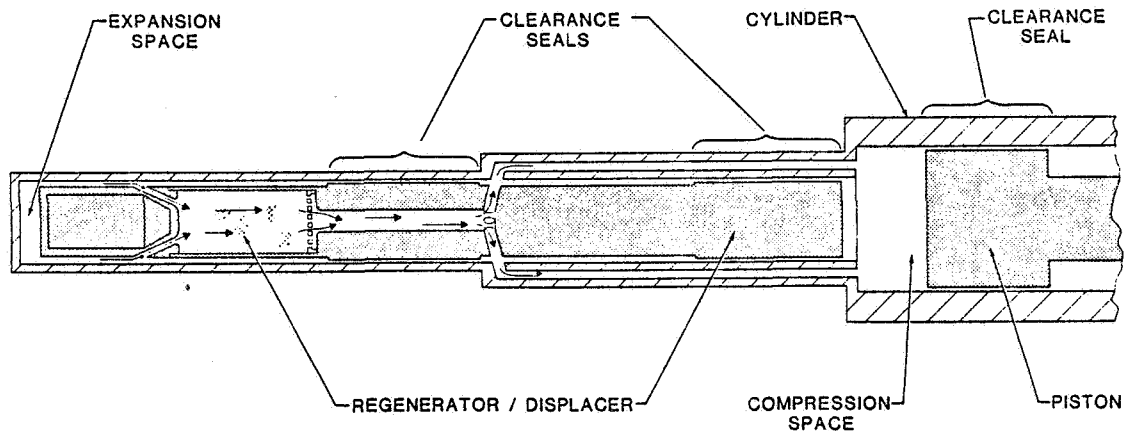


Figure 2-11. Schematic of clearance seal configuration.

Prior to applying the clearance seal concept to the refrigerator, efforts were conducted at Philips Laboratories to develop analytical methods for predicting its performance. These methods were then applied to the design and testing of a clearance seal in a rhombic-driven Stirling cryogenic refrigerator. For the test, the outside diameter of a long Rulon seal was varied by machining off small amounts, and the refrigerator performance was measured. The agreement between measurement and prediction was good.

An important consideration in clearance-seal design is the accuracy with which its annular geometry can be maintained during operation of the refrigerator. As discussed in Section 3, the leakage through a narrow annular gap varies as the cube of the gap for laminar flow. Thus, the importance of having the magnetic bearing accurately center the piston and displacer can be readily appreciated.

### 2.2.5 All-Metal/Ceramic Surfaces

The presence of impurities in the working gas of a cryogenic refrigerator is detrimental to its thermal stability. Specifically, impurities tend to migrate to the low-temperature regions of the refrigerator's working volume and freeze out on critical surfaces and in vital passages. The formation of such frozen impurity layers retards heat transfer and increases the resistance to gas flow. These phenomena lead to an increase in the operating temperature of the refrigerator, which is of course undesirable.

Impurities can either be introduced into the refrigerator with the working gas during the initial filling procedure, or be generated during operation. Past experience has shown that the initial introduction can be prevented by filling the refrigerator through cryogenically cooled gas lines. The generation of impurities during refrigerator operation, however, is a complex phenomenon which until now has eluded an effective solution.

All materials used in the working volume of a typical cryogenic refrigerator contain impurities. Some, like the metals used in the structure, regenerator matrix, piston, etc., can be outgassed (or baked) at relatively high temperatures; others, organic materials like reinforced Teflon seals and bushings for instance, cannot be outgassed and will continue to generate impurities while in intimate contact with the pure helium working gas. Some organic materials have outgassing rates which permit their integration into refrigerators when long, maintenance-free operation is not critical. This is clearly not the case in spaceborne applications.

To eliminate the possibility of working gas contamination and to prevent the associated temperature degradation, the Engineering Model refrigerator was designed to have no organic materials in contact with the helium working gas. This was accomplished by encapsulating the motor windings in titanium envelopes and by using ceramic materials for parts which would normally be made of plastics, such as insulating spacers. The only materials in contact with the helium are titanium, copper, ferromagnetic alloys, ceramics, phosphor bronze, stainless steel, nickel, and metallic joining materials.

It should be noted that the material selection criteria used in the design of the working space are identical to that encountered in the design of high



vacuum systems where contamination is also a critical problem. The key to attaining high vacua is the ability to outgas, at high temperatures, all the materials exposed to vacuum. The "all-metal/ceramic surfaces" approach taken in the refrigerator design permits a similar procedure, i.e., a thorough outgassing of all pertinent parts, which is expected to lead to high, working-gas purity.

#### 2.2.6 Electronic Axial-Control System

The use of a rectilinear drive means that the crankshaft and drive linkages, which control the piston and displacer amplitudes and phase relationship in a conventional Stirling machine, are eliminated. The MC80 refrigerator, which uses a rectilinear drive, is driven with a simple ac voltage signal. This system requires a mechanical spring on both the piston and displacer. The piston spring counteracts a pumping force caused by the slow passage of gas through the clearance seal. If this spring were not present, the piston would be eventually forced to the top of the cylinder. The displacer spring-mass resonance is chosen so that the weak pneumatic forces, exerted on the displacer by the piston motion, result in the proper amplitude and phase relationship. The dynamics of this system change during transients, such as cooldown, and with variations in the motor system, such as resistance increases caused by coil heating. These dynamic changes shift the operating point of the refrigerator, resulting in changes in cold production.

A substantial improvement over the MC80 drive system is provided by the sixth and last major feature of this refrigerator, viz., the electronic axial-control system. With it, not only are the crankshaft and drive linkages absent, but also the piston and displacer mechanical springs. As shown in Figure 2-12, the operating frequency, piston amplitude, displacer amplitude, and phase between piston and displacer ( $\phi_{\text{drive}}$ ) are set by reference levels from a control panel. The electronics provide the required reference signals for the piston and displacer. By comparing this reference to the transduced position output signals, an error signal is derived which drives the system in such a way so as to reduce this error. If the gain of the feedback loop is high, the error is extremely small, and the output exactly tracks the reference. It is in this way that the amplitudes, frequency, and  $\phi_{\text{drive}}$  of the system are controlled.

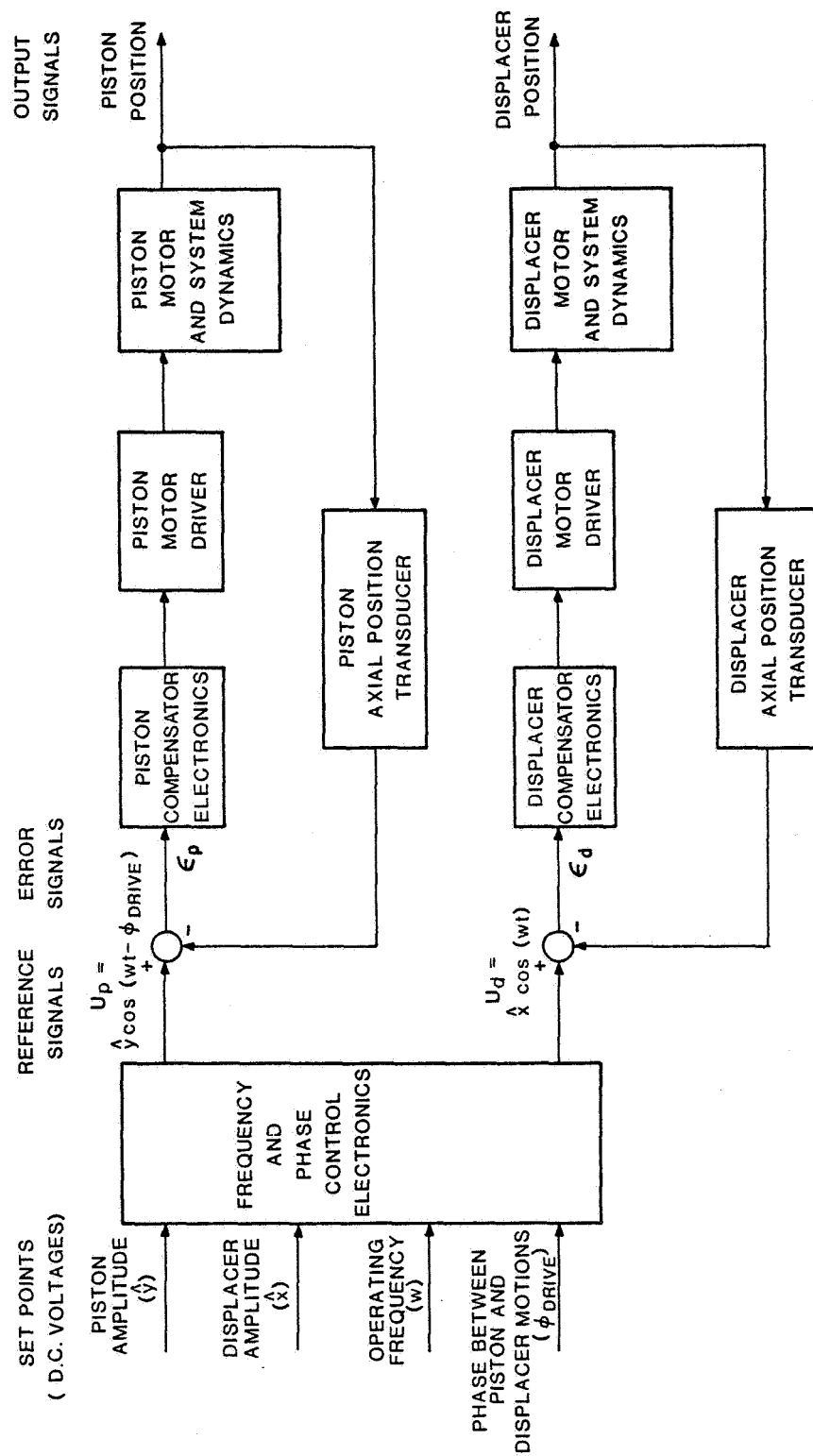


Figure 2-12. Block diagram of axial-control system.

## 2.3 Engineering Model Cooler

### 2.3.1 General

The Engineering Model cooler, shown in Figure 2-13, was designed to produce 5 Watts of cooling power at an operating temperature of 65°K and a heat rejection temperature of 300°K, with high-efficiency; and to maintain that cold production for a period of 5 years or longer. To attain the desired high-efficiency, the refrigerator is based on the Stirling cycle, a thermodynamically reversible process. To achieve the required, maintenance-free, life, the refrigerator design contains the six major features previously discussed: a rectilinear drive, linear electric motors, magnetic bearings, clearance seals, all-metal/ceramic working surfaces, and an electronic axial-control system.

The refrigerator, shown in cross section in Figure 2-14, is composed of three major subassemblies. In the expander section, gas is cyclically shuttled between the cold expansion end and the rear compression chamber which is held at ambient temperature with an external liquid-cooled heat exchanger. In the compressor section, the gas is expanded and compressed by the action of a piston. Finally, in the third section a spring-mass passive counterbalance minimizes axial vibrations when tuned to the refrigerator operating frequency. The piston and displacer elements are supported on magnetic bearings; the counterbalance element is supported on leaf springs. It is important to note that the refrigerator is symmetric about its centerline, and the linear motions of the piston, displacer, and counterbalance are directed along the same axis.

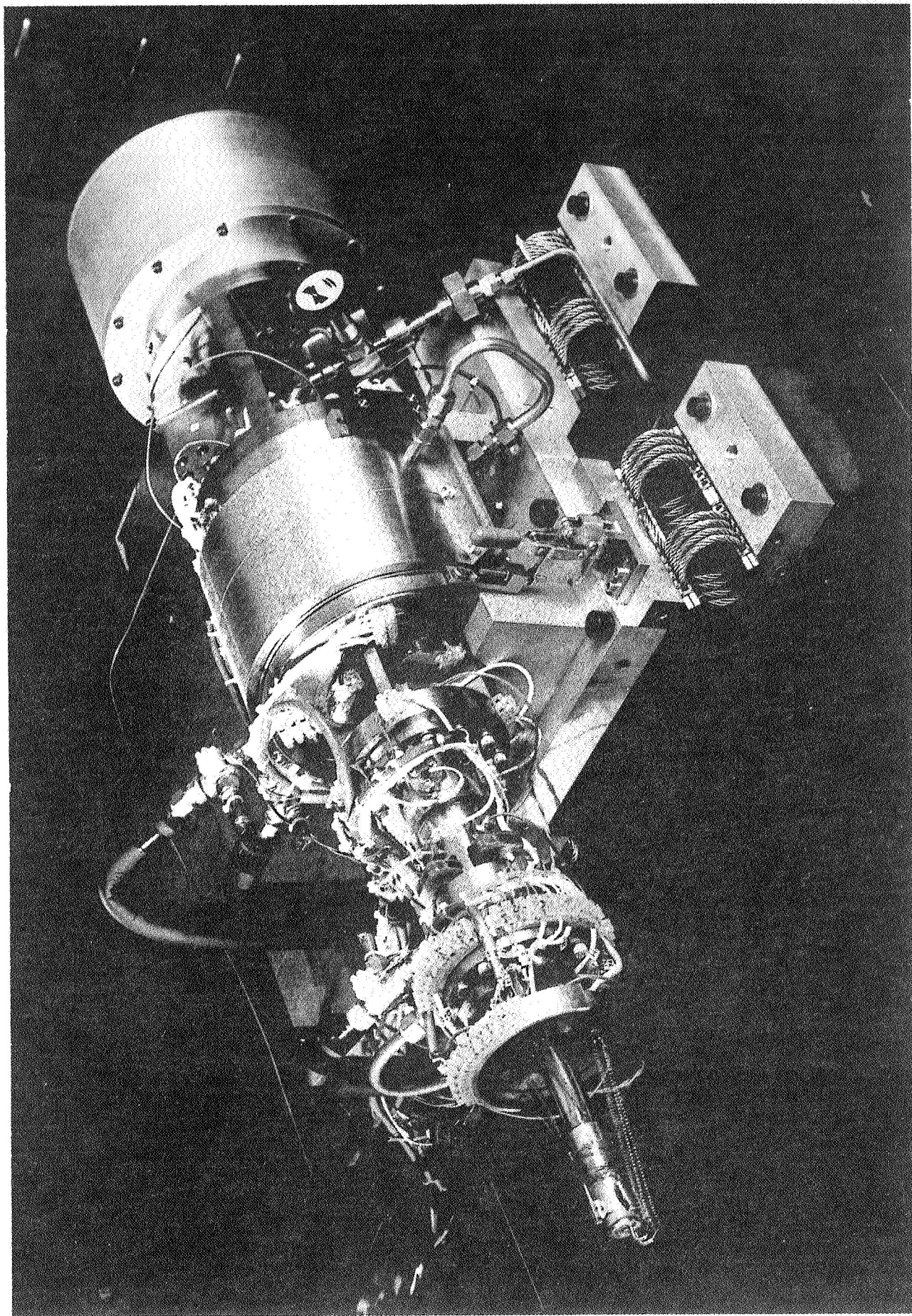


Figure 2-13. Photograph of Engineering Model cooler.

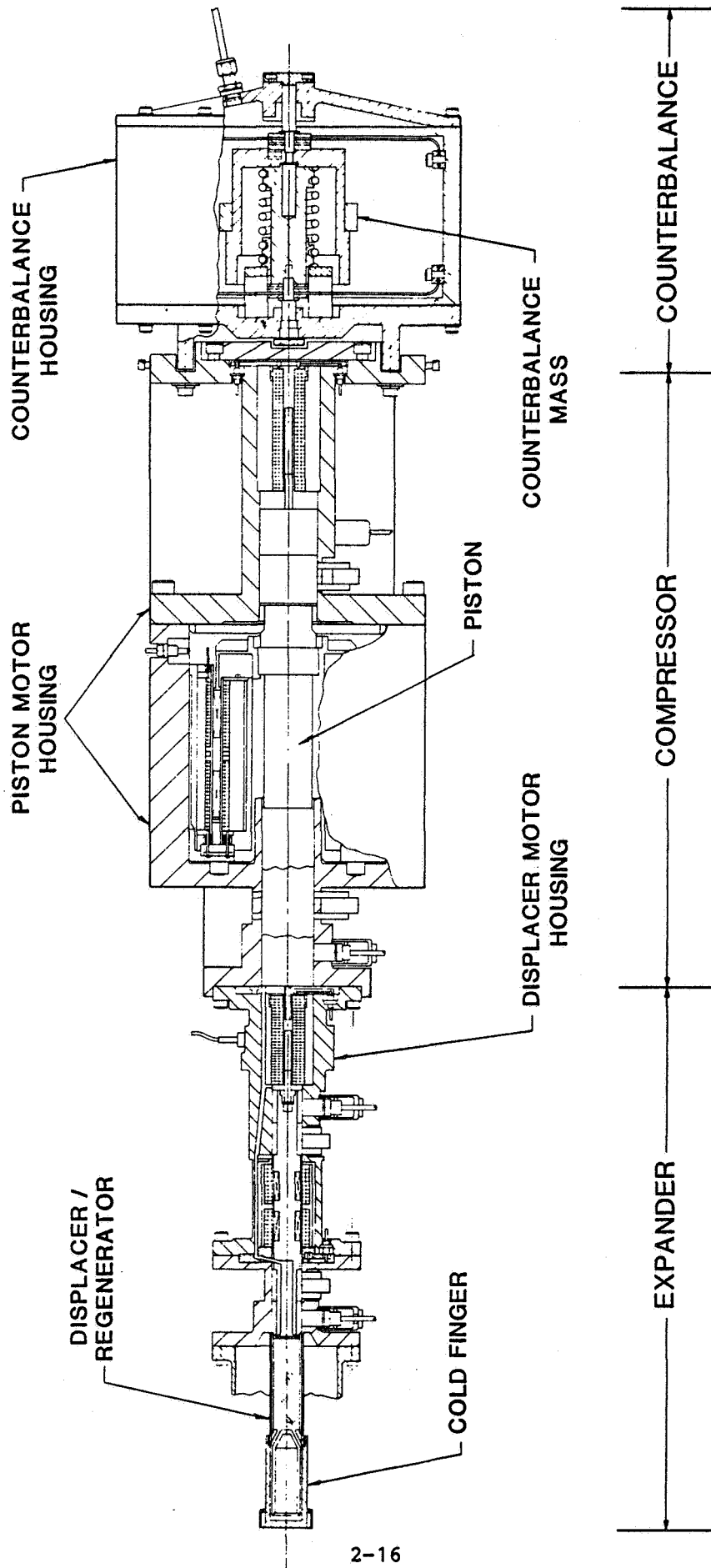


Figure 2-14. Cross-sectional view of Engineering Model Cooler.

### 2.3.2 Expander Subassembly

The expander section is shown in detail in Figure 2-15. Helium gas, the working fluid, is free to flow from the expansion space at the 65°K flange, through the heat exchanger which is maintained at 300°K with a water jacket, to the compression chamber (in the compressor subassembly). The heat-exchanger surface permits the attachment of a heat pipe instead of the water jacket. A moving regenerator maintains the temperature gradient along the length of the cold finger by storing heat energy in one half cycle to release it in the second half cycle. The magnetic bearings form the first two clearance seals, forcing the helium to flow through the regenerator and through the heat exchanger. The magnetic bearing consists of four pole pieces at right angles together with four radial position sensors (eddy current probes). The displacer is driven axially with a moving-magnet linear motor, and its motion is transduced with a linear variable differential transformer (LVDT). A gas transport manifold, surrounding the LVDT, forms the gas passage to the compression space. All electrical power connections are hermetically made using nickel and ceramic feedthroughs. A vacuum Dewar (partially shown), connected to the 300°K flange, thermally insulates the cold finger.

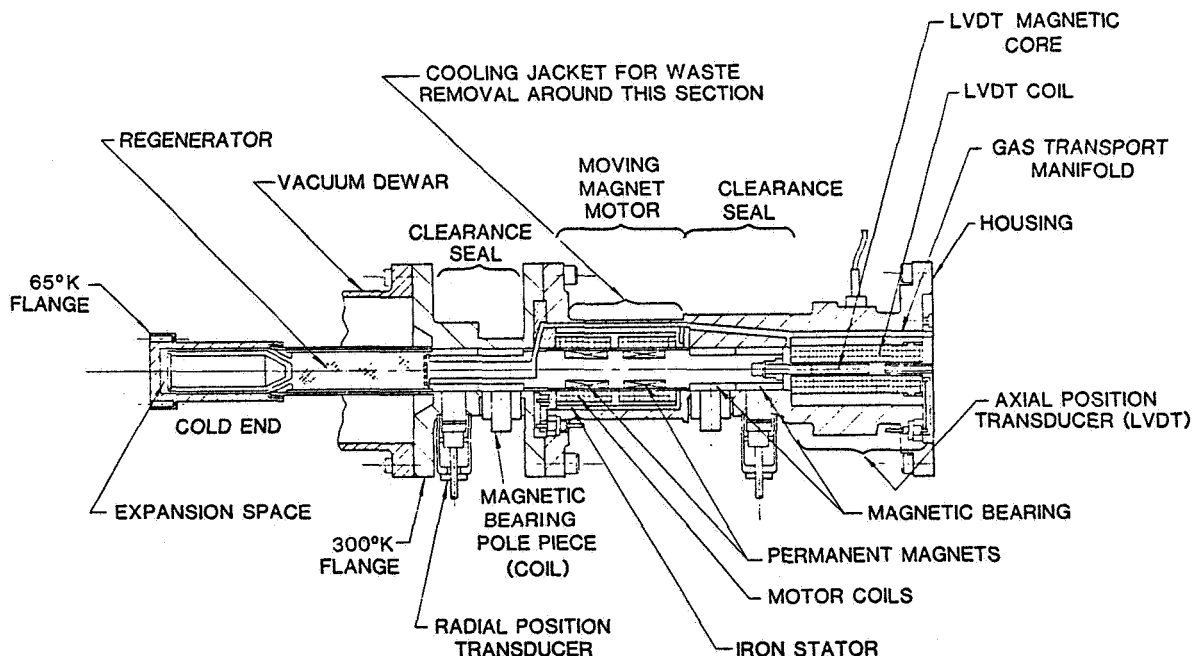


Figure 2-15. Cross section of expander subassembly.

The expander subassembly is instrumented (not shown) with: a strain-gauge pressure transducer to measure the compression pressure, thin film detectors (TFD's) to measure the temperature at various points along the housing, and two calibrated silicon-diode sensors to measure the cold-finger temperature. A resistive heater applies a heat load to the 65°K flange. Electrical connections to the transducers inside the vacuum Dewar are made through nickel and ceramic feedthroughs.

### 2.3.3 Compressor Subassembly

The compressor section is shown in detail in Figure 2-16. The magnetic bearing on the left forms the third and final clearance seal, maintaining the cyclic pressure in the compression space. The additional magnetic bearing at the rear of the piston supports the shaft but does not form a seal. As in the expander section, each magnetic bearing is formed of four pole pieces and four radial position sensors. The hollow vented piston shaft and the large volume in the center of this section constitute a buffer space for the helium gas. As in the displacer, the control of the axial motion entails the use of a moving-magnet linear motor and an LVDT.

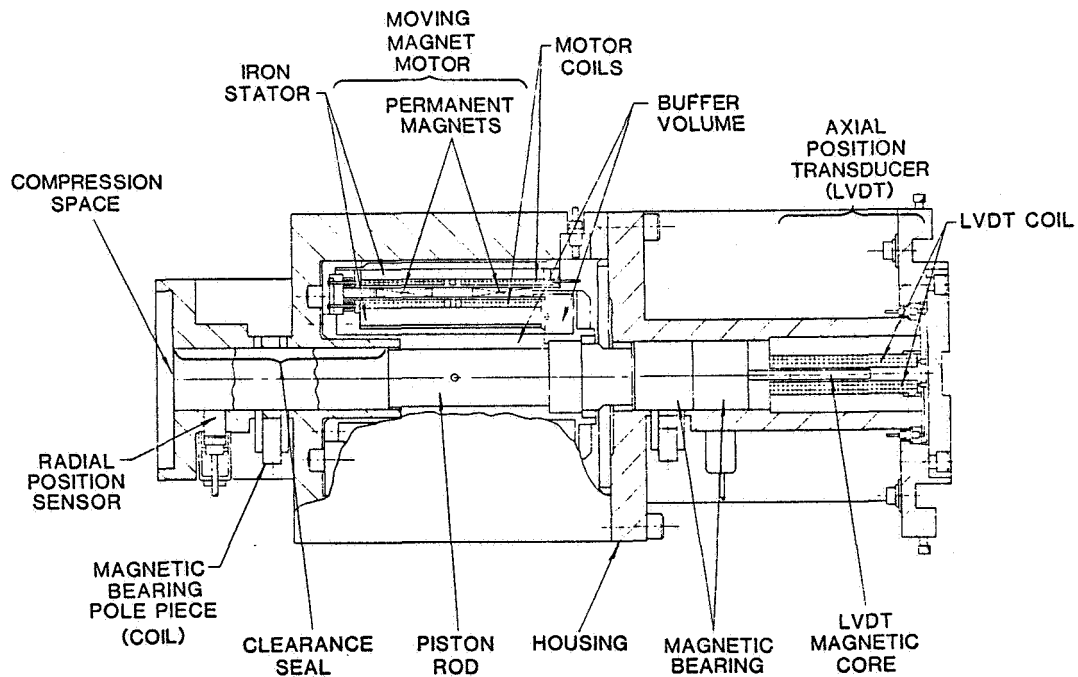


Figure 2-16. Cross section of compressor subassembly.

The compressor subassembly is instrumented (not shown) with a pressure transducer to measure the mean buffer pressure and TFD's to measure the temperature at various points along the housing. A water-cooled heat exchanger maintains the temperature of the housing in the area of the motor.

#### 2.3.4 Counterbalance Subassembly

The counterbalance is shown in cross section in Figure 2-17. It passively reciprocates in vector phase opposition to the combined piston and displacer motion when the coil-spring/moving-mass resonance is tuned to the refrigerator operating frequency. The leaf springs provide radial support, adding little damping to the system. The counterbalance housing, which is physically distinct from the compressor and expander sections and does not contact the working helium gas, is hermetically sealed to permit evacuation for lower damping. The counterbalance is instrumented with an accelerometer (not shown) mounted to the rear flange.

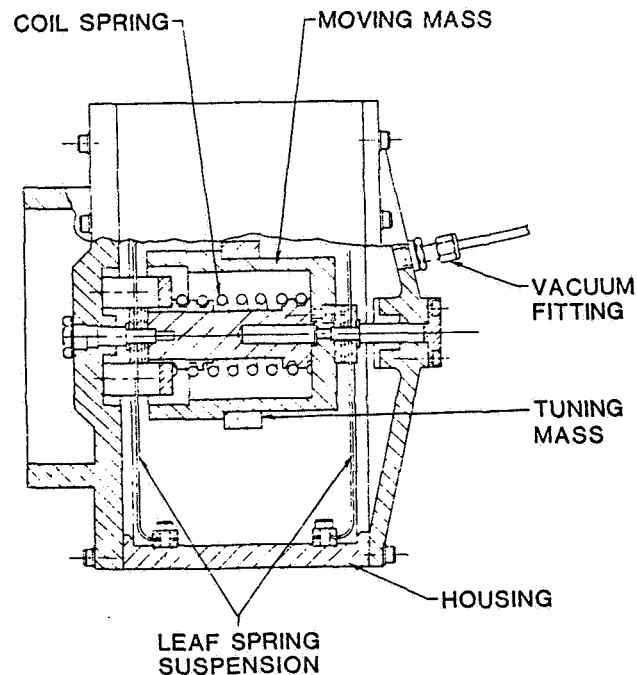


Figure 2-17. Cross section of counterbalance subassembly.



### 3. THERMODYNAMIC AND DYNAMIC DESIGN

#### 3.1 Introduction

A Stirling refrigerator generates cold by periodic expansion and compression of a working gas (see Appendix B). The expansion takes place at the desired low temperature, and the compression is maintained at ambient temperature with the aid of external cooling. The expansion and compression of the working gas is accomplished by the reciprocating motion of a piston, complemented by the phase leading reciprocation of a displacer. The latter, as its name implies, displaces gas from the cold expansion region to the ambient-temperature compression region of the machine and vice versa, through a thermal regenerator. The Engineering Model refrigerator is a single-expansion configuration with one expansion stage and one regenerator. The regenerator is built into the displacer. Refrigeration is produced at one cryogenic temperature.

Since the displacer and piston each have a linear motor and displacement transducer, each is "free", in that the motions are not mechanically imposed. The phase angle and reciprocating amplitudes are regulated by an electronic axial control system. It should be noted that there is a significant difference between a mechanical drive and a "free" linear drive. In the former, the dynamics of the system are set by the parameters of the mechanical drive; therefore, the optimization of such a system deals with thermodynamic parameters only. For high mechanical efficiency in the "free" linear approach, the dynamic parameters, such as the moving masses, have to be closely matched to the thermodynamics; therefore, optimization of the refrigerator involves a coupled thermodynamic-dynamic process which is more difficult to analyze.

Magnetic bearings and clearance seals add extra length to the expander section. Thus, the gas-flow between the compression space and the expansion space in the Engineering Model is longer than that in conventional coolers. This tends to increase the dead volumes and lower the compression ratio. As a result, this model with its magnetic bearings and clearance seals, has a larger compression space.

The thermodynamic design point requires that the piston sweep a volume of  $15.1 \text{ cm}^3$ , with a resultant pressure wave of 1.92 to 1.26 MPa. For optimal

system efficiency with a free piston and a linear motor, the diameter of the piston and the mass of the piston assembly is selected so that the assembly resonates with the gas-spring force of compression at the refrigerator operating frequency. This is achieved in this design by a piston diameter of 3.70 cm. Leakage past the piston is restricted by a clearance seal with a 25  $\mu\text{m}$  (0.001 in.) gap and a 10 cm length. Effects of piston leakage are included in the thermodynamic computations; a simplified analysis is given in Section 3.3.

The Philips Stirling Computer Program was used to design the refrigerator for minimum electrical input power. The computer results included physical dimensions of the expansion and compression spaces, operating parameters such as charge pressure and speed, and regenerator size and material. Practical considerations of weight, reliability, and complexity of fabrication were then applied to perturb the theoretically optimized design. Throughout the design process, practical considerations and thermodynamic performance were iterated to achieve the optimal, physically-realizable refrigerator. The thermodynamic parameters are summarized in Table 3-1.

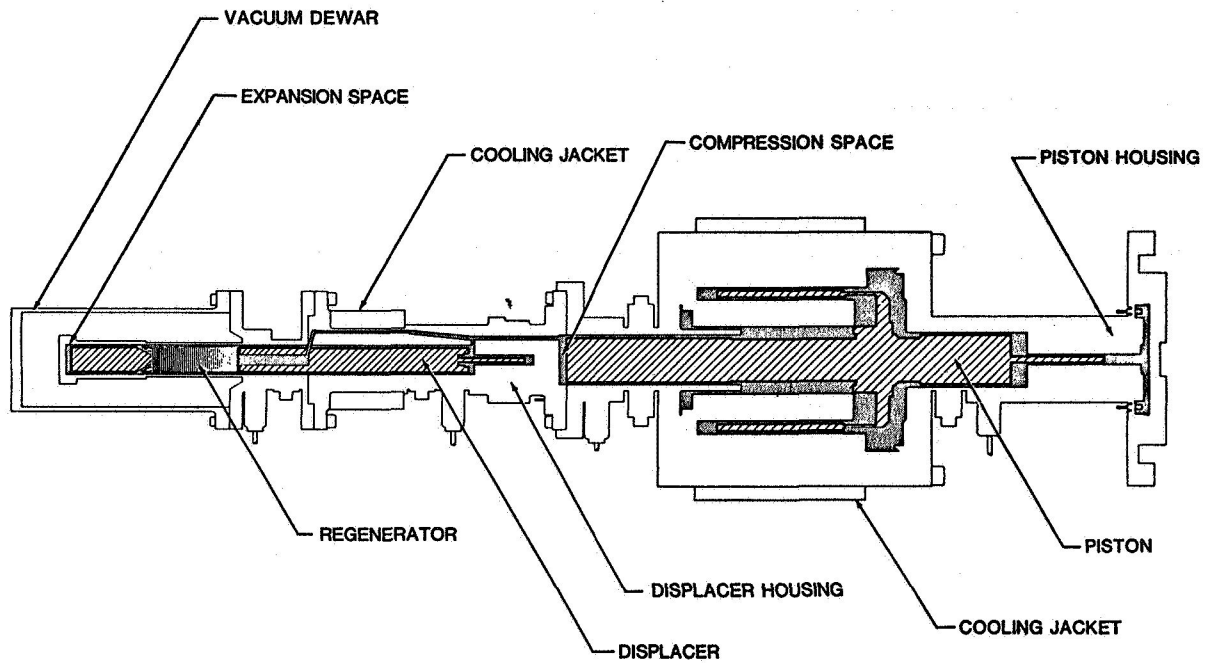
The Engineering Model was designed to be radially symmetric to reduce the effects of thermally induced stresses. The parts were fabricated of titanium alloy for reduced weight and high dimensional stability. The poor thermal conductivity of the titanium serves to insulate the cold copper flange from the ambient sections. A vacuum Dewar, lined with super-insulation, minimizes the parasitic, radiation load at the cold finger.

A simplified cross section of the refrigerator is shown in Figure 3-1. The passage of the helium working gas between the cold expansion space and the ambient-temperature compression space is indicated. The operation of the displacer, shuttling gas between the two spaces, and that of the piston, compressing and expanding the gas, is apparent in the figure. The ambient temperature behind the regenerator (displacer section) is maintained with a water-cooled heat exchanger; the water jacket is shown in Figure 3-2. In addition to the heat of compression, the ohmic power loss of the displacer motor is also removed with the water jacket. A dummy heat load is provided by a resistive heater on the cold flange. A second water jacket around the piston-motor housing removes the ohmic power loss from that motor

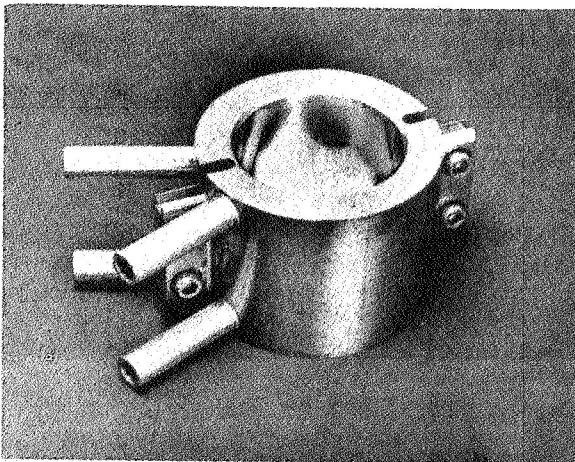
and helps maintain the refrigerator case at a constant temperature. This is done primarily to reduce temperature induced drifts in the position and pressure transducers.

TABLE 3-1. Thermodynamic Design Values.

No. of expansion stages	1
Working gas	helium
Displacer diameter	1.96 cm
Piston diameter	3.70 cm
Max. displacer amplitude	0.4 cm
Max. piston amplitude	0.8 cm
<u>Regenerator:</u>	
Type	wire mesh
Material	phosphor bronze
Wire diameter	41 $\mu\text{m}$
Fill factor	0.37
Cross-sectional area	2.74 $\text{cm}^2$
Length	6.3 cm
<u>Cold-end Heat Exchanger:</u>	
Type	annular
Mean diameter	1.98 cm
Gap width	0.02 cm
Length	4.4 cm
<u>Ambient Heat Exchanger:</u>	
Type	slit
No. of slits	20
Slit width	0.07 cm
Slit depth	0.2 cm
Slit length	6.3 cm
<u>Clearance Seals:</u>	25 $\mu\text{m}$ (0.001 in) gap
<u>Operating Parameters:</u>	
Heat sink temperature	300°K
Expansion temperature	65°K
Charge pressure	1.57 MPa (15.5 atm)
Operating frequency	26.7 Hz (1600 cpm)
Displacer amplitude	0.3 cm
Piston amplitude	0.7 cm
Displacer-piston phase angle	60°
Max. pressure	1.92 MPa
Min. pressure	1.26 MPa
Cooling power	5 W
Thermodynamic input power	90 W



**Figure 3-1. Cross section of Engineering Model showing helium passages.**



**Figure 3-2. Water jacket of ambient heat exchanger.**

### 3.2 Coupling of Thermodynamics and Dynamics of a Free-Displacer, Free-Piston, Stirling Cycle Refrigerator

#### 3.2.1 Description of Linear Drive Mechanisms

The expansion side of the refrigerator includes the displacer which contains the thermal regenerator. The moving armature of the displacer motor is an integral part of the displacer; the stator is part of the housing. The compression side contains the piston which is directly coupled to the moving magnets of its linear motor. In both motors, the magnets, reacting to current in the stationary coils, impart linear reciprocating motion to the displacer or piston.

In addition to the force exerted by the displacer motor, the displacer is also driven by the pressure differential established by the flow friction of the helium working gas, as it flows back and forth through the regenerator matrix. This pneumatic force, calculated in the Philips Stirling Program, is required to describe the mechanical dynamics of the displacer.

The piston resonates on the gas spring formed by the compression volume. The center frequency and quality factor (Q) of this spring-mass system, being a function of the thermodynamics, is also calculated in the program. Efficient operation of the refrigerator is achieved only if the proper balance between the thermodynamics and dynamics of this gas spring is attained.

#### 3.2.2 Pressure Variations in a Stirling Refrigerator

The design of this type of Stirling refrigerator requires that the pressure variations which occur in its working volume be well formulated. A theoretical expression for these pressure variations is given in References 1 and 2.

The pressure variations which occur in the refrigerator's working volume are induced by:

---

Ref. 1. J.W.L. Kohler and C.O. Jonkers, "Fundamentals of the Gas Refrigerating Machine", Philips Tech. Rev. 16, 69, 1954.

Ref. 2. R.J. Meijer, "The Philips Stirling Engine", Ingenieur, Vol. 81, p. W69, W81, May 1969.

- Motion of the piston. Its position determines the total volume of gas in the working space.
- Motion of the displacer. Its position determines the distribution of the gas, at a given time, between the compression and expansion spaces.
- Gas flow induced by motion of the piston. This flow gives rise to pressure differences in the working volumes.
- Gas flow induced by motion of the displacer. Flow losses in the regenerator give rise to pressure differences in the compression and expansion spaces.

Specifically, the pressure variation in the compression volume ( $p_c$ ) and that in the expansion volume ( $p_e$ ) can be expressed as:

$$p_c = p_m + C_y y + C_x x + C_{pc} \dot{y} + C_{dc} \dot{x} \quad (1)$$

$$p_e = p_m + C_y y + C_x x + C_{pe} \dot{y} + C_{de} \dot{x} \quad (2)$$

and the differential between the two ends of the displacer as:

$$p_e - p_c = (C_{pe} - C_{pc}) \dot{y} + (C_{de} - C_{dc}) \dot{x} = C_{pp} \dot{y} + C_{dd} \dot{x} \quad (3)$$

where:  $p_m$  = average cyclic pressure

$x$  = displacer position

$y$  = piston position

$C_x$  = constant related to pressure variation induced by position of displacer

$C_y$  = constant related to pressure variation induced by position of piston.

$C_p$  = constant related to flow loss induced by piston velocity

$C_d$  = constant related to flow loss induced by displacer velocity

$c$  and  $e$  = subscripts referring to compression and expansion sides, respectively

$$C_{pp} = C_{pe} - C_{pc}$$

$$C_{dd} = C_{de} - C_{dc}$$

$\dot{x}$  = displacer velocity =  $dx/dt$

$\dot{y}$  = piston velocity =  $dy/dt$

$t$  = time

Equations (1), (2), and (3) are valid only if constants  $C_y$ ,  $C_x$ ,  $C_{dd}$ , and  $C_{pp}$  are independent of  $x$ ,  $y$ ,  $\dot{x}$ , and  $\dot{y}$ , which is not quite the case. Consequently, these three equations are linear approximations only.

It should be noted that there are several second-order effects which contribute to the induced pressure variations, viz., gas leakage past the clearance seals, temperature variations due to heat transfer to the walls and to imperfect mixing, changes in the average temperatures in the heat exchangers and in the varying volumes due to changes in loading, among others. In addition, the flow is not laminar throughout the refrigerator; the flow resistances are thus not linearly dependent on the gas velocities.

The variations of the constants  $C_x$ ,  $C_y$ ,  $C_{dd}$ , and  $C_{pp}$  were investigated with the aid of the computer program. The variations were found to be relatively small for small perturbations about the design point; thus, Equations (1), (2), and (3) are acceptable approximations.

### 3.2.3 Cold Production and Input Power

The expressions for the pressure variations which occur in the refrigerator serve to determine the cold production and power input. If ideal processes are considered,  $P_c$  and  $P_e$  are given by the same expression:

$$P_c = P_e = P_m + C_y y + C_x x = P$$

Then, the ideal cold production ( $Q_{eo}$ ) is given by:

$$Q_{eo} = n \oint P dV_d = n\pi C_y \hat{x} \hat{y} A_d \sin \phi_{dr} \quad (4)$$

where,

- $dV_d = A_d dx$  = variation of expansion volume
- $A_d$  = cross section area of displacer
- $n$  = speed (Hz)
- $\hat{x}$  = peak displacer amplitude ( $x = \hat{x} \cos \omega t$ )
- $\hat{y}$  = peak piston amplitude [ $y = \hat{y} \cos (\omega t - \phi_{dr})$ ]
- $\omega$  = angular frequency
- $\phi_{dr}$  = phase shift between piston and displacer motions.

As Equation (4) indicates, only  $C_y$ , reflecting the pressure variations induced by the piston motion, enters into the expression for the ideal cold production of the refrigerator.

The ideal input power ( $N_p$ ) is given by the expression:

$$N_p = n \oint p \, dV_p = n\pi C_x \hat{x} \hat{y} A_p \sin \phi \, dr \quad (5)$$

where,  $dV_p = A_p \, dy$   
 $A_p =$  cross section area of piston

As can be seen in Equation (5), only  $C_x$ , the pressure variation induced by the position of the displacer, affects the ideal input power to the refrigerator.

From the above, the ideal thermodynamic efficiency =  $C_y A_d / C_x A_p$ .

The actual cold production and thermodynamic input power are calculated by the Philips Stirling Computer Program. The analysis includes: the effects of regenerator losses, flow losses, heat leakage through the regenerator matrix and walls, imperfect heat transfer between the gas and the heat exchanger wall, annulus losses, losses due to shuttle heat transfer and seal leakage. All these effects are considered in the characterization of the thermodynamic parameters. The result of the optimization is a design in which the sum of these losses is minimized.

### 3.2.4 Modeling of Electromechanics of Displacer and Piston

The equations of motion for the displacer and piston are given by,

$$m_d \ddot{x} - (p_c - p_e) A_d - K_d I_d = 0 \quad (6)$$

$$\text{and } m_p \ddot{y} - (p_m - p_c) A_p - K_p I_p = 0 \quad (7)$$

where,  $m =$  mass  
 $K =$  motor force constant  
 $I =$  motor current  
 $\ddot{x} =$  displacer acceleration =  $d^2 x / dt^2$   
 $\ddot{y} =$  piston acceleration =  $d^2 y / dt^2$

and subscripts d and p refer to displacer and piston, respectively.



The force balance from which these equations are derived is shown schematically in Fig. 3-3. As shown in Section 5 (linear motors), the moving magnet motors used in the refrigerator can be modeled as having a linear relationship between force and current. The linear term  $K = B \cdot \ell$ , where  $B$  is the flux density in the air gap of the motor and  $\ell$  is the length of wire in the gap.

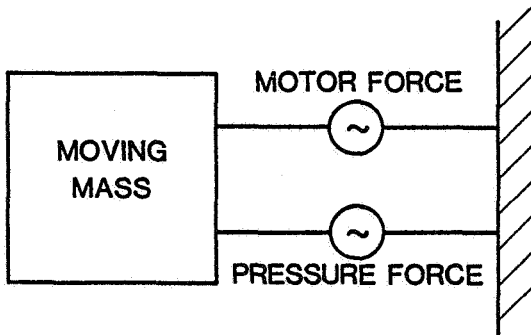


Figure 3-3. Schematic of force balance.

Using Equations (1) and (3), Equation (6) and (7) can be written as,

$$m_d \ddot{x} + C_{pp} A_d \dot{y} + C_{dd} A_d \dot{x} - K_d I_d = 0 \quad (8)$$

and 
$$m_p \ddot{y} + C_{yp} A_y \dot{y} + C_{xp} A_x \dot{x} + C_{pc} A_p \dot{y} + C_{dc} A_p \dot{x} - K_p I_p = 0 \quad (9)$$

The relationship between the voltage and current of the linear motor is shown schematically in Figure 3-4.

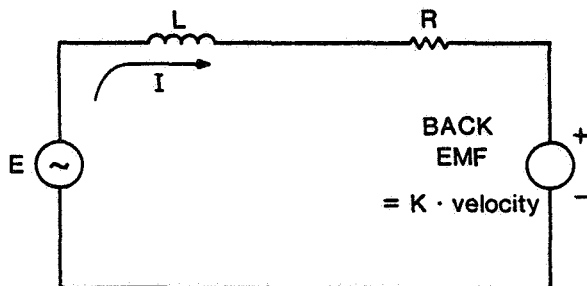


Figure 3-4. Equivalent circuit of linear motor.

The lumped circuit element  $L$  models the effect of the distributed inductance;  $R$  models the effect of the distributed resistance. The back emf term represents an energy balance between the mechanical and electrical dynamics. The two describing equations are:

$$F = K \cdot I$$

$$E_{MF} = K \cdot V$$

where  $V$  is the velocity of the moving element and  $F$  is the mechanical force imparted by the linear motor. The energy balance implies:

$$F \cdot V = K \cdot I \cdot V = E_{MF} \cdot I$$

Applying Kirchoff's voltage law to the circuit of Figure 3-4, the following equations for the piston and displacer systems are derived:

$$L_d \dot{I}_d + R_d I_d + K_d \dot{x} - E_d = 0 \quad (10)$$

$$L_p \dot{I}_p + R_p I_p + K_p \dot{y} - E_p = 0 \quad (11)$$

where,  $E$  = applied voltage of motor driver.

In the design of the refrigerator,  $x$ ,  $y$ ,  $C_y$ ,  $C_x$ ,  $C_{pp}$ ,  $C_{dd}$ ,  $C_{pc}$ ,  $C_{dc}$  are determined by the Stirling program as a result of the analysis of the thermodynamics. With these known, the solutions for  $I_d$ ,  $I_p$ ,  $E_d$ , and  $E_p$  from Equations (8) through (11) become algebraic, and the average input power  $\dot{W}_d$  and  $\dot{W}_p$  of the displacer and piston motors, respectively, can be calculated by the following expressions:

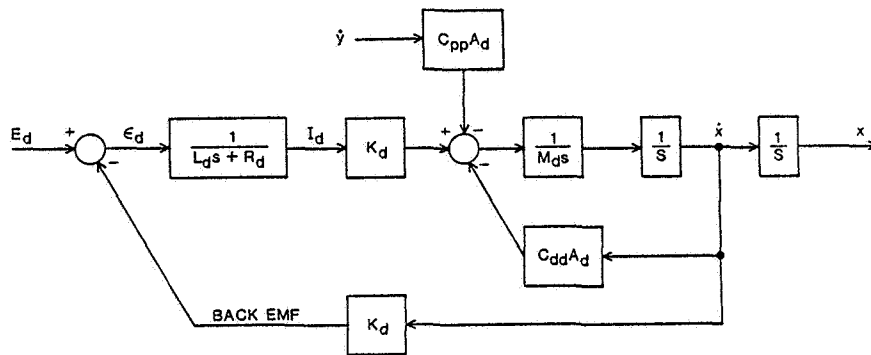
$$\dot{W}_d = n \oint E_d I_d dt$$

and 
$$\dot{W}_p = n \oint E_p I_p dt$$

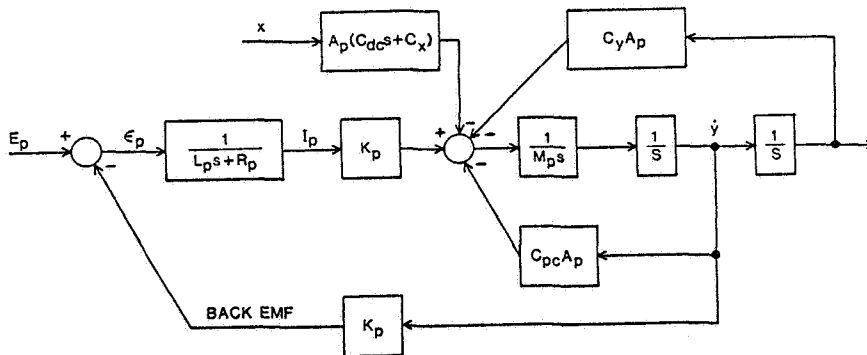
It should be noted that since the displacer motor is used to sinusoidally oscillate the displacer mass about a nominal center position, very little real mechanical output power results from the application of electrical input power. Its real component of shaft output is used only to overcome flow losses; the oscillation of the mass represents reactive power. On the other hand, since the piston resonates on a gas spring, its mechanical output power is real, and a high electromechanical efficiency results.

### 3.2.5 Control System Modeling

In the process of designing the axial control systems for the piston and displacer, the electromechanical dynamics were modeled as two decoupled systems (see Fig. 3-5). These models fit more closely the analysis of the axial control described in Section 5.3. The coupling forces of the piston on the displacer and the displacer on the piston are considered to be disturbances to the system. The fact that these forces sometimes aid the motion and reduce the electrical input power required is not germane to the modeling.



(a) DISPLACER SYSTEM



(b) PISTON SYSTEM

Figure 3-5. Block diagram of electromechanical dynamics.

The transfer functions shown in Figure 3-5 are derived by applying the Laplace transformation to Equations (8)-(11). The Laplace operator,  $s$ , is the complex frequency variable of transformation. To illustrate the derivation of the transfer functions, consider the first block in the displacer loop (Fig. 3-6).

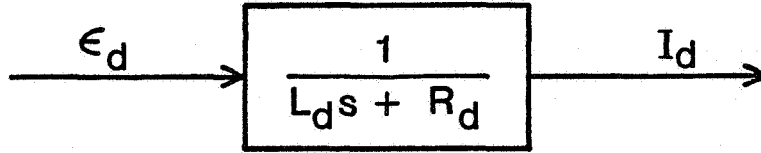


Figure 3-6. Transfer function block for displacer impedance.

This block corresponds to Equation (10), which when transformed from the time to the complex frequency domain becomes:

$$L_d s I_d + R_d I_d = \epsilon_d$$

where,  $\epsilon_d = E_d - K_d \dot{x} = E_d - K_d s x$ .

Therefore,

$$(L_d s + R_d) I_d = \epsilon_d$$

$$\frac{I_d}{\epsilon_d} = \frac{1}{L_d s + R_d}$$

The other transfer functions of the loop can be derived in a similar manner.

### 3.2.6 Summary

The differential Equations (8) through (11), which model the dynamics of the refrigerator, illustrate the coupling of the electromechanics and thermodynamics. The linear approximations for the pressure variations [Eqs. (1) - (3)], derived from the thermodynamic analysis, are dominant terms in defining equations for the mechanical dynamics. Further, through the effects of the back emf of the linear motors, the mechanical dynamics produce a load on the electronic motor driver. Finally, it is only through the operation of the axial control system, that the motion of the piston and displacer are sinusoidal with the proper phase relationship, and that thermodynamic work is produced. These system interactions are important considerations in the analysis and design of the "free" linear drive.

### 3.3 Clearance Seal Leakage

A clearance seal, formed by a long, narrow, annular gap between a reciprocating element and its cylinder wall, is not a perfect seal. It allows a finite quantity of gas to leak past but, as long as this leakage is small, the effects will be negligible. The actual leakage calculation and its effect on the thermodynamics is included in the Stirling computer program; the basics can be seen from a simplified analysis.

If the clearance gap is uniform around the circumference of the shaft, meaning that the shaft is perfectly centered in the bore, the flow can be accurately modeled as Poiseuille flow through a two-dimensional channel. Since the pressure wave imposed on the seal is oscillatory, and since the refrigerator operating frequency is low, the flow can be considered quasi-steady. The amplitude of the oscillatory leakage through the seal will be given by,

$$V = \frac{\hat{P} \pi D g^3}{12 \mu \omega L}$$

where,  $\hat{P}$  = amplitude of oscillating pressure wave.  
D = shaft diameter  
g = radial gap in clearance seal  
 $\mu$  = absolute viscosity of gas  
L = axial length of clearance seal

The leakage is most sensitive to the gap clearance, so it is apparent that small changes to this gap will result in large changes in the leakage volume. A 10% increase in the gap will increase the leakage by 33%.

In the piston, one additional effect of the clearance seal is due to the fact that it is operating under asymmetric conditions. The pressure above the piston, in the compression space, oscillates at the refrigerator operating frequency, but the pressure on the back side of the seal, in the buffer volume, is constant, equal to the charge pressure in the piston motor housing. The pressure wave itself is nonlinear, having higher peaks of overpressure than underpressure. This results in a net leakage through the clearance seal, tending to slowly pump gas from the working space into the buffer space. If this tendency were unopposed, the piston would slowly pump

its way to the top of the cylinder, displacing all of the gas from the compression space to the buffer. The axial control system maintains the proper center position of the piston, exerting an automatically regulated dc force in doing so. This dc force enables the working space pressure to pump down to a slightly lower level than the mean pressure in the buffer space, thereby effectively reducing the net leakage to zero.

#### 4. MAGNETIC BEARINGS

##### 4.1 Introduction

The mechanical advantages of clearance seals, namely low friction and long mechanical life with an all-metal/ceramic (i.e., nonlubricated) construction, were made possible through the use of magnetic bearings. Because the moving elements are electromagnetically suspended in their bores without contact, wear is eliminated and mechanical life is governed solely by electronic reliability. Contamination and thermodynamic degradation, classical problems of mechanical Stirling cycle refrigerators, are completely absent.

The work related to the magnetic bearings proceeded on many fronts. In the course of the work, four prototype bearings comprising two generations were constructed to test various aspects of the design. Analyses of the control dynamics, bearing loads, and shaft vibration were generated. Two sets of control electronics and several sets of sensor electronics were designed, breadboarded, and fabricated. Numerous test pieces were manufactured in the development of procedures to magnetically anneal the ferromagnetic material, to seal organics in metal or ceramic structures, and to hermetically join materials to the titanium alloy which would serve as the refrigerator housing. The review of this work begins with a brief description of the magnetic bearing system.

##### 4.2 Description of Bearing System

The magnetic bearing consists of three major components: the ferromagnetic pole pieces (the actuators), the eddy-current probes (the position sensors), and the electronic feedback system (the controller). The configuration of the actuators and sensors is shown diagrammatically in Figure 4-1. Each ferromagnetic pole piece exerts a radial attractive force on the reciprocating shaft when current is applied to its coil winding. By situating poles diametrically opposite, one end of the shaft may be controlled in one plane by regulating the current in each of these two poles (see Fig. 4-2). By positioning sets of poles at orthogonal planes at each end, the shaft may be suspended.

The radial position of the shaft is transduced with eddy-current sensors. The sensor probe is a flat coil situated parallel to the moving shaft (see Fig. 4-3 and Sect 4.6). By applying a high frequency voltage to this coil,

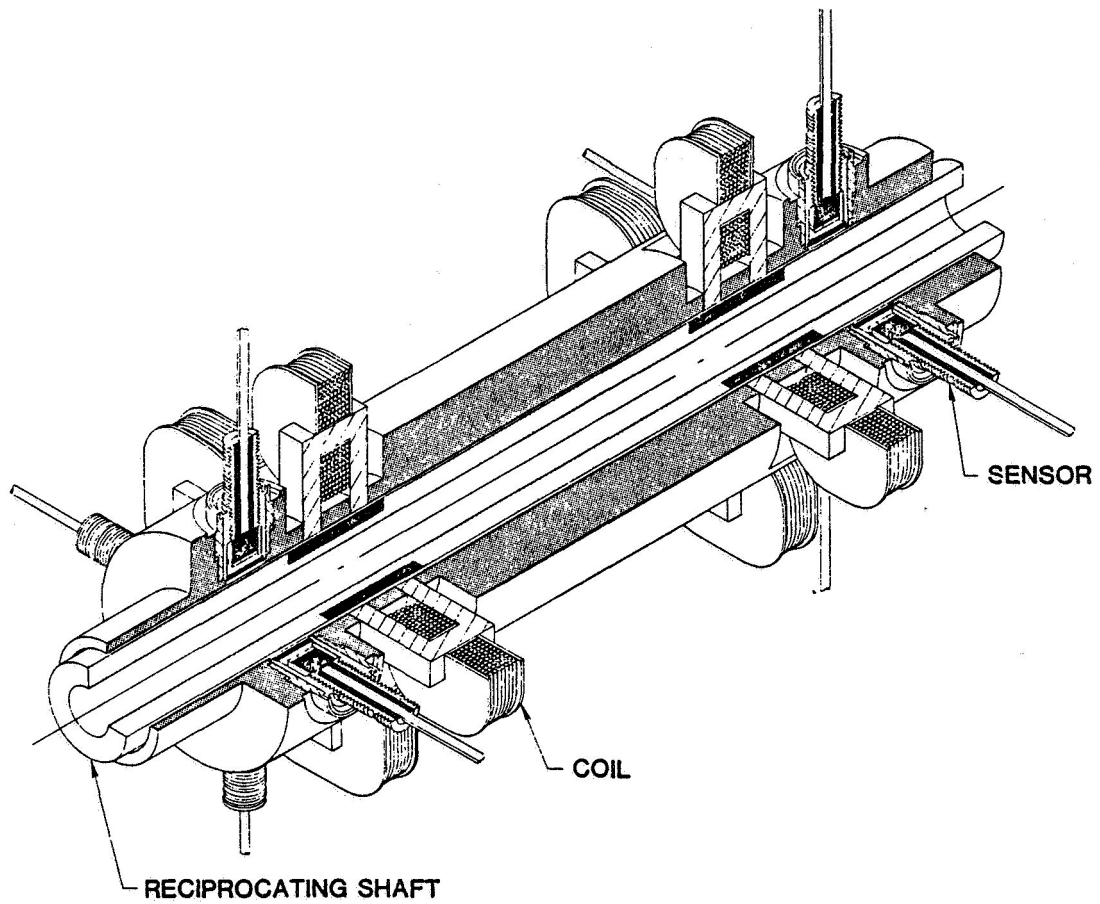


Figure 4-1. Geometry of magnetic bearing.

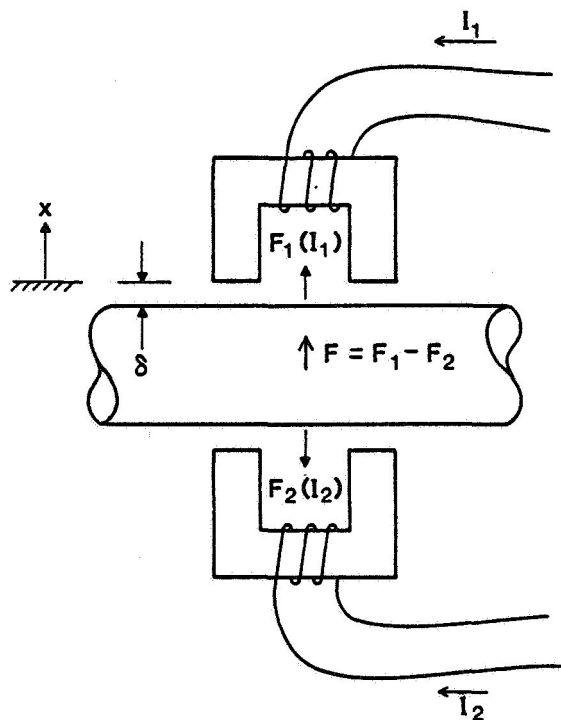


Figure 4-2. Radial force generation in magnetic bearing plane.



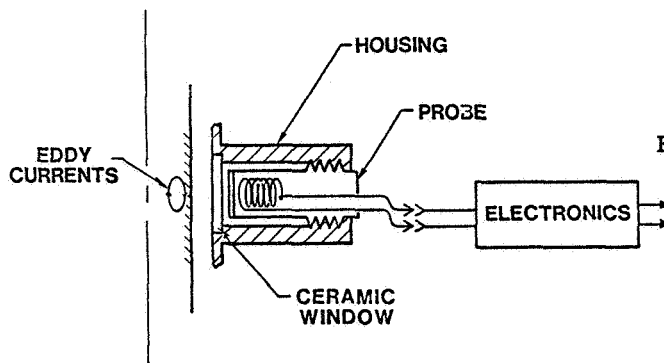


Figure 4-3. Eddy current sensor.

eddy currents are generated in the shaft, and the magnitude of these eddy currents changes as the magnetic air gap changes. Since the organic insulation on the wire and the organic potting compound of the probe would contaminate the refrigerator working gas, the probe is mounted outside the housing behind a ceramic window as shown. The sensor electronics provide the high frequency excitation for the coil and measure a signal, modulated by the effect of eddy currents, when the shaft moves. After demodulation and filtering, this signal provides the dynamic indication of shaft position.

A block diagram of the electronic controller for the bearing is shown in Figure 4-4. The pole-piece magnetics are highly nonlinear: the force is proportional to the square of the current and inversely proportional to the square of the air gap. The electromagnetic field in the iron is influenced by the effects of eddy currents, hysteresis, and magnetic saturation. The

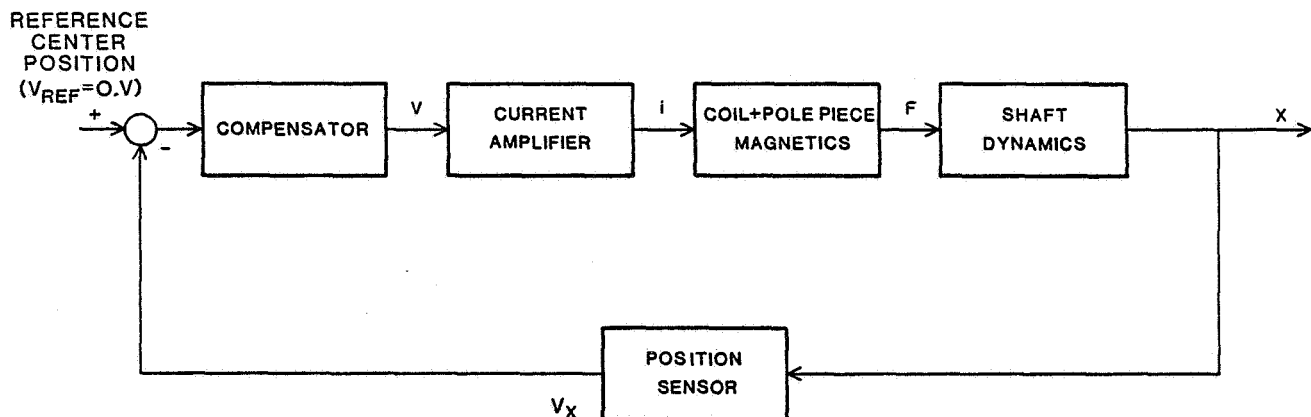


Figure 4-4. Block diagram of bearing control system.

shaft dynamics also includes a damping force caused by the gas squeeze film in the 25  $\mu\text{m}$  air gap.

The action of the feedback loop can be explained as follows. A reference center position of zero volts is compared to the transduced position voltage from the eddy current sensors. Any error between these two voltages regulates the differential current in a diametrically opposite pole piece pair so as to reduce this error. The compensator is designed to provide stability for the large restoring forces over a wide frequency band. To do this effectively, the control loop bandwidth must be large and insensitive to changes resulting from the nonlinear nature of the magnetics and dynamics. A current amplifier is used so that the destabilizing phase shifts caused by the coil inductance and actuator eddy currents are minimized.

In the following sections, the pole piece actuator and shaft dynamics are analyzed. Then, following an estimate of bearing loads and vibrational resonances and a discussion of the eddy current sensors, the design and measurement of the magnetic bearing control system is presented.

#### 4.3 Linearized Analysis of Electromagnetic Actuators and Shaft Dynamics

##### 4.3.1 General

As mentioned, the analysis and design of the magnetic bearings are hampered by the high nonlinearity of the magnetic/mechanical system. Techniques for handling nonlinear control systems directly are few; the most effective ones deal with linearization and the subsequent use of the powerful linear control theory. In the case of the bearing, linearization assumes that the radial displacement and current change little from the nominal value. Under this assumption, each of the nonlinearities is linearized for small perturbations. The feedback loop is modeled as a conventional linear regulator, and the bearing performance can be estimated using linear techniques.

The analysis of the magnetic bearing is divided into two parts. This first part is concerned with the general analysis of the magnetic/mechanical system. Linearized models of the force-current relationship, eddy-current effects in the pole pieces, and squeeze-film damping are discussed. Also, the calculation of effective mass on each bearing is derived. The second part is concerned with the analysis specific to the refrigerator configur-

ation. Here, an estimate is made of the bearing loads and shaft vibrational resonances. The results of the analyses are combined in Section 4.8.

#### 4.3.2 Analysis

##### (1) Force Constant

Consider the magnetic circuit shown in Figure 4-2. If we assume that the controlling current is divided so that positive currents are directed into the upper coil and negative currents are directed into the lower coil (which, in the simplest case, can be achieved with two diodes), then the force relationship is given by:

$$F = \frac{N^2 A \mu_o i |i|}{4(\delta+x)^2} \quad (1)$$

where,  $N$  = number of turns of coil  
 $A$  = surface area of flux path ( $m^2$ )  
 $\mu_o$  = permeability of free space (H/m)  
 $i$  = controlling current (A)  
 $\quad = i_1 \quad \text{for } i \geq 0$   
 $\quad = i_2 \quad \text{for } i < 0$   
 $\delta$  = nominal gap (m)  
 $x$  = shaft displacement about nominal (m)

The above equation is derived from the law of conservation of energy. The magnetic energy stored in the coil is,

$$W_m = 1/2 L i^2$$

where,  $L$  = coil inductance (H).

Since  $L$  changes as the mass moves, and the mechanical work done  $dW = Fdx$  must be equal to the change in magnetic energy for a constant current:

$$F = 1/2 i^2 dL/dx$$

where,

$$L = N^2 A \mu / \ell$$

and,  $\mu$  = permeability of magnetic path (H/m)  
 $\ell$  = length of magnetic path (m)

Under the following assumptions, Equation (1) was derived:

- Leakage flux can be ignored.
- Fringing flux can be ignored.
- Flux spreading at pole corners can be ignored.
- Permeability of core is high with respect to air gap; thus,  $\mu \approx \mu_0$  and  $\ell \approx 2(\delta + x)$ .

To linearize the force equation for small displacements ( $x \ll \delta$ ), we can expand Equation (1) into a Fourier series. The linearization method used is known as the Describing Function technique. It assumes that the control system which controls the bearing is predominantly low-pass so that the principal effect of the force relationship is given by its fundamental term in the series. This method is better than other techniques in that it gives a large signal force relationship without having to assume a bias or position error; however, it does assume that the magnitude of the ac current is known a priori. This knowledge is used to establish the nominal conditions for a linear model which is then valid for small perturbations about the nominal. In the case of the refrigerator bearings, the currents can be estimated from an analysis of the expected bearing loads.

Assume

$$i = \hat{i} \cos \omega t$$

then

$$F = \frac{N^2 A \mu_0 \hat{i} \cos \omega t |\hat{i} \cos \omega t|}{4\delta^2} \cdot$$

and the fundamental Fourier coefficient of  $F$  is,

$$C_1 = \frac{\frac{4}{3\pi} N^2 A \mu_0 \hat{i}^2 \cos \omega t}{4\delta^2}$$

and the linearized force relationship is:

$$\frac{F}{i} = \frac{N^2 A \mu_0 \hat{i}}{3\pi \delta^2}$$

## (2) Bias Current Effects

The driver for the magnetic bearing was designed to output a common bias into each pair of diametrically opposed pole pieces. This was done for two reasons: (1) to increase apparent bearing stiffness and (2) to bias the output transistor stage of the driver into its linear region. The apparent bearing stiffness is increased because a nonzero electromagnetic force/current relationship exists when the shaft is at its nominal center position. At the same time, the bias current produces a constant force in each pole piece which leads to bearing instability as described by Earnshaw's Theorem<sup>(1)</sup> for the passive bearing case. Dynamically, this instability is modeled as a right half plane pole. The application of a bias current has an advantage over passive biasing with permanent magnets in that the magnitude of the constant force and the slope of the force/current relationship can be changed in operation. It has the disadvantage of requiring power under no load conditions.

The control aspects of the bias current, i.e., the effect on bearing dynamics, are derived in this section. The use of the bias for the transistor output stage is explained in Section 4.7 on the driver electronics.

Referring to Figure 4-2, assume that  $I_1 = i_o + i_1$ , where  $i_o$  is the common bias applied to each coil. Thus,

$$F_1(I_1, x) = \frac{N^2 A \mu_o (i_o + i_1)^2}{4(\delta + x)^2}$$

with the parameters defined by Equation (1). Using the Taylor Series expansion for a function of two variables:

$$F_1(I_1, x) = \left( \frac{i_o^2 N^2 A \mu_o}{4\delta^2} \right) + \left( \frac{i_o N^2 A \mu_o}{2\delta^2} \right) \cdot i_1 \\ - \left( \frac{i_o^2 N^2 A \mu_o}{2\delta^3} \right) \cdot x + (\text{higher order terms})$$

---

(1) S. Earnshaw, Trans. of Cambridge Philosophical Soc. 7, 1842.

The Taylor Series expansion is used instead of the Describing Function linearization in this analysis for two reasons. First, in normal operation, the displacement from the nominal center position is small ( $x \ll \delta$ ) and thus can be usefully approximated by the slope of the line. Second, the peak ac displacement is a function of the action of the control system and can not be approximated by knowing the bearing loads alone. The Describing Function approach requires the a priori knowledge of this displacement.

In a similar manner, the force  $F_2$  from the lower pole piece in Figure 4-2 can be expanded as:

$$F_2(I_2, x) = \left( \frac{i_o^2 N^2 A \mu_o}{4\delta^2} \right) + \left( \frac{i_o^2 N^2 A \mu_o}{2\delta^2} \right) \cdot i_2 \\ + \left( \frac{i_o^2 N^2 A \mu_o}{2\delta^3} \right) \cdot x + \text{higher order terms}$$

The first term in the expressions for  $F_1$  and  $F_2$  is a dc force which results from the application of the common bias. For purposes of analysis, it is assumed that the magnetic properties of each pole piece are exactly the same, even though this rarely occurs in practice. Thus, there is no net effect from this force.

The second term in each expression is the ac force which results from the application of a controlling current when  $x = 0$ . Since the controlling current is derived only from the error signal in the position, these terms are exactly zero. It is this term, however, for small perturbations about  $x = 0$ , which produces the non-zero force/current relationship, and this is used as an approximation of the force constant in the small signal case.

Thus, when the higher order terms are ignored by assuming small displacements, the net force which results from the application of a common bias can be characterized by the third term in each expression.

$$F_{\text{net}} = F_1 - F_2 = - \frac{i_o^2 N^2 A \mu_o}{\delta^3} \cdot x'$$

Observe that this expression is equivalent to a negative spring constant producing a force proportional to position, but the force is not in-phase at low frequencies as with a normal mechanical spring. From a control-system point of view, the effects of this negative spring can be explained by referring to Figure 4-5.

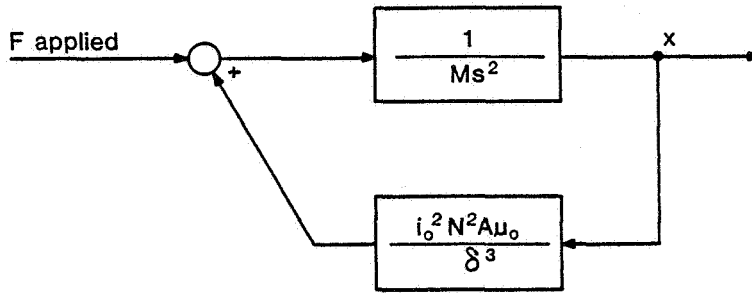


Figure 4-5. Block diagram showing linearized effects of a common bias.

The shaft dynamics are modeled as a simple inertial load. In the figure,  $M$  is the mass of the shaft, and  $s$  is the Laplace operator. The transfer function between the applied force and the displacement is:

$$\frac{X}{F} = \frac{1}{Ms^2 - \left( \frac{i_o^2 N^2 A \mu_o}{\delta^3} \right)}$$

Therefore, the open-loop bearing system has a pole in the right-half plane, and the position of this pole is a function of the square of the bias current. This is represented by the root locus diagram of Figure 4-6.

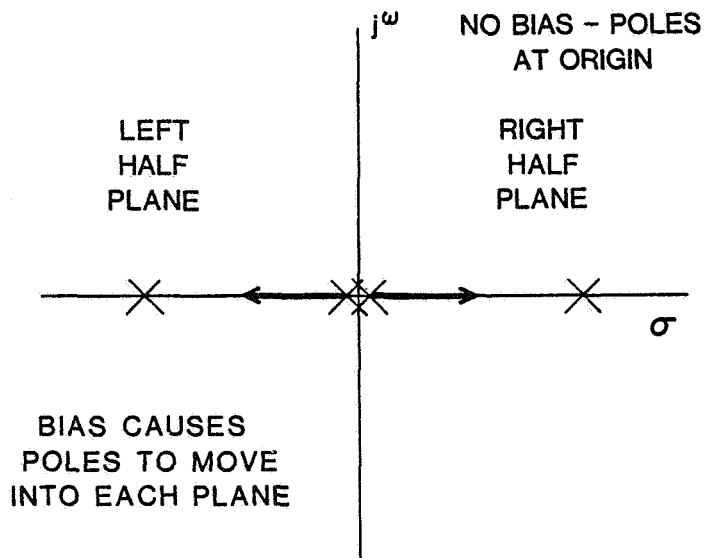


Figure 4-6. Root locus showing effects of a common bias current.

### (3) Effective Mass

The center of gravity of the suspended shaft is not exactly in the middle of the front and rear magnetic bearings as represented in Figure 4-7. The effective mass seen by each set of pole pieces (such as shown in Fig. 4-2) is a combination of both the mass and the rotational inertia of the shaft. Since each set is driven by a single-input/single-output control system, the effective mass, which must be controlled by the front and rear sets, is different and computed separately. For this analysis, the shaft is considered to be rigid, damping is ignored, and the center of gravity is assumed to be radially centered. The shaft dynamics which result in vibrational resonances and bending modes are discussed in Section 4.5. Squeeze-film damping is discussed in the following subsection. Radial eccentricity of the center of gravity is discussed in Section 4.4.

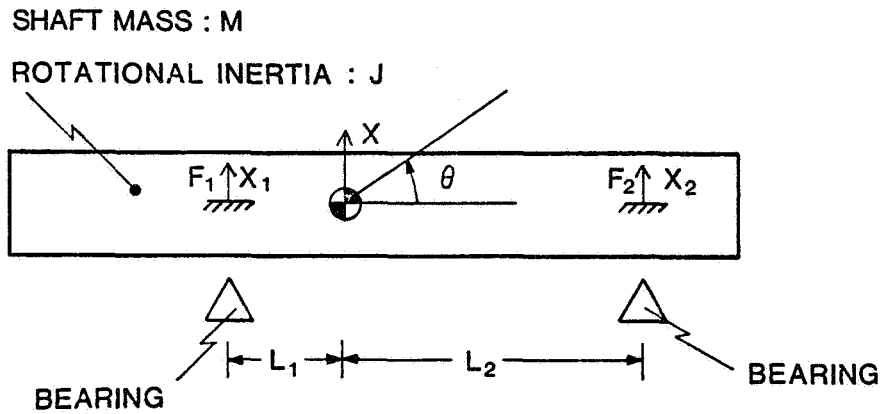


Figure 4-7. Bearing representation showing center of gravity.

For the configuration shown in Figure 4-7,

$$F_1 + F_2 = M\ddot{x}$$

$$-L_1F_1 + L_2F_2 = J\ddot{\theta}$$

where forces  $F_1$  and  $F_2$  are as shown. If it is assumed that  $\theta$  is small (see Fig. 4-8), then

$$\ddot{x}_1 = \ddot{x} - L_1\ddot{\theta}$$

$$\ddot{x}_2 = \ddot{x} + L_2\ddot{\theta}$$



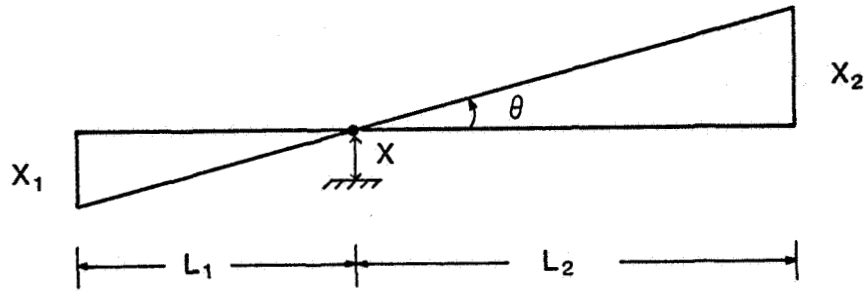


Figure 4-8. Geometry of motion about center of gravity.

These linear equations are represented in matrix notation, and the following is derived:

$$\begin{pmatrix} F_1 \\ F_2 \end{pmatrix} = \frac{1}{(L_1 + L_2)^2} \begin{pmatrix} J + ML_2^2 & -J + ML_1L_2 \\ -J + ML_1L_2 & J + ML_1^2 \end{pmatrix} \begin{pmatrix} \ddot{x}_1 \\ \ddot{x}_2 \end{pmatrix} \quad (2)$$

To calculate the effective mass that each actuator set sees, the system represented by Equation (2) is decoupled by deriving the eigenvalues of the mass matrix. The equations for the two eigenvalues are:

$$M_{1,2} = \frac{2J + M(L_1^2 + L_2^2) \pm \sqrt{4J^2 + M^2(L_1^2 + L_2^2)^2 - 8JML_1L_2}}{2(L_1 + L_2)^2}$$

Using these effective masses, the decoupled bearing dynamics are represented by the equations:

$$F_1 = M_1 \ddot{x}_1$$

$$F_2 = M_2 \ddot{x}_2$$

(4) Squeeze-Film Damping

The stability of the magnetic bearings is greatly enhanced by the effects of pneumatic forces acting in the small annular gaps. These forces provide mechanical damping at frequencies within the bandwidth of the control loop.

To see how this damping is generated refer to Figure 4-9, a cross-sectional representation of the bearing. As the shaft approaches the housing, the displaced gas is forced circumferentially around the shaft. The circumferential pressure gradient, caused by the viscosity and/or inertia of the gas, acts on the shaft to oppose the motion. The net force on the shaft is proportional to the shaft velocity  $V$ , and thus this effect is accurately represented by a mechanical damper.

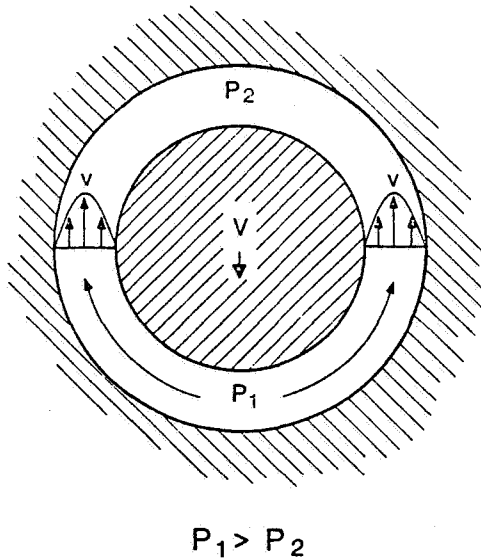


Figure 4-9. Circumferential fluid flow and resulting pressure gradient.

The equation which describes the flow of fluid in a thin annulus is the three-dimensional Reynold's equation:

$$\frac{\partial}{\partial z} \left( \frac{\rho c^3}{\mu} \frac{\partial P}{\partial z} \right) + \frac{\partial}{\partial y} \left( \frac{\rho c^3}{\mu} \frac{\partial P}{\partial y} \right) = 6 \left[ \frac{\partial}{\partial z} (\rho U c) + \frac{\partial}{\partial y} (\rho V' c) + 2 \frac{\partial}{\partial t} (\rho c) \right] \quad (3)$$

where,  $\rho$  = fluid density  
 $c$  = bearing radial clearance  
 $\mu$  = fluid absolute viscosity  
 $P$  = fluid pressure  
 $V'$  = circumferential surface velocity of shaft  
 $U$  = axial surface velocity of shaft  
 $z$  = axial Cartesian coordinate  
 $y$  = circumferential Cartesian coordinate

This equation was derived from the Navier-Stokes equations under the following assumptions which are valid for the frequencies of interest and the geometry of the refrigerator bearings:

- Inertial and body forces are negligible.
- No pressure gradient across thickness of film.
- Annulus curvature is small compared to film thickness.
- No-slip boundary condition at the walls.
- Fluid is Newtonian and thus has constant viscosity across the annulus.
- Flow is laminar.

Equation (3) can be simplified if it is assumed that the flow is incompressible and if the axial velocity of the shaft is ignored. (The near-zero rotational velocity of the shaft is also dropped from the equation.) Test data indicates that the assumed incompressibility is a valid approximation in the refrigerator since the peak pressure ratio in the gap is small compared to the mean charge pressure of the machine. Thus, for the particular application at hand, i.e., the magnetic bearings for the refrigerator, the following simplification of Reynolds' equation is valid:

$$\frac{\partial}{\partial y} c^3 \frac{\partial P}{\partial y} = 12 \mu V$$

where  $V$  is the radial velocity of the shaft.

The force on the shaft per unit length is found by integrating the pressure field over the surface area. Using appropriate boundary conditions, this equation is:

$$\frac{F}{L} = \frac{12\pi\mu V}{(1 + \epsilon)^{3/2}} \left(\frac{R}{C}\right)^3$$

where,  $R$  = radius of shaft

$\epsilon$  = eccentricity of shaft and cylinder

The damping coefficient (defined as  $b \equiv F/V$ ) is, for small eccentricity:

$$b = 12\pi\mu L \left(\frac{R}{C}\right)^3$$

#### (5) Eddy Current Effects

Eddy currents in the ferromagnetic pole pieces of the magnetic bearing influence the stability of the control system in two ways. First, they change the apparent impedance of the actuating coil. Second, they change the magnitude and phase of the force which is produced for a given applied current by effectively decreasing the area through which the magnetic flux is carried.

When eddy currents are a problem in magnetic circuits, the normal solution is to laminate the material. The thickness of the laminations is determined by the material properties of the iron, the geometry of the magnetic circuit and the frequency at which the flux is to be generated. In the magnetic bearings for the refrigerator, laminating was not an acceptable alternative because the electromagnets had to also form part of the hermetic pressure seal. In fact, the method of joining, illustrated in Figure 4-10, used a silver braze material and thus produced a greater amount of eddy currents than would be contained in the solid pole piece alone. For practical reasons, it was decided that the problem of eddy currents be handled in the bearing electronics, resulting in a somewhat lower radial stiffness than might otherwise have been attained.

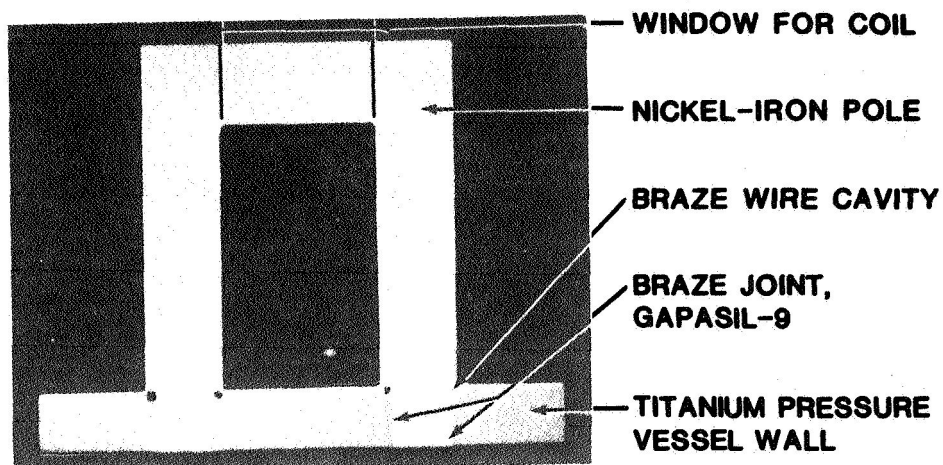


Figure 4-10. Cross section of magnetic bearing pole piece.

To see how eddy currents effect the bearing dynamics, begin with Maxwell's equations for the electromagnetic field:

$$\nabla \times \mathbf{E} = - \partial \mathbf{B} / \partial t \quad (4)$$

$$\nabla \times \mathbf{H} = \mathbf{J} \quad (5)$$

$$\nabla \cdot \mathbf{B} = 0 \quad (6)$$

The electric field  $\mathbf{E}$  and the current density  $\mathbf{J}$  obey Ohm's law:

$$\mathbf{J} = \sigma \mathbf{E} \quad (7)$$

where,  $\sigma$  is the conductivity of the material. The flux density  $\mathbf{B}$  and magnetic intensity  $\mathbf{H}$  obey the relation

$$\mathbf{B} = \mu \mathbf{H} \quad (8)$$

where  $\mu$ , the permeability of the material, is in general a function of  $H$ . The parameter  $\mu$  is often written as the product  $\mu_0 \mu_r$  where  $\mu_0$  is the permeability of space and  $\mu_r$  is the relative permeability. For a linear material, both  $\mu_0$  and  $\mu_r$  are constant.

Combining Equations (4), (5) and (7) for a material of constant conductivity:

$$\nabla (\nabla \cdot \mathbf{H}) - \nabla^2 \mathbf{H} = -\sigma \partial \mathbf{B} / \partial t$$

Using relationship (8) and Equation (6) this reduces to:

$$\nabla^2 \mathbf{B} = \sigma \mu_0 \mu_r \partial \mathbf{B} / \partial t \quad (9)$$

The pole pieces of the magnetic bearings can be approximated by thick flat plates of rectangular cross section (Fig. 4-11). For this configuration, the flux density can be considered to vary only in the direction perpendicular to the flat surface. The differential equation derived from Equation (9), which describes the flux density in this core for a sinusoidal excitation, is the diffusion equation:

$$\frac{d^2 B}{dx^2} = j \omega \mu_0 \mu_r B \quad (10)$$

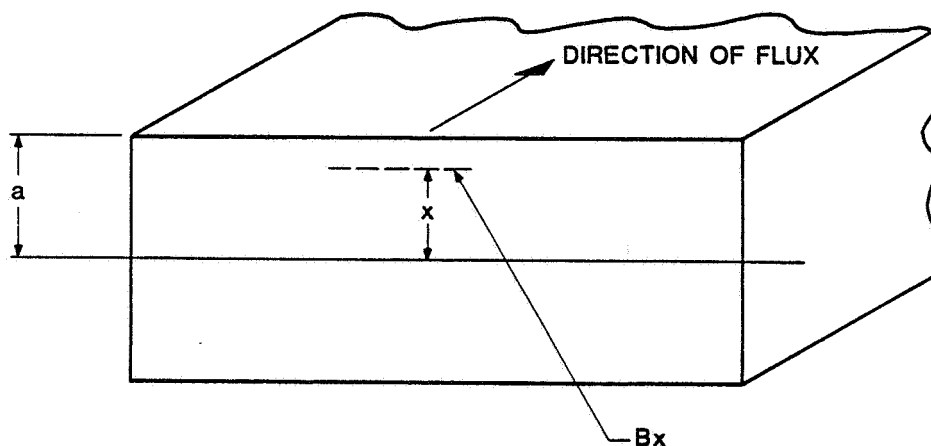


Figure 4-11. Cross section which approximates pole piece.

where  $x$  is the distance from the axis of the rectangular core of thickness  $2a$ ,  $C = \sqrt{2\pi f \sigma \mu_o \mu_r}$  and  $f$  is the sinusoidal frequency of oscillation. The average flux density of the core is defined by the equation:

$$B_m = \frac{1}{a} \int_0^a B_x dx$$

$$= \frac{B_s \cdot d}{(1+j)a} \left[ \frac{(e^{a/d} - e^{-a/d}) \cos a/d + j (e^{a/d} + e^{-a/d}) \sin a/d}{(e^{a/d} + e^{-a/d}) \cos a/d + j (e^{a/d} - e^{-a/d}) \sin a/d} \right] \quad (11)$$

where,  $B_x$  = value of  $B$  at plane  $x$  which is found by solving Equation (10)  
 $B_s$  = value of  $B$  at core surface  
 $d = \sqrt{2}/C$  skin thickness

The flux in the interior of the core is less than and lags behind, the flux at the surface. Further, the magnitude decreases and the angle of lag increases for increasing distance from the surface and increasing frequency. This is the familiar "skin effect" cause by eddy currents. To see how this results in a change in apparent impedance in the coil, refer to Figure 4-12.

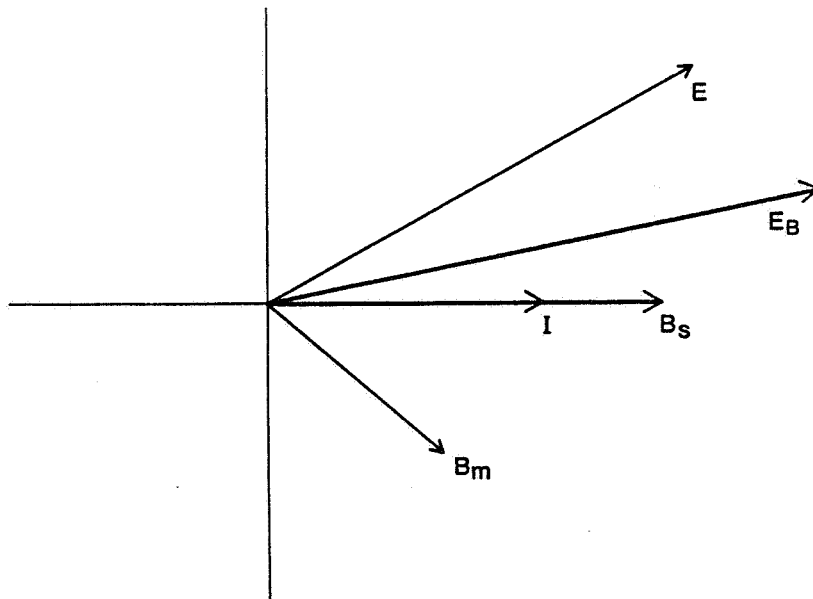


Figure 4-12. Vector diagram of current, voltage, and flux in core.

When a voltage  $E$  is impressed on the coil, the current  $I$  in the coil produces the flux density  $B_s$  when no eddy currents are generated. In the presence of eddy currents, the average flux density in the core,  $B_m$ , is phase shifted relative to the current and thus has a component in phase with the current and one which lags the current by  $90^\circ$ . The first component looks like a decrease in coil inductance when measured at the terminals of the coil. The second component appears like an equivalent resistance drop in the coil, which represents the power lost in eddy currents. In the figure,  $E_B$  represents the resultant voltage on the coil.

At high frequencies, the average flux in the core is about:

$$B_m = \frac{(1 - j) B_s \cdot d}{2a}$$

and thus it should be noted that the average flux density rolls off as the square root of frequency (from the definition of  $d$ ) and has a phase angle of  $-45^\circ$  relative to the flux at the surface [phase of  $(1 - j)$ ].

To compute the effects of the decrease of flux density in the poles, the air gap reluctance of the magnetic circuit must be taken into account. The simplest way to do this is to represent the roll-off of flux by a change in the permeability of the iron path. The effective permeability is thus:

$$\mu' = \mu \frac{B_m}{B_s} \quad (12)$$

which is, in general, a complex number and a function of frequency. The permeability  $\mu$  in the equation is the incremental permeability at the operating point, and it should be noted that the results represented by Equation (11) break down if the pole piece goes into saturation.

To use Equation (12) to calculate the force constant, the reluctance of the magnetic path is computed. This is simply the reluctance of the pole piece plus the reluctance of the armature plus the reluctance of the air gap.

$$Rel = \frac{l_{pole}}{\mu'_{pole} A_{pole}} + \frac{l_{arm}}{\mu'_{arm} A_{arm}} + \frac{2(\delta + x)}{\mu_o A_{gap}}$$



This reluctance which is a complex function of frequency is then used in place of the reluctance in Equation (1) to compute the force constant and, in the following equation, to compute the inductance:

$$L = \frac{N^2}{\text{Rel}}$$

From these equations it is observed that the effects of eddy currents are small until the reluctance of the iron approaches that of the air gap. At that point, the force constant and admittance of the bearing roll off as the square root of frequency and approach 45° of lagging phase. For control loop modeling, this effect is represented by a half pole at the break frequency. Although this is not a linear model, it was found to be useful since the eddy-current breakpoint falls well within the bandwidth of the bearing feedback loop.

This completes the general analysis of magnetic bearings. In the following sections, considerations peculiar to the specific application, i.e., magnetic bearings for a driven piston and displacer in a cryogenic refrigerator, are examined.

#### 4.4 Determination of Magnetic Bearing Loads

##### 4.4.1 Introduction

In order to properly size the magnetic bearings to adequately support the piston and displacer, the imposed loads have to be determined. Both static dc loads and time-varying ac loads will exist simultaneously. The ac loads will occur primarily at the cooler operating frequency; higher harmonics can be neglected. Loads identified for the linear reciprocating elements are imposed by two specific sources: the drive motor and the suspended mass.

- Motor Forces

- Nonuniformity in armature magnet strength.
- Misalignment of fields from armature magnets.
- Armature radial instability.
- Motor coil geometry.

- Suspended Mass Forces

- Gravity.
- Moment between center of gravity and motor force.
- Axial motion.

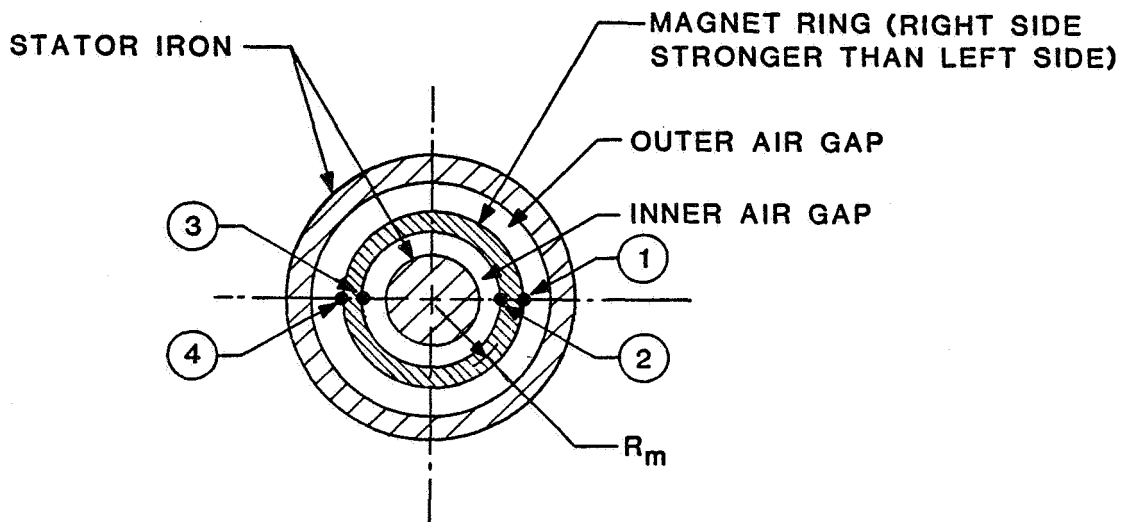
The direction and magnitude of the above forces is a function of time and of the relative orientation of the refrigerator, so it is not possible to provide an absolute value for their vector sum. However, an upper bound can be obtained, and the most probable load can be computed as the root sum square value.

For each of the above loads a generalized analysis is given in Section 4.4.2. Ac and dc loads are then calculated in Section 4.4.3 for the piston and displacer bearings, and the results are summarized for each bearing in Section 4.4.3.6. The generalized analysis of Section 4.4.2 may be used to calculate loads in future cooler designs.

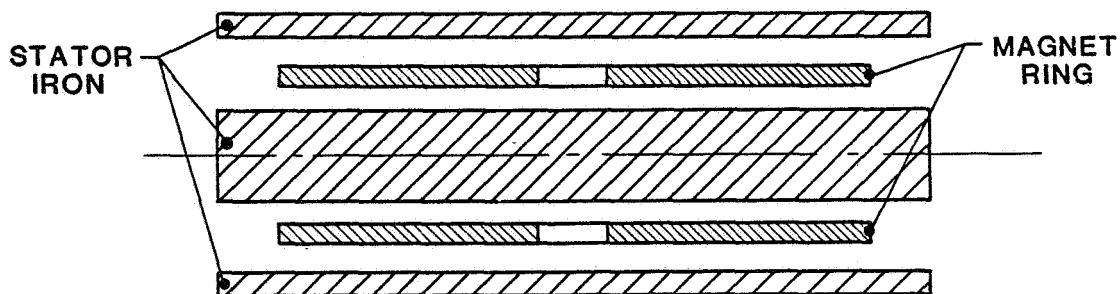
#### 4.4.2 General Analysis

##### 4.4.2.1 Strength Nonuniformity of Motor Magnets: Generalized Piston Motor Geometry

A simplified cross section geometry of the piston motor is shown in Figure 4-13. Each of the two magnet rings in the motor armature is composed of ten (10) samarium-cobalt magnet segments. Magnetic segments are used because samarium cobalt is not commercially available in large-diameter rings since high magnetic fields are required for fabrication. As shown, the rings are surrounded by iron at their inside and outside diameters.



(a) Radial cross section.



(b) Axial cross section.

Figure 4-13. Cross sections of piston motor.

The worse-case conditions exist when the magnets on one 180° section of a ring are all assumed to be a fractional amount  $\epsilon$  stronger in flux density than those on the other half of the ring. The net force is computed using a general formula for the force between two parallel plates. Generally,

$$F = \frac{B^2 A}{2\mu_0}$$

where,  $B$  = flux density (T)  
 $A$  = projected area (m<sup>2</sup>)  
 $F$  = radial force (N)  
 $\mu_0$  = permeability of space ( $4\pi \times 10^{-7}$  H/m)

By summing the forces due to the flux in the inner and outer air gap, the net static disturbance force can be estimated. Conservatively, the assumption is made that the flux distribution remains unchanged when the magnet ring is inserted in the stator. In reality, the flux will redistribute circumferentially tending to reduce the asymmetries and produce a lower net force.

Neglecting second order terms, the disturbance force is described by the equation:

$$F = \frac{2L\epsilon}{\mu_0} [R_1 B_1^2 - R_2 B_2^2] \quad (1)$$

where,  $R_1$  = outer radius of magnet ring (m)  
 $R_2$  = inner radius of magnet ring (m)  
 $L$  = length of magnet (m)  
 $B_1$  = flux density at outer radius (T)  
 $B_2$  = flux density at inner radius (T)  
 $\epsilon$  = strength nonuniformity (dimensionless)

Calculation of the disturbance effect can be simplified by using the mean flux density of the magnet ring,  $B_m$ , which is known from the magnetic circuit analysis of the linear motors (see Sect. 5.2). Equation (1) becomes:

$$F = \frac{2L\epsilon}{\mu_0} B_m^2 R_m^2 \left[ \frac{1}{R_1} - \frac{1}{R_2} \right] \quad (2)$$

where,  $R_m$  = mean radius of ring (m).

#### 4.4.2.2 Strength Nonuniformity of Motor Magnets: Generalized Displacer Motor Geometry

Figure 4-14 is a cross section of the displacer motor. The magnets are attached to the center Permerdure core which moves. Only an outer air gap exists. Two magnet rings compose the armature (Fig. 4-14b). Assuming that the magnetic flux density on one side of the motor is an amount  $\epsilon$  stronger than the other, as previously, then the armature radial force using Equation (1) becomes:

$$F = \frac{\epsilon D L B^2}{\mu_o} \quad (3)$$

where  $B$  is the mean flux density of the air gap and  $D$  is the outer diameter of the magnet ring.

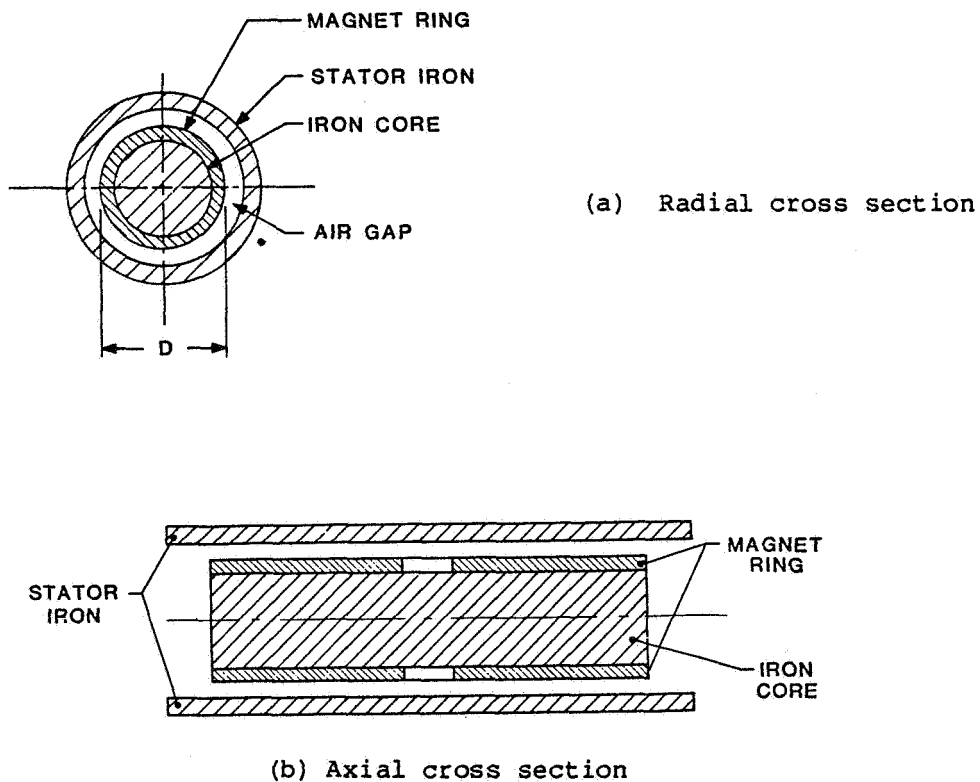


Figure 4-14. Cross sections of displacer motor.

In each of the motor designs it is not known in what direction this radial force will act since the motor armatures are free to rotate on their respective bearings. Unequal fringing (an end effect) was neglected being second order and not significant.

#### 4.4.2.3 Armature Magnetic Field Misalignment Forces

The armatures of the piston and displacer motors are built up from arc shaped magnet segments to form a ring. During the fabrication process, each segment is magnetized with a parallel (uni-directional) magnetic field, not the desired radial magnetic field (Fig. 4-15). Since there are an even number of segments around the circumference of the motor armature, in the ideal case, the effects of the parallel magnetic fields cancel and produce no net radial force.

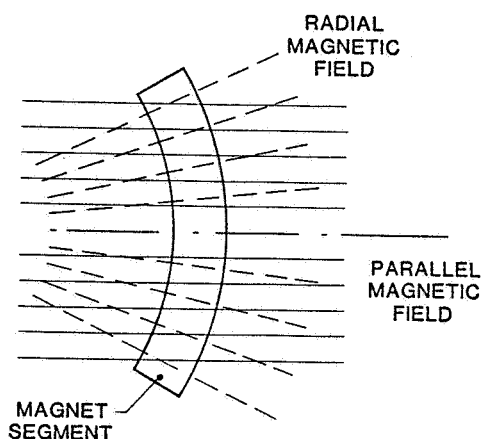


Figure 4-15. Permanent magnet segment showing parallel magnetic field which exists and ideal radial field.

In practice, however, the magnetic field of each segment is misaligned from the radial position by angle  $\theta$  circumferentially and by angle  $\alpha$  axially. Figure 4-16 shows these angles for a typical segment that produces a flux  $\phi$ .

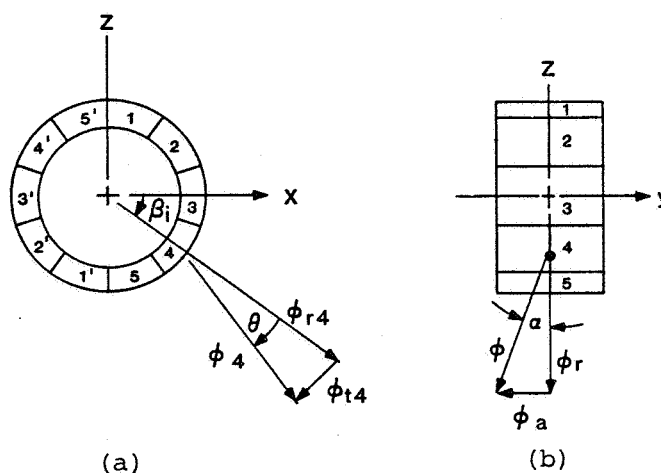


Figure 4-16: Piston-motor magnet ring showing magnet segments and field misalignments.

Radial side forces are produced by the misalignment of the magnetic field by two effects. First, the magnet segments are attracted to the stationary ferromagnetic stator and, since this attractive force is not radially symmetric, a side force proportional to the cosine of the misalignment angle results. Second, the misaligned flux interacts with the circumferential current. This current produces the axial force of the motor by interacting with the radial component of the field of the magnets. In the same way, an interaction with an axial component of the field of the magnet produces radial force and an interaction with a tangential component produces a moment on the armature.

The effect of the misalignment of the flux is reduced when the magnet ring is inserted in the iron stator (Figs. 4-13 and 4-14). The radial symmetry of the stator tends to orient the lines of flux radially, in spite of the direction of the magnetic field in the individual magnet segments. In Figure 4-16, this means that the angles  $\theta$  and  $\alpha$  are much less when the magnet ring is inserted in the ferromagnetic stator than with the magnets unloaded in air. Forces produced by attraction of the magnet ring to the stator and by the interaction of the circumferential current, while still present, are considered second order and not computed in this analysis.

#### 4.4.2.4 Armature Radial Instability

Moving magnet motor armatures are inherently radially unstable because the magnet structure is attracted to the surrounding stationary ferromagnetic material. This geometry is shown in Figures 4-13 and 4-14 for the piston and displacer motors, respectively. If the magnet ring is displaced radially, it moves closer to the stator iron; consequently, the radial force increases in the displaced direction. At the true magnetic center (approximately equal air gaps), these forces are perfectly balanced.

In general, the radial force developed has two components. First, a change in the magnetic air-gap reluctance produces an associated change in the magnetic field. For the displacer motor geometry shown in Figure 4-14, with the armature displaced from magnetic center, the reluctance decreases with the decreasing air gap and increases in the diametrically opposite increasing air gap. The flux density in the gap increases with the lower reluctance, decreases with the higher reluctance, and produces a net side force. In the piston motor geometry shown in Figure 4-13 the magnetic ring is sandwiched between an inner and outer stator. Since the relative permeability of the samarium cobalt magnets is near unity, the reluctance of the magnetic circuit changes little when the armature is displaced radially, and the resulting side force is small. Second, a change in fringing flux occurs outside of the air gap, i.e., at the boundaries of the magnet structure. This effect is more predominant in the piston motor, since there is an air gap on either side of the magnet ring; it is not significant for the displacer motor. These effects are discussed in detail below.

(1) Change in Air Gap Reluctance

• Displacer Motor

Consider Figure 4-17 which shows nonconcentric ferromagnetic cylinders displaced radially by an amount  $d$ . The local reluctance of the magnetic circuit at  $r_1$  is lower than that at  $r_2$ .

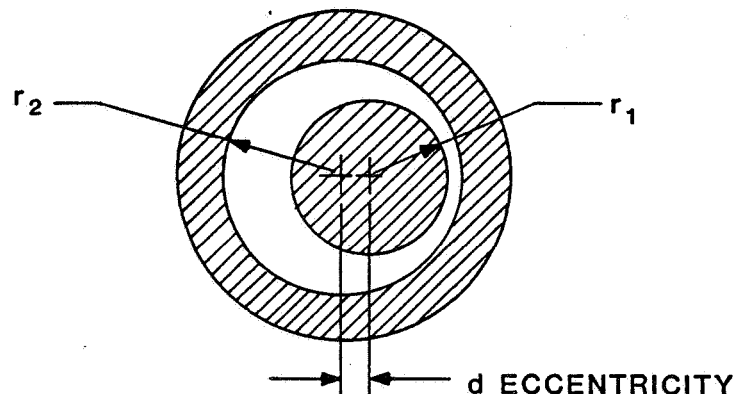


Figure 4-17. Radial instability of nonconcentric cylinders.



The geometry depicted is magnetically the same as that of the displacer motor. Since permanent magnets are attached to the inner cylinder, a radially nonsymmetric field results when the motor armature moves radially. The side force produced by this field is a function of the displacement, and thus, it is more convenient to compute an "instability stiffness" defined by  $k = F/d$ .

$$k = \frac{\pi^2 L R_m^2 B_m^2}{2\mu_0 (r_2 - r_1)} \cdot \frac{N}{m} \quad (4)$$

where,  $B_m$  = mean magnet flux density (T)  
 $R_m$  = mean magnet radius (m)  
 $F$  = force (N)  
 $L$  = axial length (m)  
 $r$  = radii (m)  
 $d$  = displacement (m)  
 $\mu_0$  = permeability of space ( $4\pi \times 10^{-7}$  H/m)

Note:  $B_{\text{gap}} = B_{\text{surface of magnets}} = B_m \frac{R_m}{r_1}$

#### • Piston Motor

The formula in Equation (4) is based on computing the change in reluctance of the air gap. The permanent magnet structure attached to the central cylinder is the source of the magnetomotive force which produces the resulting redistribution of flux in the air gap and hence an instability force.

In the piston motor geometry, a somewhat different situation exists. Figure 4-13b shows a longitudinal cross section of the piston motor. Each magnet ring has an air gap at its inside and outside diameter, the space taken by the stationary drive coils. If the magnet rings are displaced radially, it can be shown that the reluctance of the magnetic circuit remains relatively unchanged, resulting in no instability force. The reluctance is constant because of the samarium cobalt magnets, which have a relative permeability that is near unity. This would not be the case with some other magnet materials, such as Alnico, which are permeable to magnetic fields. By having a permeability which is essentially the same as air, the samarium

cobalt magnets do not change the air gap reluctance when their position in the air gap changes. Further, since the demagnetization curve for samarium cobalt is linear, as illustrated in Figure 4-18, the relative permeability is insensitive to the magnet loading (i.e., the operating point on the B-H curve). Thus, a radial "instability stiffness", equivalent to that of the displacer motor, does not exist in the piston.

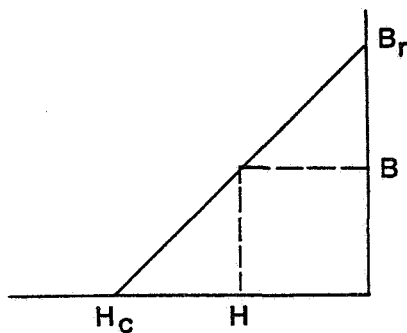


Figure 4-18. Demagnetization curve of samarium cobalt.

## (2) Fringing

Fringing forces, being 3-dimensional, can not be easily calculated directly for the geometries at hand. However, the forces were estimated using the results of two case studies with Philips Laboratories' finite-element magnetic circuit analysis (MAGGY) computer program. MAGGY solves 2-dimensional (2-D) magnetostatic problems. It can be used here only to the extent that the geometry can be approximated by a 2-D form.

### ● Piston Motor

For the piston motor, the MAGGY program was used to calculate the radial instability per unit length of the infinitely long unfolded motor shown in Figure 4-19. This 2-D model represents both the effects of fringing and the net force on the magnet ring from the change in air gap reluctance. As discussed above, however, the force produced by the changing reluctance is near zero and, thus, the resulting instability occurs predominantly from the effects of fringing. In the computer analysis, the motor armature is displaced radially, and the "instability stiffness" due to fringing was calculated to be  $1.1 \times 10^5$  N/m.

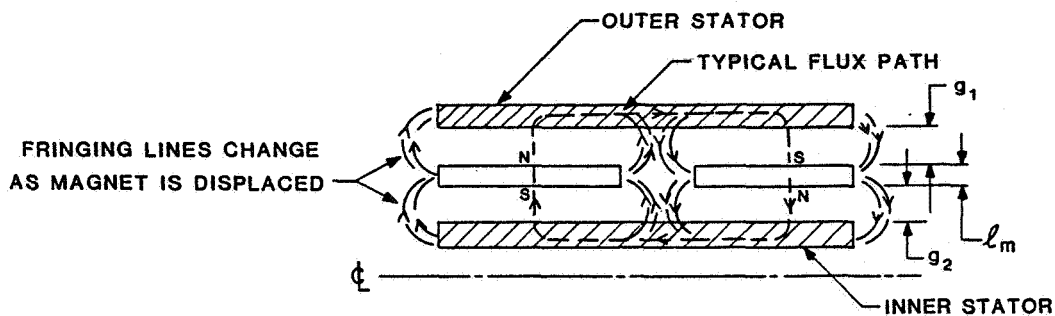


Figure 4-19. 2-D model of piston motor for determining fringing forces with MAGGY program.

In going from this 2-D geometry to that of a round motor, a correction factor for the air gap is needed. When a cylinder is radially displaced in a concentric housing, the average change in air gap over a  $180^\circ$  section of the cylinder can be shown to be a factor of  $2/\pi$  less than the actual radial motion. This correction gives an estimated instability of  $7 \times 10^4$  N/m.

#### • Displacer Motor

A MAGGY analysis was made for the displacer motor in an unfolded 2-D geometry (Fig. 4-20). For this motor, unlike the piston, the effects of fringing cannot be separated from the effects of the change in air-gap reluctance. The MAGGY result was  $1.4 \times 10^4$  N/m. The  $2/\pi$  correction factor gives  $9 \times 10^3$  N/m. If one calculates the air gap instability from

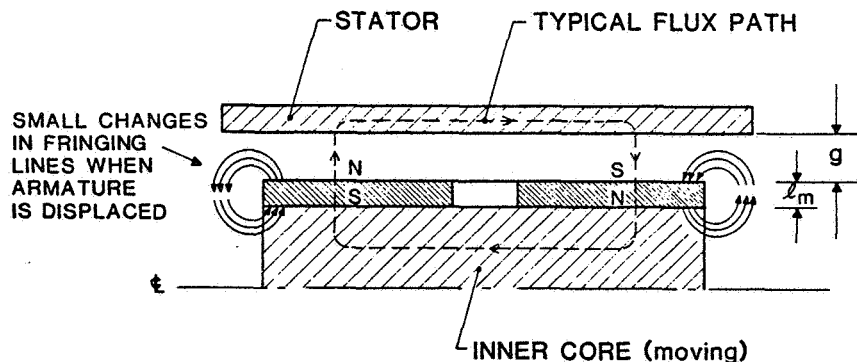


Figure 4-20. 2-D model of displacer motor for MAGGY analysis.

Equation (9), the result is  $3.9 \times 10^4$  N/m. Since Equation (4) gives a more conservative value, it is recommended even though fringing was ignored. The discrepancy between the two estimates of the instability is indicative of the approximate nature of the analysis.

### (3) Torsional Instability

The direction of the force produced by the armature radial instability is not determined in the above analysis. Although it was assumed for simplicity that the magnet ring displaces radially and that the direction of force application is the same for the two bearings, it is possible that the ring will torsion as shown in Figure 4-21. When the ring cocks to an angle  $\theta$ , the air gap becomes smaller at the two end locations. Via changes in the air gap reluctance and fringing field, the increased radial force at each smaller air gap tries to continue this rotation. Thus, the mode of the radial instability can be torsional instead of translational or some combination of both.

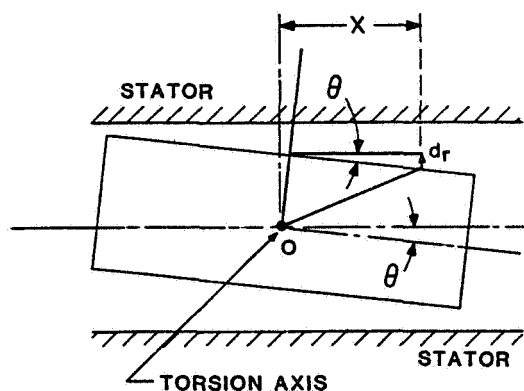


Figure 4-21. Model showing torsional instability of a magnet ring.

If second order effects of the changes in the fringing field due to rotation are ignored, then it can be assumed, without loss of generality, that the radial instability results in only translational force. The magnitude of the load at the magnetic bearings is the same, only the direction of application of the load is different for each of the bearings.

#### 4.4.2.5 Motor Coil Geometry

Ideally, the motor coils for the piston and displacer linear motors should be wound circumferentially around the magnet ring. Axial force is produced by the cross product of the circumferential current and the radial flux from the magnets, and this force is reduced if the current is not perpendicular to the flux.

In reality, geometrical asymmetries are created in the motor coil winding during its fabrication process. Of these, the most significant is the helical shape which results from having the coil progress along the length of the motor. Radial forces created by this asymmetry are relatively small. A torque is also produced, tending to rotate the piston or displacer tangential to the motor axis. In the piston, this torque has a dc component arising from the dc current required to overcome the pumping effect of the clearance seal. In both motors, an ac torque is produced which is proportional to the ac current. This ac torque results in a negligible amplitude of oscillation due to the large rotational moment of inertia of the armatures and shafts.

Figure 4-22 is a schematic of a typical motor coil of diameter  $D$  wound on a cylindrical surface of length  $\ell$ . The number of turns is  $N$  with a helical wind angle  $\lambda$ .

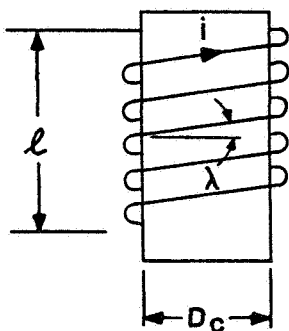


Figure 4-22. Linear motor stator-coil geometry.

The coil current  $i$  can be thought of as flowing in the axial direction through a length  $\ell$  and circumferentially through a length  $N\pi D$ . The forces produced by these currents are shown schematically in Figure 4-23. The circumferential current produces the desired axial force, whereas a tangential force is produced by axial current. This tangential force tends to

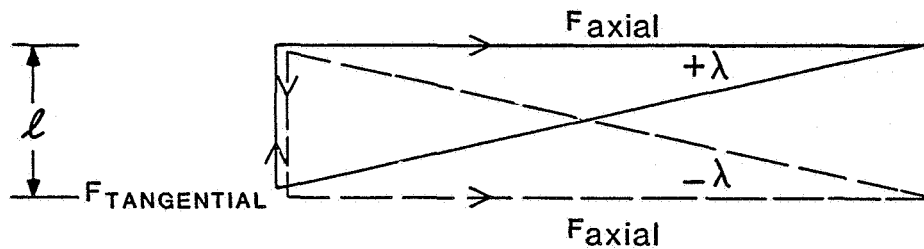


Figure 4-23. Current flow cancellation in an even-numbered layer winding.

spin the magnet armature like that of a rotary motor. If an even number of winding layers is used, and the coil is wound such that adjacent layers have opposite helix angles, then the current  $i$  in each layer will be oppositely directed along the length  $l$ , and their respective tangential forces will cancel. As shown in the figure, the axial forces add as desired.

If the winding does not have an even number of layers, torque cancellation cannot occur, and a substantially greater torque will exist tending to spin the suspended shaft. For this reason, the piston motor uses two layers and the displacer motor uses eight layers.

#### 4.4.2.6 Gravity Force

Determining the force at each bearing due to shaft weight is a simple problem in statics. Referring to Figure 4-24, the center of gravity of the shaft is located at distances  $C$  and  $D$  from bearings 1 and 2, respectively;  $F_1$  is the force on the front bearing and  $F_2$ , that on the rear bearing.

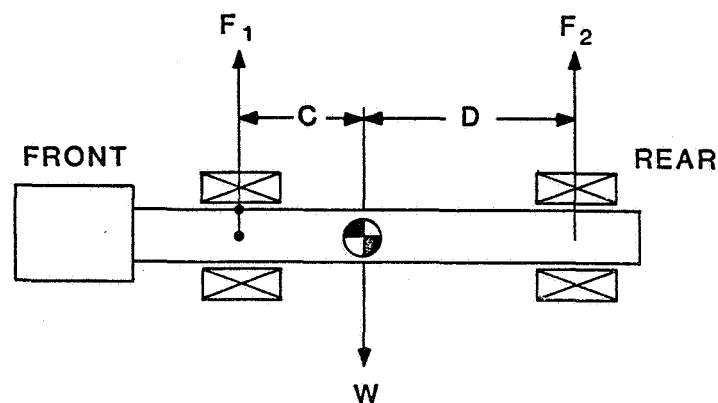


Figure 4-24. Static bearing loads.

The dc force at each bearing is:

$$F_1 = W \frac{D}{L} \quad (5)$$

$$F_2 = W \frac{C}{L}$$

where,  $W$  = weight of shaft (N)

$L$  = distance between bearings (m)

$F_1, F_2$  = bearing forces (N)

#### 4.4.2.7 Moment Between Center of Gravity and Motor Force

Although the center of gravity of the shaft will be nearly concentric with its suspended outside diameter, some eccentricity will exist between the center of gravity and the point at which the motor force is applied. The force is applied at the magnetic center of the motor armature. This force times the eccentricity produces a moment on the bearings.

$$M_i = F_i \cdot \epsilon \quad (6)$$

where,  $F_i$  = motor force (N)

$\epsilon$  = radial eccentricity (m)

$M_i$  = moment (N-m)

The bearing load imposed will be  $M_i$  divided by the bearing separation distance  $L$ . This simplified analysis does not take into account the fact that the shafts move axially as the current is applied.

#### 4.4.2.8 Forces From Axial Motion

Since the piston and displacer shafts oscillate with amplitudes  $\delta_p$  and  $\delta_d$ , respectively, about their mean positions, at any instant of time, lengths  $C$  and  $D$  (Fig. 4-24) change. Thus, all dc bearing forces develop alternating components.

For each bearing, the ac force,  $F_{ac}$ , resulting from a dc force  $F_{dc}$  is:

$$F_{ac} = F_{dc} \frac{\delta_{p,d}}{L_{p,d}}$$

where,  $L$  is the distance between the bearings, and  $p$  and  $d$  refer to the piston and displacer, respectively.

#### 4.4.3 Calculation of Piston and Displacer Bearing Loads

The formulas derived in Section 4.4.2 are now used to calculate the piston and displacer bearing loads.

##### 4.4.3.1 Strength Nonuniformity of Motor Magnets

###### (1) Piston

For the piston, using Equation (2) for the force due to the strength nonuniformity of the magnet:

$$F = \frac{2L\epsilon}{\mu_o} B_m^2 R_m^2 \left[ \frac{1}{R_1} - \frac{1}{R_2} \right]$$

with,  $L = 0.064$  m (length of two magnet rings)  
 $\epsilon = 0.04$  (+ 2% magnet strength variation)  
 $B_m = 0.4$  T  
 $R_m = 0.047$  m  
 $R_1 = 0.053$  m  
 $R_2 = 0.039$  m

$$\therefore F = -9.8 \text{ N dc.}$$

This minus sign means that the force is greater in the left direction for a magnet ring that has stronger magnetization on its right side since the force created by the inner air gap exceeds that of the outer. The force is dc in nature arising from a steady magnetic field. It acts radially through the center of the motor.

###### (2) Displacer

For the displacer motor, the force due to magnet nonuniformity is:

$$F = \frac{\epsilon D L B^2}{\mu_o}$$

with,  $B = 0.4$  T  
 $L = 0.039$  m  
 $\epsilon = 0.04$   
 $D = 0.019$  m

$$\therefore F = 3.8 \text{ N}$$



The distances A and B between the piston and displacer bearings and the center of the motor are summarized in Table 4-1. Using these dimensions, the loads on the front and rear bearings can be calculated. The results are tabulated in Section 4.4.3.6.

TABLE 4-1. Distance from Bearing to Center of Motor.

	A (Front) (m)	B (Rear) (m)	L = A+B (m)
Piston	0.103	0.121	0.224
Displacer	0.053	0.046	0.099

#### 4.4.3.2 Armature Radial Instability

##### (1) Piston

It was shown in Section 4.4.2.4 that the predominant cause of piston motor instability is the fringing effect. The instability stiffness was estimated by MAGGY to be  $7.0 \times 10^4$  N/m. The force on the magnetic bearings is computed using the worst case operational constraint that a bearing deflection amounting to 50% of the available radial clearance is permissible [ $1.3 \times 10^{-5}$  m (0.0005")]. The imposed force for this deflection is 0.9 N. This force would result from either a dc or ac deflection of the shaft. Conservatively, it is assumed that both the ac and dc forces are 0.9 N.

Another source of the radial instability force is any error in the magnetic concentricity of the motor. The radial magnetic center of the motor will not exactly correspond to the physical center of the shaft. Since the eddy current transducers sense the outside diameter of the shaft, the magnetic bearings center the physical dimensions of the shaft in its bore. The radial error of concentricity is assumed to be  $1.0 \times 10^{-4}$  m (0.004"). The resulting force is 7.0 N dc.

The bearing reactions shown in Table 4-4 of Section 4.4.3.6 are found using the dimensions in Table 4-1.

(2) Displacer

The instability stiffness for the displacer which results from the change in air gap reluctance is:

$$k = \frac{\pi^2 L R_m B_m^2}{2\mu_0 (r_2 - r_1)} \quad \text{N/m}$$

with,

$$\begin{aligned} B_m &= 0.4 \text{ T} \\ r_2 - r_1 &= \text{net air gap} = 5.3 \times 10^{-3} \text{ m} \\ r_m &= 8.2 \times 10^{-3} \text{ m} \\ L &= 0.040 \text{ m} \end{aligned}$$

$$\therefore k = 3.9 \times 10^4 \text{ N/m}$$

The force on the bearings due to a  $1.3 \times 10^{-5}$  m (0.5 mil) ac or dc displacement is 0.5 N, which is also conservatively assumed to be both ac and dc.

The force resulting from an assumed eccentricity (of the magnetic center relative to the center of the bearings) of  $1.0 \times 10^{-4}$  m (0.004") is 3.9 N dc. The bearing loads for the displacer using Table 4-1 dimensions are summarized in Table 4-6 of Section 4.4.3.6.

4.4.3.3 Gravity Loads

The data shown in Table 4-2 was used to calculate the gravity loads for the bearings; the results are tabulated in Section 4.4.3.6.

TABLE 4-2. Data Used in Calculation of Gravity Loads.

	<u>Weight</u>	<u>Distance from Front Bearing to C.G. (C)</u>	<u>Distance from Rear Bearing to C.G. (D)</u>	<u>Span (C+D)</u>
Piston	18.9 N (4.2 lb)	0.102 m	0.122 m	0.224 m
Displacer	3.4 N (0.8 lb)	0.030 m	0.069 m	0.099 m

#### 4.4.3.4 Moment Between Center of Gravity and Motor Force

Equation (6) describes the load resulting from the eccentricity between the center of gravity of the shafts and the center of application of the motor force. The assumed radial eccentricity is  $\epsilon = 1 \times 10^{-4}$  m (0.004"). The ac and dc forces produced by the linear motors were measured during operation of the refrigerator (see Table 4-3). The equation which describes the moment produced by the eccentricity is:

$$M_i = F_i \cdot \epsilon \quad (\text{N-m})$$

TABLE 4-3. Linear Motor Forces.

	<u>Piston</u>	<u>Displacer</u>
ac	131.0 N	25.0 N
dc	17.6 N	0.6 N

The bearing reactions are:  $F_1 = F_2 = \frac{M_i}{\text{Span}}$ , and are tabulated in Section 4.4.3.6.

#### 4.4.3.5 AC Loads from Axial Motion

Magnet strength nonuniformity and the radial instability of the motor are dc loads which act through the center of the motor. Gravity is a dc load which acts through the center of gravity. When the motor oscillates, ac loads are produced by these dc forces at each bearing in accordance with Equation (7). These are tabulated in the following section. The peak piston axial amplitude is 7 mm; the peak displacer is 3 mm.

#### 4.4.3.6 Composite Bearing Loads

##### (1) Piston

Table 4-4 summarizes the bearing forces  $F_1$  (front) and  $F_2$  (rear) from the previous sections.

TABLE 4-4. Summary of Piston Loads.

<u>Force Geometry</u>	<u>DC (N)</u>		<u>AC (N rms)</u>	
	<u>F<sub>1</sub></u>	<u>F<sub>2</sub></u>	<u>F<sub>1</sub></u>	<u>F<sub>2</sub></u>
Magnet-Strength, Nonuniformity	5.3	4.5	0.2	0.2
Radial Instability	4.3	3.6	0.5	0.5
Gravity	10.3	8.6	0.4	0.4
Eccentricity between center of gravity and motor force	0.1	0.1	-	-
Totals	20.0	16.8	1.1	1.1

Each of the above force components varies in direction. Consequently, the totals listed above are misleading in that it is highly unlikely that all components will act in the same direction at the same time. A more realistic or "probable value" for the total force, is the root sum square value (RSS) which is given by:

$$F_{RSS} = \sqrt{\sum F_1^2}$$

Table 4-5 summarizes the RSS forces for the piston bearings. The piston bearings were designed with a peak load capacity of 87 N dc at saturation. Section 5 on linear motors shows that these estimates are consistent with measurements taken on the piston-motor test fixture for the actual motor.

TABLE 4-5. RSS Load Summary for Piston Bearings.

	<u>DC (N)</u>	<u>AC (N)</u>	<u>Total</u>
F <sub>1</sub>	12.4	0.7	13.1
F <sub>2</sub>	10.4	0.7	11.1

(2) Displacer

TABLE 4-6. Summary of Displacer Loads.

<u>Force Category</u>	<u>DC (N)</u>		<u>AC (N rms)</u>	
	$F_1$	$F_2$	$F_1$	$F_2$
Magnet-Strength, Nonuniformity	1.8	2.0	0.1	0.1
Radial Instability	2.0	2.3	0.3	0.3
Gravity	2.4	1.0	0.1	0.1
Eccentricity between center of gravity and motor force	-	-	-	-
Totals	6.2	5.3	0.5	0.5

TABLE 4-7. RSS Load Summary of Displacer Bearings.

	<u>DC (N)</u>	<u>AC (N)</u>	<u>Total</u>
$F_1$	3.6	0.3	3.6
$F_2$	3.2	0.3	3.0

The load capacity of the displacer bearing at saturation is 53 N. It is evident that the front bearing is more heavily loaded than the rear bearing. This results from having the center of gravity of the displacer located much closer to the front bearing. However, both bearings almost equally share the motor forces, since the motor is centered between them.

4.4.3.11 Summary

The bearing loads have been shown to be relatively small compared to the load capacity of the magnetic circuit which is fabricated of high saturation nickel-iron and Permendure. These calculations are also used to compute the loading on the bearing control system, an important consideration since some forces and currents need to be known in the linearization. The analysis presented allows the calculation of the worst case and RSS bearing loads. The RSS load is more probable. It should be noted that the experimental data falls within the predicted bounds.

#### 4.5 Vibration Analysis

The bending modes of vibration of the displacer and piston were determined analytically and experimentally. These vibration modes are important since they impose loads on the magnetic bearings at frequencies where the control stiffness is rolling off. In terms of the control system prediction, this analysis is not explicitly used since the material damping in the shafts is difficult to estimate. Thus, the magnitude ( $Q$ ) of the resonance is not known, only the mode shapes and frequencies. However, this analysis was useful in the mechanical design of the piston and displacer. It helped determine the appropriate thickness of the thin wall sections, in order to achieve high resonant frequencies without presenting a significant thermal loss through conduction. The electronic compensator for the bearing was designed to provide high stability by avoiding these resonant frequencies. Further, these bending modes were identified during testing of the magnetic bearing system. Therefore, although these calculations do not enter into the control system analysis of the magnetic bearings, they did significantly affect the design and testing of the refrigerator.

The model used for the computer analysis of the displacer is shown in Figure 4-25. The analysis models the regenerator (Section 2) as a distributed mass and stiffness. The motor and bearing (Section 1) is assumed to be a rigid body, as is the cold-end manifold (Section 3). The damping in the regenerator is ignored, as is the squeeze-film damping in the clearance seals. Table 4-8 gives the inputs and outputs for the computer model. Refer to the expander subassembly in Section 2 of this report for a cross-sectional view of this shaft.

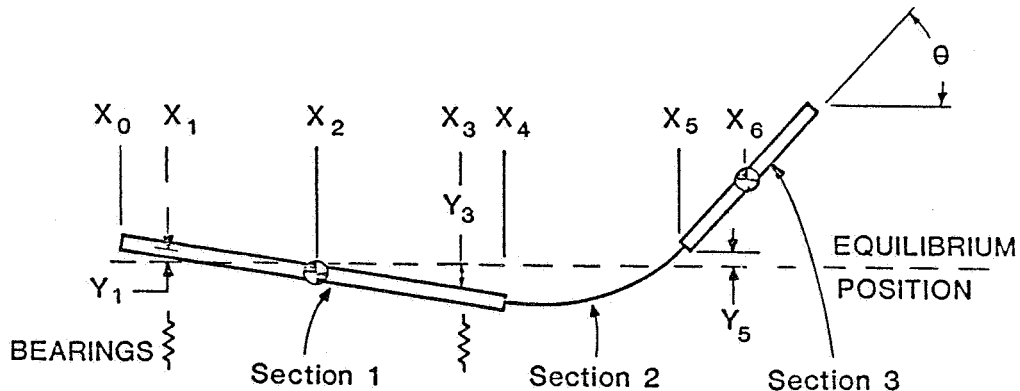


Figure 4-25. Displacer vibration model.

TABLE 4-8. Displacer Model Parameters

<u>Symbol</u>	<u>Description</u>
<u>Inputs</u>	
$I_2$	Moment of inertia of Section 1 about $X_2$ .
$M_2$	Mass of Section 1.
$I_6$	Moment of inertia of Section 3 about $X_6$ .
$M_6$	Mass of Section 3.
$\rho$	Mass per unit length of Section 2.
$E$	Stiffness modulus of structural portion of Section 2
$I$	Area moment of inertia of structural portion of Section 2.
<u>Outputs</u>	
$Y_1$	Radial displacement at $X_1$ .
$Y_3$	Radial displacement at $X_3$ .
$Y_5$	Radial displacement at $X_5$ .
$\theta$	Angular displacement at Section 3.

The piston model (Fig. 4-26) assumes the motor armature (Section 3) and the two clearance seals (Sections 1 and 5) to be rigid bodies, and the connecting tubes (Sections 2 and 4) to have finite stiffness and no mass. Table 4-9 gives the inputs and outputs for the computer model. Section 2 of this report shows a cross-sectional view of the piston shaft.

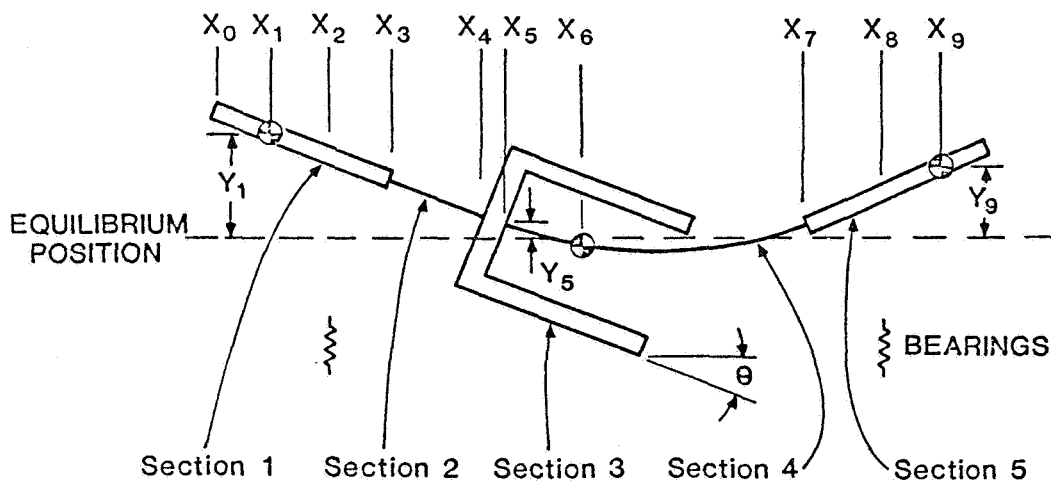


Figure 4-26. Piston vibration model.

TABLE 4-9. Piston Model Parameters.

<u>Symbol</u>	<u>Description</u>
<u>Inputs</u>	
$I_1$	Moment of inertia of Section 1 about $X_2$ .
$M_1$	Mass of Section 1.
$I_6$	Moment of inertia of Section 3 about $X_6$ .
$M_6$	Mass of Section 3.
$I_9$	Moment of inertia of Section 5 about $X_9$ .
$M_9$	Mass of Section 5.
$\rho$	Mass per unit length of Sections 2 and 4.
$E$	Stiffness modulus of structural portions of Sections 2 and 4.
$I$	Area moment of inertia of structural portions of Sections 2 and 4.
<u>Outputs</u>	
$Y_1$	Radial displacement at $X_1$ .
$Y_5$	Radial displacement at $X_5$ .
$Y_9$	Radial displacement at $X_9$ .
$\theta$	Angular displacement at Section 5.

The LVDT rod for both the piston and displacer was modeled as a cantilever beam. Since the estimate of this vibrational mode is straightforward, this calculation was not done in the computer program. The vibration of the rod adds an extremely small load on the magnetic bearings; however, since it is picked up as a spurious signal in the LVDT electronics, it appears as noise in the axial control system.

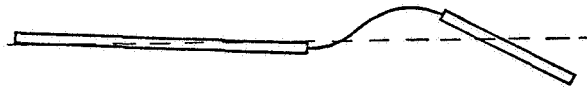
The predicted bending modes are shown in Figures 4-27 and 4-28. The frequencies are tabulated in Table 4-10.

The natural frequencies were also determined experimentally. The refrigerator components were supported at the bearing locations with flexible, low-damping mounts to approximate free-free boundary conditions. Free-free boundary conditions were desired since they best represent the character-



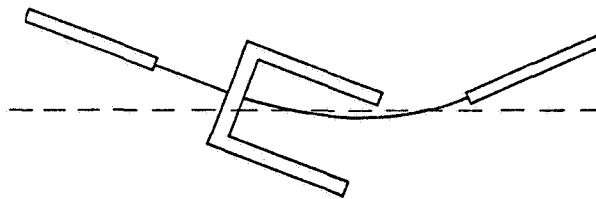


FIRST BENDING MODE

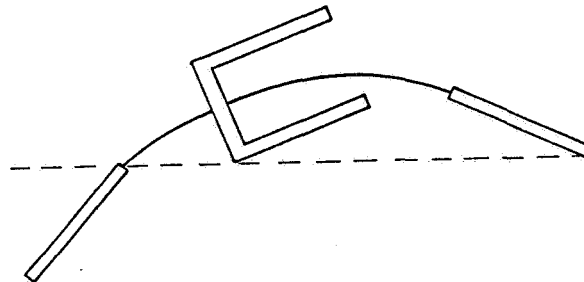


SECOND BENDING MODE

Figure 4-27. Displacer calculated mode shapes.



FIRST BENDING MODE



SECOND BENDING MODE

Figure 4-28. Piston calculated mode shapes.

TABLE 4-10. Vibration Test Results.

<u>Vibration Mode</u>	<u>Predicted Frequency (Hz)</u>	<u>Measured Frequency (Hz)</u>
<u>Displacer</u>		
1st Bending Mode	1,000	830
2nd Bending Mode	4,850	4,160
LVDT Rod 1st Bending	1,860	---
<u>Piston</u>		
1st Bending Mode	690	400
2nd Bending Mode	4,000	1,600
LVDT Rod 1st Bending	685	504

istics of the magnetic suspension system at the expected natural frequencies of the shafts. The shafts were then excited by lightly tapping with a stiff plastic tube. The resulting shaft motion was monitored at several locations using eddy-current displacement transducers. The frequency spectrum of this displacement signal was used to determine the vibrational natural frequencies. Extensive testing was performed to isolate or eliminate additional resonances generated by the test setup. The experimental results are compared with the theoretical predictions in Table 4-10.

## 4.6 Radial Position Sensors

### 4.6.1 General

The radial position of the suspended shaft in the magnetic bearing is transduced with eddy-current position sensors. The configuration of the sensor is shown in Figure 4-3. Its operation can be understood by examining the impedance of a flat coil of wire whose axis is perpendicular to a conductive medium, as shown in Figure 4-29b. The impedance of this coil is a function of the distance between the coil and the conductor; it is by measurement of changes in this impedance with changing magnetic air gap,  $b$ , that the position of the shaft is transduced.

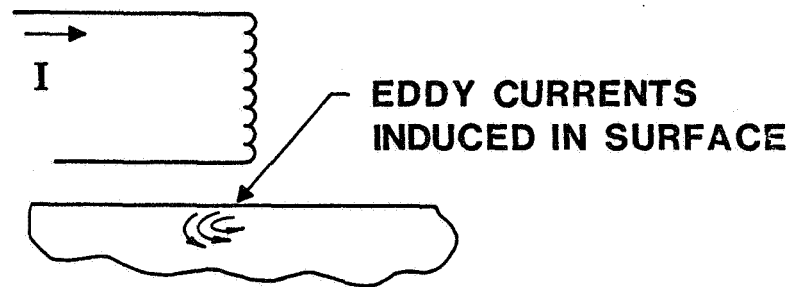
The simplest way to explain the changing impedance is by the image of the coil reflected in the conductive sheet. If the coil is situated directly on the sheet, and if the conductivity of the medium were infinite, then the flux produced by the current in the coil would be exactly cancelled by the flux produced by the eddy currents in the sheet. The eddy current flux is generated in a direction to oppose the incident flux, and, for infinite conductivity, the magnitude of the opposing flux would be exactly the same as the incident. Since the magnitude of the eddy currents decrease as the coil is moved away from the sheet, the opposing flux also decreases and the net flux is a measure of the distance between the coil and the sheet. In a medium of finite conductivity and permeability, however, the magnitude of the reflected flux would be less than the ideal and the phase would be lagging. Further, the intensity of this second-order effect is a function of the distance to the sheet. Therefore, for an ideal medium the eddy current sensor would give a perfect measurement of position; however, the real sensor has some inherent error due to the finite conductivity and permeability of the target.

The vector potential of the magnetic field in Figure 4-29 can be described by the following equations:

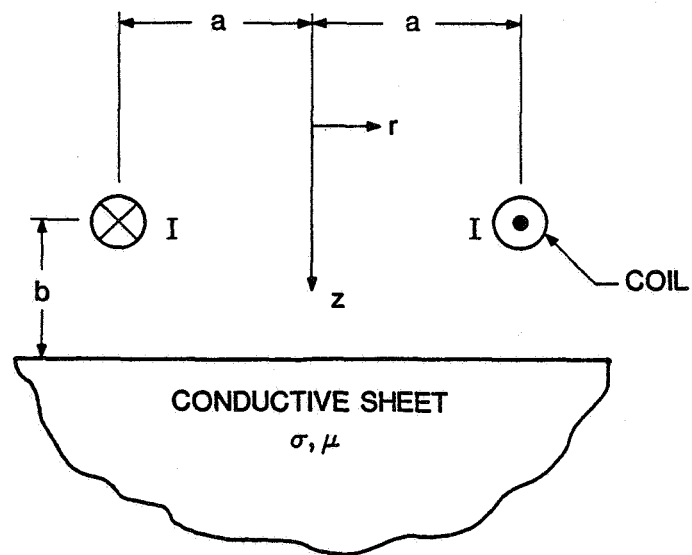
$$\nabla^2 A = 0 \quad \text{outside sheet}$$

$$\nabla^2 A = \frac{\mu}{\rho} \frac{\partial A}{\partial t} \quad \text{inside sheet}$$

where,  $A$  = magnetic vector potential  
 $B$  = magnetic flux density =  $\nabla \times A$   
 $\mu$  = permeability of sheet  
 $\rho$  = resistivity of sheet



(a) Concept.



(b) Coordinates.

Figure 4-29. Configuration of eddy-current probe.

It is assumed that the flux density normal to the surface and the field intensity tangential to the surface are continuous. As is the case with the eddy currents generated in the magnetic pole pieces, the displacement current in the sheet is ignored since the physical dimensions are relatively small compared to the wavelength.

Since the exciting current is circular, the only non-zero component of A in cylindrical coordinates (r,  $\theta$ , Z) is  $A_\theta$ , and, since the current is assumed uniform, there is no variation of A with  $\theta$ . Further, since the applied current I is sinusoidal,  $\partial A / \partial t = j\omega A$ , a phasor. For simplicity of notation, this  $\theta$  component of the phasor of A will be written simply as A in the following. Thus, outside the sheet, the vector potential obeys the equation:

$$\nabla^2 A = \frac{\partial^2 A}{\partial r^2} + \frac{1}{r} \frac{\partial A}{\partial r} - \frac{A}{r^2} + \frac{\partial^2 A}{\partial Z^2} = 0$$

which has the solution

$$A = A_1 - A_2 + dA$$

$$A_1 = \frac{\mu_0 I}{2} \int_0^\infty e^{(-\frac{kZ}{a})} J_1(k) J_1\left(\frac{kr}{a}\right) dk \quad (1)$$

$$A_2 = \frac{\mu_0 I}{2} \int_0^\infty e^{-\frac{k(2b-Z)}{a}} J_1(k) J_1\left(\frac{kr}{a}\right) dk \quad (2)$$

$$dA = \frac{\mu_0 I}{2} \int_0^\infty \left[ e^{(-\frac{k(2b-Z)}{a})} J_1(k) J_1\left(\frac{kr}{a}\right) \cdot \left( \frac{2k\mu_r}{k\mu_r + (k^2 + jp^2)^{1/2}} \right) \right] dk \quad (3)$$

where,  $J_1$  = Bessel function of first kind of order 1.  
 $\mu_0$  = permeability of free space  
 $\mu_r$  = relative permeability of sheet ( $\mu = \mu_0 \mu_r$ )  
 $p = \sqrt{\mu_0 \mu_r \omega a^2 / \rho}$   
 $k$  = variable of integration

The voltage which is induced in the coil by the sinusoidal current  $I$  can be thought of as being composed of three components  $V_1$ ,  $V_2$ , and  $dV$  corresponding to the components of the magnetic vector potential (Fig. 4-30).  $V_1$  is the voltage which would be induced by the current in the absence

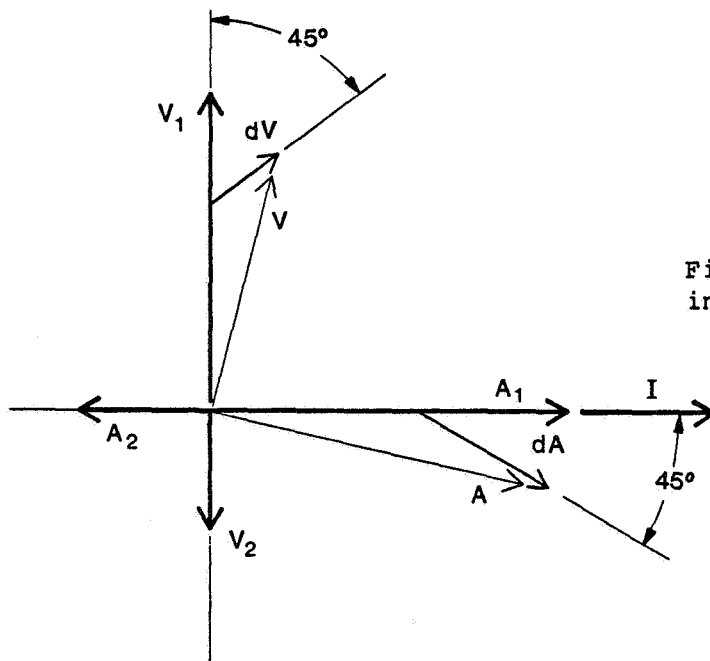


Figure 4-30. Phasor diagram of induced e.m.f. in coil.

of the sheet. It results from the self inductance of the coil and leads  $I$  by  $90^\circ$ . The second component  $V_2$  would be induced in the coil by the ideal mirror image of  $I$  (i.e., by assuming  $\rho = 0$ ). This voltage lags  $I$  by  $90^\circ$ . Finally,  $dV$  is the component resulting from the finite conductivity and permeability of the sheet. Its magnitude is a complex function of the parameters of the magnetic circuit, but generally, it leads  $I$  by  $45^\circ$ . From Figure 4-30, it should be realized that the only observable voltage is  $V$ , the sum of the three components.

Qualitatively examining Equations (1), (2), and (3), it is observed that since the Bessel functions are slowly decaying sinusoids, the predominant element in the change in magnetic vector potential with distance comes from the exponentials. Thus the sensitivity of the probe to changes in distance, as represented by Equations (2) and (3), increases with increasing radius  $a$  and with decreasing distance  $b$ . The vector potential  $dA$  will have a phase of  $-45^\circ$  at frequencies such that  $p \gg k\mu_r$ . This relationship was deduced from test data of the probes at 1 MHz.

A circuit model, which represents the change in the induced e.m.f. in the probe coil, is the simple parallel resistor-inductor circuit of Figure 4-31. This model was used to describe the impedance of the probe for measurement

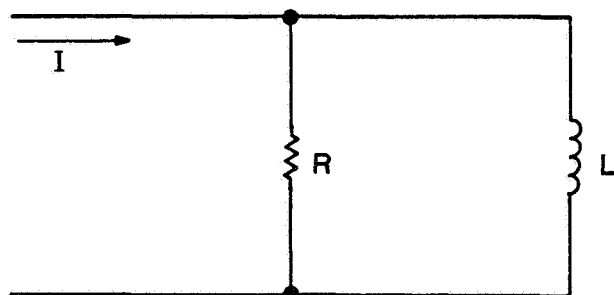


Figure 4-31. Circuit model for eddy current probe.

and electronic design. The resistor models the effective parallel resistance of the coil wire and the change in impedance caused by the eddy currents. It is the change in this resistance that the electronic module uses as a measure of position.

#### 4.6.2 Measurement and Calibration

Ideally, the radial position sensor should be highly sensitive to changes in position, be relatively insensitive to changes in temperature, have a high-frequency response, and produce little electrical noise. In the refrigerator, the only characteristic achieved easily with the eddy current probes was the frequency response.

The radial air gap used in the magnetic bearings is 25  $\mu\text{m}$ . If the shaft sags greater than 10  $\mu\text{m}$ , the additional passage of gas through the clearance seal is great enough to detrimentally affect thermodynamic performance. As

a rule of thumb, it is desired to resolve 1.0  $\mu\text{m}$  as a minimum, given this specification. As explained in Section 4.2, since the insulation on the wire and the potting compound used in the probes would contaminate the working gas, the probes are mounted behind 1 mm ceramic windows. The sensor must, therefore, resolve 1 part in 1000. Figure 4-32 shows a plot of the change in effective parallel resistance at 1 MHz of a typical probe as a function of position. The test fixture used for this measurement, shown in Figure 4-33, was mounted in a micrometer table. The resistance was measured with a high-frequency impedance meter.

Temperature affects the eddy current probes in at least three ways. The effective parallel resistance changes with the dc resistance of the probe coil. The materials used in the fabrication and mounting of the probes expand, thus physically moving the coil relative to the target. And, both the resistivity and relative permeability of the material of the shaft change with temperature, thereby changing the magnitude of the magnetic vector potential (Equation 3) and the induced voltage.

A thermal analysis of the sensor sections of the refrigerator, indicated that a worst-case temperature rise of 50°C was possible. Figure 4-34 shows the change in effective parallel resistance at 1 MHz of a typical probe over this temperature range. The fixture used for this test is shown in Figure 4-35. The shaft, shown in the figure, was the same diameter as the piston shaft and accurately machined and annealed to have a 25  $\mu\text{m}$  diametrical clearance to the housing. It was mechanically held to one side of the bore with two set screws. The probe mounts in the test housing were joined in the same manner as the refrigerator mounts. Since it is difficult to separate the various causes of temperature drift, the test fixture had to simulate the refrigerator as accurately as possible. Two thin-film detectors (TFD) were mounted in small holes in the fixture to measure temperatures when the tests were conducted in a laboratory oven.

If the frequency at which the impedance is measured is too low, the sensitivity to changes in position is poor. If it is too high, the parasitic capacitance of the connecting cable and of the layers of the probe coil, dominates the measurement. For the probes used in the refrigerator, a frequency of 1 MHz provided the best compromise. Using this exciting frequency, a sensor bandwidth of 10 kHz was easily attained.



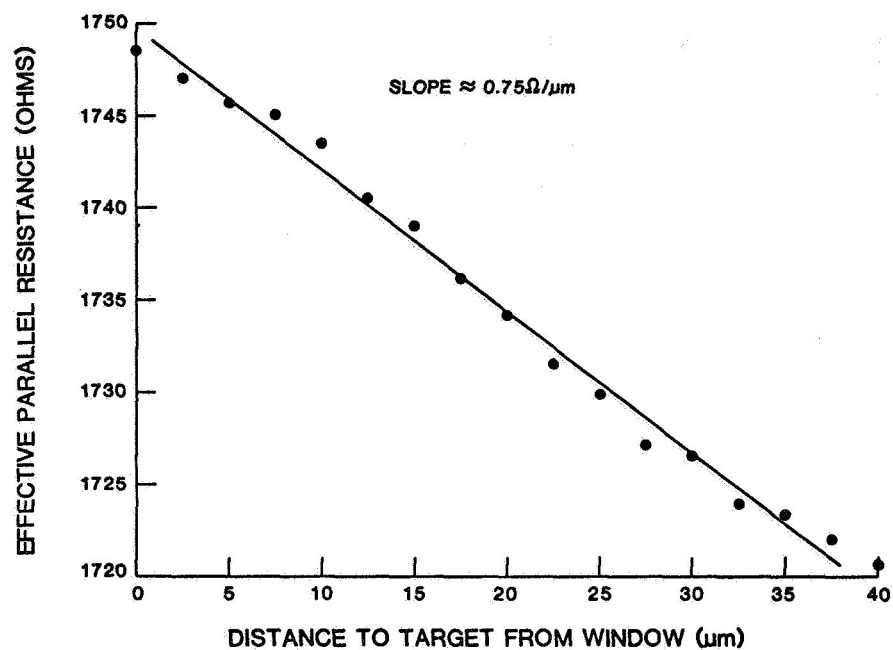


Figure 4-32. Effective parallel resistance vs. position.

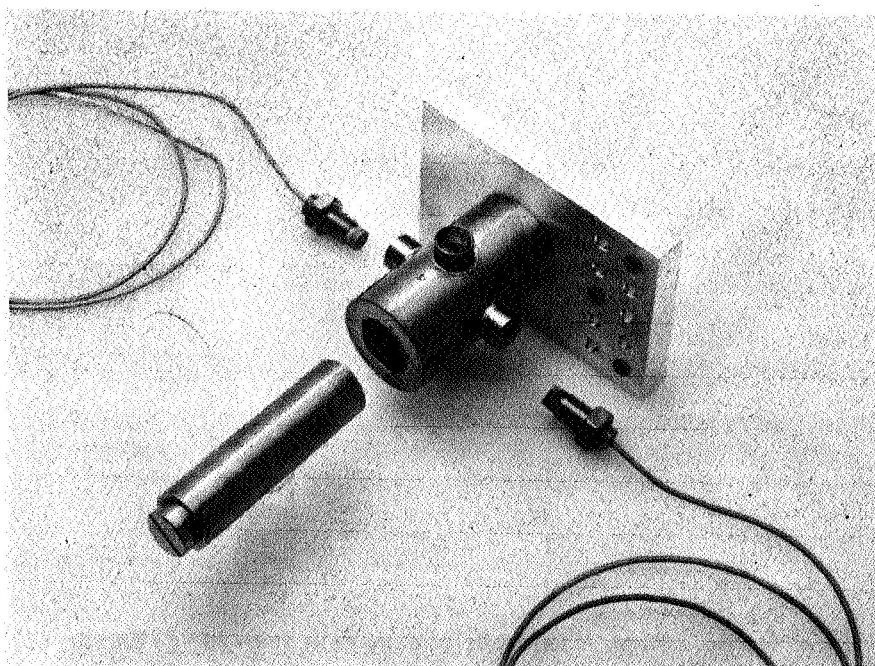


Figure 4-33. Test fixture for measuring resistance vs. position.

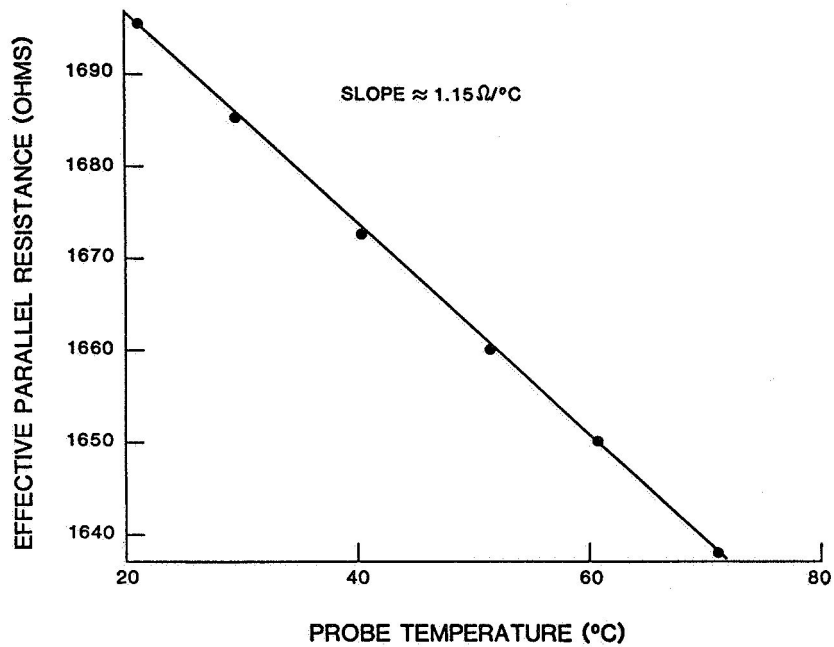


Figure 4-34. Effective parallel resistance vs. probe temperature.

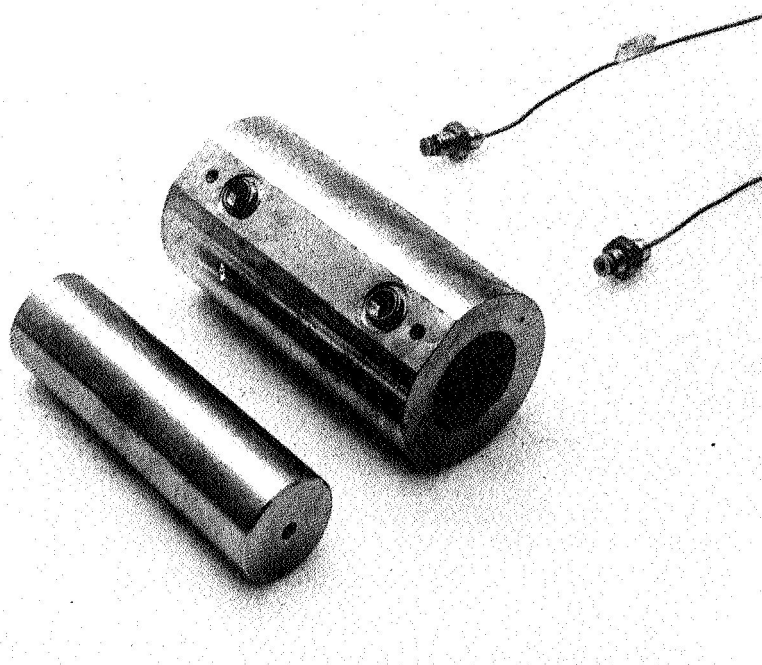


Figure 4-35. Test fixture for measuring resistance vs. temperature.

In reviewing the data of Figures 4-32 and 4-34, it is observed that the change in resistance for a 50  $\mu\text{m}$  displacement is the same order of magnitude as the change for 50°C. The probe is as good at measuring temperature as it is at measuring position. To increase the sensor sensitivity to position and at the same time decrease the sensitivity to temperature, the probes are used in a differential impedance bridge, as shown by Figure 4-36. The refrigerator was designed to be radially symmetric to minimize thermally induced stresses, so the temperature rise for each diametrically opposite set of probes is similar. Thus, a change in position results in a differential imbalance in the bridge, and a change in temperature results in a balanced common mode change. It should be noted that both test fixtures (Figs. 4-33 and 4-35) permit differential measurements.

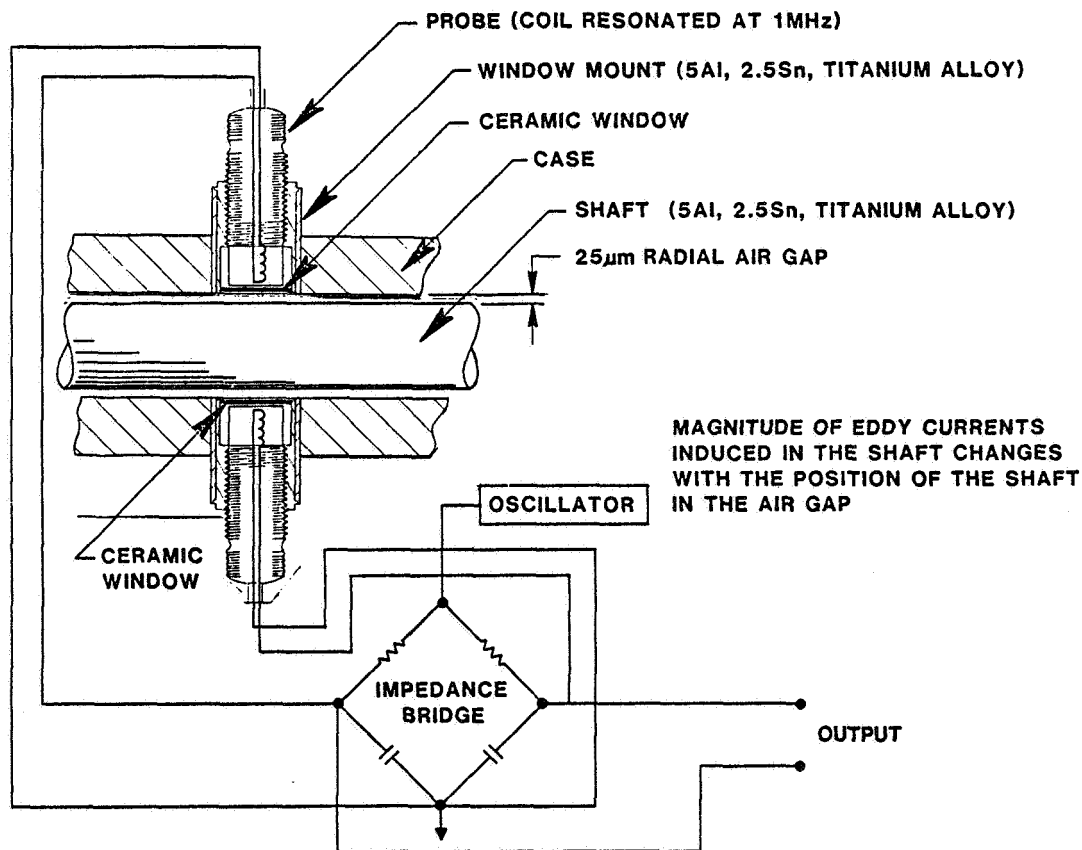


Figure 4-36. Sensor differential bridge.

In order for the bridge to balance, the drift of each probe in a differential set must match over the full 50°C temperature rise anticipated in the refrigerator. The test fixture shown in Figure 4-35 was used to measure the impedance of 32 probes over the 50 °C temperature range from which 4 sets (8 probes) were chosen. The difference in effective parallel resistance was matched to be better than 1 ohm for each of the sets over the 25°C - 75°C range (equivalent to a 1  $\mu\text{m}$  position error).

Another consideration in the use of the bridge is that the probes must be calibrated after they are mounted in the refrigerator. Given the coarse thread of the mount (1.5 mm pitch), this process required painstakingly careful adjustment.

#### 4.6.3 Sensor Electronics

A block diagram of the sensor electronics is shown in Figure 4-37. The probe pair is mounted in two legs of the impedance bridge. A capacitor is connected across each so that the parallel combination is in resonance, for increased sensitivity. Resistors are added to the upper two legs, to

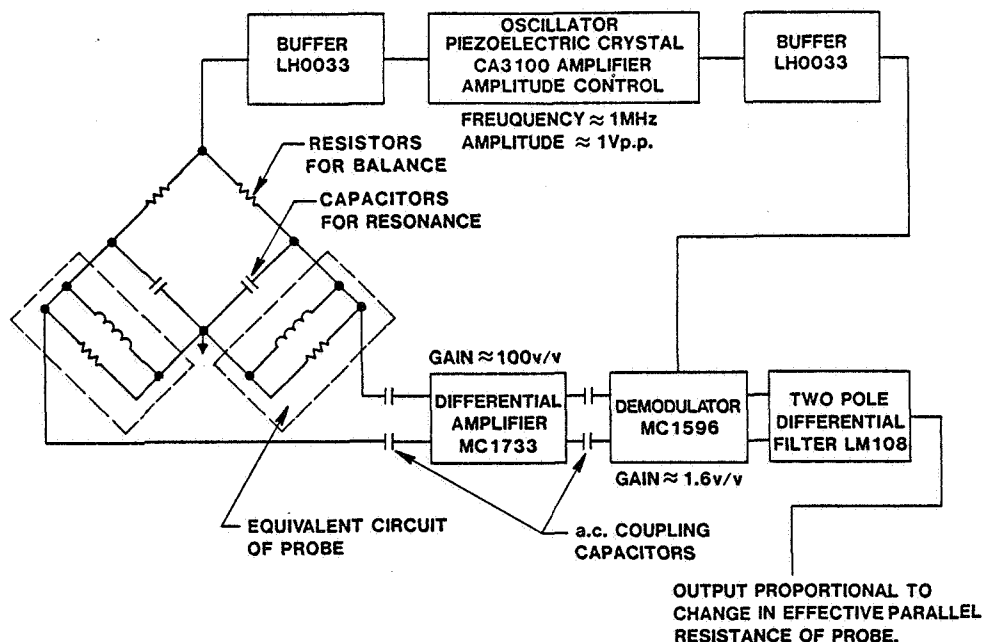


Figure 4-37. Block diagram of sensor electronics.

balance the bridge with the shaft at the center position. The impedance bridge is driven with a piezoelectric crystal controlled sinusoidal oscillator. Since changes in the amplitude of the sinusoid would appear as position errors, given the finite common-mode rejection of the amplifier, the oscillator circuit contains a closed-loop amplitude control.

The output of the bridge is amplified with a high-frequency differential amplifier. The large bandwidth of the amplifier is necessary to achieve the high common mode rejection ratio required. Most of the sensor immunity to temperature drift is provided by the common mode rejection of this stage. Demodulation of the signal comes from a high-frequency multiplier. By multiplying the differential bridge output by the reference oscillator signal, two components, corresponding to the sum and difference frequency terms, result. The difference term (baseband) is a voltage proportional to the differential effective parallel resistance of the probes. This is, therefore, the desired position output. The sum term ( $\approx 2$  MHz) is filtered by the second order, low-pass filter and is the primary source of noise in the sensor. It should be noted that the output of the bridge is carried differentially by each stage. This minimizes the amount of random noise produced and maximizes the common mode rejection of the temperature drift.

#### 4.6.4 Results

Table 4-11 summarizes the performance of the radial position sensors measured in actual refrigerator operation. As can be seen, this sensing system provides superior performance for use in the magnetic bearings.

TABLE 4-11. Characteristics of Radial Position Sensor.

	<u>Piston</u>	<u>Displacer</u>
Sensitivity	80 mV/ $\mu$ m	80 mV/ $\mu$ m
Bandwidth	10 kHz	10 kHz
Wideband Noise Level	0.25 $\mu$ m (20 mV)	0.25 $\mu$ m (20 mV)
Worst Case Drift (observed during operation)	0.25 $\mu$ m	0.75 $\mu$ m

## 4.7 Bearing Current Driver

### 4.7.1 General

The self inductance of the coils on the actuator pole pieces of the magnetic bearing produces a phase shift between the actuator applied voltage and current. As explained in Section 4.3.2, this inductance is a complex function of frequency due to the effects of eddy currents in the pole pieces. Since the magnetic bearings are position servomechanisms, i.e., the position is transduced and controlled with the application of an electromagnetic force, an inherent  $180^\circ$  phase shift already exists in the controlled dynamics ignoring squeeze film damping. Thus, any additional phase shift between the transduced position and the current which generates the force, such as that produced by the coil self inductance, can result in instability of the control system.

To minimize the phase shift from the inductance of the coil, current feedback is used in the driver for the actuator. The current in the coil is measured with a sampling resistor, and the applied voltage to the coil is regulated to keep the current in phase with the reference voltage. This scheme is illustrated in Figure 4-38. As shown in the figure, the inductance and resistance of the coil are both functions of the Laplace operator  $s$ , due to the effects of eddy currents.

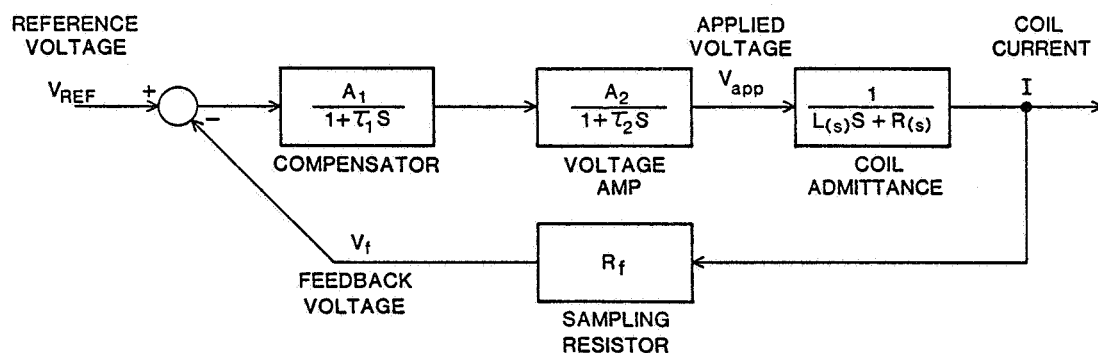


Figure 4-38. Block diagram showing transfer functions of blocks.

As with most feedback loops, the advantages of the current driver are increased frequency response, reduced phase shift, and insensitivity to changes in the internal components of the loop. This last advantage is important since both the output transistor stage of the amplifier and the

magnetic properties of the actuator are nonlinear functions of the magnitude of the current in the coil. The disadvantages of current feedback are the possibility for instability in the current loop itself, which is now a minor loop in the overall position control system, and the need for a voltage overhead in the applied voltage to the coils. The voltage overhead is needed since the magnitude of the current produced by a given applied voltage decreases as a function of frequency. Thus, at higher and higher frequencies, more voltage must be applied to keep the current at the same levels. The overhead results in an inefficient use of the amplifier and coil magnetics. Therefore, as in most uses of feedback, the primary current driver disadvantages are the increased possibility of instability and the use of additional power.

#### 4.7.2 Circuit Analysis

To insure the stability of the current feedback driver, the dynamics of the feedback loop were analyzed and compensation was provided. For simplicity, the compensator consists of a single dominant pole. This is adequate for stability since the phase shift from the coil admittance is never more than  $90^\circ$ .

The values for the parameters shown in the block diagram of Figure 4-38 are given in Table 4-12. From the table it will be noted that the dominant pole comes from time constant  $\tau_2$  in the voltage amplifier. The compensator time constant was included to filter the signal at high frequencies.

TABLE 4-12. Transfer Function Parameters.

<u>Parameter</u>	<u>Notation</u>	<u>Value</u>
Compensator Gain	$A_1$	100 V/V
Compensator Time Constant	$\tau_1$	$20 \times 10^{-6}$ sec
Voltage Amp Gain	$A_2$	6 V/V
Voltage Amp Time Constant	$\tau_2$	$1.3 \times 10^{-4}$ sec
Sampling Resistor	$R_s$	0.5 Ohm
Coil Inductance (dc)	$L(s)$	27 mH
Coil Resistance (dc)	$R(s)$	2 Ohms

The voltage amplifier shown in the figure uses a voltage feedback loop to stabilize its gain and bandwidth for changes in the parameters of its transistors. This loop also serves to make the overall gain independent of the individual gains of the transistors and thus the same for each of the eight drivers which are required for the refrigerator. The analysis of this voltage loop is straightforward and therefore not included here. The transfer function represented in the block is simply the closed loop transfer function of this amplifier.

The output transistors of the voltage amplifier are biased into their linear region of operation, thereby eliminating any deadband in their response. The small bias current, flowing into the pole piece coils, results in a power loss but also linearizes the pole piece dynamics (see Sect. 4.3).

A test fixture was constructed to simulate the magnetic bearings in the piston section of the refrigerator. The details of the construction and testing of this fixture are given in Section 4.8. The impedance of the actuator pole pieces, measured with this fixture, is given in Figure 4-39. For the measurement, the shaft was mechanically centered with shims. It

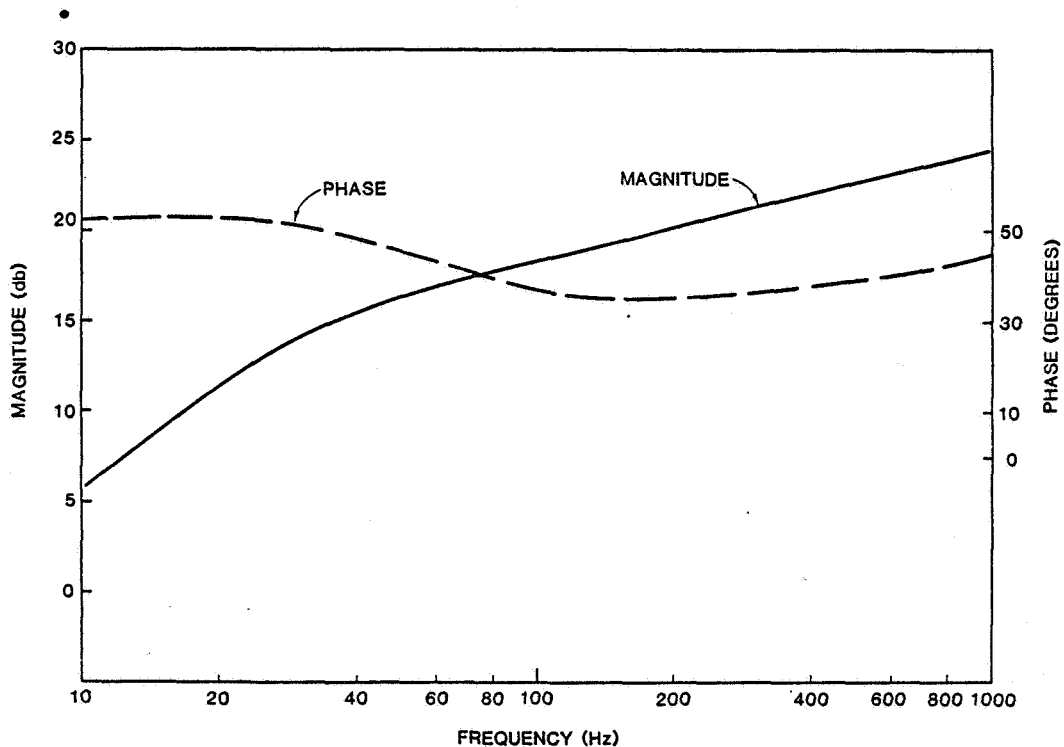


Figure 4-39. Impedance of actuator pole pieces.



should be noted that at high frequencies, the impedance increases approximately as the square root of frequency, and the phase shift approaches  $45^\circ$  as predicted by the eddy current analysis. Figure 4-40 shows a plot of the closed-loop gain of the current driver, measured in the refrigerator.

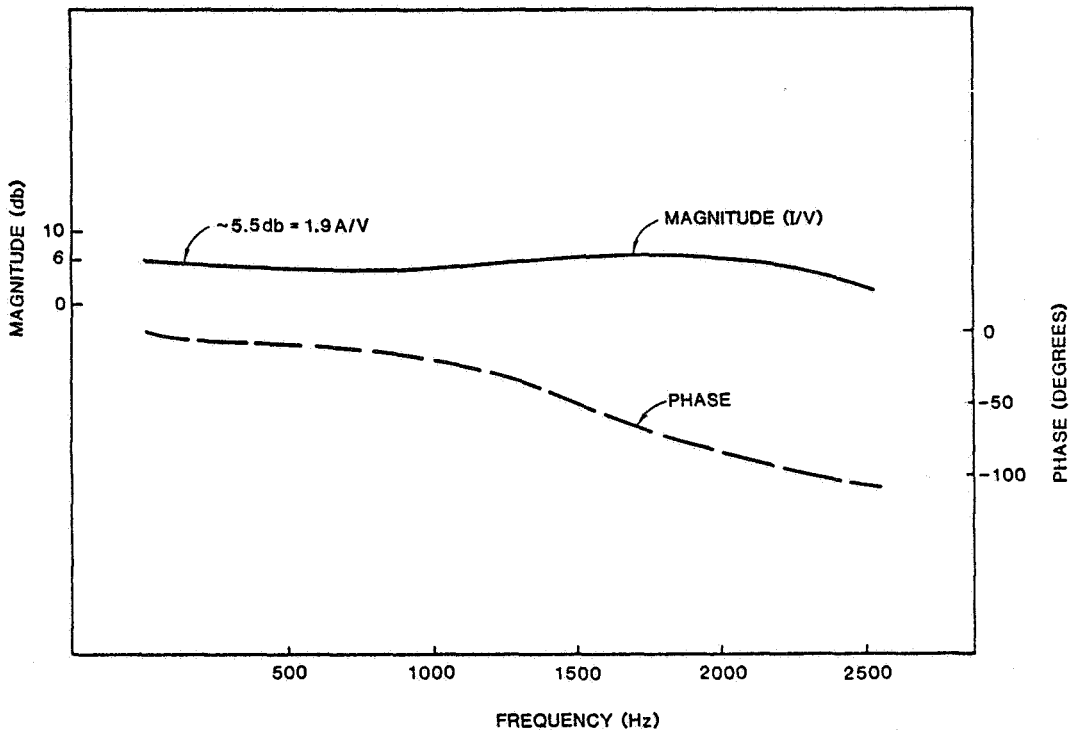


Figure 4-40. Measured closed-loop frequency response.

## 4.8 Control System Modeling

### 4.8.1 General

All of the preceeding analyses for the magnetic bearing are used in the modeling of the control system. Each effect now becomes important as an element of the electromagnetic/mechanical system impacting the problem of accurate positioning.

In a sense, the control system model for the bearing began in Section 4.6. The radial position sensor and bearing current driver were shown to be dynamically complicated. Each is composed of many active electronic elements and minor feedback loops. Here in the overall position loop, each is modeled as a simple gain and a low-pass filter. For this macroscopic view, this representation is adequate.

For illustration, the front bearing of the displacer section is used. The analysis holds for any other bearing, the major difference being the calculation of effective mass. The choice of the front displacer was arbitrary in that it is dynamically similar to any other; however, it was the first refrigerator bearing developed, and the largest body of test data was generated for it.

#### 4.8.2 Model

The linearized model for the magnetic bearing is shown in block diagram form in Figure 4-41. The model is composed of five major sections:

- Electronic compensator which consists of low-power, low-frequency signal conditioning electronics.
- Current driver which consists of higher power (40 W capability) electronics.
- Coil dynamics which model the linearized force constant and eddy current effects.
- Shaft dynamics which model damped spring-mass system.
- Radial position sensor which consists of high frequency (1 MHz) signal conditioning electronics associated with the eddy current transducers.

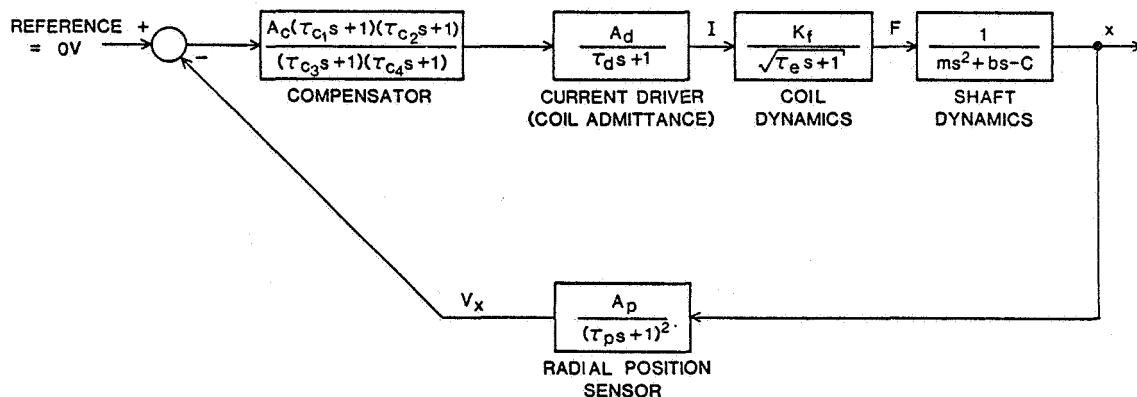


Figure 4-41. Block diagram of bearing control system.

The models for the current driver and eddy current sensor have been discussed at length; some comments are in order regarding the other three blocks.

The compensator is modeled as a lag-lead network. Actually, it contains many more active components than required for this network so that the gain and break frequencies can be independently adjusted. The low frequency lag ( $\tau_1, \tau_3$ ) is used to increase the gain at dc to obtain high static centering. The lag causes the gain to roll off, and the break frequencies ( $\sim 1$  Hz) are chosen so that no phase shift occurs at crossover. The lead ( $\tau_2, \tau_4$ ) produces a phase margin at crossover to satisfy the Nyquist criterion for stability. Typical phase margins are  $40^\circ$ . It should be noted that the gain term ( $A_c$ ) corresponds to the dc position gain, i.e., the transfer function of the compensator equals  $A_c$  at  $s = 0$ .

The coil dynamics include the force constant and the effects of eddy currents. This is modeled as a dc gain, which is essentially the term resulting from the Describing Function analysis of the nonlinear force term, and a "half pole" which models the increased reluctance caused by eddy currents. As previously stated, although this is not a linear model, it produces useful results.

The use of a single transfer function to represent the relationship between the current  $I$  and force  $F$  requires some discussion. As will be recalled from the schematic of the bearing (Fig. 4-2), the force  $F$  which causes the displacement  $x$ , is in actuality the net force produced by the two diametrically opposed pole pieces. Further, the currents in the two pole piece coils are switched such that a displacement error results in a net current so as to reduce the error. In the bearing electronics, this switching is done between the compensator and current driver; thus, individual drivers are used for each pole piece. Since the frequency response of this half-wave rectifier switching is much higher than any other loop dynamics, its effects can be ignored in this analysis. Further, the output stage of the driver includes a snubber circuit so that the current in each individual coil decays quickly when the polarity switches. Thus, the model correctly represents  $I$ , the differential current in the two diametrically opposed pole pieces, and  $F$ , the net force on the shaft.

The final block in the model is the shaft dynamics. The mass,  $M$ , in this block is the effective mass seen by each set of pole pieces; the derivation is given in Section 4.3. The damping term,  $b$ , arises from the effects of the gas squeeze film in the annular gap. The negative spring

term,  $-c$ , comes from the effects of bias currents. Although this last term is, in actuality, a force produced by the electromagnetics of the coil, it is more easily included in the shaft dynamics, as seen from the discussion in Section 4.3.

#### 4.8.3 Predictions

The front displacer bearing of the Engineering Model is examined to predict performance. This work was preceded chronologically by the design and testing of the bearing test fixture. For coherence, the test fixture is discussed in the following section (Sect. 4.9); the remainder of this section being devoted to the refrigerator. The fundamental difference in measurement between the refrigerator and the test fixture is that, in the latter, the mechanical force is transduced. The only measurement which can be made on the refrigerator bearings relates to the open loop frequency response. A discussion of how this test is performed has also been left to the following section.

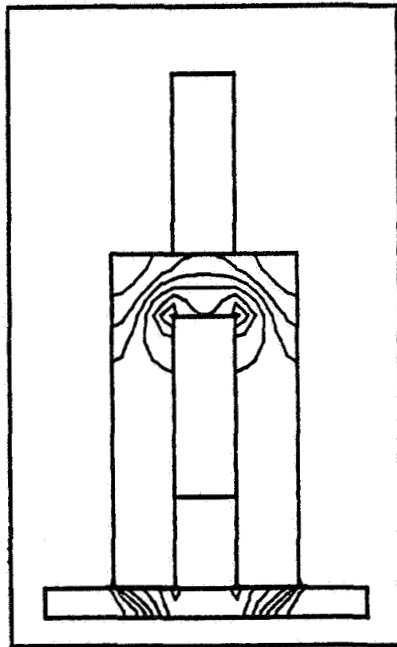
##### (1) Coil Dynamics

The parameters which describe the magnetic bearing pole pieces for the front displacer bearing are given in Table 4-13. Nickel-iron is used for the stationary pole piece because of its linear B-H curve, low coercive force and a thermal expansion coefficient which matched that of the titanium housing. Vanadium Permendure is used for the moving armature because it has the highest available saturation flux density, and the mass of this part had to be minimized.

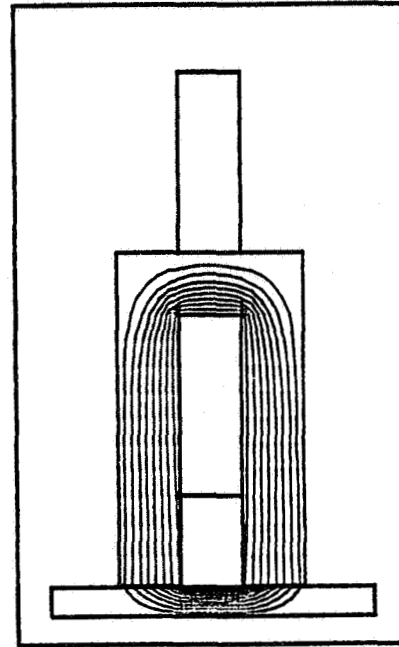
MAGGY was used to predict the flux density in the pole piece and armature. Both parts were designed to saturate at the same approximate current level. A line plot of flux and contour plot of flux density produced by the MAGGY program is shown in Figure 4-42. The bearing was designed to support the calculated loads at a low flux density, so the effects of magnetic saturation are not considered in the analysis.

TABLE 4-13. Pole Piece Parameters.

<u>Parameter</u>	<u>Notation</u>	<u>Value</u>
<u>Air Gap:</u>		
Number of Turns	N	188
Nominal Air Gap	$\delta$	25 $\mu\text{m}$
Area of Air Gap	A	$31 \times 10^{-6} \text{ m}^2$
Nominal Current	$\hat{I}$	150 mA
Permeability of Free Space	$\mu_0$	$4\pi \times 10^{-7} \text{ H/m}$
<u>Pole Piece:</u>		
Material		Nickel-Iron
Area of Pole Piece	A	$31 \times 10^{-6} \text{ m}^2$
Length of Pole Piece	$\ell$	$47.5 \times 10^{-3} \text{ m}$
Incremental Permeability	$\mu$	$20 \times 10^3$
Resistivity	$\rho$	$40 \times 10^{-8} \text{ Ohm-m}$
Surface Flux Density	$B_s$	0.37 T
Thickness	a	$3.25 \times 10^{-3} \text{ m}$
<u>Armature:</u>		
Material		Vanadium-Permendure
Area of Armature	A	$24 \times 10^{-6} \text{ m}^2$
Length of Armature	$\ell$	$11 \times 10^{-3}$
Incremental Permeability	$\mu$	$7 \times 10^3$
Resistivity	$\rho$	$47 \times 10^{-8} \text{ Ohm-m}$
Surface Flux Density	$B_s$	0.48 T
Thickness	a	$2.54 \times 10^{-3} \text{ m}$



(a) Plot of flux density.



(b) Plot of flux.

Figure 4-42. Magnetic circuit computer analysis output.

The linearized force constant,  $K_f$ , in the model is given by the equation:

$$K_f = \frac{N^2 A \mu_o \hat{i}}{3\pi \delta^2}$$

which was derived in Section 4.3.

A plot of the calculated average flux density in the nickel-iron pole piece and Permendure armature as a function of frequency is given in Figure 4-43. The defining equation, also derived in Section 4.3, is:

$$B_m = \left[ \frac{B_s \cdot d}{(i+j)a} \frac{(e^{a/d} - e^{-a/d}) \cos(a/d) + j(e^{a/d} + e^{-a/d}) \sin(a/d)}{(e^{a/d} + e^{-a/d}) \cos(a/d) + j(e^{a/d} - e^{-a/d}) \sin(a/d)} \right]$$

where  $d = 1/\sqrt{\pi f \sigma \mu_o \mu_r}$ .

The eddy-current half pole is the frequency at which the reluctance of the air gap equals the combined reluctance of the pole piece and armature. The time constant of this pole along with the calculated value for  $K_f$  is given in Table 4-14. It should be noted that the effect of the silver braze material and titanium housing are not included in the eddy current calculations. Since eddy currents are undoubtedly generated in these materials, the time constant in the table is a lower bound on the expected value.

TABLE 4-14. Parameters of Coil Dynamics Block.

<u>Parameter</u>	<u>Notation</u>	<u>Value</u>
Force Constant	$K_f$	35 N/A
Eddy Current Time Constant	$\tau_e$	5.3 msec

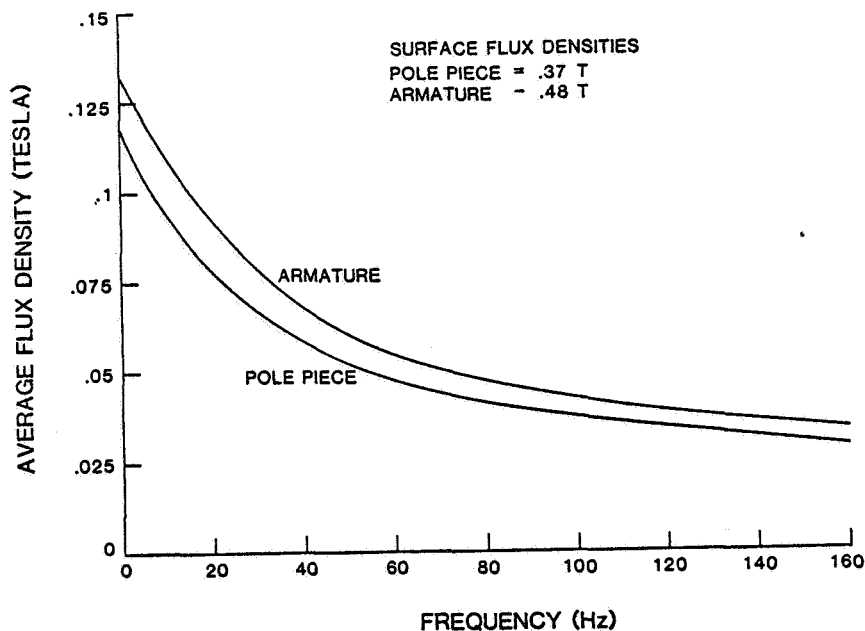
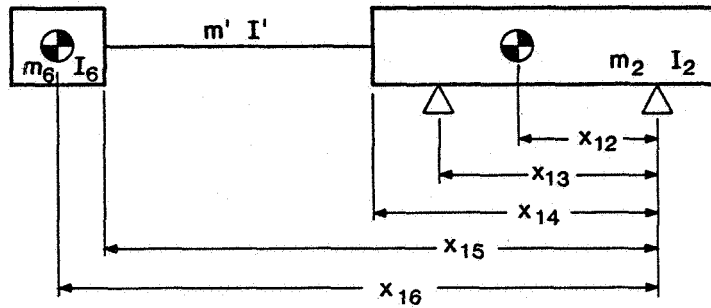


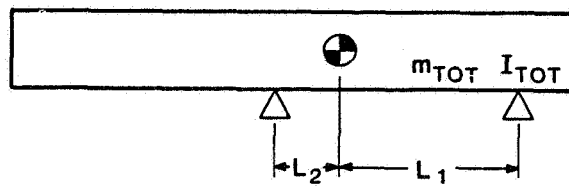
Figure 4-43. Average calculated flux density in pole piece and armature.

## (2) Shaft Dynamics

The model for the displacer distributed mass is shown in Figure 4-44a. Table 4-15 gives the values for the parameters in the figure.



(a) DISTRIBUTED SYSTEM



(b) LUMPED SYSTEM

Figure 4-44. Model of displacer mass and moment of inertia.

TABLE 4-15. Parameters of Distributed Mass System.

<u>Parameter</u>	<u>Value</u>
$x_{12}$	0.0466 m
$x_{13}$	0.0962 m
$x_{14}$	0.1345 m
$x_{15}$	0.1945 m
$x_{16}$	0.2226 m
$m_2$	0.249 kg
$I_2$	$600 \times 10^{-6} \text{ kg m}^2$
$m_6$	0.0354 kg
$I_6$	$13 \times 10^{-6} \text{ kg m}^2$
$m'$	0.067 kg
$I'$	$21.8 \times 10^{-6} \text{ kg m}^2$



Using these values, the mass, moment of inertia, and center of gravity for the lumped system, as shown in Figure 4-44b, are calculated and given in Table 4-16.

TABLE 4-16. Parameters for Lumped Mass System.

<u>Parameter</u>	<u>Value</u>
$m_{tot}$	0.350 kg
$I_{tot}$	$1.6 \times 10^{-3} \text{ kg m}^2$
$L_1$	69.0 mm
$L_2$	30.0 mm

Using the parameters of the lumped mass system, the effective mass (Sect. 4.3) which the front displacer bearing nominally sees is 0.394 kg.

The parameters of the front displacer clearance seal are given in Table 4-17. The formula for the gas damping produced by the squeeze film in the narrow annular gap:

$$b = 12\pi\mu L (R/C)^3$$

yields a value of  $b = 2 \times 10^3 \text{ N-sec/m}$ .

TABLE 4-17. Parameters of Front Displacer Clearance Seal.

<u>Parameter</u>	<u>Notation</u>	<u>Value</u>
Gap	C	25 $\mu\text{m}$
Length	L	0.0429 m
Radius	R	0.010 m
Absolute Viscosity of Helium (300°K)	$\mu$	$20 \times 10^{-6} \text{ N-sec/m}^2$

The bias current used in the front refrigerator bearings is 10 mA. The negative spring constant, C, given by the formula,

$$C = - \frac{i_o^2 N^2 A \mu_o}{\delta^3}$$

is calculated to be  $- 4.2 \times 10^3 \text{ N/m}$ .

The results for the model of the shaft dynamics are summarized in Table 4-18, below.

TABLE 4-18. Parameters of Shaft Dynamics Block.

<u>Parameter</u>	<u>Notation</u>	<u>Value</u>
Effective Mass	m	0.394 kg
Squeeze Film Damping	b	$2 \times 10^3$ N-sec/m
Negative Spring Constant	c	$4.2 \times 10^{-3}$ N/m

(3) Radial Position Sensors

The gain of the radial position sensors can be adjusted by changing the component values in the impedance bridge or by varying the gain of the low pass filter (see Sect. 4.6). In the refrigerator, the gain was adjusted to be  $80 \times 10^3$  V/m (80 mV/ $\mu$ m). The pair of low-pass filter poles are at 10 kHz. For this block, therefore,

$$\begin{aligned} A_p &= 80 \times 10^3 \text{ V/m} \\ \tau_p &= 16 \times 10^{-6} \text{ sec} \end{aligned}$$

(4) Current Driver

The gain of the current amplifier, corresponding to the closed loop transfer function gain, is 1.9 A/V. Since the open-loop gain is high, the closed-loop gain is approximately the inverse of the feedback path gain  $1/R_s$  (see Sect. 4.7). The closed loop pole is 2 kHz. Therefore, for this block,

$$\begin{aligned} A_d &= 1.9 \text{ A/V} \\ \tau_d &= 80 \times 10^{-6} \text{ sec} \end{aligned}$$

(5) Compensator

The parameters of the compensator block are shown in Table 4-19. The compensator was designed to provide 40° of phase margin, which is an adequate compromise between stability and bandwidth.

TABLE 4-19. Compensator Parameters.

<u>Parameter</u>	<u>Notation</u>	<u>Value</u>
Gain	$A_c$	7.0 V/V (17 dB)
<u>Time Constants:</u>		
Lag Pole	$\tau_{c3}$	1.5 sec
Lag Zero	$\tau_{c1}$	30 msec
Lead Zero	$\tau_{c2}$	0.5 msec
Lead Pole	$\tau_{c4}$	0.16 msec

(6) Transfer Functions

A comparison between the predicted and measured open-loop transfer function for the front displacer bearing is given in Figure 4-45. The shaft resonance which was discussed in Section 4.5 can be observed in the measured data. As already mentioned, it was not modeled since its inherent damping could not be easily estimated. Table 4-20 lists the closed-loop measured system performance parameters for all eight bearings operating in the refrigerator.

TABLE 4-20. Magnetic Bearing Performance

	<u>Piston</u>	<u>Displacer</u>
dc offset (due to shaft weight)	< 0.4 $\mu\text{m}$	< 0.5 $\mu\text{m}$
Peak ac oscillations (during operation)	< 0.7 $\mu\text{m}$	< 2.5 $\mu\text{m}$
Control loop bandwidth	375 Hz	150 Hz
Control loop phase margin	40°	40°
dc stiffness (calculated)	26 x 10 <sup>6</sup> N/m (150,000 lb/in)	5.3 x 10 <sup>6</sup> N/m (30,000 lb/in)

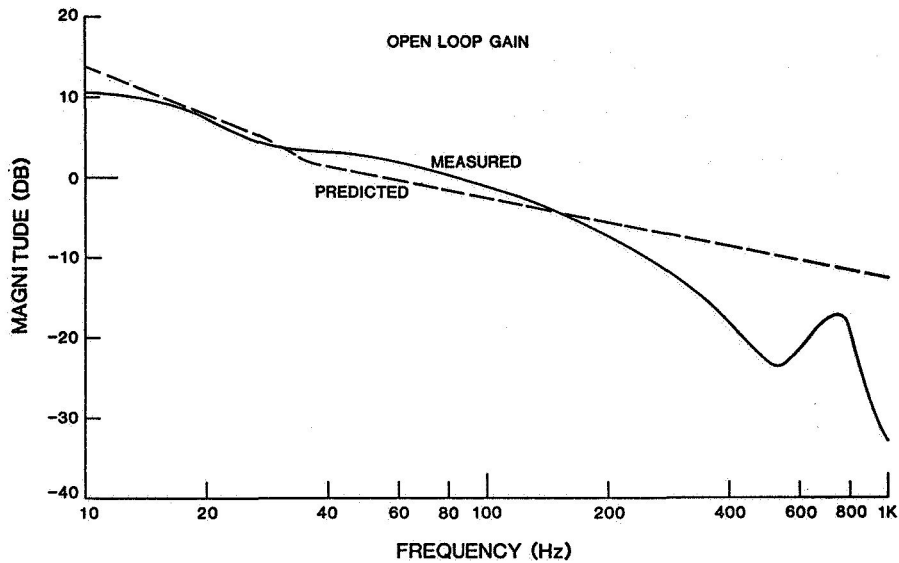


Figure 4-45. Open loop transfer function of front displacer bearing.

The step response of the front displacer bearing is shown in Figure 4-46. For this test, the reference signal of 0 V was perturbed with a square wave (see Fig. 4-41) and the transduced position was monitored. The step was about 5  $\mu\text{m}$  or  $\pm 0.1$  gap.

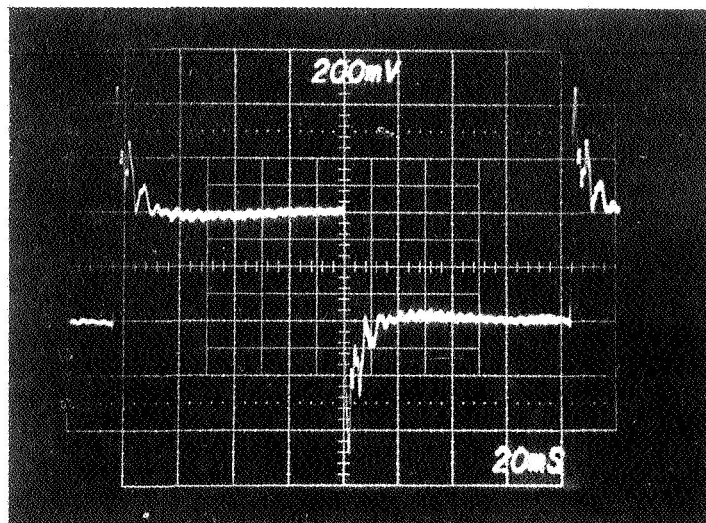
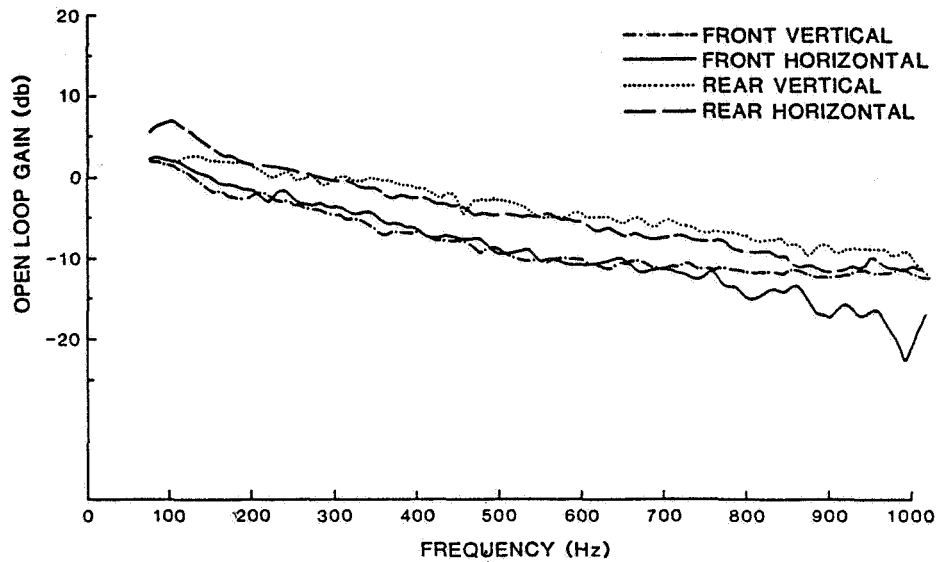


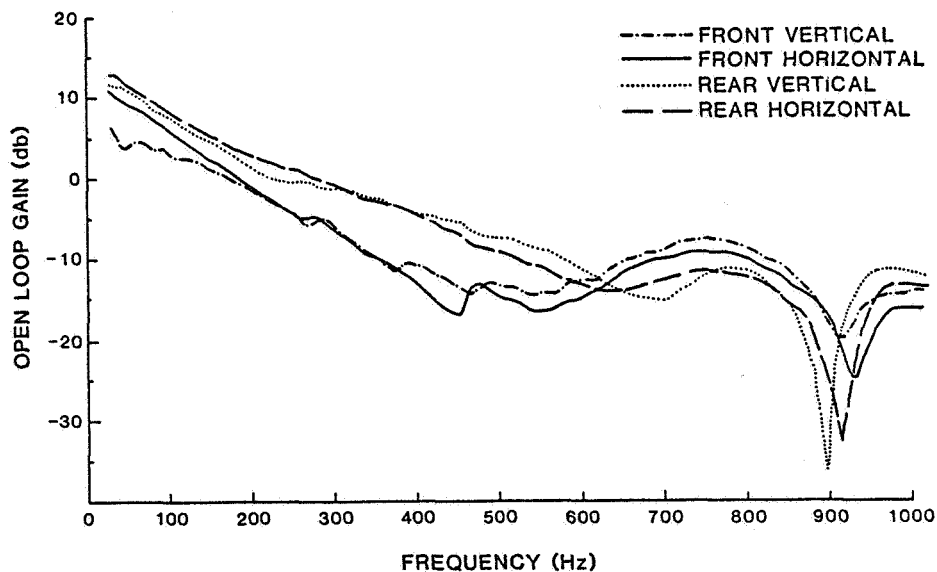
Figure 4-46. Step response of front displacer bearing.

(7) Control System Performance

For completeness, the open-loop magnitude frequency response is shown for all eight bearing control systems in Figure 4-47.



(a) Piston bearings.



(b) Displacer bearings.

Figure 4-47. Frequency response of piston and displacer bearings.

## 4.9 Bearing Test Fixtures

### 4.9.1 General

Two generations of test fixtures were designed and built for the magnetic bearings. The first, shown in Figure 4-48, proved concept feasibility. The magnetic air gap was relatively large (250  $\mu\text{m}$ ), and the parts were fabricated with wide tolerances. The pole pieces were mechanically held outside the stainless steel housing. The target for the eddy current sensors was ferromagnetic and prone to electromagnetic interference from the pole pieces. The electronics for the sensors was commercially obtained and drifted substantially with ambient temperature. The bearing driver was a packaged high-current operational amplifier; the output was diode switched into the pole pairs. A small electromagnetic actuator was provided to produce axial reciprocating motion. To the knowledge of the authors, Philips Laboratories was the first to propose the use of linear magnetic bearings, and this fixture demonstrated their usefulness in supporting small-diameter shafts (2 cm). The stiffness was very low for small displacements, although adequate for keeping the shaft suspended in the large air gap.

The second-generation test fixture, shown in Figure 4-49, was designed to accurately simulate the piston section of the refrigerator. Thus, the fabrication techniques were more involved than those of the first bearing. The parts were machined to close tolerances, with less than 3  $\mu\text{m}$  eccentricity in the 25  $\mu\text{m}$  radial gap. The pole pieces were joined via the same techniques used in the refrigerator, thus testing the procedure to braze the ferromagnetic materials and still retain their optimized magnetic properties. Three different fixtures of this generation were constructed to test different magnetic materials and fabrication techniques.

As previously stated, the advantage of the test fixture was that the radial force imparted to the shaft could be transduced. The bearing is shown on its test stand in Figure 4-50. A commercial shaker is connected to the suspended shaft via a piezoelectric force transducer. The relative displacement between the shaft and the housing is measured with eddy current transducers, which are also used for feedback. Thus, the stiffness of the bearing, i.e., force/displacement, is measured directly.

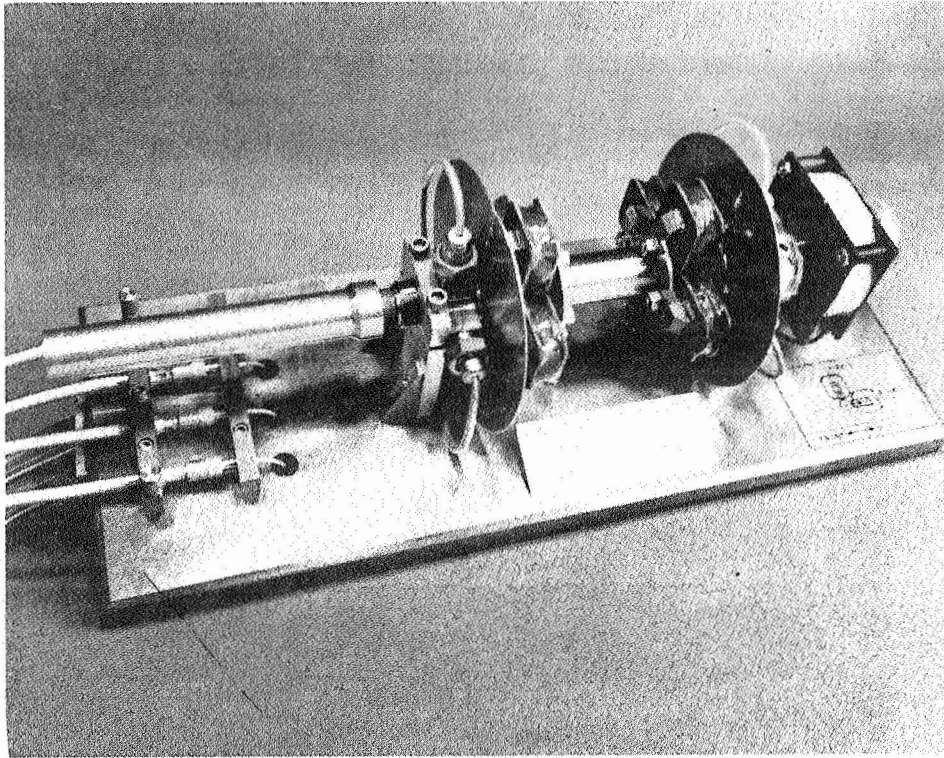


Figure 4-48. Bearing test fixture - 1st generation.

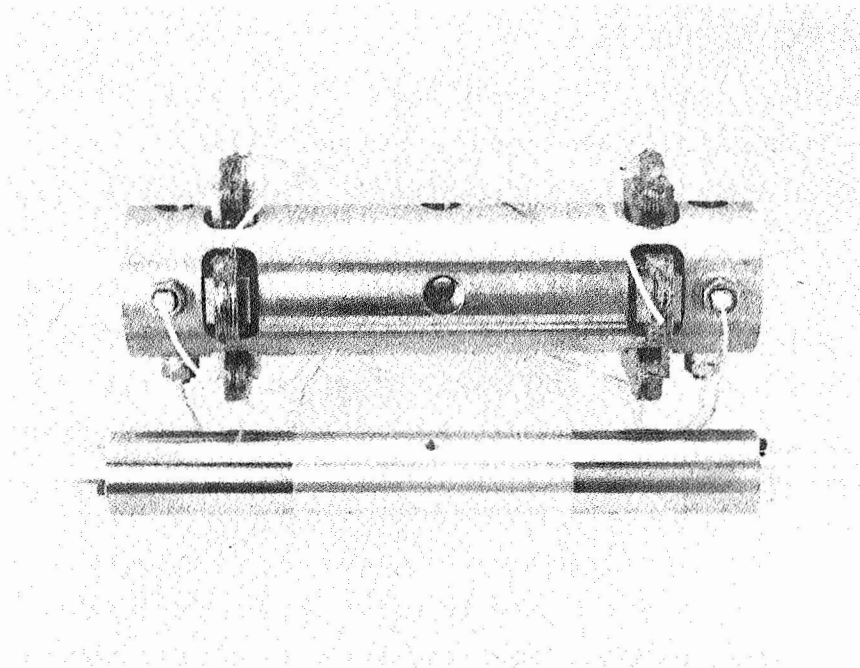


Figure 4-49. Bearing test fixture - 2nd generation.

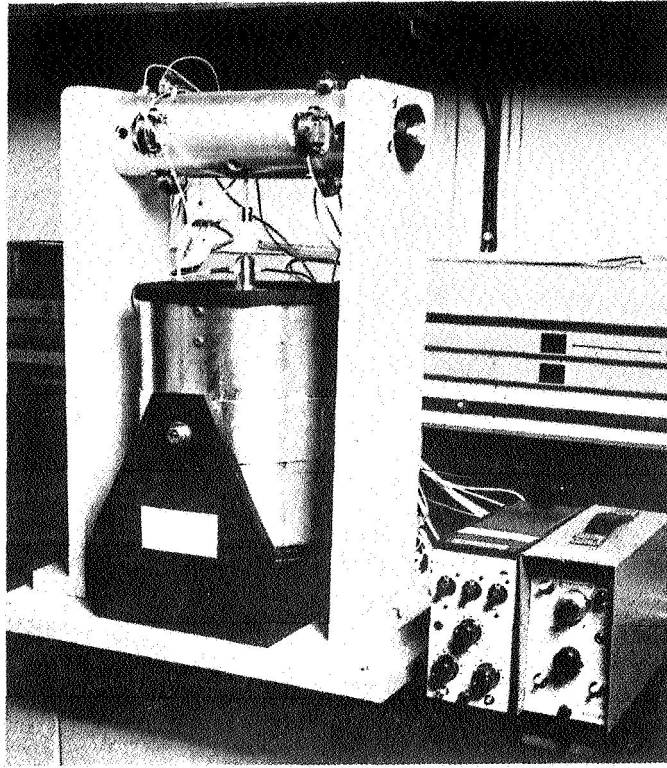


Figure 4-50. Fixture in test stand.

#### 4.9.2 Measurement Techniques

Transfer function measurement is accomplished in two ways, using either a single-frequency sinusoid or a white-noise signal. When a single-frequency sinusoid is used, a lock-in amplifier extracts the desired frequency components of the measured signal from the background noise. For a white-noise signal, a two-channel Fast Fourier Transform (FFT) spectrum analyzer is used to directly measure the transfer function between two points. In this case, the instrument measures the power spectral densities of the two inputs, and the cross-spectral density, and computes the transfer function magnitude and phase by digital processing techniques.

The measurement of open-loop frequency response for the bearing requires some explanation. As mentioned in the introduction to the bearing section, the control system model requires that the shaft be at its nominal center position. Thus, the model only works if the control system works. In the



same respect, the open-loop frequency response can only be measured if the loop is closed and stable. Otherwise, the highly nonlinear nature of the system would mask any readings.

To deduce the open-loop frequency response from a closed-loop system, the technique illustrated in Figure 4-51 was used. The test signal ( $V_{inj}$ ) is injected into the loop, and signals  $V_1$  and  $V_2$  are measured. The desired response is  $V_2/V_1$  as realized by the following:

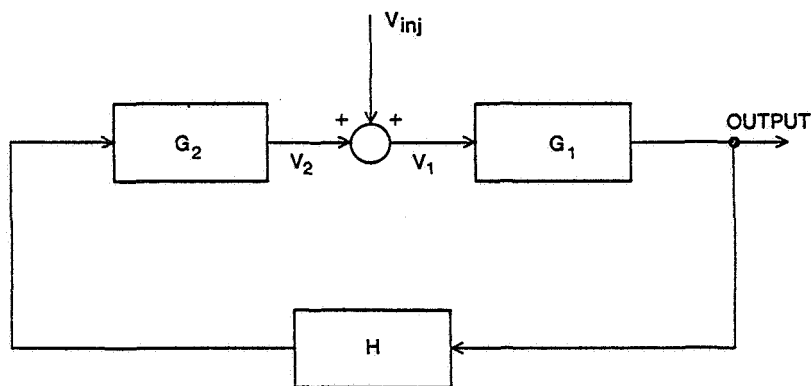


Figure 4-51. Technique for measuring open-loop frequency response.

$$V_1 = V_2 + V_{inj}$$

$$V_2 = G_1 H G_2 \cdot V_1$$

$$= G_1 H G_2 \cdot (V_2 + V_{inj})$$

Therefore,  $V_2/V_1 = G_1 H G_2$  which is the open loop response. For this analysis to be accurate, the signal  $V_{inj}$  must not load the loop. Thus the impedance looking forward should be high and the impedance looking back should be low. A non-inverting operational amplifier is included in the bearing electronics for this purpose. It should be noted from the figure that this technique works for arbitrary injected signals and does not depend on the dynamics included in the transfer function blocks.

#### 4.9.3 Results

The plot of bearing stiffness vs. frequency is shown in Figure 4-52. For this test, the excitation frequency for the shaker was varied and the force and displacement were measured. Single-frequency sinusoids were used, corresponding to the points on the curve. The flat portion of the curve at low frequencies results from the high open loop gain of the control system, while the rolloff at 20 Hz corresponds to the finite bandwidth. The stiffness increases at 200 Hz because the shaft inertia dominates the response.

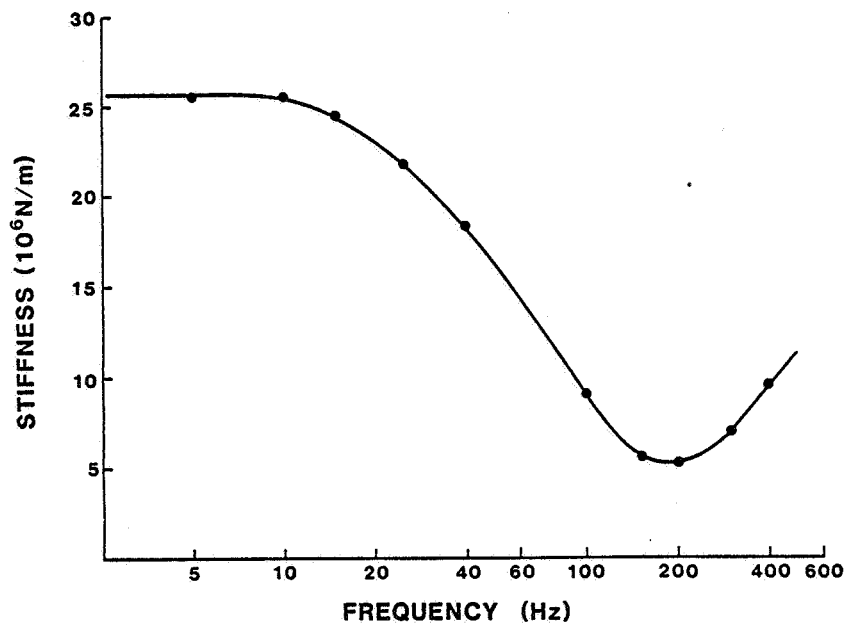


Figure 4-52. AC "stiffness" of magnetic bearing system.

To obtain the static load test data shown in Figure 4-53, various known masses were hung from the shaft, and the displacement was measured. From Section 4.4 it will be recalled that the worst dc load predicted for the piston bearings was 12.4 N (RSS) corresponding to a sag of 1.1  $\mu$ m.

Finally, using the measurement technique illustrated in Figure 4-51, the open-loop frequency response was measured. This is shown in Figure 4-54. For this test, a white noise source was used.

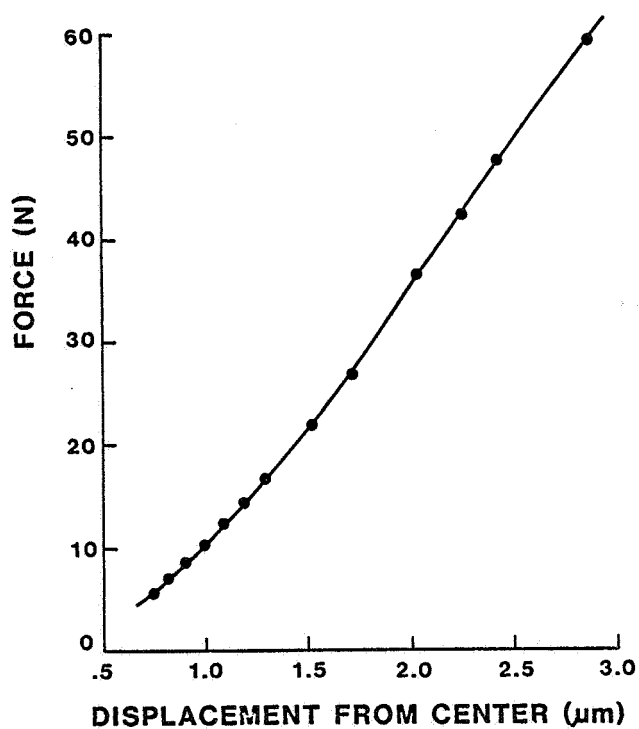


Figure 4-53. Static load characteristics of magnetic bearing.

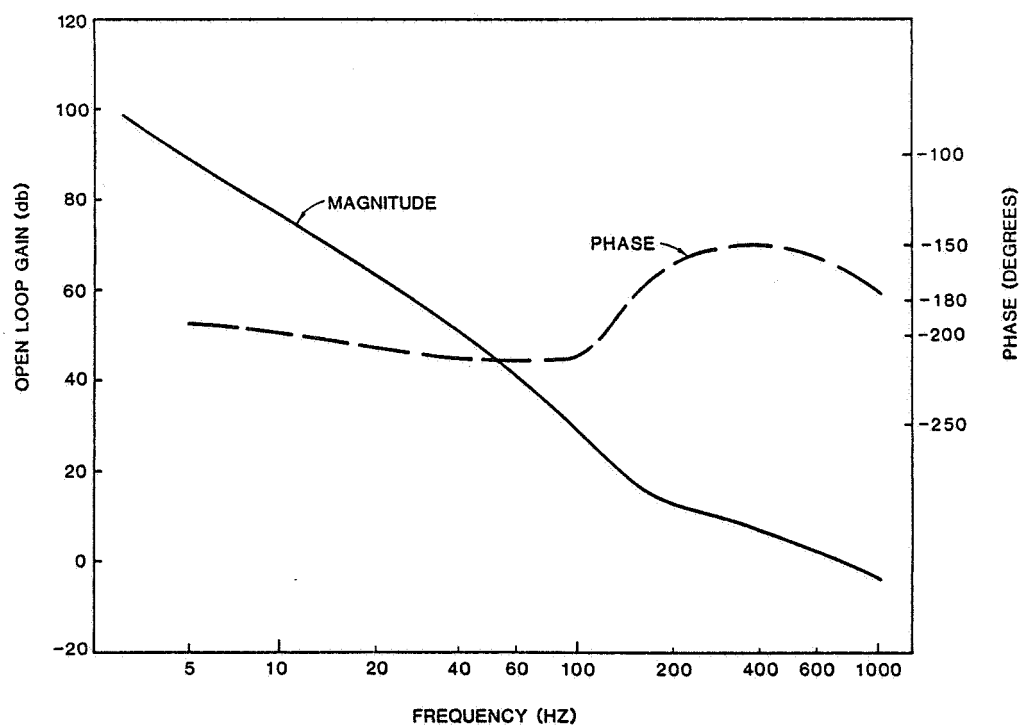


Figure 4-54. Open-loop frequency response - Test Fixture.

#### 4.10 Summary

The development of reciprocating magnetic bearings constituted one of the major efforts on the refrigerator project. It required hermetic joining of high performance ferromagnetic materials, development of the eddy-current transducers, and demanding fabrication techniques. This development was required to bring the concept of a long life refrigerator to fruition. And, as can be seen from the data presented, the development was a complete success. The magnetic bearings have a higher stiffness than that of many mechanical bearings.

## 5. LINEAR MOTORS AND AXIAL CONTROL ELECTRONICS

### 5.1 Introduction

A significant element of the refrigerator design is the application of direct-drive linear motion for the compression/expansion and displacement of gas in the Stirling cycle. This departure from the traditional conversion of rotary to linear motion eliminates a large number of life limiting bearings, a crankshaft, connecting rods, and the resulting mechanical inefficiency. By using linear motors and axial control electronics, only two linear bearings per shaft are needed, and the stroke amplitudes and piston/displacer phase angle can be adjusted during operation. Thus, the drive offers high reliability, efficiency, and versatility.

This section is in two parts. The first part involves the design, fabrication, and testing of the linear motors for the piston and displacer. As such, it discusses the magnetic/mechanical aspects of the drive. The linear motors were designed using the Philips finite element magnetic circuit analysis program (MAGGY). The computer results are discussed and compared with the measured performance. The second part deals with the electronics for controlling the motors, and thus is concerned with the electrical/magnetic aspects of the drive. To control the sinusoidal mechanical motions, an analog feedback system was designed and constructed. In both parts, the overriding focus is the intended use, viz., the linear resonant Stirling cycle. These systems were designed for this special application and take advantage of the overall drive characteristics of the cycle.

### 5.2 Linear Motors

#### 5.2.1 Description

The principle of operation of the linear motor used in this refrigerator (see Fig. 5-1) is similar to that of the actuators used in most loudspeakers. Permanent magnets, rather than a field coil, establish a steady magnetic flux field (see Fig. 5-2). The current through the coil interacts with the flux to produce a force between the coil and the permanent magnet. Since the flux is oriented radially and the coil is wound circumferentially, the force is directed along the axis of the motor, thereby producing linear motion.

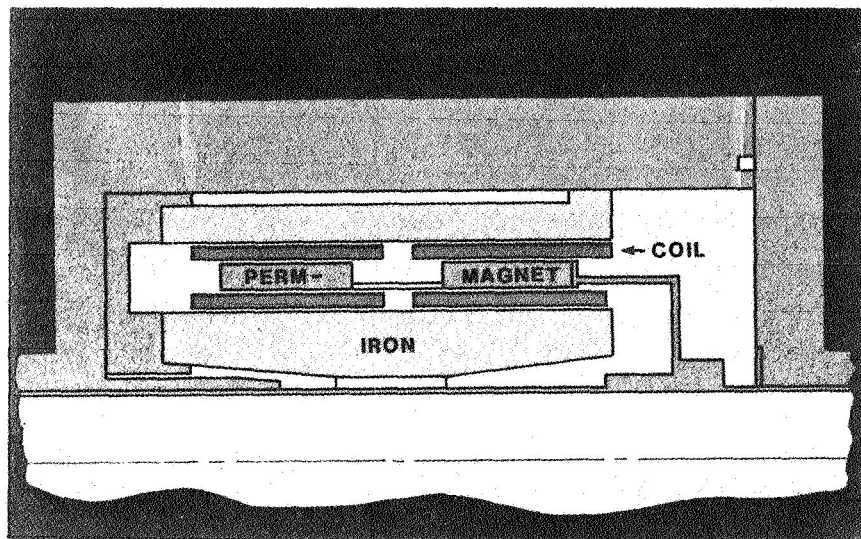


Figure 5-1. Schematic of linear motor for piston.

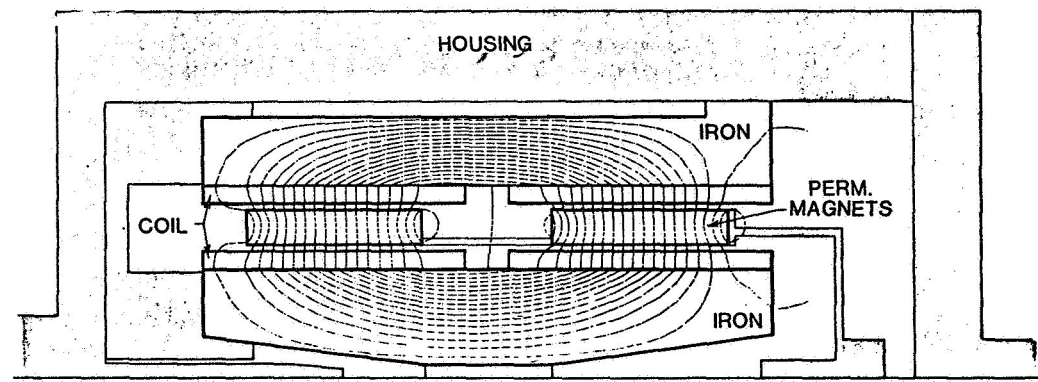


Figure 5-2. Flux plot of linear motor for piston.

The structure of the piston motor shown in Figure 5-1 is essentially two motors connected back-to-back (also see Fig. 2-6). This design helps maintain a linear relationship between the current in the coils and the resultant motor force. The coil current simultaneously increases the magnetic loading on one of the magnet rings and decreases the loading on the other ring. Since all of the flux must go through both magnet rings, the total magnetic circuit sees little change in the loading, and the flux level remains almost constant, independent of the current amplitude. A high degree of linearity for the motor force as a function of current is desirable, as nonlinearities tend to produce non-sinusoidal forces which the electronic axial control system would have to correct, thereby reducing the overall efficiency of the motor system.

Figure 5-1 also shows an inner and an outer coil section for each of the two "motor sections". The presence of substantial non-magnetic gaps (the coils) on each side of the magnet rings reduces the radial force generated between the moving-magnet armature and the stationary iron stator rings. These side forces represent a significant load for the magnetic bearings, the radial instability force discussed in Section 4.4.2.4. The effect of radially moving the magnet ring is reduced with this geometry.

An additional feature of this motor design is the ability to hermetically isolate the helium working fluid from all possible sources of organic contamination. As discussed previously, contamination results in long-term degradation of refrigerator performance, an obvious detriment. The hermetic seal is made by welding thin-walled titanium cans over the magnets and the coils. If the cans are thin enough (0.3 mm), the reduction in the motor efficiency will be small. Electrical connection to the motors is made with nickel/ceramic feedthroughs.

The displacer motor shown schematically in Figure 5-3 operates the same as the piston motor (see also Fig. 2-7). The geometry is somewhat different in that there is only one coil section for each magnet section, and the inner iron is part of the armature. The small size of this motor, governed by the diameter of the displacer, dictates these changes, but the small size also means that the side forces produced by the radial instability are less. In Section 4.4.3.3, it was seen that the calculated radial instability loads

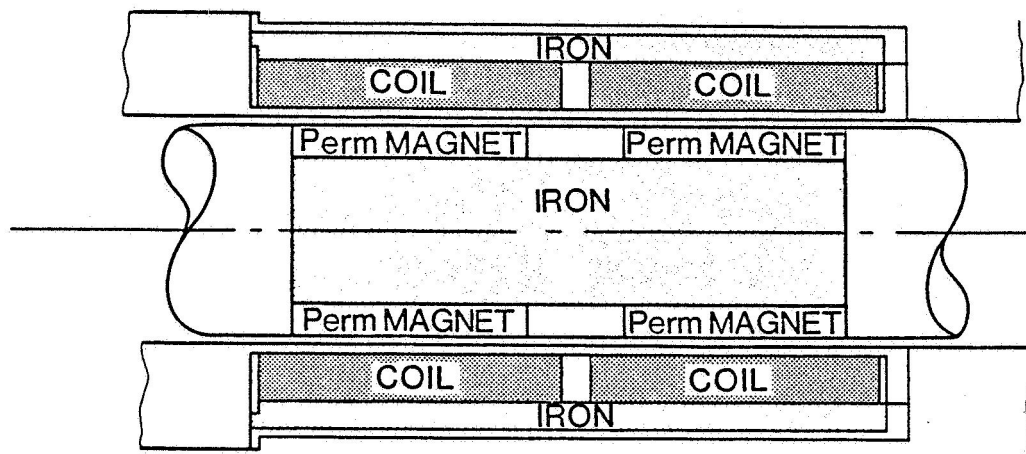


Figure 5-3. Schematic of linear motor for displacer.

for the displacer are large, although relatively insignificant compared to those associated with the much larger piston motor.

#### 5.2.2 General Analysis

##### (1) Force Constant

The electromagnetic force generated by a current flowing through a wire in a magnetic field is given by the relationship  $F = B\ell I$ , where  $F$  is the force in Newtons,  $B$  is the magnetic flux density of the field in Webers/m<sup>2</sup>,  $\ell$  is the length of wire within the magnet field in meters, and  $I$  is the current in the wire in Amperes. The problem of calculating a motor's force constant,  $C_m = F/I$  (N/A), is one of calculating the  $B\ell$  product. The length of wire is simply a function of the motor geometry and the number of turns used to wind the coil. Estimating  $B$ , the magnetic flux density produced by the permanent magnet in the air gap occupied by the coil, is more difficult. Magnetic materials are inherently nonlinear, and the magnetic flux path is not always apparent, since flux leakage is frequently significant. A reasonable approximation can be made using analytical or graphical techniques, as described in Electromagnetic Devices by Roters, 1941, but the accuracy of the approximation is a strong function of the designer's expertise. A substantially simpler and far more accurate calculation can be made by using finite-element analysis performed on a digital



computer. As previously discussed, Philips Laboratories proprietary computer package (MAGGY) is designed specifically for the solution of magnetic problems. This program has been verified through extensive use, and is typically accurate to within a few percent. All calculations of magnetic performance were made using the MAGGY program. This allowed us to optimize dimensions to obtain the maximum motor efficiency for a given motor weight, with the magnets operating at their peak energy product and the iron stator thickness minimized.

(2) Inductance

The inductance of the motor coil is another significant parameter since it effects the voltage required to drive the motor, as discussed in Paragraph (4). The MAGGY program calculates the inductance, since it is a magnetic phenomenon due to the flux linkage through the coil windings.

(3) Efficiency

Motor efficiency is defined as the ratio of the mechanical output power to the electrical input power,

$$\eta = P_{OUT}/P_{IN}$$

Since the only loss in the motor (ignoring eddy currents for now) is the heat dissipated in the coil windings,

$$P_{IN} = P_{OUT} + \frac{1}{2} \hat{I}^2 R_C$$

where,  $\hat{I}$  = motor-current peak amplitude and  $R_C$  = resistance of the coil. The model shown in Figure 5-4 defines the variables used in the calculation. The following assumptions were made:

- Eddy currents are neglected.
- The entire armature of the motor is always within the active portion of the stator so that full overlap always exists between the magnets and coils.
- The motor force constant is a true constant, independent of current or position.
- Motor inductance is constant, independent of current or position.
- All sub-coils (of which there are four for the piston motor shown in Fig. 5-1 and two for the displacer motor shown in Fig. 5-3) are connected in series electrically.

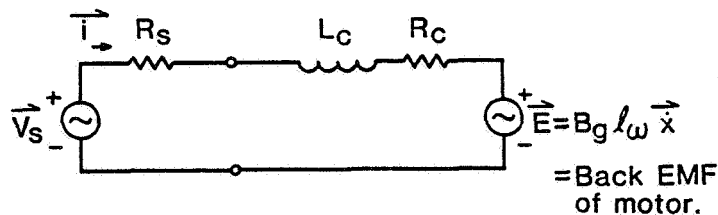


Figure 5-4. Model for calculating efficiency of linear motor.

The efficiency of the motor can be calculated with the aid of two more equations:

$$\hat{I} = \hat{F} / (N_c C_c)$$

$$R_c = \rho_{cu} \pi D_c N_c^2 / (\gamma A_c)$$

The variables used in this analysis are:

$\vec{x} = \hat{x} \cos \omega t$ ; armature position (m)

$\vec{F} = \hat{F} \cos (\omega t - \theta_F)$  [ $\theta_F = -\frac{\pi}{2}$  for pure damping load]; motor force (N)

$\vec{V}_s = \hat{V}_s \cos (\omega t - \theta_v)$ ; driver output voltage (V)

$\vec{I} = \hat{I} \cos (\omega t - \theta_F)$ ; current (A)

$N_c$  = number of turns

$C_c$  = motor force constant (Newtons/(Ampere-turns))

$L_c$  = coil inductance = (H)

$\rho_{cu}$  = resistivity of copper (Ohm-meter)

$D_c$  = mean coil diameter (m)

$A_c$  = cross sectional area of coil = length • radial thickness ( $m^2$ )

$\gamma$  = fill factor; fraction of  $A_c$  occupied by copper.

$R_s$  = source resistance of driver (Ohm)

$R_c$  = coil resistance (Ohm)

Thus,

$$\eta = \frac{1}{1 + \frac{\rho_{cu} \pi D_c \hat{F}}{\gamma A_c C_c^2 \omega \hat{x} \sin \theta_F}}$$

It can be seen from this formula that motor efficiency is independent of  $N_c$ , the number of turns used to wind the coils. As a result, the designer is free to select the number of turns necessary for the motor to operate at the available drive voltage.

For high-efficiency motors (greater than 70%), this formula can be approximately expanded as,

$$\eta \sim 1 - \left( \frac{\rho_{cu} \pi D_c n}{\gamma A_c C_c^2} \right) \left( \frac{\hat{F}}{\omega x \sin \theta_F} \right)$$

The first term is a constant dependent only on motor geometry, and is therefore a valid parameter for comparing various motor designs. The smaller this parameter, the more efficient the motor will be. The second term is a function of the load applied to the motor, demonstrating that efficiency is highest when: (1) the output force is small, (2) the operating frequency is high, (3) the stroke amplitude is large, and (4) the system is operated at resonance so that the motor is only applying real power (i.e., no reactive component and  $\theta_F = -\pi/2$ ). This second term in the efficiency equation partially explains the extremely low efficiency of the displacer motor. Most of the power in the displacer motor is reactive since it is used to accelerate the displacer mass, rather than to overcome a damping force. The efficiency assumes reactive power is "useless" since it does no net work, but in this case the displacer reactive power is certainly essential to the cooler operation.

#### (4) Coil Design

The equations relating the number of coil turns to the required operating voltage can be found by analyzing the electrical network shown in Figure 5-4. The basic network equation is:

$$\vec{V}_s = \vec{I} (R_s + R_c) + L_c \frac{d\vec{i}}{dt} + \vec{E}$$

For sinusoidal operation, this can be reduced to algebraic equations by Laplace transformation, permitting one to solve for the number of turns as a function of voltage, or vice versa.

Various powers can be calculated as follows:

- Real mechanical output power of the motor,

$$P_{\text{mech}} = \frac{1}{2} \hat{F}_x \sin \theta_F$$

- Reactive mechanical output power of the motor,

$$P_{\text{react}} = \frac{1}{2} \hat{F}_x \cos \theta_F$$

- Heat generated in the coil,

$$P_{I^2R} = \frac{1}{2} \hat{i}^2 R_C$$

- Electrical power input to the motor,

$$P_{\text{motor}} = \frac{1}{2} [\hat{V}_s \hat{i} \cos (\theta_v - \theta_F) - \hat{i}^2 R_s]$$

A final consideration in the design of the coil, especially for the displacer motor, is the temperature rise due to power dissipated in the windings. The maximum allowable operating temperature (typically about 100°C) will set the upper limit on the force that the motor can generate. This is not generally a problem for the piston motor due to the high efficiency of the motor and the large surface area available to transport the heat to the outside surface of the refrigerator.

#### (5) Stator Design - Eddy Current Analysis

The design of the iron portion of the magnetic circuit for the motor must meet several requirements. There must be sufficient cross-sectional area to carry the magnetic flux, avoiding saturation of the material. This sizing is performed relatively easily with the aid of the MAGGY computer program. The second requirement is that the iron must not permit the generation of significant eddy currents. Eddy currents are generated in any electrically conductive material that is exposed to a changing level of magnetic flux. The MAGGY program, capable of solving only static magnetic problems, cannot do this analysis. The standard analysis of eddy currents, as given in Electro-magnetic Devices by Roters, 1941, is applicable to the design of closed-path magnetic circuits, such as transformer cores. The standard method of reducing eddy currents is to laminate the magnetic

material, i.e., assemble the magnetic core from many layers of thin sheet. The formula for estimating the maximum allowable sheet thickness is,

$$\delta = \sqrt{\rho / (\omega \mu_R \mu_O)}$$

where  $\delta$  is also called the eddy current skin depth,  $\omega$  = desired frequency of operation,  $\rho$  = electrical resistivity of material,  $\mu_R$  = relative magnetic permeability of the material, and  $\mu_O$  = constant permeability of free space. This skin depth formula could be used to accurately predict the frequency at which eddy current effects begin to become significant, but only for closed-path magnetic circuits. In the case of a magnetic path with air gaps, such as the linear motor being discussed here, eddy current effects are greatly reduced. For the case where the air gap, of length  $g$ , constitutes a greater reluctance than that of the iron path, of length  $\ell$ , we find that the skin depth formula can be corrected by replacing the relative permeability of the iron,  $\mu_R$ , by  $\ell/g$ .

$$\delta = \sqrt{\rho / (\omega \frac{\ell}{g} \mu_O)}$$

In most motors the quantity  $\ell/g$  is significantly less than  $\mu_R$ . This implies that the appropriate lamination thickness is greater than that predicted by the simple skin depth formula. The only additional consideration is that the "break frequency" for eddy current effects must be chosen to be at least an order of magnitude greater than the desired operating frequency. This prevents the eddy currents from introducing any significant phase shift between the current in the motor and the force generated by the motor. These phase shifts would adversely effect the performance of the motor control system.

#### (6) Side Forces

Ideal linear motors would generate only axial forces. Real linear motors, however, will also generate radial forces, imposing additional loads on the magnetic bearings. The estimation of these loads is discussed in Section 4.4.2.

### 5.2.3 Design Parameters

Table 5-1 shows the actual design values for the piston and displacer motors; Figure 5-5 is a photograph of the piston-motor armature during fabrication. The two magnet rings were epoxied on to the hollow titanium arbor which is shown mounted on a mandrel. Figure 5-6 is a photograph of the complete motor, with the armature mounted to the piston shaft and the stator assembly ready for insertion into the housing of the piston motor.

The completed displacer is shown in Figure 5-7. The displacer motor armature is an integral part of the displacer, completely contained within the shaft diameter.

TABLE 5-1. Motor Parameters.

<u>Parameter</u>	<u>Piston Motor</u>	<u>Displacer Motor</u>
Peak force (N)	150	39.6
Phase angle of force from displacement (°)	90	180
Frequency (Hz)	26.7	26.7
Stroke amplitude (mm)	7.5	3.3
Real power output (W)	88	11
Reactive power (W)	0	44
No. of turns	136	464
Peak applied voltage	15	14
Inductance (mH)	2.2	0.63
Eddy current break freq. (kHz)	3.6	4.5
Wire size (mm)	1.06 x 2.67	0.57 x 0.88
Coil resistance (ohm)	0.198	1.69
Peak current (A)	17	8
Ohmic Loss (W)	29	52
Efficiency (%)	75	-

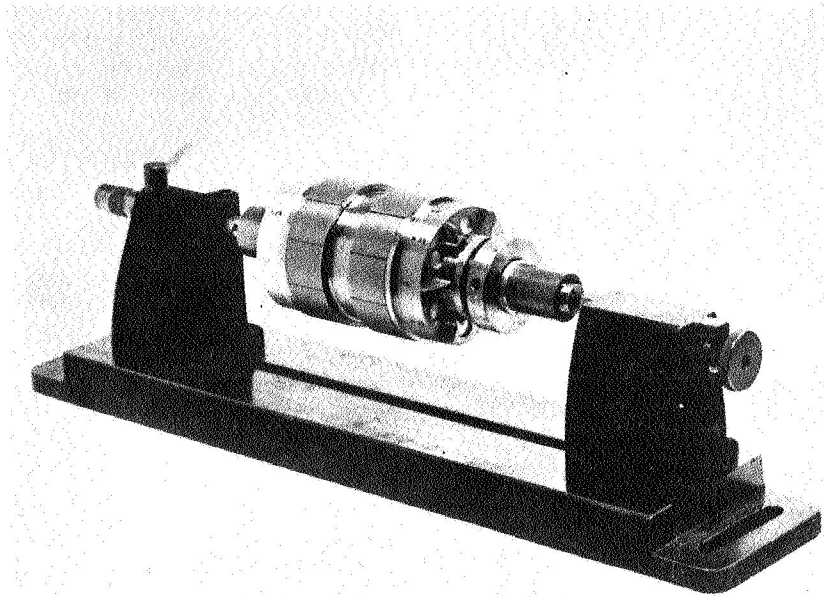


Figure 5-5. Armature of piston motor with permanent magnets attached (on mandrel).

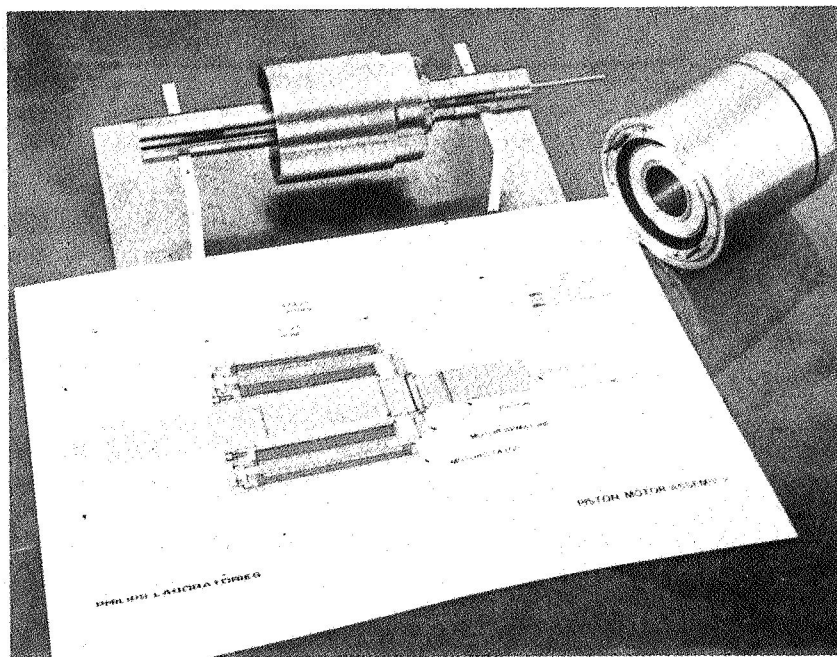


Figure 5-6. Piston motor showing armature mounted to shaft and stator assembly ready for insertion into motor housing.

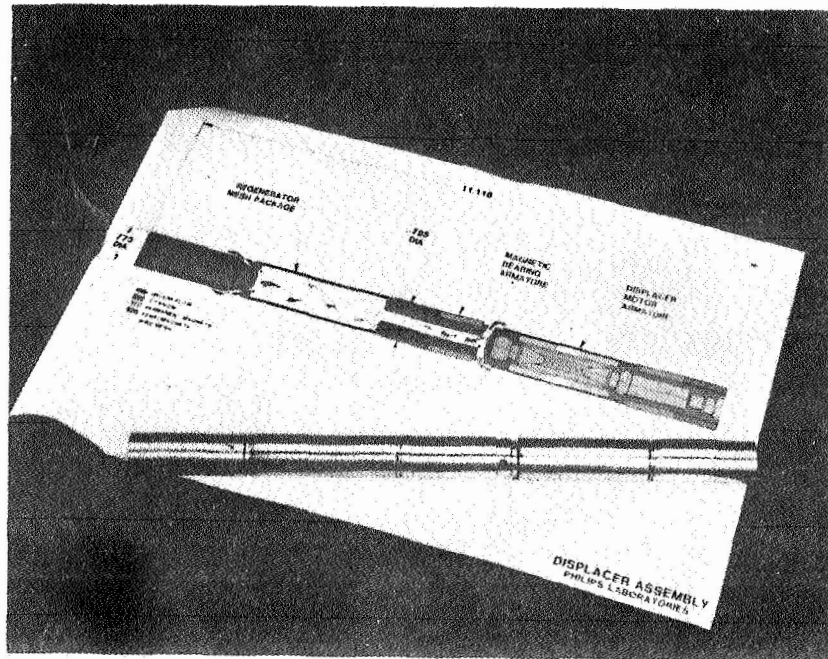


Figure 5-7. Completed displacer.

#### 5.2.4 Piston-Motor Test Fixture

##### (1) Objectives

As part of the effort to develop the linear motors, a task was undertaken to experimentally determine various characteristics of the piston motor. These included the electrical characteristics which affect the design of the control system and the mechanical characteristics which affect the design of the bearings supporting the piston.

The electrical characteristics of interest were the force constant (N/A), the inductance and resistance of the motor, and the total power losses due to ohmic loss, eddy currents, and magnetic hysteresis.

The mechanical characteristics of interest were the static and dynamic side forces which must be carried by the bearings, the operating efficiency, the operating temperature of the coil, and the rotational torque component of the force produced by the motor at various orientations.

These measurements were made at various operating speeds, motor orientations, and loadings, to validate the motor design methodology.



(2)      Test Fixture Design

The design of the test fixture (see Fig. 5-8) can be divided into four categories: the motor (on the left); a gas spring (on the right); a means for attaching the two; and a system to keep the apparatus aligned.

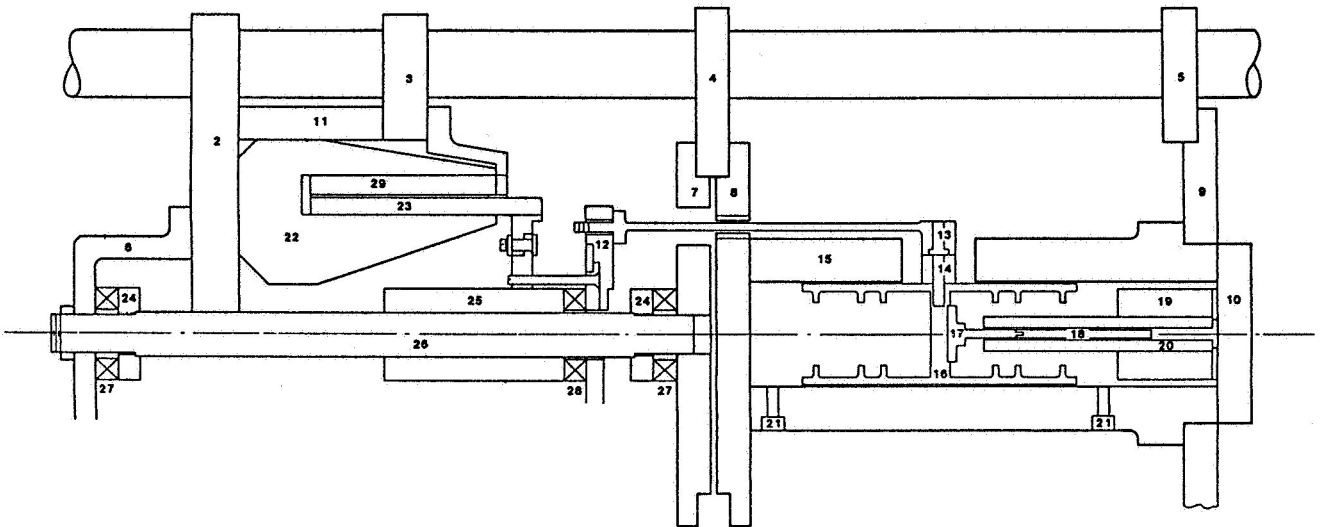
The motor, consisting of the stator (22) and the armature (23), is, of course, the motor to be tested. The stator is held stationary by the mounting plates (2, 3, and 11). The armature is attached to a linear air bearing (25) which, in turn, is attached through a force transducer (28) to the gas-spring mechanism.

The gas spring consists of a cylinder (15) and a two-sided piston (16). The cylinder is pressurized so that in moving the piston a considerable force is required to compress the gas, yielding its spring-like characteristic. This gas spring was designed so that its nonlinearities, inherent to all gas springs, would be comparable to those found in the cooler, thus producing a representative environment for testing.

Rulon sleeves were used on the piston as a combination clearance seal and bearing. Rulon's low coefficient of friction gave low power dissipation, and a 0.0003 in. radial gap produced an acceptable clearance seal.

Three sets of ports (21) are used to attach a system of valves. The valves are used to change the mean pressure within the cylinder, thus changing the stiffness of the gas spring. By this means, the motor system can be tuned to resonate at any operating frequency within the limits of interest. This valve system can also dissipate energy by allowing gas to flow between the cylinder halves. By controlling this flow, any desired loading can be produced.

The connection between the motor and the spring has two important characteristics. The first is the flexibility inherent to the long, thin rods (13). This minimizes the side forces produced by any misalignments which may exist. The second is the freedom which the bracket (12) allows. By simply loosening six bolts, the armature can be rotated to any desired orientation with respect to the stator.



- |                               |                          |                              |
|-------------------------------|--------------------------|------------------------------|
| 1) ALIGNMENT RODS (3)         | 11) STATOR MOUNTING RING | 21) PORTS (6)                |
| 2) MOUNTING PLATE             | 12) SLIP RING LINKAGE    | 22) STATOR                   |
| 3) MOUNTING PLATE             | 13) RODS (3)             | 23) ARMATURE                 |
| 4) MOUNTING PLATE, GAS SPRING | 14) ROD BUSHINGS (3)     | 24) F.T. CONNECTOR           |
| 5) MOUNTING PLATE, GAS SPRING | 15) GAS SPRING CYLINDER  | 25) BEARING                  |
| 6) MOUNTING PLATE             | 16) PISTON               | 26) SHAFT                    |
| 7) MOUNTING PLATE, GAS SPRING | 17) LVDT CORE SUPPORT    | 27) X-Y FORCE TRANSDUCER (2) |
| 8) MOUNTING PLATE, GAS SPRING | 18) LVDT CORE            | 28) TORQUE-COMPRESSION F.T.  |
| 9) MOUNTING PLATE, GAS SPRING | 19) LVDT BODY HOLDER     | 29) MAGNET ASSEMBLY          |
| 10) END CAP                   | 20) LVDT BODY            |                              |

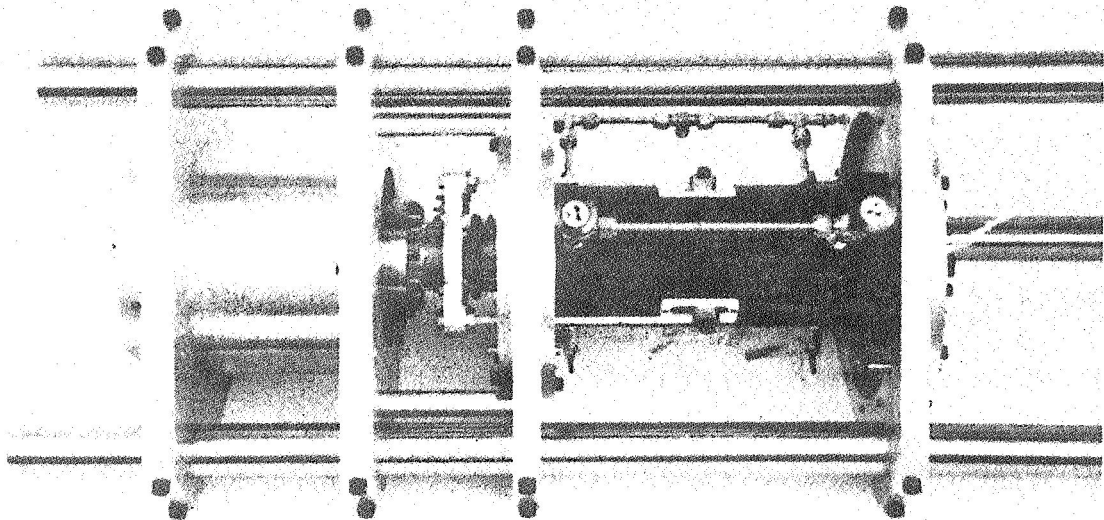


Figure 5-8. Piston-motor test fixture.

The bearing (25) must accurately align the armature and the stator. An air bearing was used for its low-power dissipation, accurate location, and light-weight construction.

The overall alignment of the test fixture is achieved by a system of three 1-1/2 in. steel bars (1) and eight mounting plates (2 - 9). These are tightly toleranced, yielding alignments comparable to those found in the actual machine.

### (3) Methods of Data Acquisition

Incorporated into the fixture design are three force transducers and a linear variable differential transformer (LVDT). These sensors allow the system to be controlled and the measurements to be taken. The two force transducers located at the ends of the shaft (27) measure the side forces which the magnetic bearings will encounter. The third force transducer, mounted between the armature and the spring mechanism (28), measures the axial force and torque. The LVDT (20, 21) is mounted inside the cylinder and measures the position of the oscillating armature.

With the output from the LVDT and the axial force transducer, resonance can be detected when the mean pressure in the cylinder is correct. The spring is tuned to resonance by adjusting the pressure in the cylinder. Measurements are taken only when the system is at resonance.

The LVDT was also used as the position transducer in an axial-position control system. Since the test fixture simulated the refrigerator in terms of resonant behavior and magnitude of nonlinearities, it offered an opportunity to test the piston motor driver (see Sect. 5.3) and to experiment with feedback compensation techniques. Thus, insight was gained into the operation of the axial control system before the refrigerator parts were completed.

• Mechanical Data. The side forces which must be overcome by the magnetic bearings are sensed directly by the two X-Y force transducers (27). Similarly, the axial force and the rotational torque component of the current in the motor are sensed by the axial force and torque transducer (28). The motor efficiency is the ratio of the mechanical power produced by the motor to the electrical power supplied to the motor. The power supplied to the

motor can be determined by measuring the input voltage and current. The power produced by the motor can be determined from the output of the LVDT and the axial force transducer. Finally, the operating temperature of the coil can be determined from its change in resistance, since the resistivity of copper is a function of temperature.

• Electrical Data. The force constant is the ratio of the axial force produced by the motor to the current through the coils. The inductance and resistance of the motor can be determined from the magnitude and phase angle of the motor voltage and current. The total power loss can be determined in the same manner as the efficiency, being the difference of the input and output powers instead of the ratio. The ohmic power loss can be estimated knowing the resistance of the motor and the current in it. The remaining power loss is due to eddy currents and hysteresis.

#### 5.2.5 Test Results

##### (1) Piston Motor

Force Constant. The axial force constant was predicted to be 8.8 N/A, using the MAGGY program. The measured value, representing the average of 16 measurements, was  $8.77 \text{ N/A} \pm 0.24 \text{ N/A}$  standard deviation.

Efficiency. Table 5-2 gives the test data from six independent measurements of motor performance. Run No. 4 is the closest to the design operating conditions of 150 N peak force and 7.0 mm peak amplitude. This run indicates a theoretical efficiency of 74% and a measured efficiency of 75%. The other runs show the performance at various off-design points. Agreement between the theoretical and measured values is excellent.

Inductance. The motor inductance predicted by the MAGGY program was 2.2 mH; the measured value was 2.0 mH.

Temperature Rise. The temperature of the motor coil was obtained by measuring its resistance. Measurements showed a temperature rise of about 0.5°C per watt of power dissipation in the coils.

TABLE 5-2. Piston Motor Efficiency.

Run No.	Frequency (Hz)	Peak Motor Force (N)	Peak Displacement (mm)	Peak Motor Current (A)	Peak Motor Voltage (V)	Electrical Input Power (W)	Mechanical Output Power (W)	Measured Efficiency (%)	Theoretical Efficiency (%)
1	25	93	3.63	11.0	7.37	38	27	71	70
2	25	145	2.79	17.0	8.27	61	31	51	56
3	25	108	5.83	12.8	10.8	65	49	75	78
4	25	161	7.42	17.6	14.9	126	94	75	74
5	26.7	187	7.35	20.0	16.4	163	115	71	70
6	26.6	186	7.46	20.3	16.4	163	116	71	71

$$\text{Predicted Efficiency } \eta = \frac{1}{1 + (1.58 \times 10^{-5} \text{ m/N}) (\hat{F}/\hat{Y})}$$

where,  $\hat{F}$  = motor performance (N)

$\hat{Y}$  = peak displacement (m)

Side Forces. The measurements indicated that the static side forces (due to magnetic asymmetries and ignoring weight) were less than 10 N on all axes, and the dynamic side forces (due to coil and/or mechanical asymmetry) were less than 5 N. The magnitudes of these forces agree with the estimates given in Section 4.4.3 for loads on the piston magnetic bearings.

Torque Generation. Although the motor is a linear motor, it will generate some torque due to the same asymmetries responsible for the side forces discussed above. The torque was somewhat difficult to measure, but a conservative upper bound was 5 N-m at 25 Hz. Given the large moment of inertia of the piston assembly, this level of torque would result in a torsional oscillation of only 1° peak rotation.

(2) Displacer Motor

The displacer motor was tested statically to measure the force constant. The predicted value was 5.0 N/A; the measured value was 3.7 N/A. The discrepancy may be due to the Permendure core of the armature approaching saturation, since the design value of the flux density was as high as 2.2 Tesla and saturation is nominally at 2.4 Tesla. This high flux level was necessary because the small diameter of the displacer motor severely limited the motor performance, allowing no margin for conservative design.

5.2.6 Summary

The design procedures described here have resulted in the successful development of linear motors which met all requirements of the current refrigerator program. Analytical and numerical performance-prediction techniques were validated to a high degree of accuracy. Future efforts in the design of linear motors should concentrate on weight reduction and simplification of fabrication techniques. The performance of the displacer motor may be improved substantially by allowing for a larger-diameter armature. The applicability of the larger-diameter motor for such coolers would need to be verified through a thermodynamic analysis.

## 5.3 Axial Control Electronics

### 5.3.1 Description

The electronics which control the axial motion of the piston and displacer via the linear motors comprise an analog feedback servomechanism. In this system, shown in Figure 5-9, the transduced position of the piston and displacer are fed back and compared to a reference signal generated from the phase controller electronics. The resulting error is compensated, amplified, and drives the motors in such a way as to reduce the error. Since the reference for each motor is a sinusoid with the proper phasing, the positions of the piston and displacer will track, with the proper amplitude and phase, to produce cold.

The electronics which make up the axial control system include the frequency controller, the phase controller, two loop compensators, two linear motor current amplifiers, and two LVDT position sensors. The purpose of each is apparent from Figure 5-9.

The frequency controller produces an amplitude and frequency stable sinusoidal reference for the refrigerator. The frequency is adjustable via a

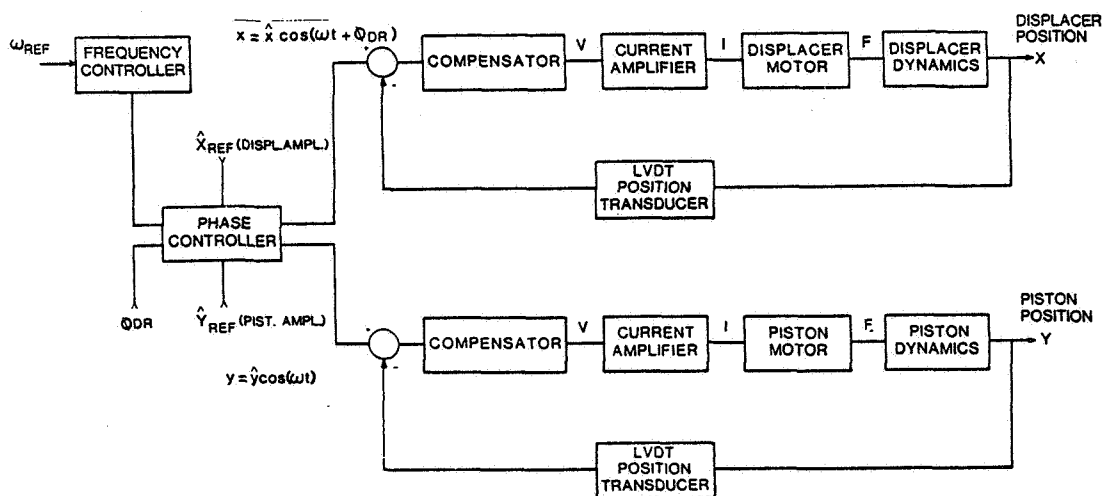


Figure 5-9. Electronic axial control system.

potentiometer on the control panel. Frequency stability is important for maintaining the piston in resonance and for the operation of the passive balancer (see Sect. 7). Amplitude stability is important because the controller provides the amplitude reference for the piston and displacer which typically come within 1 mm of the top of the housings. Finally, the quality of the sinusoidal frequency, i.e., the absence of harmonic distortion, is important because of the nature of the feedback system. The motors will try to track any distortion in their references, consuming unnecessary power and producing housing vibrations at the higher harmonics.

The phase controller uses the frequency reference and produces the reference signals for the displacer and piston motor systems. The amplitude and phase relationship of the individual references are adjusted via control panel potentiometers, and can be changed while the refrigerator is operating. This feature makes the cooler versatile in operation and valuable as a research tool.

The motor drivers were designed to be current amplifiers, meaning that the current in the motor is driven to be in phase with the input voltage to the amplifier. This scheme minimizes the destabilizing phase shift caused by the motor inductance. To properly design the amplifier, the load which the amplifier sees, must be accurately known. Thus, a mechanical to electrical analogy was derived, which describes the motor system as an electrical circuit. Using this, the internal loop compensation of the amplifier was designed.

Some minor changes were made to the LVDT sensor electronics to improve its temperature stability. These involved the addition of a crystal-controlled, amplitude-stable, sinusoidal oscillator.

The position loop compensators were designed to stabilize the control system and to minimize the sensitivity of the system to internal changes in the dynamics. The design of the compensators required an understanding of the remaining loop components: the current drivers, linear motors, mechanical dynamics, and axial position transducers.

In the following sections, the design and testing of the electronic components of the axial control system are explained.



### 5.3.2 Frequency Control Electronics

The frequency controller for the refrigerator is a linear voltage-controlled oscillator (VCO). The VCO was designed around a hybrid tunable quadrature, sinewave oscillator which is commercially available. The operating range of the controller is from 20 to 30 Hz. The operating frequency, which is displayed, is adjusted via a ten-turn potentiometer mounted on the control panel. To improve the amplitude stability of the commercial oscillator, an electronic amplitude control module was incorporated. The control module stabilizes the oscillator output to 10 V p-p  $\pm 0.01\%/^{\circ}\text{C}$ .

The frequency controller can also be bypassed if it is desired to generate operating frequencies outside the range of the controller. An external frequency generator can be connected to an input on the control panel, which becomes the frequency reference for the refrigerator through the operation of an analog switch. In this case, the operating frequency is not displayed.

A block diagram of the frequency controller is shown in Figure 5-10. The analog multipliers are used in a feedback loop to vary the unity-gain

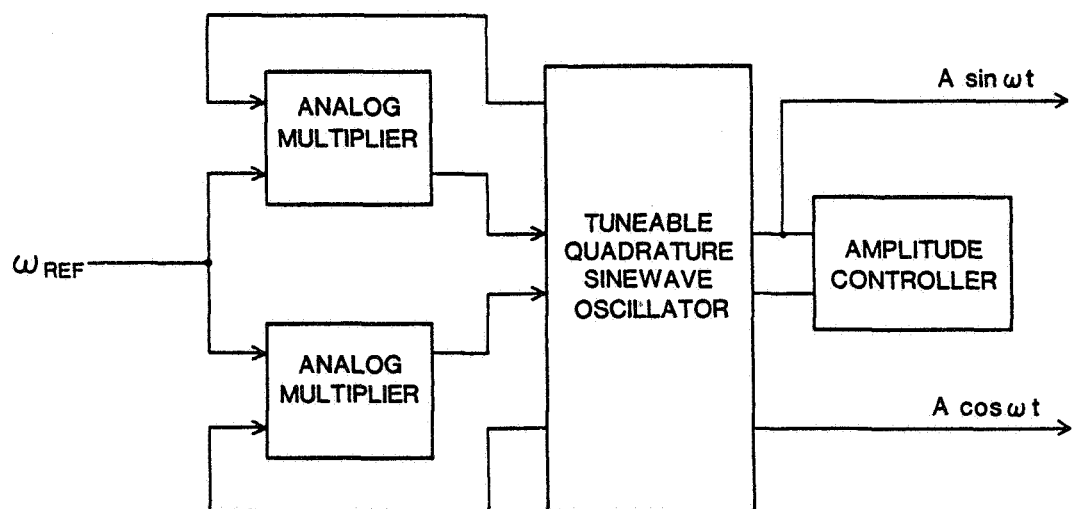


Figure 5-10. Block diagram of frequency controller.

crossover frequency of the internal oscillator integrators as a function of the reference voltage. Thus, as the reference voltage potentiometer is varied, the crossover frequency of the open loop gain of the oscillator changes. Since the crossover frequency corresponds to the oscillator running frequency, a linear control of the frequency is achieved.

Table 5-3 is a summary of the measured oscillator frequency and the frequency displayed on the control panel. Harmonic distortion measurements of both the sine and cosine outputs were taken. (Data for the cosine signal, which is used as the cooler reference, is shown in Figure 5-11.) The total harmonic distortion of the controller is less than 0.2% for the sine output and 0.1% for the cosine output.

TABLE 5-3. Controller Frequency - Measured vs. Displayed.

<u>Frequency (Hz) (Displayed)</u>	<u>Frequency (Hz) (Cosine)</u>	<u>Frequency (Hz) (Sine)</u>
21.00	21.028	21.029
22.00	22.026	22.027
23.00	23.016	23.016
24.00	24.010	24.010
25.00	25.008	25.008
26.00	25.997	25.998
27.00	26.996	26.995
28.00	27.990	27.989
29.00	28.976	28.977

---

Test equipment - HP DVM 3466A  
 HP Universal Counter 5335A  
 Dannetz Gain/Phase 305PA3009A

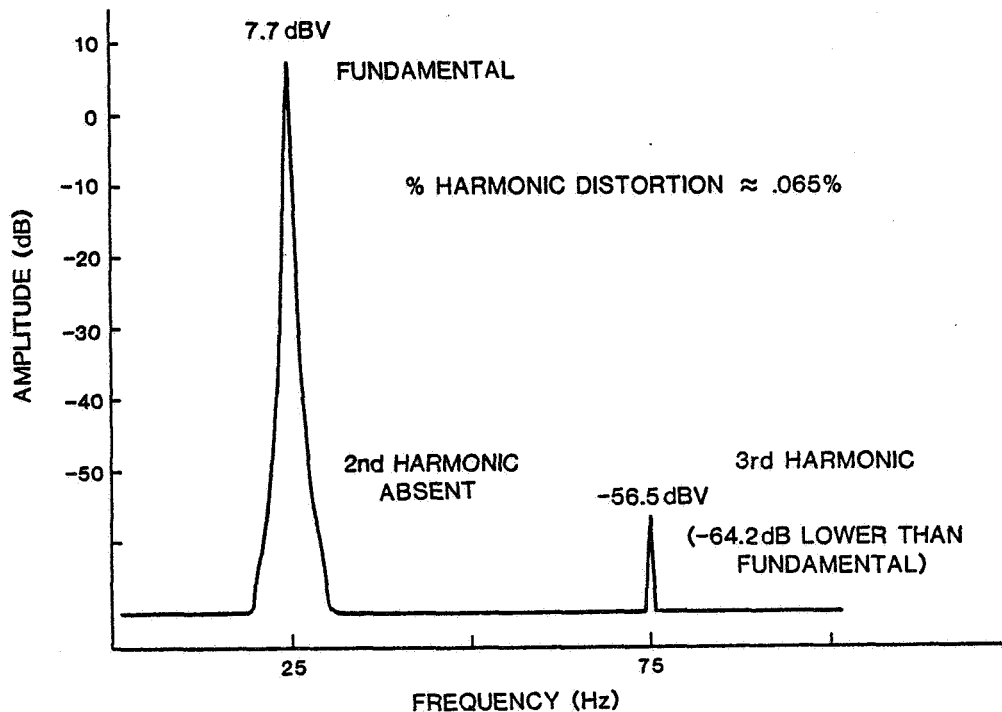


Figure 5-11. Harmonic distortion of cosine output of frequency controller.

### 5.3.3 Phase Control Electronics

Since there is independent control of the axial positions of the piston and displacer, the refrigerator thermodynamics can be perturbed by varying the amplitude of each or the phase relationship between the two. An active phase controller was designed with the capability of adjusting the phase between the piston and displacer positions from + 50° to + 90° with an accuracy of better than 0.5° over the operating frequency range of 20 to 30 Hz. The controller also incorporates the electronics required to change the amplitude of the piston and displacer motions.

A block diagram of the phase controller is shown in Figure 5-12. The reference signal from the frequency controller is simultaneously applied to one input of a multiplier and to a controlled phase shifter. The output of the phase shifter is applied to the other multiplier input. The output product of the multiplier is thus proportional to the sine of the phase angle between the two inputs. This signal is compared to the phase reference voltage ( $\phi_{\text{ref}}$ ) which is adjusted via a potentiometer on the control panel. The resulting error adjusts the phase of the phase shifter so as to reduce the error. An amplifier ( $A_3$ ) and loop compensation is provided for closed loop stability. The phase is displayed on the control panel.

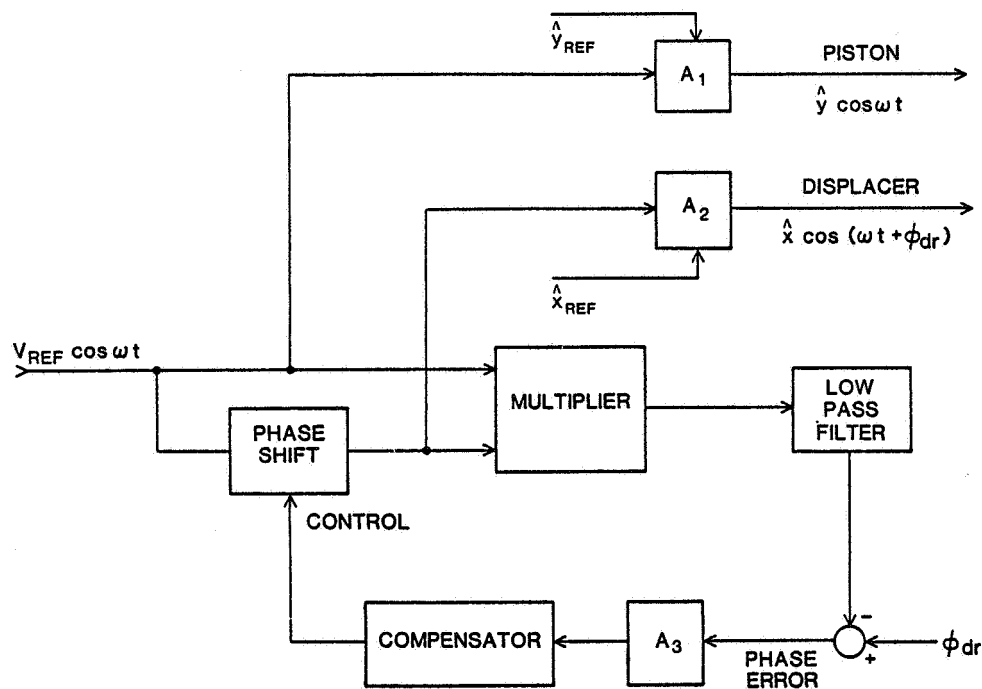


Figure 5-12. Block diagram of the phase controller.

The signal from the frequency controller is used as the reference for the piston system. The gain of amplifier  $A_1$  is adjusted via a control panel potentiometer and determines the amplitude of the piston motion. In a similar manner, the output of the phase shifter determines the reference for the displacer motion using amplifier  $A_2$ . Thus, by controlling the three reference voltages,  $\hat{y}_{\text{ref}}$ ,  $\hat{x}_{\text{ref}}$ , and  $\phi_{\text{ref}}$ , different operating conditions can be achieved.

### 5.3.4 Motor Driver

The piston and displacer motor drivers are linear amplifiers with a deliverable power capability in excess of 300 W rms. The amplifiers were designed in a bridged output configuration in order to effectively increase the applied motor voltage capability above the 28 V power supply. This additional voltage "headroom" compensates for motor parameters which change as a function of operating frequency. The disadvantage of the bridge configuration is that the load is in effect "floating" above ground, which makes closed-loop current control difficult. Further, the maximum efficiency of the amplifier is reduced by a factor of two because of the additional power transistor in series with the load.

Figure 5-13 is a block diagram of the motor driver, the electronics for which comprise two closed loops. The inner loop, which has  $V'$  as an

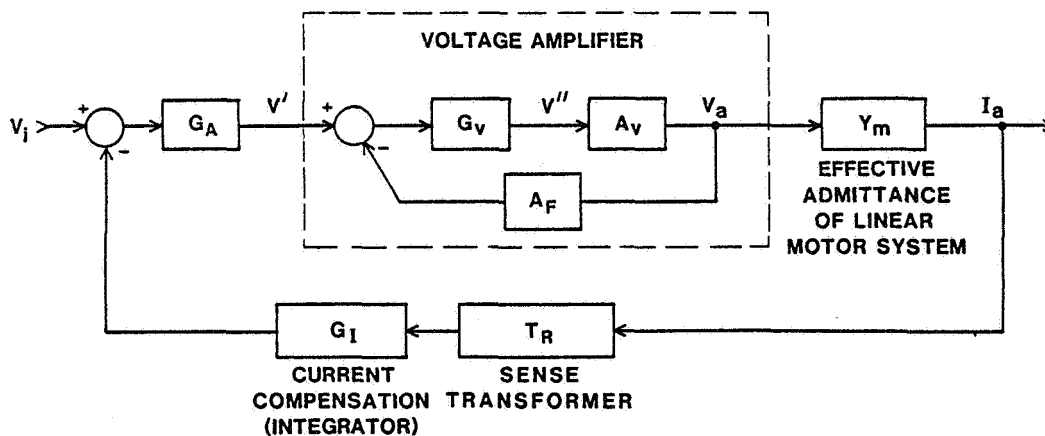


Figure 5-13. Block diagram of motor current amplifier.

input and  $V_a$  as an output, is a voltage amplifier. Voltage feedback is used to increase the amplifier bandwidth and to desensitize the amplifier gain to parametric changes in the electronic components. In the bridge configuration, the differential voltage feedback further serves to balance the bridge output. In the block diagram,  $A_V$  represents the open loop gain of the amplifier,  $G_V$ , the voltage loop compensation (lead network), and  $A_F$ , the differential operational amplifier which comprises the feedback path.

In Figure 5-13, the outer loop performs the closed loop current control.

The current is sensed via a ferrite core transformer ( $T_R$ ) which is in series with the motor windings. The secondary output voltage of this transformer is integrated to produce a voltage proportional to the ac current. Thus, the motor armature current is transduced with a minimal amount of power loss.

In order to design the current loop compensation ( $G_A$ ), the effective motor impedances ( $1/Y_m$ ), a function of the motor load, are required. To estimate these impedances, the equivalent circuits for the piston and displacer motor systems, linear approximations of the refrigerator dynamics at the operating point, are derived. This mechanical/electrical analog is simplified by assuming that the linear motor can be modeled as an ideal transformer. This means that: the mechanical force is modeled as a current; velocity is modeled as a voltage; mass as a capacitor; a spring as an inductor; and a mechanical damper as a resistor. That the motor is correctly modeled as a transformer is realized by recalling that the back emf voltage =  $B \cdot l \cdot \text{velocity}$  and the motor force =  $B \cdot l \cdot \text{current}$  (see Fig. 5-14) where  $B \cdot l = K$  is called the motor constant.

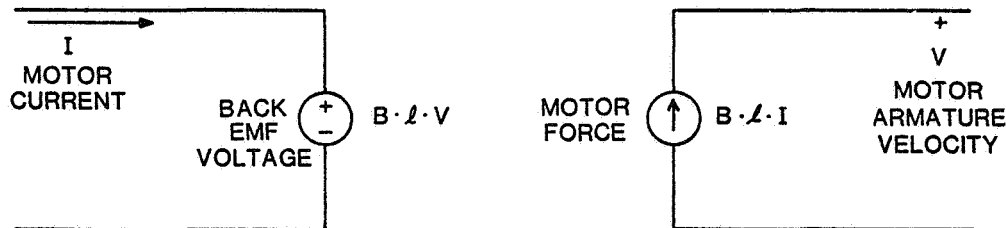


Figure 5-14. Transformer equivalent model of linear motor.

The derivation of the equivalent impedance of the piston system is shown in Figure 5-15. In the electrical portion, the source resistance of the amplifier is modeled as resistor  $R_s$ . The lumped motor armature resistance and inductance is represented by  $R_{pc}$  and  $L_{pc}$ , respectively. In the mechanical portion is the damped spring mass system. The motor operates at or near mechanical resonance (power factor of 1). This is achieved as a result of the balance between the inertial force of the piston mass and the spring force of the gas. Therefore, the reflected inductance and capacitance of the load using the motor-transformer analogy is also in resonance and has an infinite impedance. The mechanical damper, when reflected into

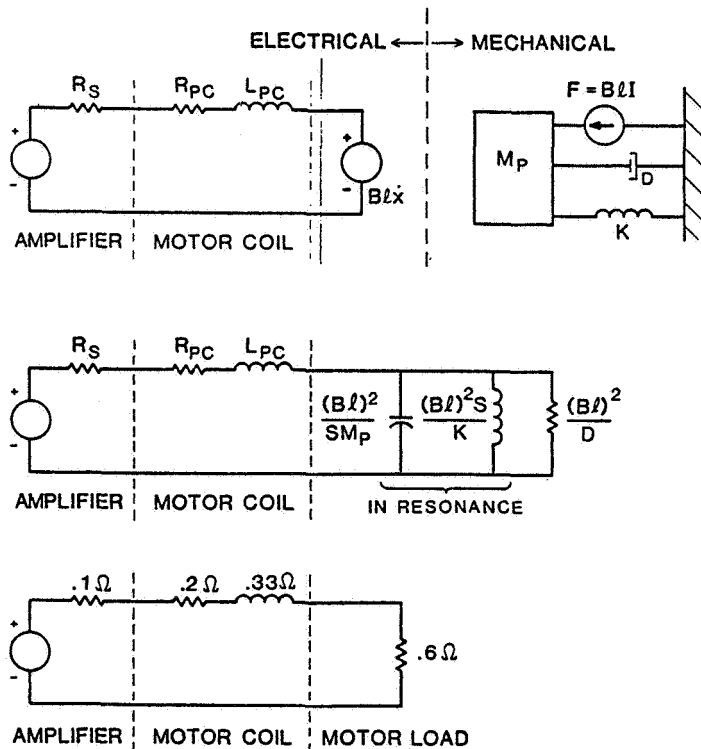


Figure 5-15. Effective impedance of piston system.

the primary, represents the total dynamic load which is in series with the piston motor coil. The third circuit in Figure 5-15 is thus the simplified impedance of the piston system.

Since the displacer assembly was not designed to operate in resonance (there is no spring), the effective impedance at the operating point is a function of the displacer mass and the flow losses in the regenerator (see Fig. 5-16). The dynamic load of the displacer is primarily reactive, and the net power delivered to the thermodynamics (excluding ohmic losses) is very small, on the order of a few watts. The effect of the mass is also small, and thus the equivalent circuit of the displacer motor is effectively equal to, simply, the motor coil impedance.

With the equivalent circuits of the piston and displacer motors defined, the current loop compensation and the peak currents and voltages required at the operating point are determined. Once the output requirements were defined, the amplifier input stages were designed to meet operating drive requirements of the output stage. For both drivers a peak current of 25 amps at the operating frequency was achieved with less than 1% sensitivity to internal component variations. The full power bandwidth of both current drivers was designed to be greater than 1.5 kHz.

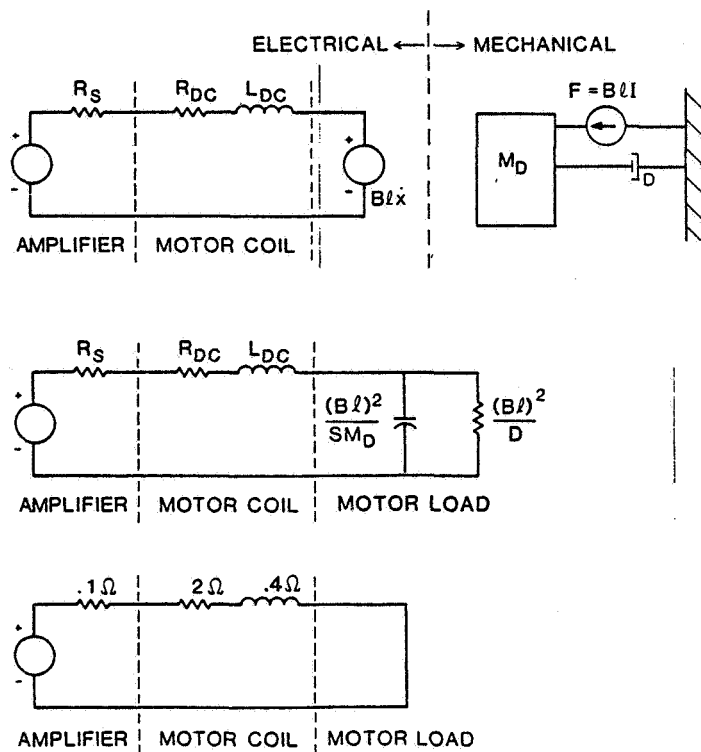


Figure 5-16. Effective displacer system impedance.

### 5.3.5 Axial Position Transducers

The LVDT position transducer used in the axial control loops are a modified version of a commercially available transducer. The LVDT produces an electrical output proportional to the displacement of a non-contacting magnetic core. It is basically a differential transformer whose primary coil and two secondary coils, connected in series, are symmetrically spaced on a cylindrical form (Fig. 5-17). When the primary coil at the center of the LVDT is excited by an ac source, voltages are induced in the two secondary coils. The motion of the core varies the mutual inductance of each secondary to the primary. If the core is centered between the secondary windings, the voltage induced in each secondary is identical and  $180^\circ$  out of phase, so that the net output of the transducer is zero. If the core is moved off center, the induced voltage in the secondary coil that it moves toward increases, while the induced voltage in the opposite coil decreases. This provides a differential voltage output that varies linearly over a limited range, with changes in core position.

In addition to the ac excitation of the primary, synchronous demodulation of the output is needed to extract the direction and amplitude information.



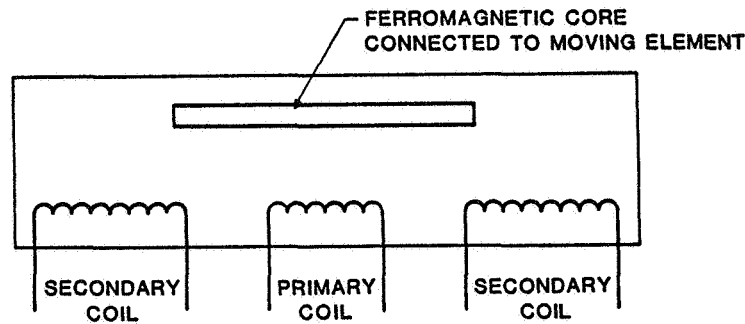


Figure 5-17. Schematic of LVDT.

This demodulated output is a rectified ac signal which after filtering will be a representation of the exact position of the core with respect to the zero position.

A temperature-stable 10 kHz oscillator and amplitude controller was incorporated into the existing transducer electronics in order to improve position accuracy and the operating temperature range. The output stage of the transducer electronics incorporates a 4 pole, 1 kHz low-pass filter to attenuate the excitation frequency, thus limiting the sensed modulation frequency to only a few hundred Hertz. This means that the bandwidth of the control loop is constrained to be in the hundred hertz range.

#### 5.3.6 Position Control Compensation

A general block diagram of the piston and displacer axial-control loops is shown in Figure 5-18. The gain and frequency response of the position transducers, motor drivers, and system dynamics are defined. The compensator is designed to optimize the position loop response. The two major objectives for the control loop is to minimize the sensitivity of the system to internal changes in the dynamics and to achieve a phase margin of at least 40° for stability. The final piston and displacer control loops resulted in less than 10% sensitivity to system changes at the operating frequency and a phase margin of 50° with bandwidths of 65 Hz and 105 Hz, respectively.

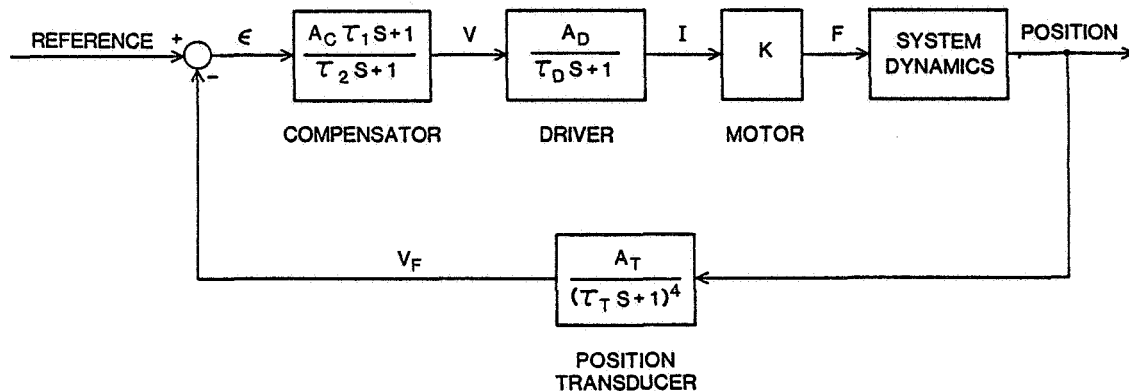


Figure 5-18. General block diagram of piston and displacer axial control loop.

The frequency response of the piston motor system, i.e., the transfer function with current ( $I$ ) as an input and the transduced position ( $V_F$ ) as an output, is shown in Figure 5-19. Note that, as discussed, the system displays a resonant behavior at 26.7 Hz. The relatively fast rolloff of gain at 1 kHz results from the filtering of the LVDT carrier.

A similar plot for the displacer motor is shown in Figure 5-20. It should be noted that the transfer function resembles a typical servomechanism response. The absence of a mechanical spring means that no resonance exists.

The compensators for the piston and displacer systems are lead-lag networks, as represented by the block in Figure 5-18. The parametric values are given in Table 5-4.

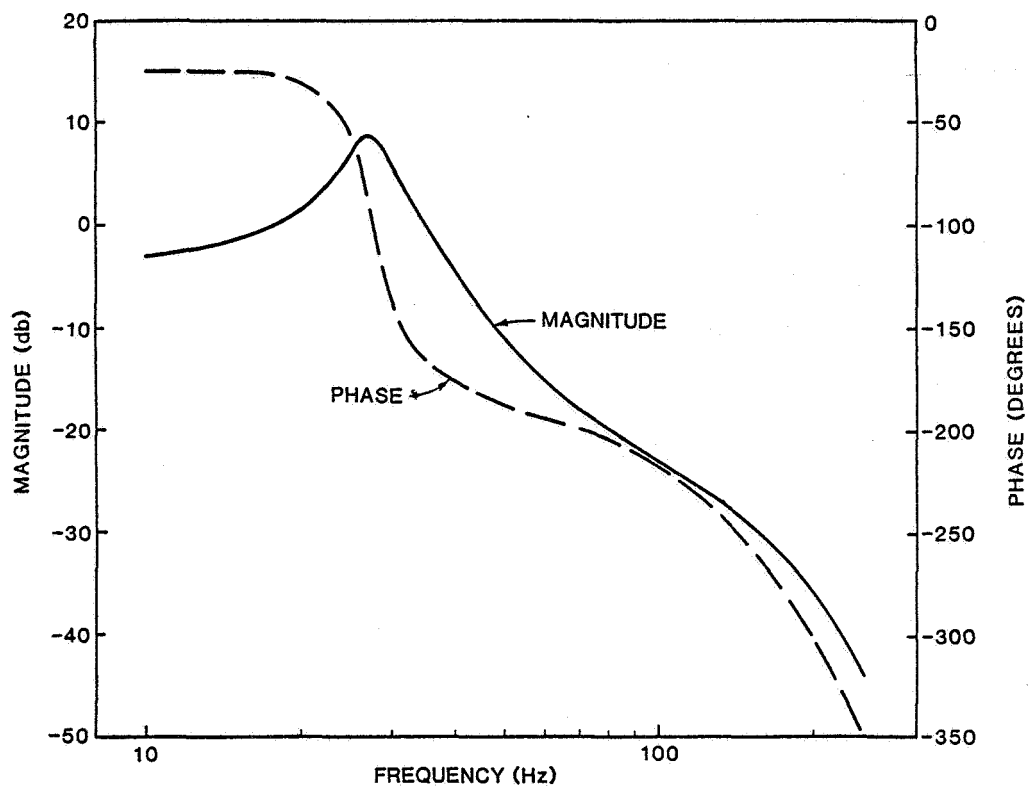


Figure 5-19. Frequency response of piston dynamics.

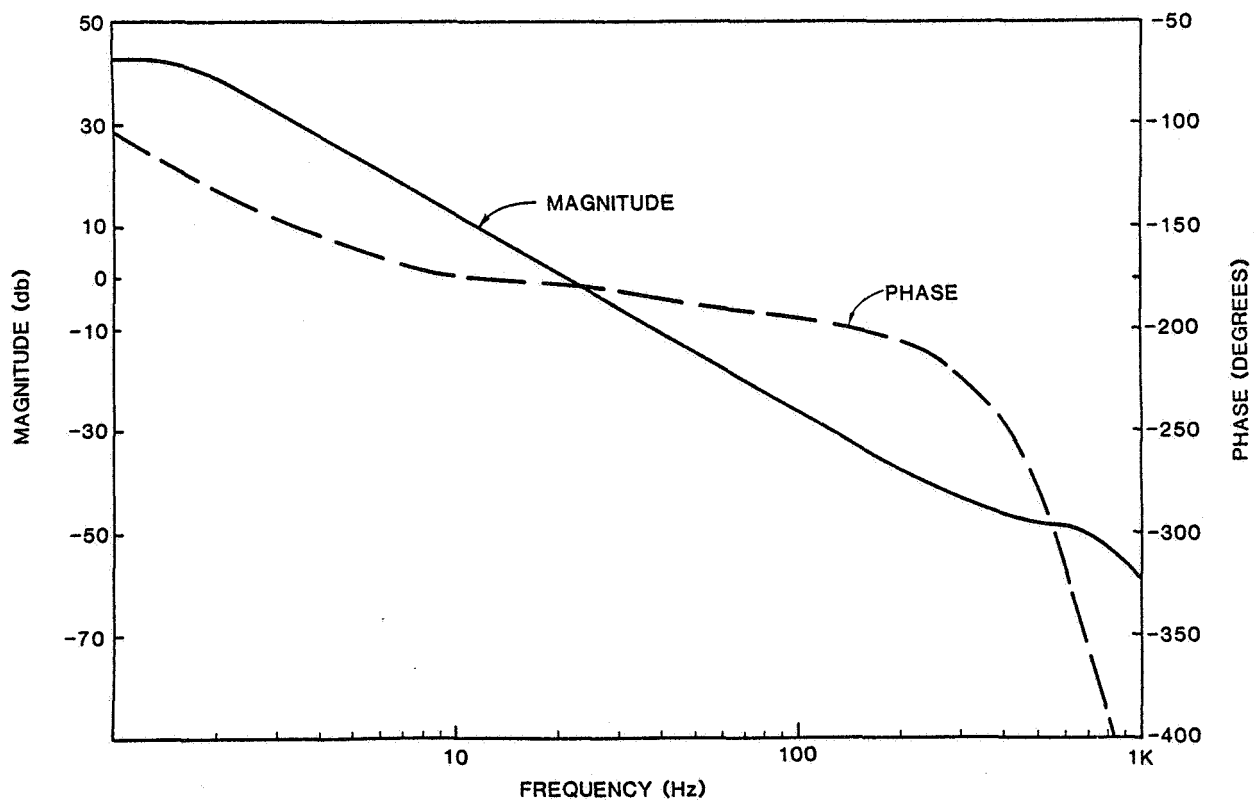


Figure 5-20. Frequency response of displacer dynamics.

TABLE 5-4. Parametric Values of Piston and Displacer Compensators.

<u>Parameter</u>	<u>Notation</u>	<u>Value</u>
Piston:		
Compensator Gain	$A_C$	1.66
Compensator Zero	$\tau_1$	$8.2 \times 10^{-3} \text{ s}$
Compensator Pole	$\tau_2$	$8.3 \times 10^{-4} \text{ s}$
Driver Gain	$A_D$	3.2 A/V
Driver Pole	$\tau_D$	$1 \times 10^{-4} \text{ s}$
Displacer:		
Compensator Gain	$A_C$	5.04
Compensator Zero	$\tau_1$	$4.9 \times 10^{-3} \text{ s}$
Compensator Pole	$\tau_2$	$3.4 \times 10^{-4} \text{ s}$
Driver Gain	$A_D$	3.5 A/V
Driver Pole	$\tau_D$	$9 \times 10^{-5} \text{ s}$

#### 5.3.7 Summary

The electronics worked well in controlling the axial motion of the piston and displacer. A high degree of accuracy was obtained in the axial position, and the control was stable to outside disturbances. With the inclusion of the frequency controller and phase controller, the electronic system is self-contained. No additional laboratory equipment is required to operate the refrigerator.

Future plans in the area of axial control will involve the design of a high efficiency switching driver and efforts to increase the bandwidth of the control system.

#### 5.4 Conclusions

The development of the linear motors and axial control electronics underlines the synergistic approach taken in the design of the refrigerator. The simplification of the drive mechanism, the low number of mechanical parts, the versatility of being able to change operating parameters during operation, and the accuracy of the analog servomechanism were achieved as a result of the union between the motors and electronics of the rectilinear drive.

## 6. ELECTRONICS

This section describes the electronics for the safety interlock system, closed loop controller for the cold-finger heater load, battery backup, and pressure transducer amplifiers. In addition, the layouts of the control panel and card cages of the instrument rack are described.

### 6.1 Interlock System

The interlock system is a set of electronics which monitors the operation of the refrigerator and can safely turn off the unit if one of the monitored parameters exceeds its normal operating range. The interlock does not attempt to decide whether an out of range indication (ORI) is real or due to spurious noise, and does not attempt to restart the machine in the event of an error. Since the Engineering Model was designed to be a laboratory prototype, this simple approach was deemed adequate. It is reliable in that it will always indicate a real ORI, even though it is prone to false trips.

The interlock system for the refrigerator has been an ongoing development effort. The changes to the original design resulted from subassembly and parametric testing of the refrigerator components and from testing of the overall system. Some of these modifications were implemented after system failures had occurred. Of these, the most significant failure was the reciprocation of the piston and displacer without the activation of the magnetic bearing suspension. This failure was attributed to a sequence of errors, operator as well as electronic, that rendered the protection system inoperative. Corrective action was taken to prevent similar failures from recurring as well as to establish guidelines for a more sophisticated, second-generation interlock system.

The present interlock is comprised of four circuit boards located in card cage #1 of the instrument rack. Three of the four boards are called interlock/multiplexer boards; the fourth board is called the interlock controller board.

Each interlock/multiplexer board has a 10 channel monitoring capability with each channel scanned every 500  $\mu$ s. In addition to multiplexing the input signals, the reference for each channel is also multiplexed, simultaneous-

ly. The signals are then compared to determine whether an out-of-range input has occurred. If an ORI is detected, the clock is disabled, and a digital "interlock" interrupt signal is output. Table 6-1 shows the board and channel number corresponding to each of the signals monitored during operation of the refrigerator. The interlock multiplexer boards were arbitrarily designated as Boards Number 1, 2 and 3, according to their position in the card cage. Boards #1 and #2 monitor primarily displacer and piston related signals, respectively. These include the radial position of each shaft, the housing temperature, mean pressure, and the oscillator used for the radial position sensors. In addition, the unit is shutdown if the power supply voltage drops below 21 V (temporary power is supplied by a battery backup, see Sect. 6.3). If a total power shutdown should occur, a 5 minute time delay prevents restarting of the refrigerator after power is restored. This allows the electronics time to stabilize. Board #3 monitors

TABLE 6-1. Interlock System Channel Assignment.

<u>Channel No.</u>	<u>Board No. 1 (Displacer)</u>	<u>Board No. 2 (Piston)</u>	<u>Board No. 3</u>
0	Front vertical bearing position	Front vertical bearing position	-
1	Front horizontal bearing position	Front horizontal bearing position	Displacer LVDT
2	Rear vertical bearing position	Rear vertical bearing position	Displacer control-loop position error
3	Rear horizontal bearing position	Rear horizontal bearing position	-
4	Radial position sensor oscillators	Radial position sensor oscillators	-
5	Operator manual shutoff	-	-
6	Housing temperature	Housing temperature	Piston LVDT
7	-	Average charge pressure (low limit)	Piston control-loop position error.
8	Cooling-jacket flow switch	-	-
9	AC source interruption/power supply shutdown or failure	Startup time delay	-

both the LVDT and the axial control-loop position error for the displacer and piston.

The interlock controller board has two modes of operation (ON, STANDBY) which are key switch selectable from the control panel. In the "ON" mode, the controller uses a priority decoder to select the refrigerator shutdown procedure (a function of the board that detected the ORI). The controller then latches the board and channel number of the ORI and displays them on the control panel. The shutdown procedures of the controller are as follows:

- If a Board #1 or #2 ORI is detected, the piston and displacer shafts are servoed to their respective axial center positions.
- If a Board #3 ORI is detected, either of the following occurs:
  - If a displacer LVDT overstroke or control-loop position error is detected, the displacer motor amplifier will be disconnected and the displacer motor leads will be shorted together. The piston motor will be servoed to its center position.
  - If a piston LVDT overstroke or control-loop position error is detected, the piston motor amplifier will be disconnected and the piston motor leads will be shorted together. The displacer motor will be servoed to its center position.

The "ON" mode is the normal mode of operation for the refrigerator. Servoing the motors to center is the quickest, safest, shutdown procedure, and it is only avoided when the ORI indicates a problem with the axial control. In that event, shorting the motor leads provides dynamic braking, but results in a longer time for the shafts to stop.

After an ORI has been detected and the corresponding shutdown performed, the interlock system can be reset by simultaneous depression of the two front-panel momentary "RESET" switches (see Fig. 6-1). The interlock controller, however, will not reset if an additional ORI is detected and will reset only after all ORI's have been corrected. In addition, during refrigerator operation, the piston and displacer motors can be servoed to their respective center positions by simultaneously depressing the "SINGLE STEP" momentary switch and the right-side "RESET" switch on the control panel (operator manual shutoff in Table 6-1).

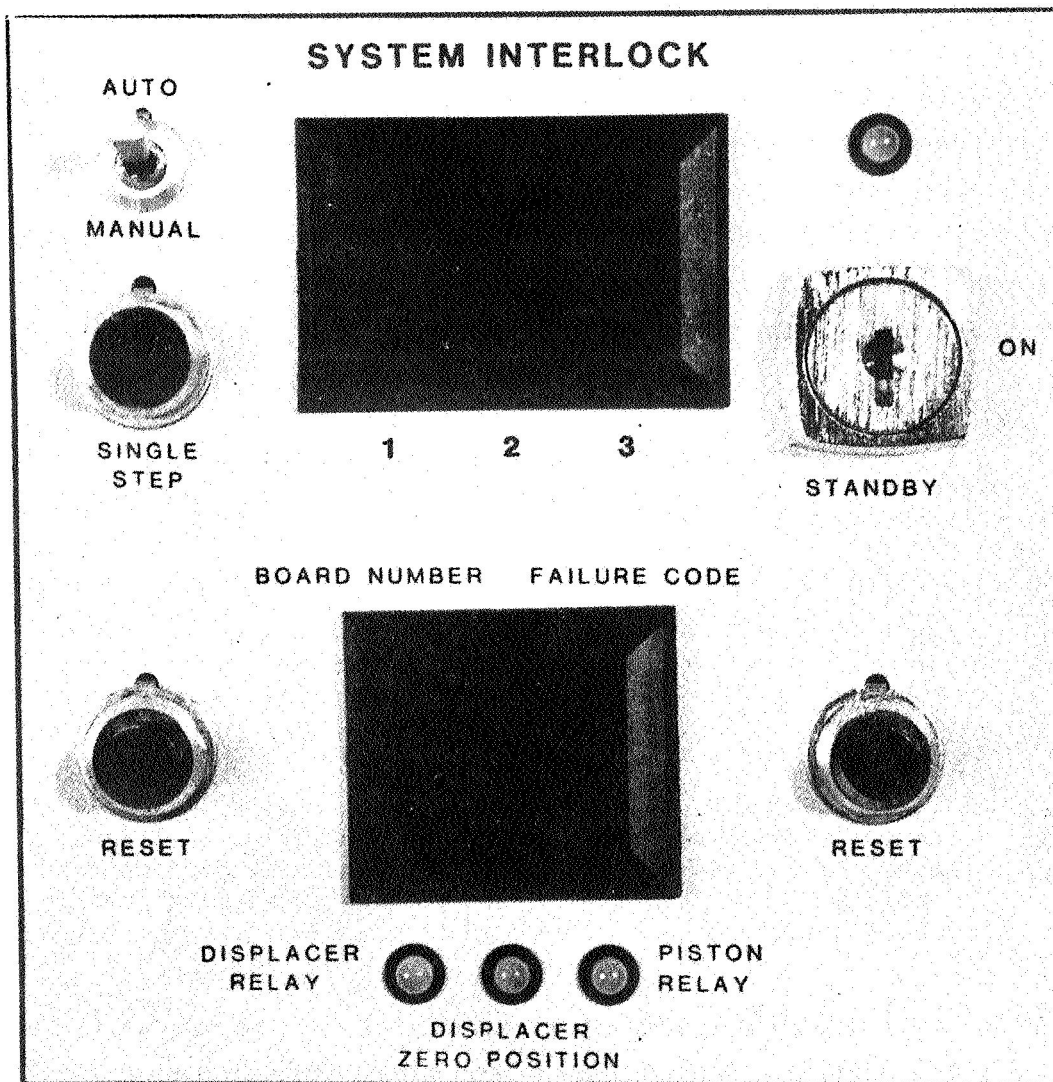


Figure 6-1. System interlock control panel.

In the "STANDBY" mode, only the piston and displacer radial position signals and oscillators are monitored. If an ORI is detected, the corresponding linear motor amplifier is disconnected and the motor leads shorted together. In addition, the controller automatically loads potential ORI's from the three interlock/multiplexer boards into a serial memory for display on the control panel. The display can be scanned manually or automatically and can be reloaded by depressing both front panel reset switches (which also resets the controller if no ORI's are detected). This mode is useful for debugging since it allows all ORI's in the monitored signals to be displayed. It is never used to operate the machine.



## 6.2 Heater (Load) Control

To simulate a heat load on the refrigerator, a wire-wound resistive heating element was mechanically secured on top of the cold finger assembly. Since the resistance of the heating element varies as function of temperature, a closed-loop heater controller is required to maintain a constant power dissipation on the cold finger, independent of resistance changes in the element.

The power range of the heater controller can be adjusted from 0 to 10 W with an accuracy at the nominal 5 W load of better than 0.1%. The controller uses a four-wire interconnecting cable (2 power leads, 2 sense leads) to eliminate the effects of extremely long lead lengths ( $> 20$  ft) on the accuracy. The power dissipated in the heating element is set by a ten-turn potentiometer on the control panel and displayed on a panel meter. Since the load to the cold finger is required only when the unit is producing cold, safety interlocks were incorporated into the electronics to prevent potential damage to the cold finger from high temperatures. The 28 V supply, in addition to being fused on the board, is routed through a power relay so that the heater controller can be quickly disconnected from the system power. The controller is disabled if the cold temperature exceeds  $120^{\circ}\text{K}$  or if either the piston or displacer driver output relay is disengaged (indicating that the motors are not operating).

A block diagram of the heater controller is shown in Figure 6-2. An analog multiplier, in the feedback path, senses the power dissipated in the heating element. The current through the heater is measured with a 5 ohm sampling resistor. The voltage across the heater is measured differentially and attenuated to be within the operating limits of the multiplier. The output of the multiplier is filtered, amplified, and then compared to the reference set point, the difference being the control loop error. In the forward path, a differential amplifier with a gain of 100 is followed by a voltage power amplifier with a gain of 500; the result is an open-loop gain of 94 dB with dominant poles at 0.15 Hz and 6 kHz. A high dc open-loop gain, which reduces control loop errors, is easily achieved. The controller does not need a high-frequency response, since the thermal time constant of the cold finger is longer than 1 minute. From a control system

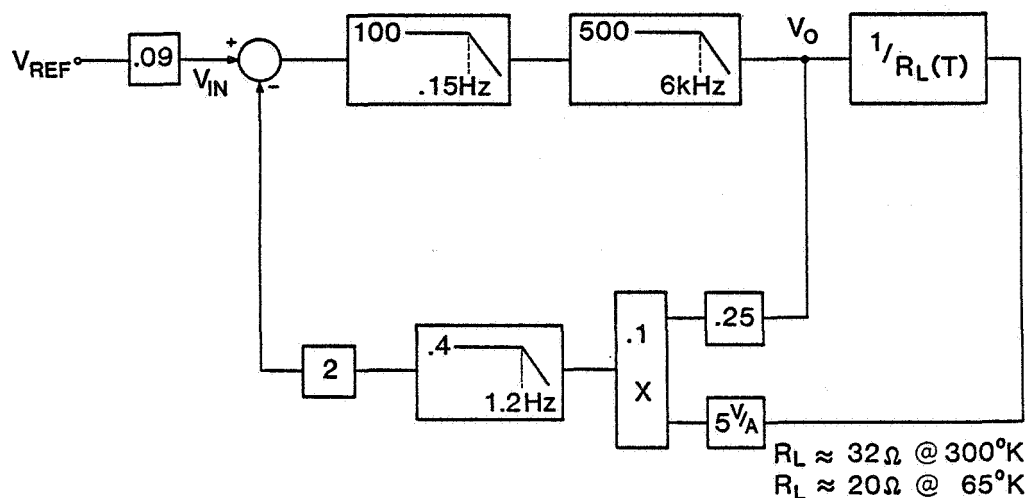


Figure 6-2. Block diagram of heater controller.

analysis, the minimum control loop error for the heater controller, neglecting multiplier nonlinearities, is defined as:

$$\% e_{p_{\min}} = \left[ v_{in} - \frac{v_o + \frac{4980}{R_L} v_o^2}{5 \times 10^4} \right] \times 100$$

Tests were performed on the controller to determine the overall accuracy within the 0 to 10 W range. Table 6-2 shows the percent error at each power setting between the actual power dissipated in the heating element and the power reference which is displayed.

TABLE 6-2. Measurement of Accuracy of Heater Controller.

Indicated Power (Watts)	Actual Power (Watts)	% Error
1.00	1.04	4.0
2.00	2.04	2.0
3.00	3.03	1.0
4.00	4.01	0.3
5.00	5.00	0.03
6.00	5.98	0.3
7.00	6.96	0.6
8.00	7.95	0.6
9.00	8.93	0.8
10.00	9.91	0.9

### 6.3 Battery Backup

The power for the refrigerator electronics, magnetic bearings, and motor is supplied by a three-phase, ac input, scr power supply. In the event of an ac power interruption or supply failure during operation of the refrigerator, a battery backup is provided to temporarily supply power to maintain the magnetic suspension until the refrigerator is safely shut down. This safety feature prevents the reciprocating shafts (moving due to inertia) from radially contacting the housing.

The battery backup consists of eighteen 2 V, 25 ampere-hour, sealed, lead-acid, rechargeable cells. These cells, connected in series, form a 36 V 25 ampere-hour battery. In this configuration eighteen voltages are available to supply either control or system power. The system uses five voltages, four for control circuitry (2, 6, 24 and 34 V) and one for refrigerator power (28 V). When the battery backup system is on line, power is supplied to the refrigerator for about 10 minutes before it is automatically disconnected. During this time the refrigerator interlock detects the switch-over and commands the piston and displacer shafts to the center (see Sect. 6.1). This procedure guarantees a safe shutdown of the refrigerator while minimizing excessive battery drain. High power MOSFETS are used to switch-in the battery backup within 80  $\mu$ s after a power failure has been detected.

### 6.4 Pressure Transducer Amplifier

The pressure transducers measure the static and dynamic pressures in the buffer and compression spaces of the refrigerator. Two transducers are located in the compression area for redundancy and verification of sensitivity calibration under dynamic conditions. A third transducer monitors the average pressure in the buffer space (to the rear of the piston).

The transducer amplifiers are differential voltage amplifiers. The pressure sensitivity of each transducer/amplifier system is adjusted to 1.00 mV/psi. These signals are buffered and monitored via control panel BNC connectors. The buffer pressure signal, displayed on a panel meter, is used in the interlock system to verify that the refrigerator charge pressure is within operating limits.

## 6.5 Instrument Rack Assembly

### 6.5.1 Description

The refrigerator instrument rack assembly (see Fig. 6-3) is comprised of ten subassemblies:

- Piston Amplifier
- Displacer Amplifier
- Card Cage #2
- Card Cage #1
- Control Panel
- Service Panel
- Cooling Fan
- 2.4 kW DC Power Supply
- Battery Backup
- Cryogenic Thermometer Controller

The board locations in Card Cages #1 and #2 are shown in Tables 6-3 and 6-4, respectively.

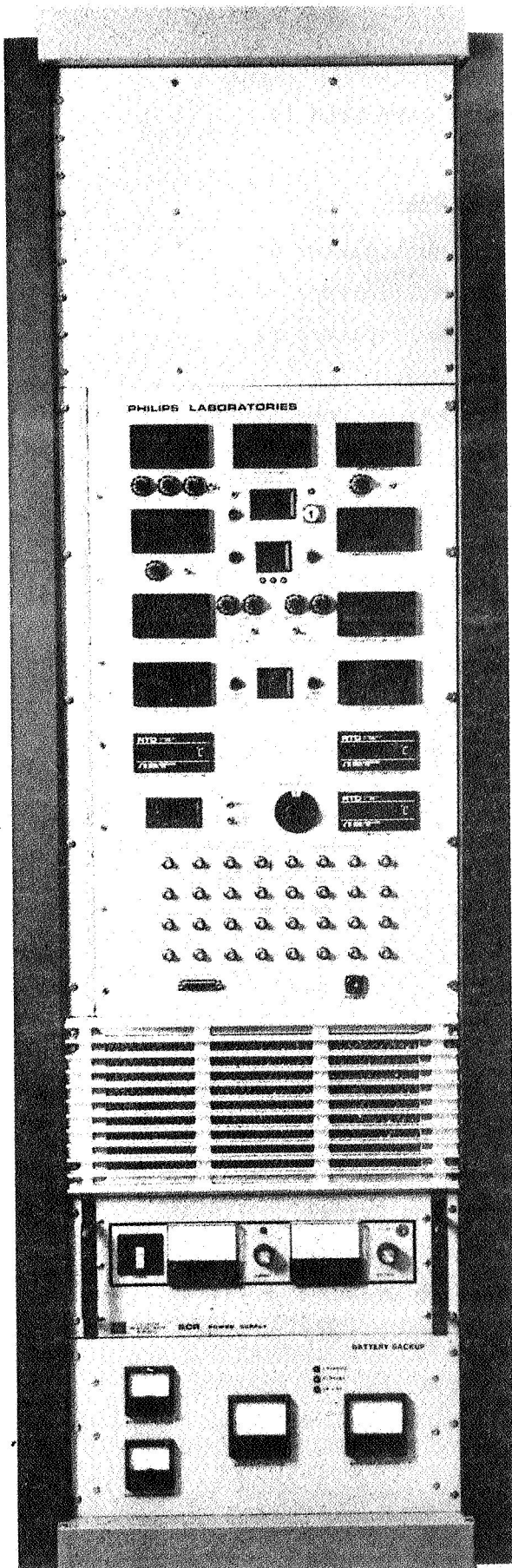


Figure 6-3. Photograph of Instrument Rack.

TABLE 6-3. Board Locations of Card Cage #1.

<u>Board Location</u>	<u>Board</u>
1	Interlock Multiplexer #1
2	Interlock Multiplexer #2
3	Interlock Multiplexer #3
4	Interlock Controller
5	Piston/Displacer Compensator
6	10 Channel Multiplexer
7	10 Channel Multiplexer
8	Piston/Displacer Phase Controller
9	Frequency/Amplitude Controller
10	Cold Finger Heater Controller
11	+ 5 V/+ 12 V dc/dc Converter
12	(Not available for use)
13	<u>+ 15 V</u> dc/dc Converter

TABLE 6-4. Board Locations of Card Cage #2.

<u>Board Location</u>	<u>Board</u>
1	Front Vert. Bearing Driver - Displacer
2	Front Horiz. Bearing Driver - Displacer
3	Rear Vert. Bearing Driver - Displacer
4	Rear Horiz. Bearing Driver - Displacer
5	Front Vert. Bearing Driver - Piston
6	Front Horiz. Bearing Driver - Piston
7	Rear Vert. Bearing Driver - Piston
8	Rear Horiz. Bearing Driver - Piston
9	-
10	-
11	-
12	-
13	<u>+ 15 V</u> dc/dc Converter

### 6.5.2 Control Panel

The major controls, connectors, displays, and indicators for operating the refrigerator are located on the control panel of the instrument rack. The following is a brief description of the panel shown in Figure 6-4.

	<u>Control</u>	<u>Description</u>
1	FREQUENCY DISPLAY	Displays operating frequency of refrigerator (Hz).
2	SYSTEM POWER DISPLAY	Not operational.
3	RELATIVE PHASE DISPLAY	Displays relative phase between displacer and piston (see 9).
4	FREQUENCY POTENTIOMETER	Sets operating frequency of refrigerator in manual mode (20 to 30 Hz range).
5	AMPLITUDE POTENTIOMETER	Not operational.
6	OFFSET POTENTIOMETER	Offsets center position of piston stroke with respect to compression space center position.
7	OFFSET SWITCH	Enables/disables offset potentiometer control.
8	PHASE POTENTIOMETER	Sets relative phase between displacer and piston (50° to 90° range).
9	PHASE DISPLAY SELECT SWITCH	<u>Center position</u> : displays relative phase between displacer and piston (from LVDT signals). <u>Up position</u> : displays phase between displacer and piston reference signals. <u>Down position</u> : displays relative phase between piston current and position.
10	HEATER POWER DISPLAY	Displays power dissipated by heater on cold finger (Watts).
11	COMPRESSION PRESSURE DISPLAY	Displays mean charge pressure of refrigerator (psi).
12	HEATER POTENTIOMETER	Sets power dissipated by heater on cold finger (0 W to 10 W range).
13	HEATER SWITCH	Enables/disables heater during refrigerator operation.

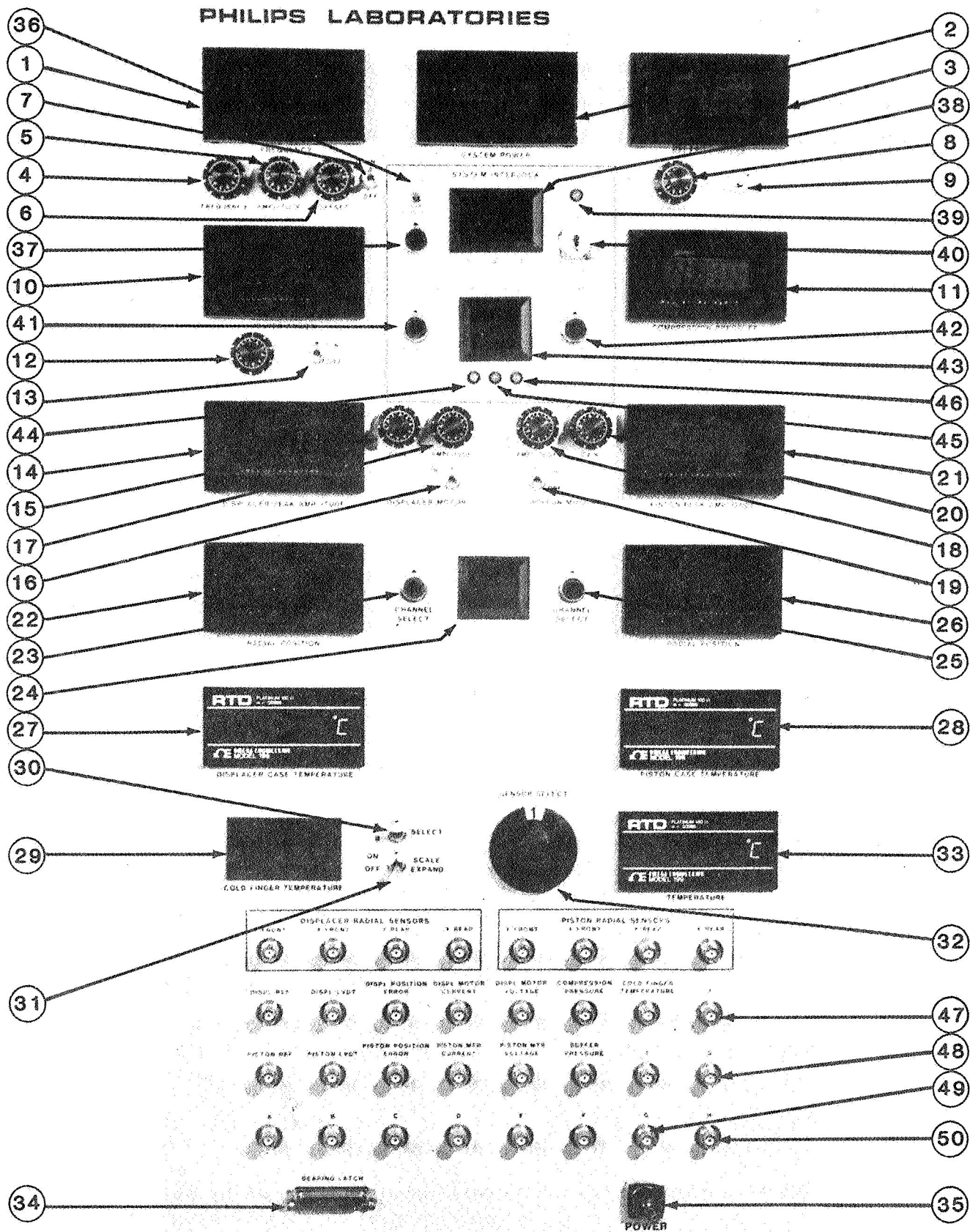


Figure 6-4. Control panel of Instrument Rack.



	<u>Control</u>	<u>Description</u>
14	DISPLACER PEAK AMPLITUDE	Displays displacer peak axial amplitude during refrigerator operation (mm).
15	DISPLACER GAIN POTENTIOMETER	Attenuates gain of displacer axial-control loop.
16	DISPLACER RELAY SWITCH	Enables/disables displacer motor relay via interlock controller.
17	DISPLACER AMPLITUDE POTENTIOMETER	Sets displacer axial amplitude. (Reference to axial control).
18	PISTON AMPLITUDE POTENTIOMETER	Sets piston axial amplitude. (Reference to axial control).
19	PISTON RELAY SWITCH	Enables/disables piston motor relay via interlock controller.
20	PISTON GAIN POTENTIOMETER	Attenuates gain of piston axial-control loop.
21	PISTON PEAK AMPLITUDE DISPLAY	Displays piston peak amplitude during refrigerator operation (mm).
22 26	RADIAL POSITION DISPLAY	Displays, as a function of channel selected, the horizontal or vertical radial displacement of piston or displacer from center of bore (mils).
23 25	CHANNEL SELECT SWITCH	Push button selects channels for radial position displayed. (See Table 6-5).
24	CHANNEL DISPLAY INDICATOR	Indicates channel selected for each radial position display. (See Table 6-5).
27	DISPLACER CASE TEMPERATURE DISPLAY	Displays temperature of displacer motor housing.
28	PISTON CASE TEMPERATURE DISPLAY	Displays temperature of piston motor housing.
29	COLD FINGER TEMPERATURE DISPLAY	Displays cold finger temperature ( $^{\circ}\text{K}$ ).
30	SENSOR SELECT SWITCH	Selects one of two silicon diode temperature sensors mounted on cold finger.
31	SCALE EXPAND SWITCH	When switch is off, cold finger temperature display reads to $0.1^{\circ}\text{K}$ at all temperatures. When switch is on, temperature reads to $0.05^{\circ}\text{K}$ between $30^{\circ}\text{K}$ and $100^{\circ}\text{K}$ , and $0.1^{\circ}\text{K}$ above $100^{\circ}\text{K}$ .

	<u>Control</u>	<u>Description</u>
32	SENSOR SELECTOR SWITCH	Selects one of 11 temperature sensors (TFD's) mounted on refrigerator housing to be displayed on 33 (see Table 6-6).
33	TEMPERATURE DISPLAY	Displays one of eleven selectable TFD sensors (see Table 6-6). Note that no indication is given below 70°K for TFD's on the cold finger.
34	BEARING LATCH	Input connector for applying an external signal to latch x and y axes of piston and displacer magnetic bearings (used for calibration).
35	POWER KEY SWITCH	Energizes power supply.
36	AUTO/MANUAL SWITCH	When interlock system is on "standby", selects whether out-of-range channels on each interlock board are automatically or manually scanned.
37	SINGLE STEP SWITCH	When interlock system is on "standby" and in manual mode, out-of-range channels on each interlock board are scanned via single step push-button switch.
38	FAILURE CODE DISPLAY	Displays out-of-range channels of each interlock board when interlock system is on "standby".
39	INTERLOCK INDICATOR	When indicator is "red", interlock system is on "standby"; when indicator is "green", interlock system is "on".
40	INTERLOCK KEY SWITCH	Switches interlock system to either "standby" or "on" modes.
41 42	RESET SWITCH	When interlock system is on "standby", simultaneous depression of both switches reloads the display memory. In "on" mode, simultaneous depression of both switches resets interlock system.
43	BOARD NUMBER/FAILURE CODE DISPLAY	Displays board number and corresponding channel of first ORI detected when interlock system is "on".
44	DISPLACER RELAY INDICATOR	When indicator is "red", displacer relay is off and motor leads are shorted; when indicators is "green", relay is on and axial-control loop is closed (see Sect. 6.1).

	<u>Control</u>	<u>Description</u>
45	DISPLACER/PISTON ZERO POSITION INDICATOR	When indicator is "green", operation is normal. When indicator is "red" interlock has servoed either the piston or displacer to center (indicated by "green" on either 46 or 44).
46	PISTON RELAY INDICATOR	When indicator is "red", piston relay is off and motor leads are shorted. When indicator is "green", relay is on and axial-control loop is closed (see Sect. 6.1).
47	BNC #1	Output connector for buffered displacer compensator output signal.
48	BNC #3	Output connector for buffered piston compensator output signal.
49	BNC "G"	Output connector for buffered frequency reference signal.
50	BNC "H"	Input connector for external frequency reference signal.

TABLE 6-5. Radial Position Displayed Versus Channel Selected.

<u>Channel No. Indicated on Display (24)</u>	<u>Radial Position Shown on Display (22)</u>	<u>Radial Position Shown on Display (26)</u>
0	Front Vert. (Displacer)	Rear Vert. (Displacer)
1	Front Horiz. (Displacer)	Rear Horiz. (Displacer)
2	Front Vert. (Piston)	Rear Vert. (Piston)
3	Front Horiz. (Piston)	Rear Horiz. (Piston)
4	Rear Vert. (Displacer)	Front Vert. (Displacer)
5	Rear Horiz. (Displacer)	Front Horiz. (Displacer)
6	Rear Vert. (Piston)	Front Vert. (Piston)
7	Rear Horiz. (Piston)	Front Horiz. (Piston)

TABLE 6-6. Temperature Displayed Versus Position of Sensor Selector Switch.

<u>Switch Position</u>	<u>Temperature Displayed</u>
0	OFF.
1	Piston cooling-jacket water inlet.
2	Piston cooling-jacket water return.
3	Piston magnetic bearing coil (rear vertical).
4	Piston magnetic bearing coil (front vertical).
5	Displacer magnetic bearing coil (rear vertical).
6	Displacer upper magnetic bearing coil (front vertical).
7	Displacer lower magnetic bearing coil (front vertical).
8	Cold finger (above 70°K).
9	Cold finger (above 70°K).
10	Ambient cooling-jacket water return.
11	Ambient cooling-jacket water inlet.

## 7. COUNTERBALANCING SYSTEM

### 7.1 Design

#### 7.1.1 General Description

The vibration imposed on the cooler by the longitudinal motions of the piston and displacer is countered by a passive vibration absorber. In its simplest form, this device is a mass mounted on an axial spring that is tuned to resonate at the cooler operating frequency. If damping is low, the force produced by the motion of this counterbalance becomes equal and opposite to the net unbalance force. This technique is viable because the axial motions of the piston and displacer are directed along the same centerline.

A passive absorber was chosen because of its relative simplicity and low cost. One disadvantage of a passive absorber is that only the fundamental frequency is balanced. Higher harmonics of motion (particularly those of the piston caused by the harmonic content of the pressure wave) are not compensated. Nonetheless, a high degree of balance is achieved; this is attributed to the high spring linearity and low damping. Another disadvantage is the requirement of contact between the moving mass and spring, with the potential for wear and fatigue.

#### 7.1.2 Leaf Spring Suspension

The vibration absorber can operate in all attitudes with respect to gravity. To accomplish this in a friction-free way, the mass is suspended on crossed leaf springs. Figure 7-1 is a schematic of the configuration. The four leaf springs accurately center the mass in the housing (not shown) and provide a high radial stiffness. To keep the oscillating mass reasonably light [3.0 kg (6.7 lb)], a large amplitude of oscillation is required of the flexure springs [5.1 mm (0.20 in.)]. The nonlinearity of the leaf-spring force is designed to be minimal, and the alternating stress levels are kept low.

The key to achieving a low axial stiffness for the leaf-spring suspension is the termination radius used ( $R$  in Fig. 7-1). The radius provides the necessary axial compliance as the strip deflects. Instead of stretching (as

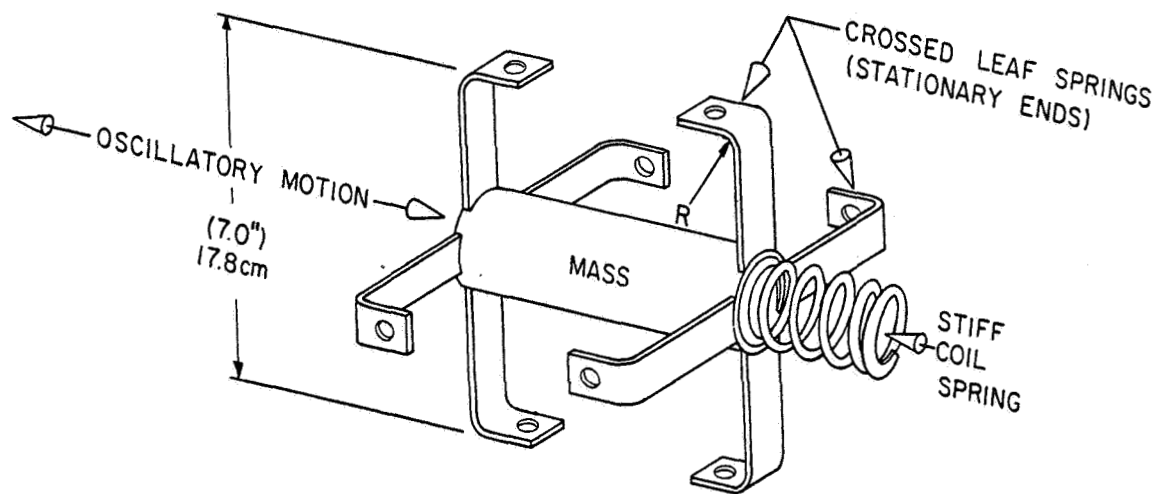


Figure 7-1. Schematic of vibration absorber.

a flat strip would do), the radius bends and induces much lower stresses. The axial deflection obtainable for a given length strip is also much greater than that for a flat spring.

The analytically predicted leaf-spring stresses were verified using strain gauges on test strips. Figure 7-2 is a theoretical plot of bending stress and traverse stiffness of a crossed set of springs. This is plotted as a function of the  $R/L$  ratio where  $R$  is the termination radius and  $L$  is half the length of the spring. An overall spring length of 180 mm (7.0 in.) was used as a constraint to keep the counterbalance assembly within the envelope of the cooler. The dotted lines show the actual design values. The spring stress is  $1.2 \times 10^8 \text{ N/m}^2$  (17,000 psi). Since the endurance stress level for AISI 1095 steel strip is  $8.8 \times 10^8 \text{ N/m}^2$  (120,000 psi) at  $10^7$  cycles, a safety margin of 7 exists.

The high transverse stiffness of  $3.8 \times 10^5 \text{ N/m}$  (2200 lb/in.) keeps the mass centered within 0.05 mm (0.002 in.) during operation. Without this high centering accuracy, a shaking-force couple would be imposed on the cooler from the coil-spring force.

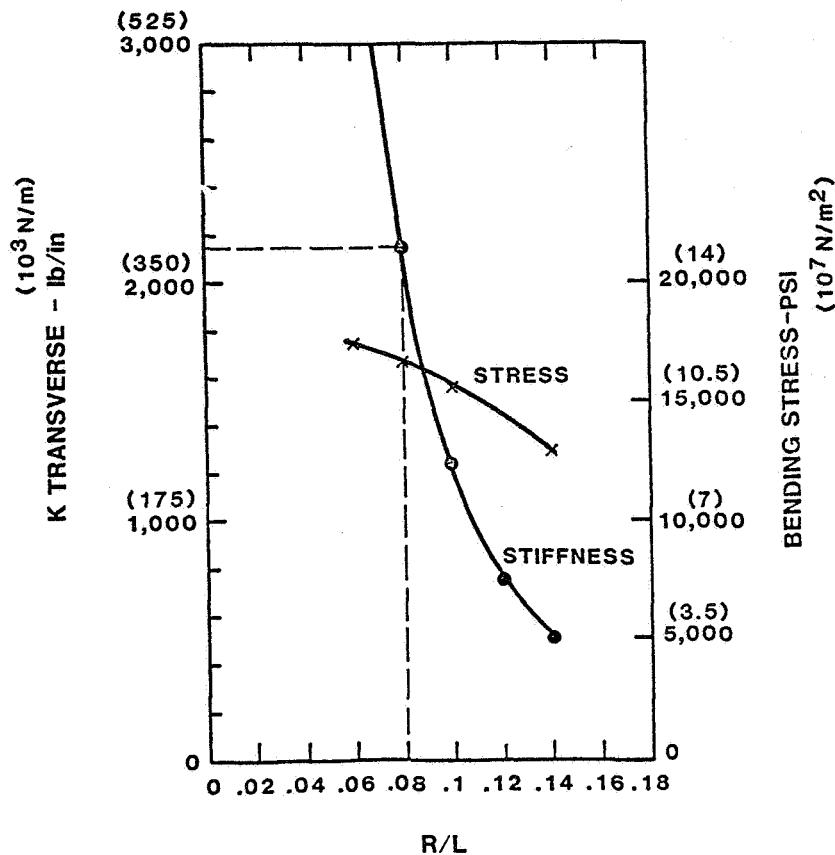


Figure 7-2. Transverse stiffness and bending stress for flexure springs.

### 7.1.3 Coil Spring

One end of the coil spring is attached to the counterbalance while the opposite end is attached to the stationary housing. A modified helical-groove mount is used at both locations. The spring is threaded onto the mount and held in place by the interference fit between the spring inner diameter and the outer diameter of the mount. By machining away material from a portion of the threaded mount, the number of active turns in compression are adjusted. In this manner, the spring rates in tension and compression are made nearly identical.

After a short period of operation, it was observed that small movements between the coil spring and its mount were generating particles by a process called fretting. Substantial wear was noted in both the spring and the mount at the points of contact. Although the particles would not result

in refrigerator damage since the counterbalance housing is separated from the working space of the machine, the spring wear would seriously limit the life of the passive absorber. This problem has been temporarily eliminated by clamping the spring to the mount to minimize the motion. The problem is expected to reoccur; a permanent solution is needed. It should be noted that even though wear is always a potential problem when moving parts have mechanical contact, relatively long life is still a possibility.

#### 7.1.4 Resonant Behavior

The housing of the vibration absorber was designed to hold vacuum. Calculations showed that air damping of the mass would be negligible compared to the inherent damping in the coil spring, but experimental verification was warranted. Published data for steel indicates damping of about 0.8%. Actual hysteresis tests on the spring/mount combination showed an energy loss per cycle of 1.7%.

To work properly, the suspension system must not have mechanical resonances close to the cooler operating speed (25 - 28 Hz). The lowest or fundamental frequency calculated for each mode of oscillation is as follows:

Coil spring	343 Hz
Flexure strips	250 Hz
Counterbalance mass (radial)	107 Hz
Counterbalance mass (torsional)	150 Hz

To fine-tune the natural frequency of the counterbalance to coincide with the cooler operating frequency, a small removable "tuning mass" was provided. The weight of the mass was adjusted until the proper resonant frequency was reached. Various operating points are possible by replacing the tuning mass, and several were fabricated for performance testing with the refrigerator. Once the operating frequency of the refrigerator was determined, a specific tuning mass was chosen.



### 7.1.5 Summary

#### Counter mass

Amplitude:	5 mm (0.20 in)
Mass:	3.0 kg (6.7 lb)
Operating speed:	26 Hz nominal

#### Coil Springs

Stiffness:	$75 \times 10^3 \text{ N/m}$ (430 lb/in)
Peak stress:	$2 \times 10^8 \text{ N/m}^2$ (28,000 psi)
Peak force:	380 N (85 lb)
Nonlinearity:	0.9%

#### Suspension Springs

Transverse stiffness:	$750 \times 10^3 \text{ N/m}$ (4,300 lb/in)
Peak stress:	$1.2 \times 10^8 \text{ N/m}^2$ (17,000 psi)
Nonlinearity:	2.3%

#### System

Damping energy:	1.7% ( $Q = 360$ )
Spring nonlinearity:	3.2%
Overall spring rate:	$8.0 \times 10^4 \text{ N/m}$ (460 lb/in)
Refrigerator mass:	70 kg (155 lb)

### 7.2 Performance Estimates

In this section two performance parameters are examined: the amount of force transmitted through the cooler mount to the base, and the residual shaking force on the cooler. The first represents the vibrational load imparted by the cooler on any vehicle to which it is mounted; the second, the vibrational load imparted to any device fastened to the cooler housing. The latter parameter was also measured experimentally and the counterbalance damping factor determined. This experimental work is outlined in Section 7.3.

The vibration absorber is modeled as a 2 degree of freedom system (Fig. 7-3). The mount for the cooler of mass  $M$  on its supporting base has a

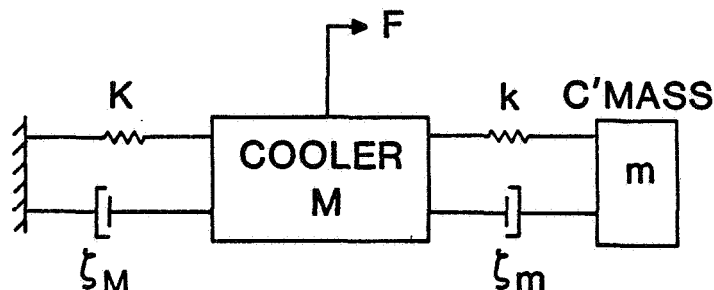


Figure 7-3. Vibration model of cooler/counterbalance system.

spring constant  $K$  and damping factor  $\zeta_M$ . The counterbalance mass  $m$  resonates at the cooler operating frequency on a coil spring with constant  $k$  with damping  $\zeta_m$ . A force  $F$  acts on the housing due to the oscillating motion of the piston and displacer. A transfer function (TF) can be derived for this system which is the ratio of the force transmitted to the base (which is to be minimized) to the inertial disturbance force  $F$ . When the damping in the counterbalance is very low, the transfer function can be approximated by:

$$TF \approx 4 \frac{M}{m} \zeta_M \zeta_m \frac{f_M}{f_m} \quad (\text{at peak attenuation})$$

where,  $f_M$  = natural frequency of cooler mount (Hz)  
 $f_m$  = natural frequency of counterbalance (Hz)

The smaller the damping of the counterbalance or cooler mount and the lower the natural frequency of the cooler mount, the better the performance. The natural frequency and damping of the cooler mount (see Fig. 2-13) was measured to be 5.7 Hz and 0.07, respectively, at low amplitudes. The 1.7% coil spring hysteresis yields an equivalent damping factor of 0.0014.

Figure 7-4 is a plot of the calculated magnitude of the transfer function between the force transmitted to the base and the disturbance force versus frequency, assuming a tuning frequency of 26 Hz. At the resonant frequency, 48 dB of attenuation results, which is a reduction factor of 250 in force. The inertial shaking force of the piston and displacer was calculated to be 380 N; the calculated residual force imposed on the cooler mount is thus 1.6 N.

The steepness of the transfer function plot in Figure 7-4 shows that if the counterbalance is detuned only 0.5% (roughly 0.1 Hz), then the degree of attenuation decreases to 40 dB or a factor of 100 to 1. This is 2.5 times worse than when optimally tuned.

Since the vibration absorber and cooler represent a 2 degree of freedom system, there are two natural frequencies associated with its vibration. One of these frequencies occurs at 26.5 Hz (see Fig. 7-4); this is only 0.5 Hz above the cooler speed. The second resonance, relating to the mount, is low enough to be of no concern. As experimentally confirmed, if the 26.5 Hz mode is imposed, the counterbalance amplitude increases without

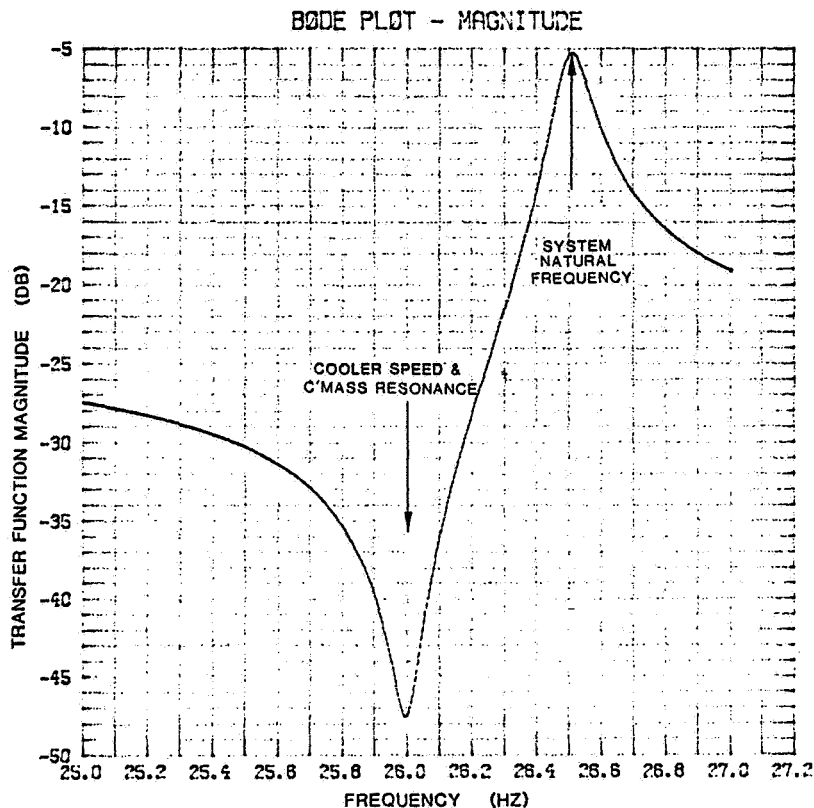


Figure 7-4. Transfer function of force transmitted to base.

bound. Further, since at this frequency the counterbalance mass resonates in phase with the motion, the transmitted force is amplified. Limit stops are provided in the housing to limit the travel of the counterbalance if this should accidentally occur.

The vibration of the housing is described by another transfer function (RF), the residual shaking force on the cooler divided by the imposed inertial disturbance force  $F$ . The magnitude of the vibration was measured experimentally during operation (Sect. 7.3).

Figure 7-5 is a calculated plot of this transfer function; the peak attenuation is 23 dB or 13 to 1. A simplified expression is:

$$RF \approx \frac{M}{m} 2 \zeta_m \quad (\text{at peak attenuation})$$

Only the ratio of the masses and the damping in the counterbalance coil spring affect performance. The mass ratio is known, and from a measurement of the reduction in shaking force from an accelerometer attached to the counterbalance housing, the damping factor  $\zeta_m$  can be estimated.

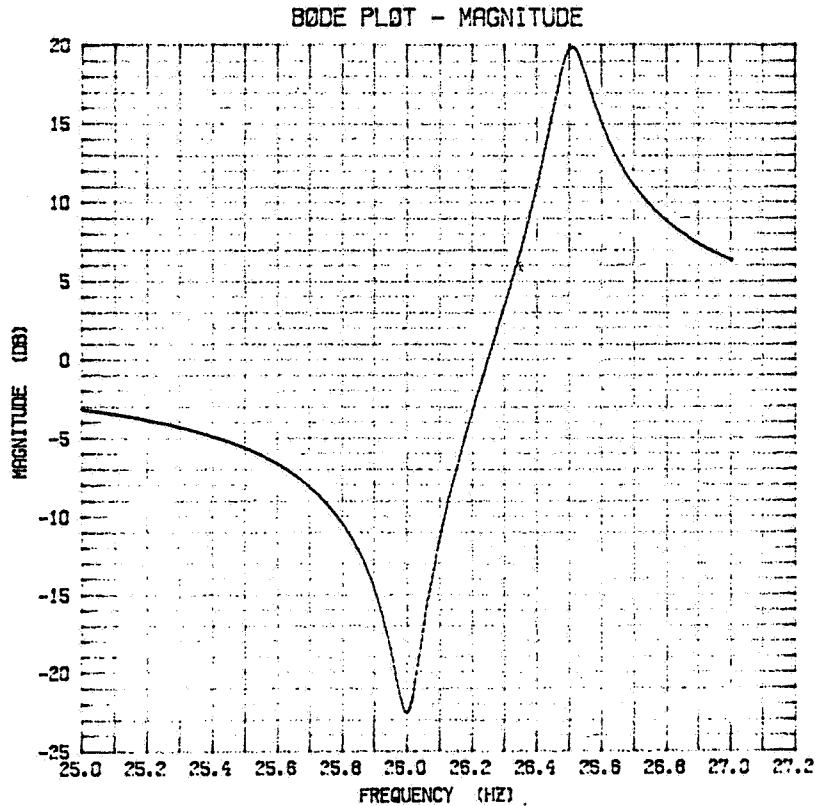
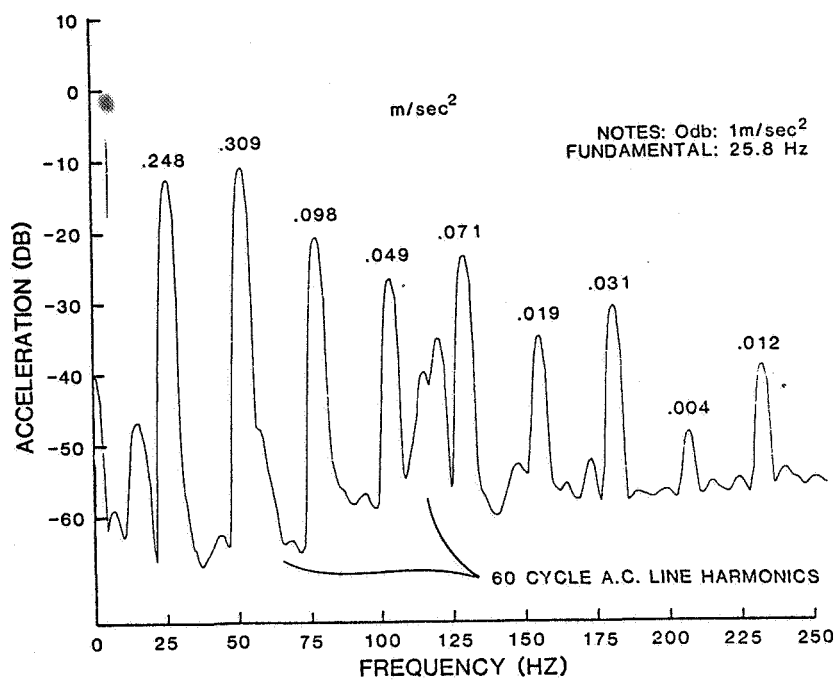


Figure 7-5. Transfer function of residual force on cooler.

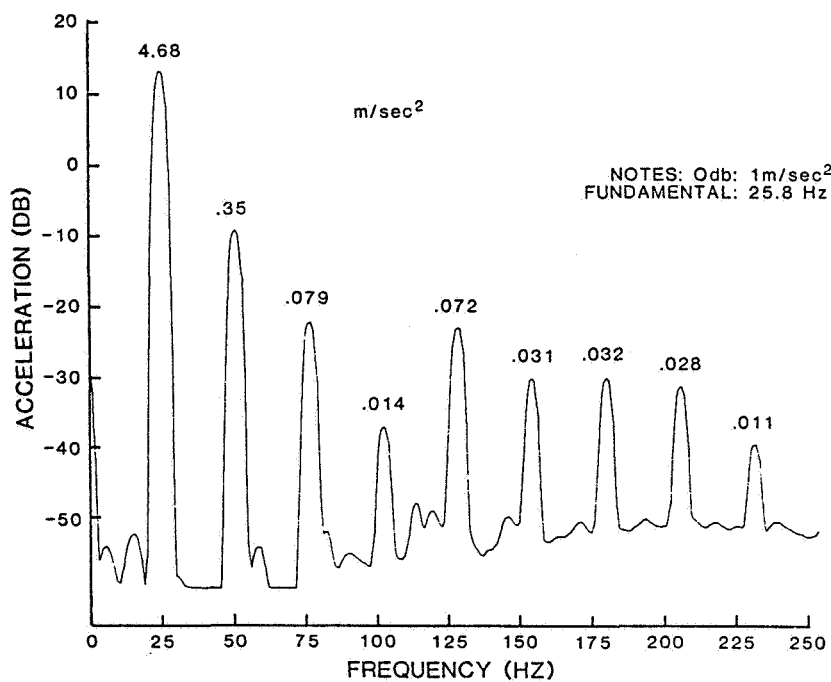
### 7.3 Performance Data

An accelerometer was mounted to the cooler without the counterbalance installed. Test data was obtained using a piston amplitude of 7.3 mm and a displacer amplitude of 3.0 mm at 26 Hz. Figure 7-6a is the recorded spectrum of vibration that resulted. The first peak of  $4.7 \text{ m/sec}^2$  at 26 Hz represents the fundamental vibration at the cooler operating frequency. The second peak is the first harmonic at 52 Hz and is  $0.35 \text{ m/sec}^2$ . One would expect the counterbalance system to substantially reduce the fundamental but have little influence on the others.

Data with the counterbalance installed shows this to be true. Figure 7-6b is a plot of accelerometer output versus frequency and shows that the fundamental was reduced to  $0.25 \text{ m/sec}^2$ , for a total change of 26 dB. This is a reduction in vibration of 19 to 1. The predicted performance, as discussed in Section 7.2, was 23 dB or a reduction of 13 to 1. The close



(a) Without counterbalance.



(b) With counterbalance.

Figure 7-6. Vibration spectrum of cooler.

agreement indicates that the damping in the counterbalance suspension is extremely low. When the counterbalance was tested without vacuum, a very small change in performance was noted as expected.

Figure 7-6b indicates that the first harmonic (52 Hz) decreased 1 dB with the counterbalance installed. The small nonlinearity in the spring suspension is evidently reducing this harmonic but increasing the higher harmonics.

#### 7.4 Summary

The performance of the counterbalance is summarized in Table 7-1.

TABLE 7-1. Performance of Counterbalance.

	Fundamental (26 Hz)	2nd Harmonic (52 Hz)	3rd Harmonic (78 Hz)
Without Balance:			
Peak acceleration ( $\text{m/sec}^2$ )	6.6	0.51	0.11
Peak displacement ( $\mu\text{m}$ )	252.	19.3	4.1
Peak transmitted (N)	27.	2.1	0.4
With Balance:			
Peak acceleration ( $\text{m/sec}^2$ )	0.35	0.44	0.14
Peak displacement ( $\mu\text{m}$ )	13.4	16.8	5.3
Peak transmitted (N)	1.4	1.8	0.6

## 8. MECHANICAL FABRICATION, CLEANING, AND ASSEMBLY

### 8.1 Fabrication

The fabrication of this refrigerator required extremely high precision. In the design of the parts, consideration had to be given to the fabrication sequence, the heat-treating and heat-processing schedules, and the long-term stability of the completed components and assemblies. This effort required the close collaboration of designers, engineers, instrument-makers, and technicians. The work was truly multi-disciplinary, since many decisions involved trade-offs between mechanical and electronic complexity. The success of the project was due in large part to the ability of those involved to recognize the significance of these interactions.

One of the early decisions was the choice of materials to be used for the refrigerator. Titanium was selected as the primary material due to its excellent long-term stability, ensuring that the dimensions of the parts would not change after fabrication if suitable care was used. Additionally, titanium offers an excellent strength-to-weight ratio, making it desirable for spaceborne applications. Since tight tolerances and close clearances were involved, thermal-expansion coefficients were important. Almost all metal parts were made of titanium, with the major exceptions being magnetic materials. Where minimum size or weight was the overriding concern, as in the displacer motor armature and the moving armatures for the magnetic bearings, vanadium Permendure was chosen as the ferromagnetic alloy, since it has the highest flux-carrying capacity available. For motor stators, silicon iron was used. It has reasonably high flux capacity and electrical resistivity, and is available in a greater variety of sizes than Permendure. Magnetic-bearing pole pieces were made of a nickel-iron alloy which exactly matched the coefficient of thermal expansion of titanium. These pole pieces were brazed into the housings, and the heavy walls of these parts required the thermal match. The cold-cap at the end of the cold finger was fabricated of copper, thermal conductivity being the most important parameter. Where electrical insulation was required, two different types of ceramics were used. It should be noted that all of these materials are inorganic. The complete absence of any organics from the working space of the refrigerator ensures successful operation for long periods of time with

no degradation in cold performance. All parts of the machine can be vacuum baked at 100°C to drive out any adsorbed gaseous contamination.

Mechanical joints were made using a wide variety of techniques. The most straightforward joint is a flange, except that the flanges in this machine are required to align the housings to a tolerance of 2  $\mu\text{m}$ . This was accomplished by careful surface finishing and the use of dowel pins in the flange face. The pins are a light press fit into one side of the flange, and a line-to-line fit in the other side.

Many of the internal joints in the machine are braze joints in which a filler metal is used to permanently join two components at an elevated temperature. Careful planning was required to combine the brazing processes with the other heat-treating processes. Magnetic materials had to be joined and magnetically annealed at the same time, in order to achieve optimum magnetic properties as well as a strong joint. The titanium parts were generally stress-relieved during the brazing operation, and this had to be done at a point in time when the heavy machining operations were completed. In some cases, many components of widely varying wall thickness were joined simultaneously, requiring careful consideration of the heating and cooling rates to prevent permanent distortion. Before ceramic parts could be brazed, they had to be prepared with several metallization steps. Braze metals had to be identified which would not react adversely with any of the metal components. In some cases a nickel transition piece was first joined to one of the parts, to allow the joining of two incompatible metals (such as copper to titanium). Quality control required testing every joint for helium leak-tightness, using a mass-spectrometer.

Another joining technique used was miniature TIG (tungsten inert gas) welding. This was used to form the hermetic seal for the thin cans around the motor coils, to hold the ceramic window assemblies in place, to join the two sections of the displacer, and to attach the end caps on the piston. The advantage of TIG welding is its highly localized heat which can be used on high-precision, finished parts without causing distortion. Additionally, the joint itself is very small, less than a millimeter thick, so it can be used on small components or in tight locations.



A fourth joining technique was soldering. This was used to insert the feed-through assemblies into the titanium housing walls (with a nickel transition piece brazed to the titanium). It was also used to attach the displacer-motor magnets to the Permendure armature after the magnets were metallized. The primary advantage of soldering is the low temperature required, about 250°C.

Fabrication of the parts themselves involved a great deal of high-precision machining, with tolerances less than 5  $\mu\text{m}$ . Special fixtures were frequently required, as was careful planning of the fabrication sequence. In general, the many special cases required careful attention to detail and innovative approaches.

## 8.2 Cleaning and Assembly

### 8.2.1 Cleaning

A series of cleaning procedures were formulated. All components were subjected to a rigorous cleaning prior to assembly. This was to insure the absence of particulates and the compatability of mating parts. Three phases of cleaning were used: rough cleaning, degreasing and particulate removal, and final cleaning.

#### (1) Rough Cleaning

All components were rough cleaned by immersion in a Freon solution within an ultrasonic cleaning bath. Each component was visually examined to insure that machining chips were removed from blind holes and crevices, and that all surfaces were free of particles which could indent or score these surfaces during inspection. After inspection, all interfaces were mated to insure ease of assembly and were checked for alignment.

#### (2) Degreasing and Particulate Removal

To this point, all components had been handled freely without consideration of total cleanliness. A more thorough cleaning operation was applied to remove small particulates, skin particles and oils. During these procedures all handling was conducted with lint-free gloves.

Each component was immersed in a bath of alcohol and swabbed with lint-free wipes. This was followed by extensive flushing with a Freon TE solution, until the emerging solute was free of any visible particles. Components were microscopically examined for any remaining particles, and then individually sealed within plastic containers for storage. This phase of cleaning was also applied to all fasteners and hand tools to be used during assembly.

(3) Final Cleaning

All components, fasteners, hand tools, and jigs were individually cleaned within a Freon vapor degreasing bath containing an ultrasonic cleaner. Each item was lowered into the Freon vapors and ultrasonic bath and repositioned at intervals to expose all holes and crevices to the vapors. The final cleaning step was to raise the item above the fluid level and use a wand jet-spray to flush all areas.

The plastic containers used to cover the components were also subjected to this method of cleaning, although more emphasis was placed on flushing with the jet spray. The components were then individually enclosed in the cleaned plastic containers while within the confines of the cleaning tank. This reduced the possibility of airborne particles adhering to the cleaned surfaces. The components were then transported to the clean room assembly area via instrument cart.

Related assembly aids too large to be cleaned in the vapor bath (i.e., surface plate, support cart for the surface plate, and instrument cart) were swabbed with Freon TE prior to entering the clean room.

8.2.2 Assembly

In some instances it was considered more favorable to perform certain stages of assembly outside the clean room. These were performed within a laminar flow hood adjacent to the cleaning tank used for final cleaning. The subassemblies completed within the laminar flow hood were:

- Installation of piston stator in compressor housing.
- Soldering piston stator leads to housing feedthroughs.
- Soldering piston LVDT leads to ceramic insulator and housing feedthroughs.
- Coupling piston and motor armature together and safety-wiring screw heads.
- Soldering displacer stator leads to expander housing feedthroughs.
- Soldering displacer LVDT leads to ceramic insulator and housing feedthroughs.
- Installation of end cap over displacer LVDT body.
- Instrumentation of cold finger.

All the above operations were followed by a repeat of the final cleaning procedures; the subassemblies were then transported to the clean room.

(1) Cold Finger Instrumentation

Instrumentation of the cold finger (see Fig. 8-1) included the mounting of temperature sensors and the electrical heater which simulated the 5 W load. The copper cold cap atop the cold finger accommodates two silicon diode temperature sensors. The sensors, a product of Lake Shore Cryotronics Inc., were calibrated by the supplier to cover a 4°-330°K range with a maximum error of  $\pm 0.09^\circ\text{K}$ . The output reading was checked at a single point prior to assembly, by immersing each sensor in  $\text{LN}_2$  and reading the temperature directly on the calibrated digital thermometer supplied with the system. The sensors were mounted in two holes machined in the cold finger after a coating of thermal paste (a mixture of silver powder and silicone oil) was applied. A redundant sensor was added under the heater button. This, a two point TFD, was inserted into a copper disk directly atop the cold cap with thermal paste added to the mating surfaces. The TFD's are used to check the high-temperature calibration of the silicon diode sensors. The digital thermometer used to read them (Omega Engineering Inc.) does not extend into their nonlinear region below 70°K.

The resistor heater element was mounted above the copper disk with thermal paste between the faces, and secured with a threaded stud.

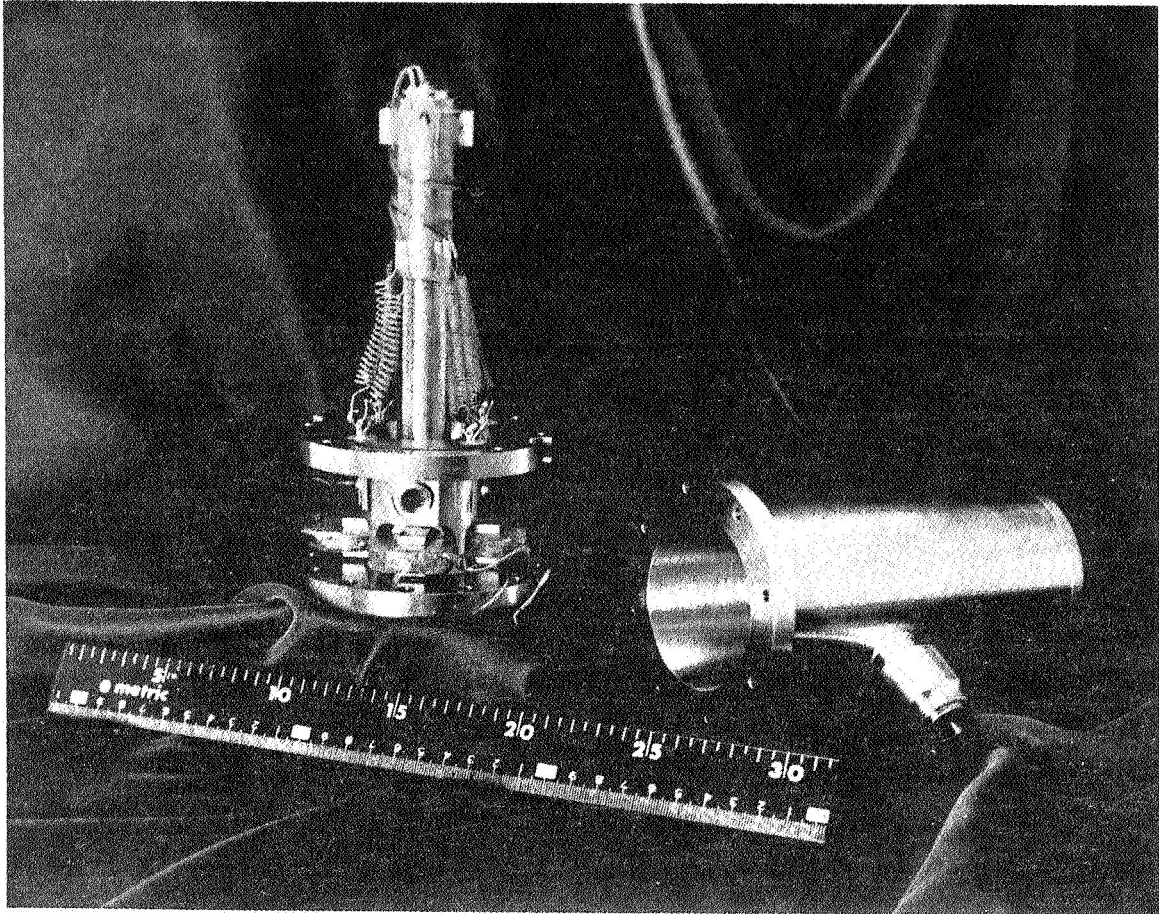


Figure 8-1. Cold finger/Dewar showing instrumentation.

The wires coupling the sensors to the feedthroughs of the cold-finger flange are Teflon-coated copper, 18 inches long, and formed in a spiral. The four heater leads are single-strand, Teflon-covered copper, 18 inches long, and also formed in a spiral. The first four inches of the wires from the freezer cap are wrapped around the cold finger as a heat sink, and secured to the finger with a lacquer varnish. Electrical continuity for the heater and sensors was checked while the cold finger was immersed in  $\text{LN}_2$ .

(2) Tools

To perform the final assembly, the following accessories were required:

- Granite surface plate.
- Two (2) Vee blocks.
- Steel parallels.
- "C" clamps.
- Torque wrenches.
- Allen hex driver snap-on sockets.
- Allen wrenches.
- Allen balldrivers.
- Ratchet drive wrenches.
- Tweezers
- Pliers
- Microscope
- Jigs and fixtures.

The above items were cleaned as per final cleaning procedures with the exception of the surface plate, the microscope, and support cart which were swabbed with Freon using lint-free wipes in the ante-room of the Clean Room.

### (3) Compressor Subassembly

The final assembly was performed in the Clean Room (Class 100) by two persons attired in standard clean-room garb consisting of lint-free gloves, hooded gown, boots, and safety glasses.

Each component was removed from its plastic container and positioned under a microscope (100X). If any particles were observed, the component was recleaned as per the final cleaning procedure and re-examined upon its return to the Clean Room.

Two Vee blocks were positioned in tandem on a surface plate between two parallels clamped to the surface plate (Fig. 8-2). This allowed one or both of the blocks to slide freely within the parallels. One side of the compressor housing, the motor section, was positioned on one Vee block with the piston installation fixture (not shown) coupled to the compression end of the housing with four screws.

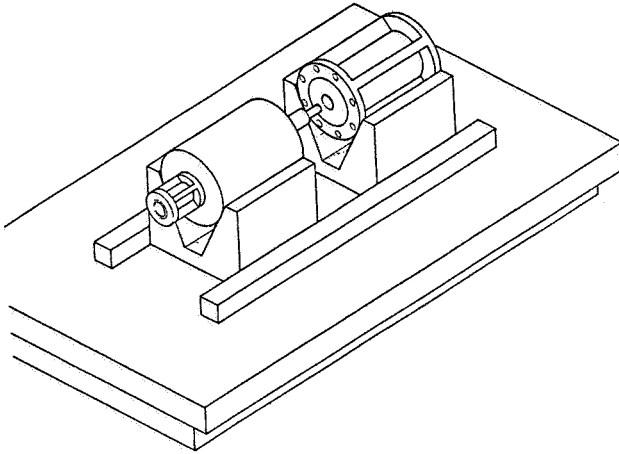


Figure 8-2. Schematic of compressor subassembly during assembly procedure.

The installation fixture consisted of an aluminum sleeve with a flange at one end and a threaded steel rod passing through the center. The end of the threaded rod (i.e., the end extending into the housing) was in contact with a Delrin rod, which was in contact with the piston head. Starting with the threaded rod fully extended into the housing, the piston was inserted into the housing until it contacted the rod. The threaded rod was slowly unscrewed, allowing the magnetic attraction between the magnet armature and the stator within the housing to draw the piston to its center position. When this was achieved, the aluminum fixture was removed from the end of the housing. The exposed piston head was temporarily covered with a blanking plate.

The other side of the compressor housing, the LVDT section, was mounted on the second Vee block and a metal C-ring installed in the flange face groove.

Both Vee blocks were drawn together, allowing the piston to enter the LVDT section, until both housing sections were coupled and aligned via two dowel pins at the interface.

The two housing sections were locked together with silver-plated cap screws. The screws were silver plated to prevent galling; stainless steel screws in titanium had galled in the threads after a single use. Lubrication was not permitted, and tests conducted on screws with different types of plating showed that silver-plated screws could be used repeatedly without galling or flaking.

The rear face of the LVDT housing section was capped with a cover plate, using Allen cap screws. The completed compressor subassembly is shown in Figure 8-3.

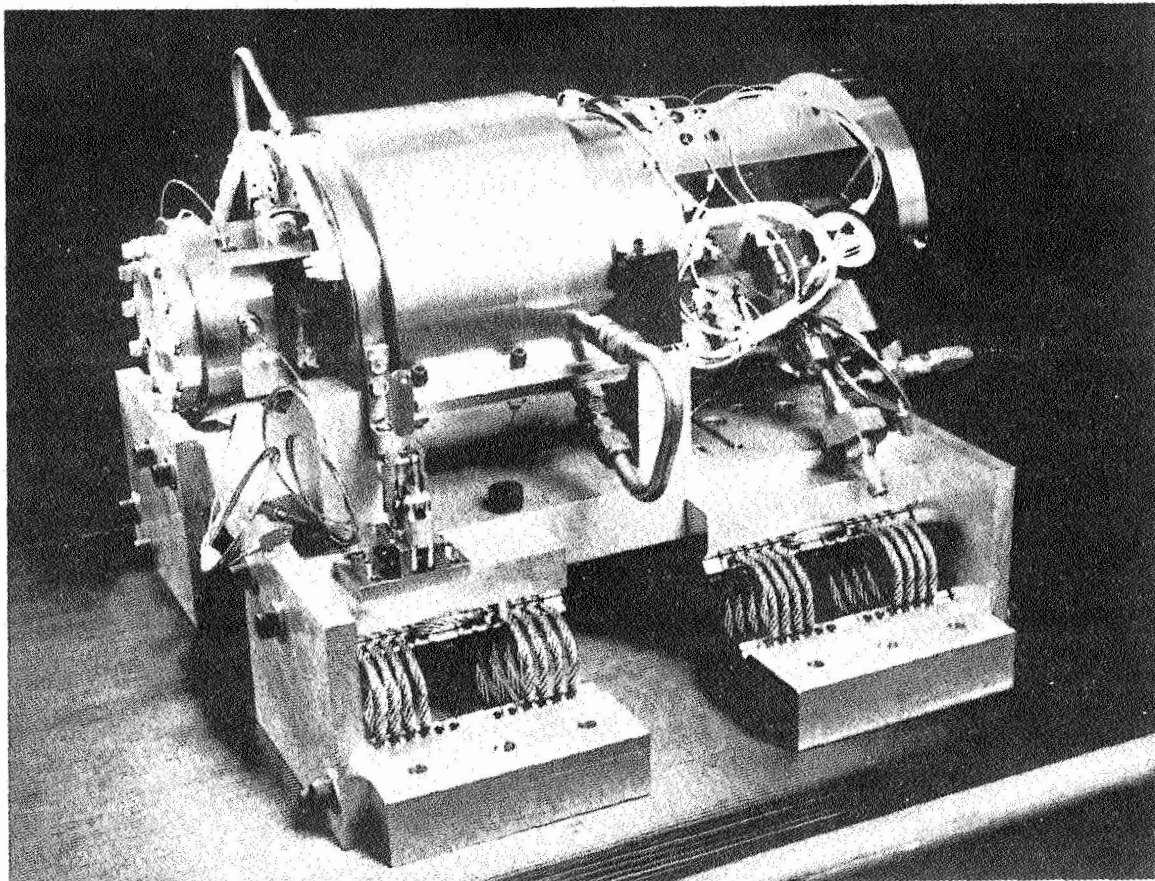


Figure 8-3. Completed compressor subassembly.

(4) Expander Subassembly

The displacer motor housing section was mounted on a test stand with Allen cap screws securing the flange. The displacer was supported by hand and inserted into the housing. The magnetic attraction of the motor armature was not powerful enough to warrant a special fixture, as that used for the piston armature insertion. A C-ring was installed in the face groove of the housing, and the cold finger section was moved over the protruding end of the displacer, and coupled with the motor section. The two housing sections were locked together with Allen cap screws (the alignment of the two bores



in the housing sections was previously established by dowel pins installed through the flanges.) Figure 8-4 shows the completed expander subassembly on its test stand.

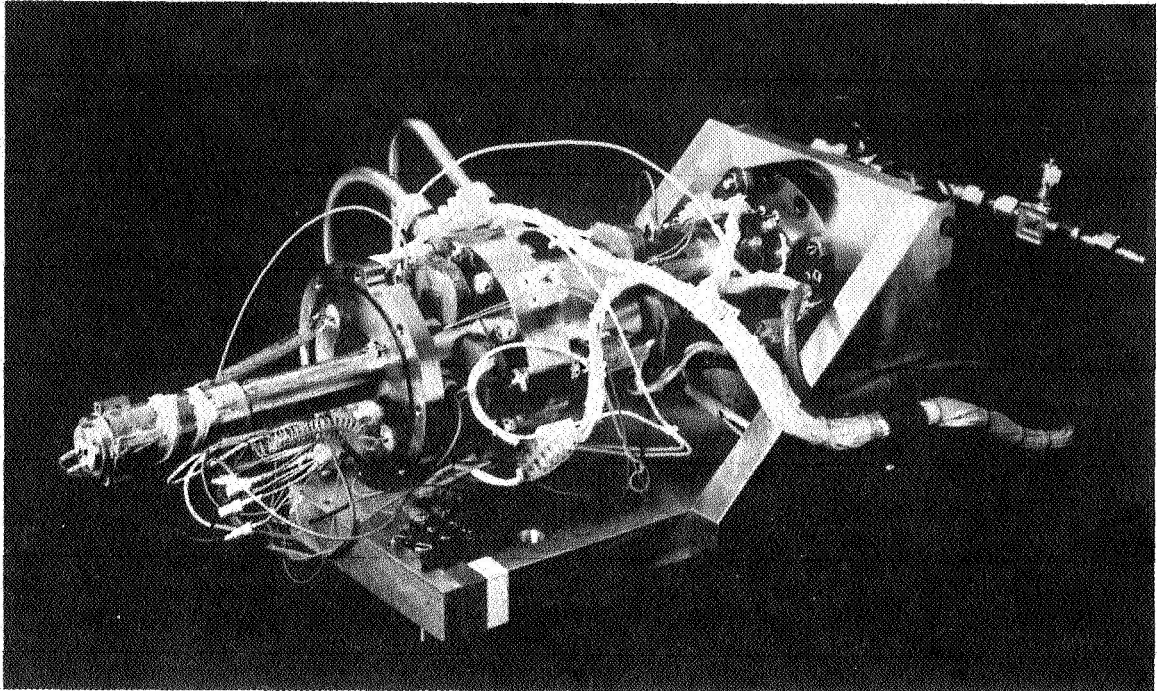


Figure 8-4. Completed expander subassembly on test stand.

(5) Final Assembly

The blanking plate on the compressor housing was removed, and the expander assembly was detached from the test stand. A C-ring was installed in the face groove of the piston motor housing section, and the expander assembly was coupled to the housing and secured with cap screws. All screws were supported with plain and Bellville washers under the heads, to reduce scoring of the flanges. The screw heads had previously been cross-drilled for locking wires. The final assembly step was the installation of the pressure transducers; two were inserted into the compression volume and one into the buffer volume.

The completed refrigerator assembly was lifted free of the Vee blocks, placed on a test support cradle, clamped in position, and transported to the test area.



## 9. TEST RESULTS

### 9.1 Measurements

The Engineering Model refrigerator was completed and produced cold in March 1982. The test results obtained for the components of the refrigerator are given in the previous sections of this report. This section discusses the thermodynamic tests.

For a thermodynamic load, the resistive heater, connected to the cold finger, was set to produce the nominal 5 watts. The control of this heating element is explained in Section 6. The cold temperature was measured with the calibrated silicon diode sensors.

Table 9-1 compares the predicted performance (calculated with the Philips Stirling Computer Program) and the measured performance. The lower operating frequency was used because the piston mass was higher than predicted. The charge pressure, which determines the stiffness of the compression volume gas spring, could also have been increased to keep the system in resonance.

TABLE 9-1. Design Versus Measured Performance.

<u>Quantity</u>	<u>Design Value</u>	<u>Measured Value</u>
Piston motor mass (kg)	1.85	1.92
Displacer moving mass (kg)	0.32	0.35
Piston amplitude (mm)	7	7.3
Displacer amplitude (mm)	3	3.0
Phase between piston and displacer (°)	60	67
Operating frequency (Hz)	26.7	25.0
Charge pressure (atm)	16	16
Ambient heat-exchanger temperature (°C)	15	12
Electric input power to motors (W)	155	220
Cold production (W)	5	5
Cold temperature (°K)	65	64.6

The discrepancy in the electrical input power to the motors can be explained in two ways. First, the measurements include the power of the higher harmonics of the operating frequency. The power dissipated at these harmonics results from the action of the axial control system and is not included in the Stirling program.

Secondly, the electrical input power to the displacer motor, at the fundamental frequency, is substantially higher than that predicted. The measured dynamic force constant was lower than predicted, requiring higher input currents to generate the required force. The flux density of the Permendure in the motor armature was designed to be very close to magnetic saturation, with a magnitude as high as 2.2 Tesla. At this level of flux density, the uniformity of the material becomes critical, as does the manner in which it is annealed. Since the diameter of this motor was restricted by the small size of the displacer, no margin was available for a conservative design.

## 9.2 Cooldown Curve

The cooldown curve (temperature vs. time) is shown in Figure 9-1. As can be seen, the cold temperature with no heat load applied reaches 40°K in about 35 minutes.

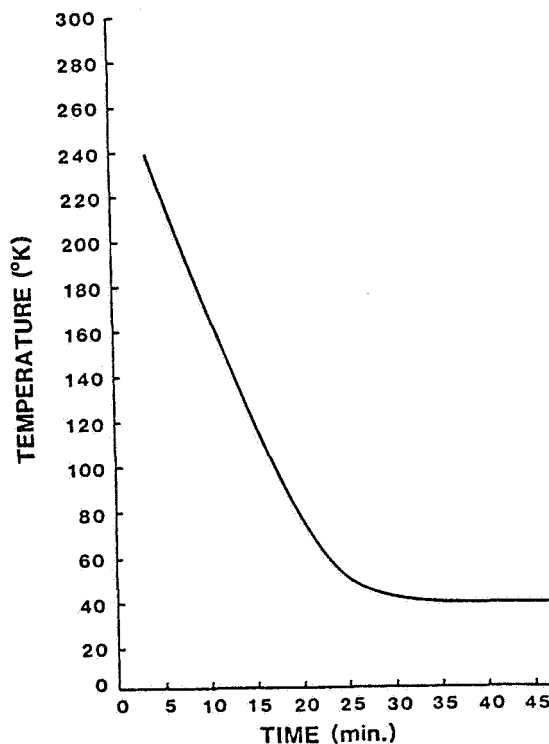


Figure 9-1. Cooldown curve (temperature vs. time).

### 9.3 Performance Verification

To verify its thermodynamic performance, the refrigerator was tested for 50 hours at one operating point. During this test, no degradation in temperature was noted, within the accuracy of the silicon diode sensors ( $0.1^{\circ}\text{K}$ ). Random noise in the sensor was less than  $0.5^{\circ}\text{K}$ . The test parameters are given in Table 9-2.

TABLE 9-2. Parameters for 50 Hour Performance Verification.

Total Operating Time	63.6 hr
Maximum Continuous Operating Time	35 hr
Start/Stop Cycles	16
Applied Load Power	3.7 W
Cold Temperature	$63.5^{\circ}\text{K}$
Piston Stroke Amplitude	6.5 mm
Displacer Stroke Amplitude	3.0 mm
Phase Between Piston and Displacer	$60^{\circ}$
Charge Pressure	18 atm
Operating Frequency	27.8 Hz
Water Temperature of Cooling Jacket for Ambient Heat Exchanger	$14.4^{\circ}\text{C}$

A comment regarding the different operating conditions shown in Tables 9-1 and 9-2 is in order. Specifically, it should be noted that differences exist in the frequency, phase, and piston amplitude, among others. Further, the operating conditions discussed in the linear motor section and counter-balance section are also different from either of these. Since these parameters are easily adjusted via the control panel while the refrigerator is operating, this illustrates that the thermodynamic performance need not be sacrificed for electromechanical constraints. For example, although the parameters in Table 9-1 most closely approximate the design point, the parameters in Table 9-2 result in a lower electrical input power to the piston and better motor efficiency, although the displacer motor input power is higher. In a similar manner, given other electromechanical constraints, the system parameters may be electronically adjusted to achieve certain trade-offs, without seriously affecting thermodynamic performance and without requiring a mechanical redesign. This versatility is an inherent result of the electronic control, and a significant advantage to users of this refrigerator.

## 10. CONCLUSIONS

The goal of this program was to prove the concept feasibility of using a mechanical cryogenic refrigerator for long-life applications. By developing and integrating into an engineering model cooler the six major novel features of a rectilinear drive, linear motors, magnetic bearings, clearance seals, all-metal/ceramic surfaces, and an electronic axial-control system, this goal was achieved, and the fundamental principle of mechanical, "wearless", operation was proven.

This program was conceived as the first of three phases in the evolution of a spaceborne cryogenic cooling system. The second phase, the flight prototype model, has been started. Emphasis will be placed on improving efficiency, optimizing electromechanical subsystem interactions, and meeting Shuttle qualification requirements. The first step in the development is a parametric characterization of the Engineering Model cooler, since this unit, with electronic control of its mechanical dynamics, offers an excellent opportunity to better understand the Stirling cycle and its sensitivity to dynamic parameters.

D2

APPENDIX A

A Small Free-Piston Stirling Refrigerator

by

A. K. de Jonge

(14th Intersociety Energy Conversion Engineering Conference,  
Boston, Mass, Aug. 5-10, 1979)

## A SMALL FREE-PISTON STIRLING REFRIGERATOR

A.K. de Jonge  
Philips Research Laboratories  
Eindhoven, The Netherlands

## ABSTRACT

Theoretical studies have been done on the performance characteristics of Stirling machines with free moving pistons. This has amongst others resulted in the development of a small Stirling refrigerator with a capacity of 1 W at 77K driven by a linear electric motor. The unit is a hermetically closed machine with helium as working medium, having no bearings or crankshafts and no side forces on the piston and displacer.

These design features have resulted in a long lifetime. After a description of the design of the small free piston Stirling refrigerator, a new way to describe the pressure fluctuations in the Stirling system is given. Using this description and the characteristics of the linear motor the equations of movement of the piston and the displacer are derived. After this, experimental results are given.

WITHIN THE PHILIPS CONCERN a small cryogenic cooler, based on the free displacer Stirling principle, has been designed and developed with a capacity of 1 W at 77K. The main application is in the field of infrared radiation detection. In the design of the machine with a free piston, a free displacer and a linear motor only two sliding seals on piston and displacer are present which need no lubrication. With the linear motor inside the crankcase the machine can be hermetically sealed. The whole concept leads to a machine with a very long life requiring no maintenance and having negligible degradation.

The machine, which is produced under the name MC.80 [1\*], has indeed shown a long lifetime and a very stable lowest temperature (under the name MMC-80 a military version of the machine is also available from Philips USFA, Eindhoven).

This paper gives a simplified description of the pressure fluctuation in the machine which leads to an explanation of the behaviour of a free displacer refrigerator. Also the linear drive system of the machine will be discussed.

## DESCRIPTION OF THE CRYOGENIC COOLER

A schematic drawing of the machine is given in fig. 1. The machine consists of a

\* ) Numbers in [ ] designate References at end of paper.

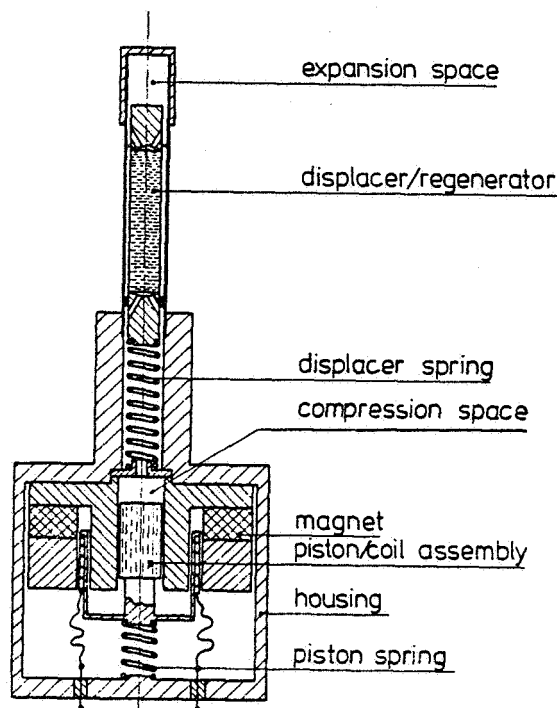


Fig. 1. - Schematic cross section of the MC.80 Stirling refrigerator with electrodynamic drive.

piston unit and a cold finger part. The piston is directly coupled to the moving coil of the linear motor. This linear motor consists of a permanent magnet system (ferroxdure is used in the MC.80, samarium-cobalt in the MMC-80). A roughly constant field is made in the gap around the iron inner cylinder. In this gap the coil driving the piston moves up and down as the result of an AC current through the coil. The centre position of the coil (and piston) is held by a small mechanical spring. All forces on the piston are in the direction of the movement, so no side forces are present and a dry running material can be used as seal. The cold finger of the machine consists of a displacer with a diameter of 9.4 mm (in the MMC-80) moving up and down in the cylinder. The displacer contains an inside gauze regenerator whereas the gaps between displacer and outer cylinder at the bottom part and the upper part are acting as cooler and freezer respectively. The displacer is

mounted on a mechanical spring. Here again only forces in the direction of movement are present and so the displacer seal can be dry running too.

#### THE PRESSURE FLUCTUATION IN A STIRLING SYSTEM

In previous publications about the Stirling theory (see e.g. [2] and [3]) the total pressure variation in the engine is given as a function of the movements of the two moving elements, the phase between the movements and the temperatures and sizes of all spaces in the engine. As in this engine the strokes nor the phases are known from the start, it is better to calculate the fluctuation as a vectorial sum of different fluctuations due to the different movements. The four main causes of pressure variations are:

1. The piston position determines the total volume.
2. The displacer position determines the amount of gas in the expansion and compression space, so influences the pressure.
3. The piston movement gives rise to gasflow causing pressure differences in the spaces.
4. The displacer movement again leads to flow with the same effects as under 3.

Ad 1. Keeping the displacer in a fixed position and moving the piston leads to a pressure [2], [3]

$$p = p_m + \frac{p_m S_p}{V_0 B} y = p_m + C_y y \quad (1)$$

in which

$p_m$  = average cycle pressure  
 $S_p$  = piston surface area  
 $y$  = piston position  
 $V_0 B$  = total cycle volume, normalised to  $T_c$

$$B = \sum_i \frac{V_i T_i}{V_0 T_c}, \quad T_i = \frac{T_c}{T_i}$$

$T_c$  = temperature compression space

Ad 2. If the piston is in a constant position and the displacer moves, the pressure will be given by:

$$p = p_m + \frac{p_m S_d (\tau - 1)x}{V_0 B} = p_m + C_x x \quad (2)$$

in which  $S_d$  is the displacer cross-sectional area,  $\tau = T_c/T_e$  the temperature ratio between the two varying spaces and  $x$  the displacer position. Change of the position of the displacer gives rise to a pressure change as gas from a space of one temperature, e.g.  $T_c$ , is moved to a space of temperature  $T_e$ .

The cycle pressure, not disturbed by flow loss, can be given by

$$p = p_m + C_y y + C_x x \quad [4] \quad (3)$$

Ad 3 and 4.

The flow losses give rise to different pressures in different parts of the engine. The pressure difference across a certain resistance due to the flow can be given by (assuming laminar flow)

$$\Delta p = \frac{c_1 \eta}{\rho v d_h} \frac{1}{d_h} \frac{1}{2} \rho v^2 = c \cdot v$$

in which

$l$  = length of resistance  
 $d_h$  = characteristic diameter  
 $\rho$  = gas density  
 $v$  = gas velocity  
 $\eta$  = viscosity  
 $c$  and  $c_1$  are constants.

The velocity of the gas at some point in the engine is the vectorial sum of two velocities proportional to the velocity of the piston  $\dot{y}$  and that of the displacer  $\dot{x}$  respectively. The pressure difference across a certain flow resistance can be translated into pressure changes on both sides of the resistance.

All this leads to the total pressure fluctuation in the variable compression and expansion volumes of:

$$p_c = p_m + C_y y + C_x x + C_{pc} \dot{y} + C_{dc} \dot{x}, \quad (4)$$

$$p_e = p_m + C_y y + C_x x + C_{pe} \dot{y} + C_{de} \dot{x} \quad (5)$$

$$\text{and } p_e - p_c = (C_{pe} - C_{pc}) \dot{y} + (C_{de} - C_{dc}) \dot{x} = C_{pp} \dot{y} + C_{dd} \dot{x}$$

The simple description of the pressures given here is only valid if the constants  $C_y$ ,  $C_x$ ,  $C_{dd}$  and  $C_{pp}$  are independent of  $x$ ,  $y$ ,  $\dot{x}$  and  $\dot{y}$ , which is not quite true but is a reasonable approximation as shown below. There are also other causes of pressure variations such as piston leakage, temperature variations due to heat transfer to walls and bad mixing, change of average temperatures in heat exchangers and varying spaces due to load changes etc. Also the flow is not laminar everywhere so flow resistances are not linearly dependent on gas velocities.

A numerical investigation has been made based on our existing Stirling computer cal-

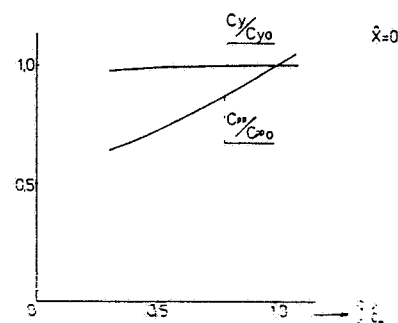


Fig. 2. - Relative variation of  $C_y$  and  $C_{pp}$  versus relative piston amplitude

culations on the MMC-80 how the "constants" mentioned above vary. The variations of  $C_y$ ,  $C_{pp}$  as a function of the amplitude of the piston  $\hat{y}$  (displacer in a fixed position) are plotted in fig. 2.  $C_y$  varies slightly due to a change in temperature at different places in the engine.  $C_{pp}$  varies more due mainly to the non-laminar  $pp$  flow. The variations of  $C_x$  and  $C_{dd}$  are plotted in fig. 3 as a function of the amplitude of the displacer  $\hat{x}$  (piston in a fixed position). This again indicates only a slight variation in  $C_x$  and more in  $C_{dd}$ .

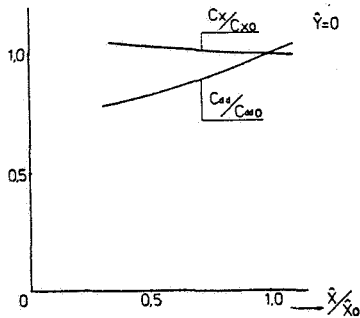


Fig. 3. - Relative variation of  $C_x$  and  $C_{dd}$  as a function of relative displacer amplitude

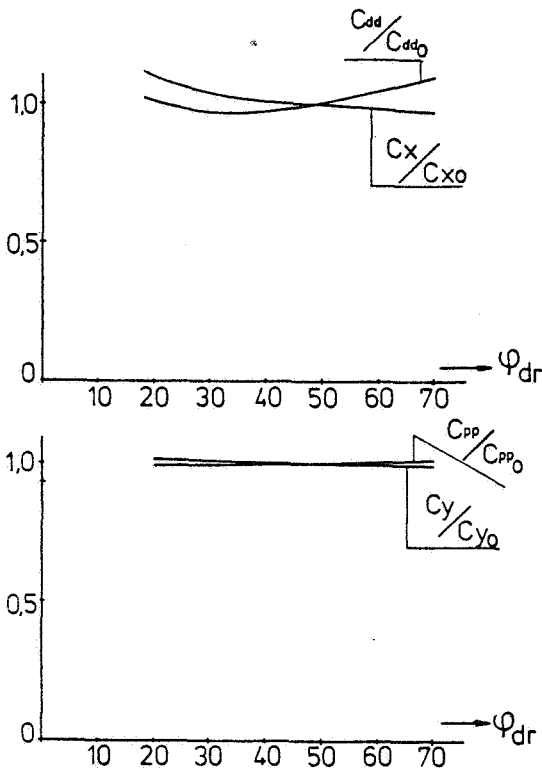


Fig. 4. - Effect of phase shift on the constants  $C_x$ ,  $C_{dd}$ ,  $C_y$  and  $C_{pp}$  with constant piston and displacer amplitude

In figure 4 the variations of the constants are calculated as a function of the phase angle ( $\varphi_{dr}$ ) between displacer and piston movement. The variations are small.

#### CALCULATION OF PRODUCTION AND INPUT POWER

With the above mentioned expression for the pressure it is easy to calculate the ideal cold production ( $Q_{eo}$ ) and ideal input power ( $N_p$ ) of a machine.

$$Q_{eo} = n \oint p \, dV_d = -n\pi C_y \hat{x} \hat{y} S_d \sin \varphi_{dr} \quad (6)$$

where

$dV_d = S_d dx =$  volume variation of expansion  
volume

$n$  = number of cycles per second

$x = \hat{x} \cos \alpha$

$y = \hat{y} \cos (\alpha - \varphi_{dr})$

$\alpha = \omega t$

$\omega$  = angular frequency

Only the pressure fluctuation due to the piston movement ( $C_y$ ) is important for  $Q_{eo}$ .

The input power is given by

$$N_p = n \oint p \, dV_p = n\pi C_x \hat{x} \hat{y} S_p \sin \varphi_{dr}, \quad (7)$$

with  $dV_p = S_p dy$ ,

indicating that only  $C_x$ , the pressure fluctuation due to the displacer movement, gives  $N_p$ . If  $C_x > 0$ , which is the case if  $\tau > 1$ ,  $N_p$  is positive when  $\sin \varphi_{dr}$  is also  $> 0$ , which is the case for a refrigerator. If  $\tau < 1$ , then the machine is a hot gas engine. Then  $C_x < 0$  and  $N_p$  is negative with positive  $\sin \varphi_{dr}$ .

#### MOVEMENT OF THE FREE DISPLACER

The equation of movement of the displacer is given by

$$M_d \ddot{x} + (p_e - p_c) S_d + C_{vd} \dot{x} = 0$$

in which  $M_d \ddot{x}$  is the acceleration force ( $M_d$  is the displacer mass),  $(p_e - p_c) S_d$  is the driving force on the displacer and  $C_{vd} \dot{x}$  is the spring force (friction is neglected).

With the pressure equations this leads to

$$M_d \ddot{x} + C_{dd} S_d \dot{x} + C_{vd} x = (-C_{pp}) S_d \dot{y}, \quad (C_{pp} < 0).$$

Now this is the equation for a damped oscillator with a driving force. The driving force  $(-C_{pp}) S_d \dot{y}$  is due to the piston movement, the  $pp$  damping force  $C_{dd} S_d \dot{x}$  to the displacer movement.

With  $y = \hat{y} \cos (\alpha - \varphi_{dr})$  and  $x = \hat{x} \cos \alpha$ :

$$M_d (\omega^2 - \omega_d^2) \hat{x} \cos \alpha + C_{dd} S_d \hat{x} \omega \sin \alpha = (-C_{pp}) S_d \omega \hat{y} \sin (\alpha - \varphi_{dr})$$

$$\text{with } \omega_d^2 = \frac{C_{vd}}{M_d}$$



$$\text{Then } \tan \varphi_{dr} = \frac{M_d(\omega_d^2 - \omega^2)}{C_{dd}S_d \omega} \quad (8)$$

$$\text{and } \dot{x} = C_{pd}\dot{y} \cos \varphi_{dr}, \text{ with } C_{pd} = \frac{-C_{pp}}{C_{dd}} \quad (9)$$

If  $\omega = \omega_d$  (displacer is tuned to the running frequency)  $\varphi_{dr} = 0$ , and thus no cold production takes place.

If  $\omega_d > \omega$ , then  $\varphi_{dr} > 0$  and the machine can run as a refrigerator.

In fig. 5  $\dot{x}$  and  $\varphi_{dr}$  are given as a function of  $\omega_d/\omega$ . When  $\omega_d/\omega$  increases,  $\varphi_{dr}$  increases but  $\dot{x}$  decreases.

(9) substituted in (6) gives:

$$Q_{eo} = -n\pi C_y C_{pd} S_d \dot{y}^2 \sin \varphi_{dr} \cos \varphi_{dr}$$

The optimum will be at  $\varphi_{dr} = 45^\circ$  thus

$$Q_{eo \max} = \frac{-n\pi C_y S_d C_{pd} \dot{y}^2}{2}$$

Then according to (9)

$$\frac{M_d(\omega_d^2 - \omega^2)}{C_{dd}S_d \omega} = 1 \text{ or } C_{vd} = M_d \omega^2 + C_{dd}S_d \omega$$

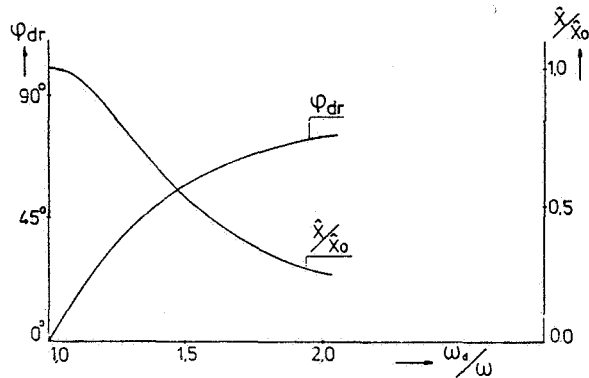


Fig. 5. - Phase shift and relative amplitude of the displacer versus  $\omega_d/\omega$

Introducing a friction force described as the first harmonic of  $F_{fr} = F \dot{x} / |\dot{x}|$  (8) then becomes

$$\tan \varphi_{dr} = \frac{M_d(\omega_d^2 - \omega^2)}{C_{dd}S_d \omega + 4F/\pi/\dot{x}}$$

and (9)

$$\dot{x} = C_{pd}\dot{y} \cos \varphi_{dr} - \frac{4F/\pi}{C_{dd}S_d \omega}$$

Both amplitude  $\dot{x}$  and  $\varphi_{dr}$  have been decreased slightly so that the maximum of  $Q_{eo}$  will decrease and will be at a slightly smaller value of  $\varphi_{dr}$ .

## MOVEMENT OF THE PISTON

The equation of movement of the piston is

$$M_p \ddot{y} + (p_c - p_m)S_p + B_g l_v \dot{y} + C_{vp} y = 0 \quad (10)$$

in which  $M_p \ddot{y}$  is the acceleration force ( $M_p$  is mass of moving part),  $(p_c - p_m)S_p$  the gas force on the piston,  $C_{vp} y$  the spring force and  $B_g l_v \dot{y}$  the electromagnetic force.  $B_g$  is the magnetic field in the gap,  $l_v$  the length of wire present in the gap and  $i$  the current through the coil [5] (the friction force is neglected).

The electric current, neglecting the inductance of the coil, is given by:

$$i = \frac{U_o \cos(\beta + \varphi) - U_m}{R_i} = \frac{U_o \cos(\beta + \varphi) - B_g l_v \dot{y}}{R_i}$$

$U_o \cos(\beta + \varphi)$  is the voltage of the source ( $\beta = \alpha - \varphi_{dr}$  and  $\varphi$  is the phase between voltage and piston movement),  $U_m$  is the inductive voltage due to the movement of the coil and thus equal to  $B_g l_v \dot{y}$ .

When substituted in the equation of motion (10), this gives:

$$(M_p \omega^2 - S_p C_y - C_{vp}) \dot{y} \cos \beta + B_c \omega \dot{y} \sin \beta =$$

$$S_p C_x \dot{x} \cos(\beta + \varphi_{dr}) - B_u U_o \cos(\beta + \varphi)$$

The pressure formula has also been used here and the flow loss has been neglected.

Further

$$y = \dot{y} \cos \beta$$

$$x = \dot{x} \cos(\beta + \varphi_{dr})$$

$$\text{and } B_c = \frac{(B_g l_v)^2}{R_i} \text{ and } B_u = \frac{B_g l_v}{R_i} \text{ have been}$$

introduced.

The spring constant for the piston consists of two parts,  $C_{vp}$  the mechanical spring constant (which is small) and  $C_y S_p$ , the spring constant of the gas spring.  $y S_p$  Solving the equation (also using eq. (8) and (9) gives:

$$\tan \varphi = \frac{B_c \omega + S_p C_x C_{pd} \sin \varphi_{dr} \cos \varphi_{dr}}{S_p C_x C_{pd} \cos^2 \varphi_{dr} - (M_p \omega^2 - C_y S_p - C_{vp})}$$

Thus  $\varphi$  is independent of the applied voltage ( $U_o$ ), but strongly dependent on the resonance conditions.

$$\text{Also } \dot{y} = \frac{B_u U_o \sin \varphi}{B_c \omega + S_p C_x C_{pd} \sin \varphi_{dr} \cos \varphi_{dr}}$$

so the amplitude of the piston movement is proportional to the applied voltage.

The power delivered to the piston is:

$$N_p = \frac{1}{T} \int_0^T U_m i dt = \frac{\omega \dot{y}}{2} (B_u U_o \sin \varphi - B_c \omega \dot{y})$$

The electric input power is

$$N_{el} = \frac{1}{\pi} \int_0^{\pi} U_o \cos(\beta + \varphi) idt = -\frac{B_u U_o}{2B_c} (B_u U_o - \omega \varphi B_c \sin \varphi)$$

The electric efficiency then is

$$\eta_e = \frac{N_p}{N_{el}} = \frac{A \sin^2 \varphi}{(1+A)(A+\cos^2 \varphi)} \text{ with } A = \frac{N_p}{B_c (\omega \varphi)^2 / 2}$$

The maximum efficiency,  $\eta_e = \frac{1}{1+A}$ , is reached at  $\varphi = 90^\circ$ .

For optimum  $\eta_e$  and optimum  $Q_{eo}$

$$M_p = \frac{C_{yp} S_p + C_{pd} S_p C_x / 2}{\omega^2} + C_{vp} \approx \frac{p_m S_p (\frac{C_y}{p_m} + \frac{C_{pd} C_x}{2 p_m})}{\omega^2}$$

So neglecting  $C_{yp}$  the mass of piston plus coil is inversely proportional to  $\omega^2$ . As  $M_p$  cannot be taken too low, for constructional reasons,  $\omega$  is limited by this condition. Only by increasing  $p_m S_p$  to a high value can  $\omega$  be increased again. In practice  $\omega = 314$  (50 cycles) is a very acceptable value.

#### EXPERIMENTS WITH THE MMC-80

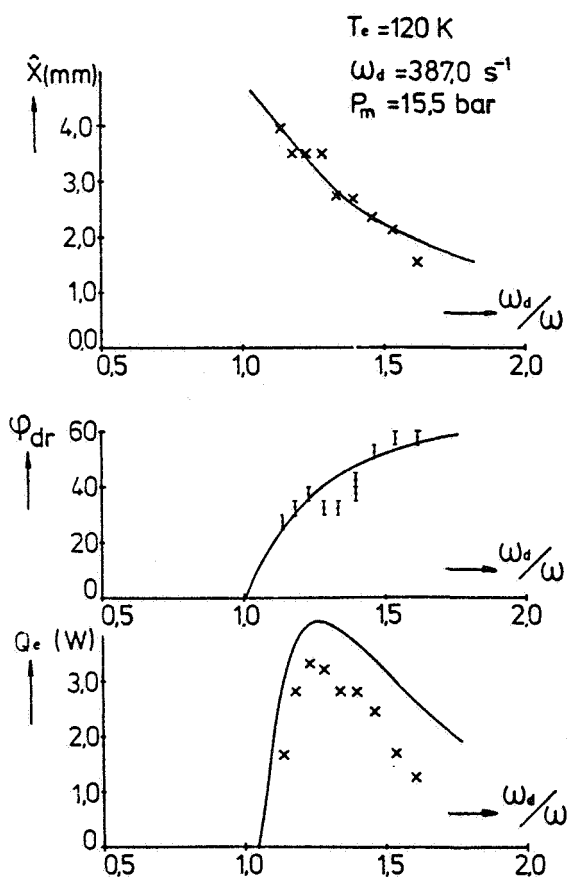


Fig. 6. - Comparison between calculated and experimental results. Displacer amplitude, phase shift and cold production versus  $\omega_d/\omega$

The experimental results with the MMC-80 have been compared with the above described theory, amended with some effects neglected above. These effects are i.e. the inductance of the coil, the variation of the length of the wire ( $l_w$ ) present in the gap and the variation of the constants  $C_p$ ,  $C_v$ ,  $C_{pp}$  and  $C_{dd}$  as derived from numerical Stirling calculations.

Fig. fig. 6 the amplitude of the displacer  $\hat{x}$ , the phase ( $\varphi_{dr}$ ) and the cold production  $Q_e$  have been plotted against  $\omega_d/\omega$ . In this test the piston amplitude  $\hat{y}$ , the temperature of the freezer  $T_e$  and the average pressure  $p_m$  have been kept constant. With an assumed<sup>m</sup> displacer friction of  $F = 0.5$  N, which is a realistic value in this case, the agreement between theory and experiment is reasonably well for  $\hat{x}$  and  $\varphi_{dr}$ . The measured cold production is lower than the calculated  $Q_e$ , which is most often the case in cold-spot machines where the total heat losses are of the same order as the gross cold production. Thus small errors in the loss calculations lead to large errors in net cold production.

In fig. 7 results are given of measure-

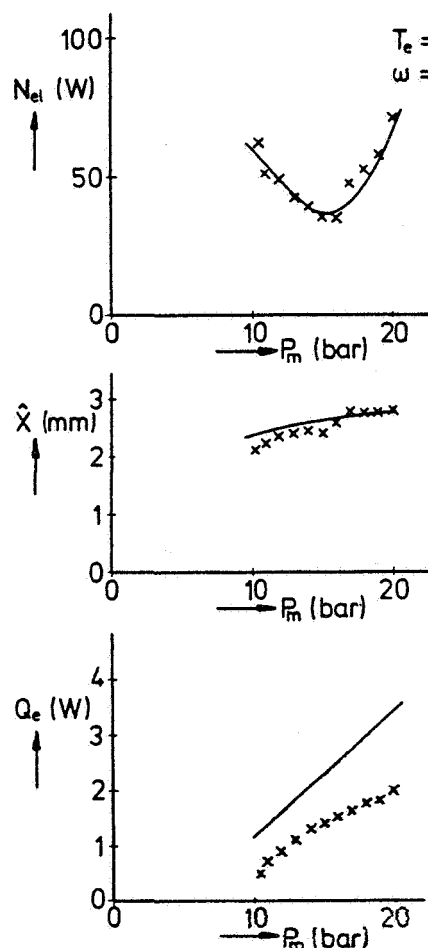


Fig. 7. - Electrical input, displacer amplitude and cold production versus mean pressure with constant  $\omega$

ments where  $p_m$  has been varied and  $\omega$  kept constant. In that case the theory predicts a constant  $\varphi_{dr}$  and  $\dot{x}$ , a linear variation of  $Q_{eo}$  and  $N_p$ , versus  $p_m$  (the piston stroke  $\dot{y}$  is kept constant).

As the electric power  $N_{el}$  is given by:

$$N_{el} = N_p / \eta_e = B_c (\omega \dot{y})^2 / 2 \frac{(1+A)(A+\cos^2 \varphi)}{\sin^2 \varphi}$$

$N_{el}$  will show a minimum at a value of  $p_m$  where the piston is in resonance. Here again good agreement has been found between theory and experiment.

## CONCLUSION

The above method of describing the pressures inside the Stirling cycle as a vectorial sum of different terms depending only on the respective positions and velocities of both displacer and piston offers a simple way of understanding the characteristics of a free displacer Stirling refrigerator driven by a linear motor.

However, a more detailed numerical calculation of the different constants is needed for design purposes. The variation in the constants, and some effects which have been neglected in the simplified theory are yet so large that they cannot be disregarded if good agreement is to be obtained between theory and experiment.

## REFERENCES

1. G.J. Haarhuis, "A Magnetically Driven Stirling Refrigerator". IECEC 7 London, p.422 1978.
2. J.W.L. Köhler and C.O. Jonkers, "Fundamentals of the Gas Refrigerating Machine". Philips Techn. Rev. 16, p.69, 1954.
3. R.J. Meijer, "The Philips Stirling Engine". Ingenieur, vol. 81, May 1969, p. W69, W81.
4. G. Prast and A.K. de Jonge, "A Free Piston Stirling Engine for Small Solar Power Plants". 13th IECEC p.182, 1978.
5. J. Polman, A.K. de Jonge and A. Castelijns, "Free Piston Electrodynamic Gas Compressor". Proc. 1978 Purdue Compressor Technology Conference, Purdue University 1978, p.241.

## NOMENCLATURE

p	pressure
T	temperature
$\tau$	temperature ratio
S	surface area
M	mass
V	volume
B	total volume, normalised to $T_c$ and reduced to $V_0$
x	displacer position
y	piston position
$\omega$	angular frequency
$\varphi$	phase shift between piston and applied voltage
$\varphi_{dr}$	phase shift between piston and displacer
n	cycles per second

t	time
$\alpha$	$\omega t$
$\beta$	$\alpha - \varphi_{dr}$
$\frac{1}{t}$	1/t
Q	cold production
N	power
$\eta$	efficiency
$U_0$	amplitude of the applied voltage
$U_m$	inductive voltage due to the movement of the coil
$R_i$	resistance of the coil
$B_g$	magnet field in the gap
$l_g$	length of wire present in the gap
$i_v$	electric current
$B_c$	constant = $(B_g l_v)^2 / R_i$
$B_u$	constant = $(B_g l_v) / R_i$
A	ratio between $N_p$ and $B_c (\omega \dot{y})^2 / 2$
$F_{fr}$	friction force acting on the displacer
$C_x$	constant of pressure variation due to displacer position
$C_y$	constant of pressure variation due to piston position
$C_p$	constant of flow loss due to piston velocity
$C_d$	constant of flow loss due to displacer velocity
$C_{pp}$	= $C_{pe} - C_{pc}$
$C_{dd}$	= $C_{de} - C_{dc}$
$C_{pd}$	= $-C_{pp} / C_{dd}$
$C_v$	spring constant

## Subscripts

m	mean value
c	compression side
e	expansion side
i	volume i
d	displacer
p	piston
0	reference value

## APPENDIX B

### Basic Theory of Stirling-Cycle Refrigerator



In this section a brief outline of the basic principles of the Stirling cycle is presented.<sup>(1,2)</sup> From an elementary theory the general properties of the cycle will be derived with a discussion of the most important losses. It should be noted that the presentation is essentially taken from Part Two of reference 1. For a more extensive treatment of the subject reference should be made to the original paper<sup>(3)</sup>.

### Fundamental Cycle

In the ideal Stirling cycle, the cold is produced by the reversible expansion of a gas. The gas performs a closed cycle, during which it is alternately compressed at ambient temperature in a compression space and expanded at the desired low temperature in an expansion space, thereby reciprocating between these spaces through one connecting duct, wherein a regenerator provides for the heat exchange between the outgoing and the returning gas flow. Figure 1 shows stages in carrying out the ideal cycle.

In this diagram, A is a cylinder, closed by the piston B, and containing a nearly perfect gas. A second piston, the displacer C, divides the cylinder into two spaces, D at room temperature and E at the low temperature, connected by the annular passage F. This passage contains the regenerator G, a porous mass with a high heat capacity; the temperature in the passage is shown in the graph. The cycle, consisting of four phases, runs as follows:

- I Compression in space D by the piston B; the heat of compression is discharged through the cooler H.

<sup>1</sup> Dr. J. W. L. Köhler "The Gas Refrigerating Machine and Its Position in Cryogenic Technique," Progress in Cryogenics 2, 41-67 (1960) London, Heywood and Company Ltd.

<sup>2</sup> A. Daniels, "Cryogenics for Electro-Optical Systems," Electro-Optical Systems Design, vol. 3, pp. 12-20, July 1971.

<sup>3</sup> J. W. L. Köhler and C. O. Jonkers, Philips Tech Rev. 16 69-78, 105-115 (1954)

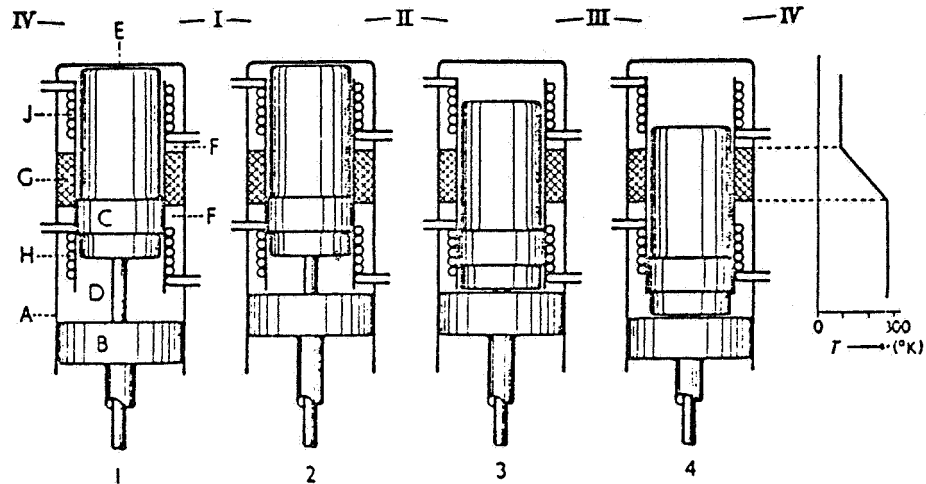


Figure 1. The ideal Stirling cycle. The Figure shows the different positions 1-4, according to Figure 2. I-IV refer to the four phases of the cycle. The graph on the right shows the temperature distribution in the machine

II Transfer of the gas through the regenerator to space E by movement of the displacer. The gas is reversibly cooled down in the regenerator, the heat of the gas being stored in the regenerator mass.

III Expansion in the cold space by the combined movement of the piston and the displacer; the cold produced is discharged through the freezer J, and utilized.

IV Return of the gas to space D; thereby the gas is reheated, the heat stored in the regenerator being restored to the gas.

With no regenerator present the gas flowing to the expansion space would arrive there at ambient temperature, whereas the returning gas would arrive in the compression space at the low temperature; this effect would cause such a tremendous cold loss that the whole process would become futile. In an ideal regenerator, a temperature gradient is established in the direction of the gas flow. This causes the gas to be cooled down reversibly, so that it arrives in the expansion space with the temperature prevailing there.

Figure 2 shows the p-V diagram of this schematic cycle, neglecting the dead space. It consists of two isotherms and two isochores; at  $T_C$  (compression temperature) the amount of heat  $Q_C$  is rejected, at  $T_E$  (expansion temperature) the amount of heat  $Q_E$  is absorbed.

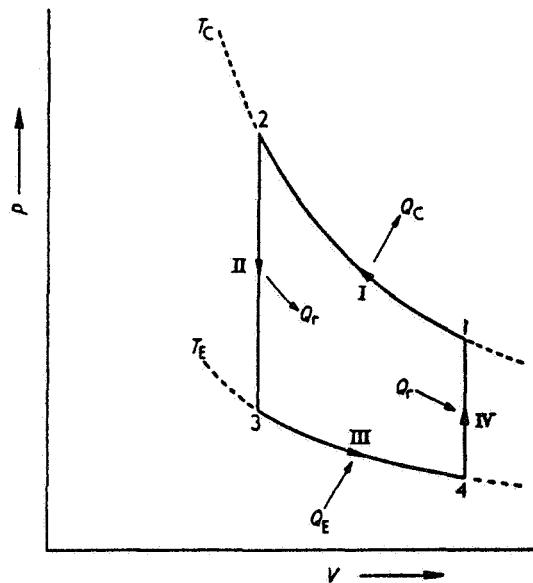


Figure 2. p-V diagram of the ideal cycle, between the temperatures  $T_C$  and  $T_E$ , where the amounts of heat  $Q_C$  and  $Q_E$  are discharged and absorbed, respectively. The heat  $Q_r$ , rejected in phase II, is stored in the regenerator and absorbed in phase IV

Actually, the discontinuous movement of the pistons is difficult to achieve. In practice, the pistons are actuated by a crank mechanism and are thus moving harmonically; for the machine to act as a refrigerator, the expansion space E (Figure 1) has to lead in phase with respect to the compression space D. The harmonic motion and the volume of the heat exchangers (the so-called 'dead space') cause the four phases of the cycle to merge somewhat, so that they cannot be distinguished very well; the gas is not exclusively compressed in the compression space, but also in the expansion space, and the same holds for the expansion. It can be shown however that the difference in output between the discontinuous and the harmonic process is only a few percent.



The fundamental cycle is explained here with the help of the displacer machine. The reason is that actual machines are also of this type. It will be obvious, however, that the cycle may be described more generally by two synchronously changing volumes interconnected by a cooler, a regenerator, and a freezer, whereby the volume that is leading in phase becomes the expansion space wherein the cold is produced. Formulae for the pressure variation, the refrigerating capacity, and the shaft power for this general case will be given in the next section.

#### Performance of the Ideal (Isothermal) Cycle

In the ideal machine, the thermal contact in the heat exchangers is assumed to be perfect, so that the gas temperature there is equal to the temperature of the walls; the same temperature is supposed to prevail in the adjoining cylinders, which temperatures thus are constant with time. The regenerator is also assumed to be perfect, so that no regeneration loss occurs and the gas temperature there is also constant with time. The working fluid is supposed to be a nearly perfect gas; this condition can be met sufficiently by using hydrogen or helium in practice.

(1) Pressure variation. For the expansion space  $V_E$  (temperature  $T_E$ ) and the compression space  $V_C$  (temperature  $T_C$ ) we write

$$\left. \begin{aligned} V_E &= \frac{1}{2} V_0 (1 + \cos \alpha) \\ V_C &= \frac{1}{2} w V_0 [1 + \cos(\alpha - \phi)] \end{aligned} \right\} \quad (1)$$

where  $V_0$  is the maximum volume of the expansion space,  $w$  the ratio of the swept volumes of the compression and the expansion space, and  $\phi$  the phase difference between these spaces; the crank angle  $\alpha (= 0$  for  $V_E = V_{\max}$ ) changes linearly with time ( $\alpha = \omega t$ ). The volumes of the freezer, the regenerator, and the cooler, which form the connecting channel (the dead space), will be indicated by  $V_S$  with the corresponding temperature  $T_S$ . The variation of the pressure  $p$  with time (or  $\alpha$ ) now follows from the condition that the mass of the system as a whole is constant:

$$\frac{M}{R} p \left[ \frac{V_E}{T_E} + \frac{V_C}{T_C} + \sum \frac{V_i}{T_i} \right] = \text{constant} = C \cdot \frac{M V_0}{R 2 T_C}$$

where M is the molecular weight of the gas, R is the gas constant, and C is a constant. After introduction of  $V_E$  and  $V_C$  from equation (1) and of the symbols

$$\tau = \frac{T_C}{T_E}, \text{ the temperature ratio}$$

and

$$s = \sum \frac{V_i}{V_0} \cdot \frac{T_C}{T_i}, \text{ the total dead space}$$

(reduced to the swept volume of the expansion space  $V_0$  and normalized to the temperature of the compression space  $T_C$ ), this reduces to

$$\frac{C}{p} = \tau \cos \alpha + w \cos(\alpha - \phi) + \tau + w + 2s$$

This expression is easily transformed into

$$\frac{C}{p} = A \cos(\alpha - \theta) + B = B[1 + \delta \cos(\alpha - \theta)]$$

with the abbreviations

$$A = \sqrt{(\tau^2 + w^2 + 2\tau w \cos \phi)}; \quad B = \tau + w + 2s$$

$$\frac{A}{B} = \delta; \quad \tan \theta = \frac{w \sin \phi}{\tau + w \cos \phi}$$

The constant A may be interpreted as two times the total change of volume, while B equals two times the mean total volume, both reduced to  $V_0$  and normalized to  $T_C$ . For the pressure p we thus find

$$p = \frac{C}{B} \frac{1}{1 + \delta \cos(\alpha - \theta)}$$

which may be written more conveniently

$$p = \frac{p_{\max}(1-\delta)}{1+\delta \cos(\alpha-\theta)} = \frac{p_{\min}(1+\delta)}{1+\delta \cos(\alpha-\theta)} \quad (2)$$

with the introduction of  $p_{\max}$  and  $p_{\min}$  for the maximum and minimum values of the pressure during the cycle.

Expression (2) shows that the pressure variation with time is not purely harmonic. In practice, the deviation of harmonic behaviour is rather small however (the function is symmetrical with respect to  $p_{\max}$  and  $p_{\min}$ , which points are  $180^\circ$  apart), as the value of  $\delta$  seldom exceeds 0.4. This means that the pressure ratio of this type of machine

$$\frac{p_{\max}}{p_{\min}} = \frac{1+\delta}{1-\delta}$$

is about 2, a remarkably low value compared with what is normal in refrigerating apparatus. The presence of the phase angle  $\theta$  shows that the pressure variation is not in phase with the variation of the expansion or the compression space; it is easily checked that its phase is intermediate between that of these spaces ( $\theta \rightarrow \phi$  for  $\tau \rightarrow 0$ ). It will be found, for this reason, heat is absorbed in the expansion space and liberated in the compression space. For later reference, given here is the expression for the mean pressure  $p_m$ , deduced by integrating the pressure with respect to the crank angle  $\alpha$ :

$$p_m = p_{\max} \sqrt{\left(\frac{1-\delta}{1+\delta}\right)} \quad (3)$$

(2) Heat absorption in cylinders. The heat absorbed per cycle in the expansion space ( $Q_E$ ) and in the compression space ( $Q_C$ , a negative quantity) is given by

$$Q_E = \oint p dV_E, \quad Q_C = \oint p dV_C$$

That these expressions, which are normally used for spaces with a constant gas content, may also be used in the case where gas enters and leaves the space can be proved by an involved thermodynamic reasoning which is omitted here. It is easily seen that the value of the integrals depends only on the components of  $p$  which have the same phase as  $dV_E$  and  $dV_C$ ; this means that  $0 < \theta < \phi$  if the machine has to operate as a refrigerator. Evaluation of the integrals leads to

$$\left. \begin{aligned} Q_E &= \frac{\pi}{a} V_0 p_m \frac{w \sin \phi}{B} \\ Q_C &= -\tau Q_E \end{aligned} \right\} \quad \dots(4)$$

with

$$a = 1 + \sqrt{1 - \delta^2} \simeq 2$$

For practical use, equation (4) may be transformed into  $q_E$ , the heat absorbed per second (or the refrigerating capacity) by inserting  $n$ , the number of revolutions per minute. If  $V_0$  is expressed in  $\text{cm}^3$ ,  $p_m$  in  $\text{kg cm}^{-2}$ , and  $q_E$  in watts, it is found that

$$q_E = \frac{5.136}{a} V_0 p_m \frac{n}{1000} \frac{w \sin \phi}{B} \quad (\text{in watts}) \quad \dots(4a)$$

Expression (4a) shows that, besides with  $V_0$  and  $n$ , the output is proportional to  $p_m$  and inversely proportional to the function  $B$ , which was defined as the mean reduced and normalized volume. The consequences of the dependence on the mean pressure and the temperature ratio ( $\tau$  is also contained in  $s$ ), which constitutes one of the features of the process, will be discussed at more length later. According to expression (4a) an increase of the dead space  $s$  reduces the output, as could be expected. A discussion on the influence of the design constants  $w$  and  $\phi$  would be very elaborate and lengthy and is therefore outside the scope of this report; their choice depends largely on the losses of the process.

(3) Shaft power and efficiency. For the work  $W$  needed to drive the machine one may write

$$W = -Q_E - Q_C$$

Thus

$$W = (\tau - 1)Q_E = \frac{\pi}{a}(\tau - 1)V_0 \rho_m \frac{w \sin \phi}{B} \quad \dots(5)$$

Using equation (5) the efficiency of the cycle is

$$\eta = \frac{Q_E}{W} = \frac{1}{\tau - 1} = \frac{T_E}{T_C - T_E} \quad \dots(6)$$

The efficiency of the ideal cycle thus equals that of the Carnot cycle; this is obvious as the cycle is completely reversible.

Although in actual machines the performance is reduced by losses, to be discussed in the next section, the ideal cycle has to be considered as the reference process, because most essential facts can be deduced from it.

Before closing this section two remarks on the representation of the process will be made. The first remark concerns the representation in a thermodynamic diagram (e.g.,  $p$  vs  $V$ ,  $T$  vs  $S$ , etc.). These diagrams always relate to a fixed quantity of the working fluid, which has to be in internal equilibrium (equal  $p$  and  $T$  throughout); this quantity is passed through a number of thermodynamic states and (at least in a closed system) is returned ultimately to its initial state, so that a cycle is described. Looking at the Stirling process, it is found that, in so far as cyclic behaviour is concerned, nothing abnormal is at hand. However, the system is not homogeneous at all, as different parts of it have a different temperature. As a consequence, different gas particles describe completely different cycles between different temperatures; to mention only two extreme examples, some particles are reciprocating between the compression space and a point in the cooler, while other particles are reciprocating between a point in the freezer and the expansion space. That, because of this situation, normal diagrams have lost their value is shown by the fact that one would have to draw an infinite number of diagrams for the diverse particles with different cycles, which obviously leads

nowhere. The only diagram which still has some sense is the  $p$ - $V$  diagram, as the system is homogeneous in  $p$ . But in such a diagram one is not allowed to draw isotherms or adiabates, as these lines have lost their meaning. To avoid this difficulty when drawing Figure 2, the dead space was assumed to be zero; in that case isotherms may be drawn, since only then the gas is at thermal equilibrium during the compression and the expansion. When the adiabatic losses are discussed in the next section, this subject will have to be returned to. The second remark concerns the description of the cycle in a schematic form. The transfer of the gas from the compression space to the expansion space and vice versa is performed with constant volume of the gas; this is the simplest representation, as the transfer can be effected by the movement of the displacer only. But this way of transfer is only one example of a multitude of possibilities which exhibit the common property that regeneration is possible. As another example consider transfer at constant pressure, which way of transfer approximates the harmonic cycle much better. The only reason why this manner of transfer is not used to explain the cycle is that it can only be accomplished by simultaneous movement of the piston and the displacer, which obviously is more complicated. This point is stressed because at many places in literature the transfer with constant volume is considered to be one of the main characteristics of the Stirling cycle, to contrast it with the cycle of Claude (with separate compressor and expander), where the transfer is performed at constant pressure. As explained, this view does not correctly locate the distinction between the two cycles, the real difference being that in the Stirling cycle the gas is reciprocating through one connecting duct, wherein the heat exchange is brought about by regeneration, whereas in the Claude cycle the connecting circuit consists of a counter-flow heat exchanger (with two channels). Apart from the restriction contained in the first remark the Stirling cycle thus closely resembles the Claude cycle thermodynamically.

### The Actual Cycle

As stated already, the actual cycle differs from the ideal one by the occurrence of losses. For a fuller discussion on this subject reference is made to the original paper<sup>(2)</sup>, here only the most characteristic effects will be treated.

The losses can affect the process in two different ways, viz., by increasing the shaft power and by decreasing the refrigerating capacity; the smaller the ideal values of these quantities, the more pronounced will be the relative effect. Figure 3 illustrates that increase of the shaft power exerts the greatest influence at high refrigerating temperatures, while decrease of the output creates the most adverse effects at low temperatures. In this way a temperature range arises, the "optimum working range", wherein the actual efficiency differs least from the ideal one (i.e., where the figure of merit is highest). This range may be shifted both to higher and to lower temperatures by suitable design; moreover, its limits greatly depend on present and future technological possibilities.

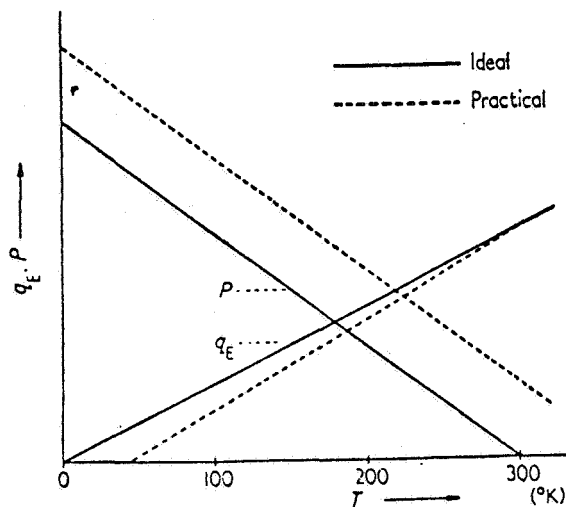


Figure 3. Graphs of the shaft power  $P$  and the refrigerating capacity  $q_E$  as a function of temperature. The full lines apply to the ideal process, the dotted lines to an actual machine with losses

The increase in shaft power is mainly due to three causes, namely, the mechanical loss of the drive, the flow loss (that is, the power needed to force the gas through the narrow connecting circuit) and the adiabatic loss. The first two losses need no further comment, but the adiabatic loss will be discussed at greater length. In the ideal isothermal process it was assumed that the temperature in the cylinders is constant with time. This means that the thermal contact between the gas and the wall in the cylinder spaces is assumed to be so perfect that these walls can be employed as well to establish the contact between the gas and the surroundings, that is, to serve as cooler and freezer. In this case, separate heat exchangers are of no use and must be omitted; this ideal machine thus consists of the two cylinders and the regenerator and is therefore referred to as the "three-element machine".

Actually, the separate heat exchangers are introduced because the thermal contact between the gas and the cylinder walls is always so poor that insufficient heat exchange with the surroundings can be established through these walls; for this case the name "five-element machine" is used. As a consequence, the temperature of the gas in the cylinders changes nearly adiabatically with time. This adiabatic behavior has only a minor influence on the efficiency (it would be too involved to give the full explanation here; it is based on the fact that these processes occur in both cylinders with the same phase, so that the temperature ratio is independent of time) but in this case the heat (or the cold) must be transported from the cylinders to the heat exchangers. This transport can only be effected by the reciprocating gas which performs it by assuming different temperatures when flowing in opposite directions, with the result that the mean temperature in each cylinder deviates from that in the adjoining heat exchanger. Figure 4 shows schematically the temperature distribution in the machine. It will be observed that the mean temperature in the expansion cylinder is lower than that of the freezer and that the mean temperature in the compression cylinder is higher than that of the cooler. This means that the ratio of the cylinder temperatures is higher than that of the temperatures of the



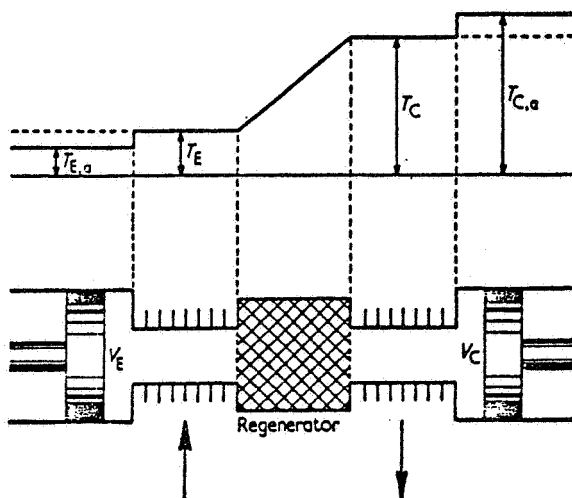


Figure 4. Temperature distribution in the adiabatic 'five-element machine'. The contact with the surroundings is effectuated by the cooler and the freezer. The mean temperature in the compression space  $T_{C,a}$  is higher than the cooler temperature  $T_C$  as heat must be transported from the cylinder to the cooler; by the same argument the mean temperature in the expansion space  $T_{E,a}$  is lower than that of the freezer  $T_E$ .

heat exchangers, which causes an increase in shaft power. Strictly speaking, the expression "adiabatic loss" is therefore misleading and should be replaced by "transport loss". It is adhered to though, because ultimately the adiabatic behavior is the fundamental cause that has necessitated the introduction of separate heat exchangers. Because the value of the temperature ratio  $\tau$  is larger in the adiabatic than in the isothermal case, one would expect also a decrease in refrigerating capacity; this influence is very small, however, as the larger value of  $\tau$  is nearly compensated by a decrease of the quantity  $B$ , the mean relative volume of the working circuit, which quantity has another form in the adiabatic case.

In the above discussion the use of the expressions "adiabatic compression" or "expansion" has been intentionally avoided. The reason is that the gas is compressed and expanded everywhere in the working space; its behavior during these processes, however, depends largely on the condition of heat transfer prevailing in the various sections of the volume. While in the cylinders the gas temperatures change nearly adiabatically, this is not the case in the connecting circuit;

in the regenerator, for example, the heat transfer is so high, that the behavior is practically isothermal. Thus, while the actual Stirling process is certainly not isothermal, it would be incorrect to call it adiabatic. This situation thus furnishes still another example for the previously made remark that thermodynamic diagrams are of little value for this process.

The decrease of the refrigerating capacity is mainly due to two effects, the flow loss and the insulation loss. Again no comment is made on the flow loss. Also the insulation (and conduction) loss proper needs no discussion. There exists another loss, however, that acts as an insulation loss as well which has the utmost importance for the quality of the process. This loss, caused by the non-ideal behavior of the regenerator, will now be discussed.

It is obvious that in the Stirling process ideal regeneration is possible in principle as the same amount of gas passes the regenerator in both directions with the same temperature difference, so that the amount of heat rejected and absorbed by the gas for both directions of flow is the same, since the specific heat is independent of pressure (which is practically the case for nearly perfect gases). The following argument shows the extreme importance of a small departure from ideality of the regenerator, caused by non-ideal heat transfer. In the regenerator a quantity of heat  $Q_r$  must be absorbed and rejected in each cycle. Owing to imperfections, this amount is reduced to  $\eta_r Q_r$ , where  $\eta_r$  is the efficiency of the regenerator. This means that only part of the available heat is transferred to the regenerator. The rest, that is  $(1-\eta_r)Q_r$ , is carried along with the gas through the regenerator, so that the gas arrives too hot in the expansion space. This remainder,  $\Delta Q_r$ , thus constitutes the regeneration loss. As this loss must be made up from the cold produced  $Q_E$ , it must be compared with this quantity. Calculations show that

$$\frac{\Delta Q_r}{Q_E} = C_r(1-\eta_r)\frac{T_C-T_E}{T_E} \quad \dots(7)$$

The constant  $C_r$  depends mainly on the compression ratio; its value is approximately 10. For example, take  $T_C = 300^\circ\text{K}$ ,  $T_E = 75^\circ\text{K}$ , and the regeneration loss  $1 - \eta_r = 1\%$ ; then

$$\frac{\Delta Q_r}{Q_E} = 10 \times 1 \times 3 = 30 \text{ per cent}$$

Thus each percent of regeneration loss involves a loss of 30 per cent in refrigerating power; below  $30^\circ\text{K}$  this figure even increases to greater than 90 percent, meaning that at such temperatures the entire cold production is consumed by the regenerator. It is thus no exaggeration to call the regenerator the heart of the machine.

The regenerator used in actual gas refrigerating machines consists of a mass of fine metal wire, forming a light felt-like substance. With this type of material, efficiencies of 99 per cent and higher can be obtained; the thermal conductivity of the material is very low.

This section will be ended with a short discussion on the problem of how to minimize the total sum of the losses; this problem is very involved indeed, so that only a very broad outline can be given. As an example, the regenerator will be considered. The losses of the regenerator make themselves felt in three different ways, viz., the regeneration loss (reducing the cooling power), the flow loss, and the dead space (this is not a real loss as the shaft power is also decreased; it exerts its influence through the other losses, as these increase relatively). The regeneration loss can be reduced by making a longer regenerator; this, however, increases the flow loss and the dead space. One may also give the regenerator a larger cross-section; this reduces the flow loss and somewhat the regeneration loss, but increases the dead space. Thus it is possible to find optimum dimensions for the regenerator. The same hold for the freezer and the cooler, where the regeneration loss is replaced by the loss due to insufficient heat transfer. Moreover, the losses are governed by the choice of the values of  $w$  and  $\phi$ . Finally, the

## PHILIPS LABORATORIES

outside of the cooler and the freezer must be made optimal. Thus a very large number of design parameters are to be fixed such that the total result gives an optimum condition; it will be obvious that a lot of experience is needed to find the right solution quickly. This is compensated by the fact that once a system of calculation is worked out, it holds for any size of machine.

## BIBLIOGRAPHIC DATA SHEET

1. Report No.	2. Government Accession No.	3. Recipient's Catalog No.	
4. Title and Subtitle DESIGN AND FABRICATION OF A LONG-LIFE STIRLING CYCLE COOLER FOR SPACE APPLICATION Phases I and II - Engineering Model		5. Report Date March 1983	
		6. Performing Organization Code	
7. Author(s) F. Stolfi, M. Goldowsky, C. Keung, L. Knox, E. Lindale R. Maresca, J. Ricciardelli, P. Shapiro		8. Performing Organization Report No. PL-11-CR83-0307	
9. Performing Organization Name and Address PHILIPS LABORATORIES A Division of North American Philips Corp. Briarcliff Manor, New York 10510		10. Work Unit No.	
		11. Contract or Grant No. NAS5-25172	
		13. Type of Report and Period Covered  Final Report 29 Sept 1978 - 31 Dec 1982	
12. Sponsoring Agency Name and Address NASA GODDARD SPACE FLIGHT CENTER Greenbelt, Maryland 20771		14. Sponsoring Agency Code	
15. Supplementary Notes			
16. Abstract  A laboratory model of a Stirling cycle cryogenic refrigerator capable of producing 5 Watts of cooling at 65° Kelvin was designed, fabricated, and tested. The cooler successfully demonstrated the concept feasibility of providing refrigeration for long-life, reliable operation in spaceborne missions, through the development of several innovative electro-mechanical features. Linear, moving-magnet, electric motors provide a direct-drive mechanism having no crankshafts, linkages or flexing electrical leads. The moving mechanical elements, the piston and displacer, are supported with linear magnetic bearings which provide non-lubricated, contact-free operation. The pressure seals are formed by long, narrow, annular gaps, thereby eliminating the possibility of performance degradation by mechanical wear. Electronic control of the axial position of the piston and displacer permits independent adjustment of their amplitudes and phase relationship during operation. All internal parts are fabricated of only metal and ceramic components, thereby removing all forms of organic contamination. This synergistic approach omits all the life limiting aspects of conventional Stirling cycle machines. This report details the steps taken to combine the thermodynamic, mechanical, magnetic, and electronic features of this work into a successfully operating refrigerator. Results of tests conducted on the refrigerator and its major component parts are discussed.			
17. Key Words (Selected by Author(s))  Stirling Cycle Cryogenic Refrigerator Linear Magnetic Bearing Electronic Control System Cooler Clearance Seals  Linear Motor Thermodynamics		18. Distribution Statement	
19. Security Classif. (of this report)	20. Security Classif. (of this page)	21. No. of Pages 223	22. Price*